NUMERICAL STUDY ON METALLIC PHOTONIC BAND-GAP STRUCTURES FOR TERAHERTZ WAVEGUIDING

Elif DEĞİRMENCİ

B.Sc., M.Sc.,

A Dissertation submitted in fulfilment of the requirements for the award of
Doctor of Philosophy (Ph.D.)

Dublin City University
Faculty of Engineering and Computing,
School of Electronic Engineering

Research Supervisor
Dr. Pascal LANDAIS

February, 2012

Declaration

I hereby certify that this material, which I now submit for assessment on the programme of study leading to the award of Doctor of Philosophy is entirely my own work, that I have exercised reasonable care to ensure that the work is original, and does not to the best of my knowledge breach any law of copyright, and has not been taken from the work of others save and to the extent that such work has been cited and acknowledged within the text of my work.

Signed: Student ID: 57123276

(Elif DEĞİRMENCİ)

Date:

To Fatih

Acknowledgements

First and foremost, I would like to thank my supervisor and advisor Dr. Pascal Landais for giving me the opportunity. It has been a pleasure to work with him. I appreciate his guidance, support and patience during these years.

Many thanks to all present and former members of Radio and Optical Communications Lab, Sylwester, Krzysztof, Robert, Karl, Kevin, Kai, Daniele, Josue, Colm, Haymen, Ramon, Severine, Fred, Prince, Liam for making the lab such a nice place to work. I would also like to thank Dominik for our fruitful discussions.

A very special thanks to Dr. Conor Brennan, for his help in opening the door to DCU for me. Thanks to former members of the RF Modelling and Simulation Group, Marie, Diana, John, Patrick, Biji for their help in my first couple of months in DCU.

Thanks to Zeliha and Ozlem for their friendship and being there for me. I have greatly enjoyed the time we have spent together.

Last but not least, I would also like to thank my parents and family for their continuing love and support. Very special thanks to my husband Fatih, for his invaluable love, support, and patience. I could not have done this without him.

Abstract

This work focuses on numerical calculations of metallic photonic band-gap structures. Photonic crystals are man-made structures that reflect electromagnetic waves whose frequency value falls within the photonic crystal band-gap. Metallic photonic crystals have been used due to certain advantages over dielectric crystals, which can be relevant for guiding THz radiations. The THz range is localised between microwave and optical frequency regions. THz frequencies have been studied for possible applications in many areas such as, imaging, security, medical, material characterization, spectroscopy to name a few. Metallic photonic crystals are used for various THz waveguides' designs, with the aim of sustaining high power THz transmission.

The transmission properties as well as dispersion relations of metallic photonic crystal are investigated by means of Finite Element Method. Throughout the study, FEM results are often compared to some other methods in order to validate the calculation steps in our modelling process and to assess the boundary conditions. In the simulations frequency dependency and losses have been taken into account.

Dispersion diagrams and guided modes have been studied to achieve further understanding on the transmission characteristics of metallic photonic crystal waveguides. Excellent agreement has been obtained from the comparison of dispersion

diagrams and the transmission spectra of waveguides. Special care has been paid to achieve optimized design parameters that give wide bandwidths with high transmission levels. Other passive components have also been studied such as filters, bends and splitters. In order to improve their transmission characteristics, several designs have been investigated. Consistently high transmission levels have been achieved with our waveguides over a wide range of THz frequencies. It was possible to provide innovative designs for the bend and linear waveguides. The transmission spectra of these waveguides have been analysed and a deep understanding of the metallic photonic crystal waveguide has been achieved.

Table of Contents

Declaration **ii**

Dedication **iii**

Acknowledgements **iv**

Abstract **v**

List of Figures **xi**

List of Tables **xxii**

1 INTRODUCTION **1**

2 FUNDAMENTALS OF PHOTONIC CRYSTALS **5**

2.1 Photonic Crystal Theory 9

2.1.1 The Macroscopic Maxwell's Equations 10

2.1.2 Scaling Properties of Maxwell's Equation 14

2.2 Theory of the Photonic Band-Gap 15

2.2.1 The Brillouin Zone and the Reciprocal Lattice 16

2.2.2 Dispersion relation 19

2.3 Band-Gap of 1D Photonic Crystals 20

2.4 Band-Gap of 2D Photonic Crystals 22
2.4.1 Square Lattice 23
2.4.2 Triangular Lattice 25
2.5 Devices Based on the Photonic Crystals 32
2.6 Conclusion 37
References 38

3 MODELLING TOOLS 45
3.1 Plane Wave Expansion Method 46
3.2 Transfer Matrix Method 52
3.3 Finite Difference Time Domain Method 54
3.4 Finite Element Method 59
3.5 Conclusion 65
References 66

4 TERAHERTZ TECHNOLOGY 71
4.1 Applications of THz 72
4.2 THz Radiation 75
4.2.1 THz Generation 75
4.2.2 THz Detection 78
4.3 Terahertz Waveguides 79
4.4 Conclusion 82
References 83

5 THE ANALYSIS OF METALLIC PHOTONIC CRYSTALS 92
5.1 Optical Properties of Metals 93
5.2 2D Metallic Photonic Crystals 103

5.2.1 Properties of Metallic Photonic Crystals 104
5.2.2 Metallic Band-Gap 105
5.3 Dispersion Analysis of Metallic Photonic Crystals 107
5.3.1 Square Lattice 108
5.3.2 Triangular Lattice 115
5.4 Transmission Characteristics of Metallic Photonic Crystals 119
5.4.1 Square Lattice 124
5.4.2 Triangular Lattice 135
5.5 Band-Gap Maps 146
5.6 Conclusion 149
References 151

6 LINEAR DEFECTS IN 2D METALLIC PHOTONIC CRYSTALS 157
6.1 Introduction 158
6.2 Dispersion Analysis 160
6.3 Square Lattice Waveguide 161
6.4 Triangular Lattice Waveguide 169
6.5 Transmission Analysis 174
6.5.1 Validation of the Two-Dimensional Approximation 177
6.5.2 Square Lattice Waveguide 180
6.5.2.1 W1 Waveguide 183
6.5.2.2 W2 Waveguide 190
6.5.3 Triangular Lattice Waveguide 194
6.5.3.1 W1 Waveguide 197
6.5.3.2 W3 Waveguide 200
6.6 Conclusion 205

References 207

7 METALLIC PHOTONIC CRYSTAL DEVICES 209

7.1 Bend Waveguides 210

7.1.1 90° Bend Waveguides 211

7.1.2 60° Bend Waveguides 222

7.2 Power Splitters 229

7.2.1 T-Splitters 230

7.2.2 Y-Splitters 235

7.3 Conclusion 237

References 239

8 CONCLUSIONS AND FUTURE WORK 244

A LIST OF PUBLICATIONS 248

B BÉZIER CURVE APPROXIMATION 251

List of Figures

2.1 Schematic illustrations of one-, two-, and three-dimensional photonic crystals. 7

2.2 Schematic of an example of 1-D photonic crystal. 9

2.3 Photonic band structure of 1D photonic crystals, the ratio of the thickness of alternating layers is 0.5 where the dielectric constants are a) $\varepsilon_1 = 13$ and $\varepsilon_2 = 13$, b) $\varepsilon_1 = 13$ and $\varepsilon_2 = 12$, c) $\varepsilon_1 = 13$ and $\varepsilon_2 = 1$. The grey areas depict the photonic band-gaps. 22

2.4 Square Lattice a) Lattice generated by the basis vectors b) The corresponding reciprocal lattice and reciprocal vectors c) First Brillouin zone (Wigner-Seitz primitive cell) and irreducible region denoted as square and triangle, respectively. 24

2.5 Triangular Lattice a) Lattice generated by the basis vectors b) The corresponding reciprocal lattice and reciprocal vectors c) First Brillouin zone (Wigner-Seitz primitive cell) and irreducible region denoted as hexagon and triangle, respectively. 25

2.6 Directions and electromagnetic field vectors for TE and TM polarizations considered for 2D photonic crystals. 27

2.7 The photonic band structure for a square array of dielectric columns embedded in air, ε_1 = 11.7 and ε_2 = 1, with r = 0.2a. The photonic band gaps are shown by shaded areas a) TM polarization b) TE polarization. 29

2.8 The photonic band structure for a triangular of dielectric columns embedded in air, ε_1 = 1 and ε_2 = 11.7, with r = 0.48a. The photonic band gaps are shown by shaded areas a) TM polarization b) TE polarization. 30

2.9 Band-gap map for a square array of silicon in air, red and black regions show band-gap islands of TE and TM modes, respectively. . 32

2.10 Band-gap map for triangular array of holes in silicon, red, black and yellow regions show band-gap islands of TE, TM modes and both, respectively. 33

2.11 Schematics of two-dimensional photonic devices made of photonic crystals. a) a microcavity, b) a waveguide, c) a waveguide bend, d) a waveguide splitter. Here those circles can be considered as the air holes etched in a solid slab, or as rods/pillars standing in air. 34

2.12 Schematic figure of photonic crystal fiber 36

3.1 Illustration of Yee cell for a 3D case where a cubic voxel is used representing E and H fields. On the Yee cell, E field components are arranged to form the edges of the cube while the H fields are normal to the face of the cube. 55

3.2 Schematic illustration of PML boundary layers surrounds a 2D computational domain. 58

3.3 The computational domain of the photonic crystal discretized with triangular mesh in FEM and rectangular grid in FDTD method. The figure shows that a circle, which represents rods or holes, resolved well than uniform Cartesian grid. FEM mesh converge using triangular mesh without staircase approximation on the boundaries as in the grid based meshing. 61

3.4 TM band structure of 2D photonic crystal in square lattice of silicon rods in air, radius $r = 0.2a$. Solid black lines represent the bands calculated using the PWE method. The bands calculated using FEM are represented with red dots. 64

3.5 TE band structure of 2D photonic crystal in square lattice of silicon rods in air, radius $r = 0.2a$. Solid black lines represent the bands calculated with the PWE method. The bands calculated with FEM are represented with red dots.. 65

4.1 The THz gap in the electromagnetic spectrum. 71

5.1 a) Real part and b) imaginary part of the relative permittivity of copper, silver, gold, and aluminium calculated using frequency-dependent Drude model for THz frequencies, represented by square, triangle, cross and circle, respectively. 98

5.2 a) Real part and b) imaginary part of the conductivity of copper, silver, gold, and aluminium calculated using frequency-dependent Drude model for THz frequencies, represented by square, triangle, cross and circle, respectively. 98

5.3 Reflectivity as a function of frequency described by Drude model for copper, silver, gold, and aluminium in the THz frequency range represented by square, triangle, cross and circle, respectively. . . . 100

5.4 Skin depth as a function of frequency for copper, silver, gold, and aluminium in the THz frequency range represented by square, triangle, cross and circle, respectively. 101

5.5 The unit cell of a square lattice 110

5.6 The photonic band structure of a square lattice of metal cylinders in vacuum for E-polarization. The PhC is characterized by a 50 μm lattice period in square lattice pattern with a radius of $0.2a$. The left inset shows the high symmetry points at the corners of the irreducible Brillouin zone, the right inset the square lattice pattern. . 111

5.7 The photonic band structure of a square lattice of metal cylinders in vacuum for H-polarization. The PhC is characterized by a 50 μm lattice period in square lattice pattern with a radius of $0.2a$. The left inset shows the high symmetry points at the corners of the irreducible Brillouin zone, the right inset the square lattice pattern. . 112

5.8 Electric field distribution of first 6 eigenmodes at Γ point of a square lattice of metallic circular cylinders for E-polarization. In the figures the maximum of electric field is normalized to unity. 114

5.9 The spectral range and position of band-gaps for E-polarization for varying rod sizes. 114

5.10 Schematic of triangular lattice pattern; the unit cell of a triangular lattice is highlighted. Cartesian coordinates and the lattice directions used for calculations i.e. Γ - M and Γ - K are also depicted. . . 115

5.11 The photonic band structure of a triangular lattice of metal cylinders in vacuum for E-polarization. The PhC is characterized by a 50 μm lattice period in triangular lattice pattern with a radius of $0.2a$. The left inset shows the high symmetry points at the corners of the irreducible Brillouin zone, the right inset the triangular lattice pattern. 116

5.12 The photonic band structure of a triangular lattice of metal cylinders in vacuum for H-polarization. The PhC is characterized by a 50 μm lattice period in triangular lattice pattern with a radius of $0.2a$. The left inset shows the high symmetry points at the corners of the irreducible Brillouin zone, the right inset the triangular lattice pattern. 117

5.13 Electric field distribution of first 6 eigenmodes at Γ point of a triangular lattice of metallic circular cylinders for E-polarization. In the figures the maximum of electric field is normalized to unity. 118

5.14 Schematic illustration of photonic crystal rods in square array, showing the lattice parameters r and a. 125

5.15 Schematic illustration of the geometry used in calculations. Red circles correspond to metallic cylinders. Perfectly matched layers are used to surround computational area in order to prevent reflections. 126

5.16 a) Transmission spectra are calculated for 4 layers of square lattice structure in Γ - X direction. b) Photonic band structure of a square lattice of metallic rods in Γ - X direction. The rods radius is $r = 0.2a$ where a = 50 μm. Shaded areas represent common photonic band-gaps for any crystal direction. 127

5.17 Transmission spectra of E-polarization of metallic photonic crystals in square lattice array for number of layers along the Γ - X direction. 128

5.18 Electric field distribution in metallic photonic structure in square lattice array with rod radius is $0.2a$, where lattice constant a = 50 μm at a) 3 THz and b) 3.5 THz 130

5.19 Transmission, reflection and absorption spectrum of E- and H-polarizations for 4 layers of metallic photonic crystal structure in square lattice array with lattice constant of 50 μm for different rod sizes along Γ - X direction. Transmission, reflection in dB scale and absorption in linear scale. Black dash line shows results for H-polarization while red solid line shows the E-polarization for a) $r = 0.2a$, b) $r = 0.3a$ and c) $r = 0.4a$ 131

5.20 Transmission spectra of 4 layers of metallic photonic crystal structure in square lattice array for E-polarization Γ - X direction. Transmission is calculated for different lattice period a) 50 μm b) 75 μm c) 100 μm for rod radii equal to $0.2a$ (red solid line), $0.3a$ (blue dash line), $0.4a$ (black dash dot line). 133

5.21 Transmission spectra of 4 layers of metallic photonic crystal structure in square lattice array with rod radius is $0.2a$, where lattice constant a = 50 μm for a) E- and b) H-polarizations in Γ - X direction for various incident angles. c) Transmission is as function of incident angles for E- and H-polarizations at 3THz. 134

5.22 a) Transmission spectra are calculated for 5 layers of triangular lattice structure in Γ - M and Γ - K directions. b) Photonic band structure of a triangular lattice of metallic rods in E-polarization. The rod radius is $r = 0.2a$ where a = 50 μm. Shaded areas represent common photonic band-gaps in any crystal direction for E-polarization. 137

5.23 Transmission spectra of E-polarization of metallic photonic crystals in triangular lattice array for number of layers along the Γ - M direction. The rods radius is $r = 0.2a$ where lattice constant, a = 50 μm. 138

5.24 Calculated transmission, reflection in dB scale and absorption in linear scale for 5 layers of triangular lattice structure in Γ - M direction for E- and H-polarizations for rod radii a) $r = 0.2a$, b) $r = 0.3a$ and c) $r = 0.4a$, where lattice constant $a = 50\mu m$. 139

5.25 Calculated transmission, reflection in dB scale and absorption in linear scale for 5 layers of triangular lattice structure in Γ - K direction for E- and H-polarizations for rod radii a) $r = 0.2a$, b) $r = 0.3a$ and c) $r = 0.4a$, where lattice constant a = 50 μm. 142

5.26 Transmission spectra of 5 layers of metallic photonic crystal structure in triangular lattice array for E-polarization $\Gamma - M$ direction. Transmission is calculated for different lattice period a) 50 μm. b) 75 μm. c) 100 μm with rod radii $0.2a$ (red solid line), $0.3a$ (blue dash line), $0.4a$ (black dash dot line). 143

5.27 Transmission spectra of 5 layers of metallic photonic crystal structure in triangular lattice array for E-polarization Γ - K direction. Transmission is calculated for different lattice period a) 50 μm. b) 75 μm. c) 100 μm with rod radii $0.2a$ (red solid line), $0.3a$ (blue dash line), $0.4a$ (black dash dot line). 144

5.28 Transmission spectra of 5 layers of metallic photonic crystal structure in triangular lattice array with rod radius is $0.2a$, where lattice constant a = 50 μm for E-polarization in a) Γ - M and b) Γ - K directions for various incident angles. c) Transmission is as function of incident angles for Γ - M and Γ - K directions at 3 THz. 145

5.29 a) The schematic illustration and direction of incoming wave of simulated structure, b) band-gap map of metallic photonic crystal structure in square lattice pattern, c) the gap-map for metallic photonic crystal in square lattice, courtesy of Smirnova $et\ al.$ (38). . 147

5.30 a) The schematic illustration and direction of incoming wave of simulated structure, b) band-gap map of metallic photonic crystal structure in triangular lattice pattern, c) the gap-map for metallic photonic crystal in triangular lattice, courtesy of Smirnova $et\ al.$ (38). 147

6.1 Schematic illustration of single line defect (W1) photonic crystal waveguide in square lattice array. The defect breaks the periodicity in the x-axis while it is still periodic in the y-axis. The supercell used in dispersion calculations is highlighted. 162

6.2 Dispersion diagram of a W1 waveguide where one row of rods is removed from square lattice composed of metal cylinders in air. Dispersion curves for waveguide are obtained in the Γ - M (1,1) direction of the square lattice. Blue solid lines show the photonic band-gap structure of square lattice in the same direction. Inset shows the supercell used in the dispersion calculations of W1 waveguide. 164

6.3 Dispersion diagram of a W2 waveguide where two rows of rods are removed from the square lattice composed of metal cylinders in air. Dispersion curves for waveguide are obtained in the (1,1) direction of the square lattice. Blue solid lines show the band-gap structure of metallic square lattice in Γ - M direction. Inset shows the supercell used in the dispersion calculations for W2 waveguide. 166

6.4 Dispersion diagram of a) W1 and b) W2 metallic photonic crystal waveguides in a square array of copper rods in air; the radius of the rods is $r = 0.2a$. The dots show even modes while open dots show odd. The thick lines show the band diagram of the perfect photonic crystal. Eigen frequencies of the guided modes are calculated with FDTD method, courtesy of Qiu *et al.* (4). 167

6.5 Visualisation of E-field distribution of guided modes in a W1 line defect waveguide a) even mode at 5.071 THz b) odd mode at 4.642THz for $k = 0.5$, illustrating the difference in symmetry. 167

6.6 Visualisation of E-field distribution of guided modes in a W2 line defect waveguide a) even mode at 3.15 THz b) odd mode at 3.55 THz for $k = 0.5$, illustrating the difference in symmetry. 168

6.7 Schematic illustration of a photonic crystal waveguide (W1) formed by introducing a line defect along the Γ - K direction of a triangular lattice of metallic rods in air. The defect breaks the periodicity in the x-axis while it is still periodic in the y-axis. The supercell used in dispersion calculations is highlighted. The width of W1 waveguide, $w = a\sqrt{3} - 2r$, a is the lattice constant and r is the rod radius. 169

6.8 Photonic band structure of a W1 waveguide where a row of rods is removed from the triangular lattice composed of metal cylinders in air. Dispersion curves for waveguide are obtained in the in the Γ - K (1,1) direction of the triangular lattice. Blue solid lines show the band-gap structure of metallic triangular lattice in the same direction. Inset shows the supercell used in the dispersion calculations for W1 waveguide. 171

6.9 Photonic band structure of a W3 waveguide where a row of rods is removed from the triangular lattice composed of metal cylinders in air. Dispersion curves for waveguide are obtained in the Γ - K (1,1) direction of the triangular lattice. Blue solid lines show the band-gap structure of metallic triangular lattice in the same direction. Inset shows the supercell used in the dispersion calculations for W3 waveguide. 172

6.10 Visualisation of E-field distribution of guided modes in a W1 line defect waveguide for the lowest order mode which is an even mode at 3.412 THz for $k = 0.5$. 173

6.11 Electric field distributions of the guided modes within the band-gap of the W3 waveguide. a) for $k = 0.25$, for frequencies corresponding to 1.755, 2.357, 3.097 THz and b) for $k = 0.5$ at frequencies 3.115, 3.436 and 3.145 THz respectively for the first three lowest order guided modes, starting from the one which has the lowest frequency. 174

6.12 Transmission/reflection spectrum simulated in 3D (black/red solid line) and in 2D (black/red dash line) for a linear waveguide formed by removing one row of rods from a metallic PhC. The PhC is characterized by a 50 μm lattice period in square lattice pattern of 50 μm height rods, with a radius of $0.2a$. 178

6.13 The transmission spectra of W1 square lattice waveguide as a function of waveguide length for perfect metal, copper, silver, gold and aluminium. 181

6.14 a) Dispersion diagram, b) transmission spectrum of W1 waveguide of copper rods in air in square lattice pattern for E-polarization. The radius of rods is $0.2a$, with lattice constant of 50 μm. 184

6.15 The electric field distribution of square lattice W1 waveguide for the frequencies corresponding to a) single mode propagation in the first band gap at 2.5 THz, and transmission dips at b) 3.38 THz, c) 4 THz and d) 4.81 THz, respectively. 186

6.16 a) Transmission, b) reflection and c) absorption spectra different W1 waveguides in square lattice array with rod sizes $0.2a$ (red solid line), $0.3a$ (blue dash line), $0.4a$ (black dash dot line) with lattice constant of 50 μm. Transmission, reflection in dB scale and absorption is calculated in linear scale. 188

6.17 a) Dispersion diagram, b) transmission spectrum of W2 waveguide of copper rods in air in square lattice pattern for E-polarization. The radius of rods is $0.2a$, with lattice constant of 50 μm. 191

6.18 a) Transmission, b) reflection and c) absorption spectra different W2 waveguides in square lattice array with rod sizes $0.2a$ (red solid line), $0.3a$ (blue dash line), $0.4a$ (black dash dot line) with lattice constant of 50 μm. Transmission, reflection in dB scale and absorption is calculated in linear scale. 193

6.19 The transmission of triangular lattice waveguide as a function of waveguide length. 195

6.20 a) Dispersion diagram, b) transmission spectrum of W1 waveguide of copper rods in air in triangular lattice pattern for E-polarization. The radius of rods is $0.2a$, with lattice constant of 50μm. 198

6.21 a) Transmission, b) reflection and c) absorption spectra for different W1 waveguides in triangular lattice array with rod sizes $0.2a$ (red solid line), $0.3a$ (blue dash line), $0.4a$ (black dash dot line) with lattice constant of 50 μm. Transmission, reflection in dB scale and absorption is calculated in linear scale. 201

6.22 a) Dispersion diagram, b) transmission spectrum of W3 waveguide of copper rods in air in triangular lattice pattern for E-polarization. The radius of rods is $0.2a$, with lattice constant of 50 μm. 202

6.23 a) Transmission, b) reflection and c) absorption spectra for different W3 waveguides in triangular lattice array with rod sizes $0.2a$ (red solid line), $0.3a$ (blue dash line), $0.4a$ (black dash dot line) with lattice constant of 50 μm. Transmission, reflection in dB scale and absorption is calculated in linear scale. 203

7.1 a) Schematic of the five bend designs and b) transmission spectra for five different 90° bend designs as a function of frequency, from 1 to 4.5 THz. For each given design a schematic illustration of W1 bend waveguides is depicted on the right hand side of the spectrum, for bends I to V. W2 bend waveguide geometries are similar to W1 except for the width of the waveguides. Black dashed-line corresponds to the W1 while red solid is for W2 bend waveguide. 212

7.2 a) Schematic of the five bend designs and b) reflection spectra for five different 90° bend designs as a function of frequency, from 1 to 4.5 THz. For each given design a schematic illustration of W1 bend waveguides is depicted on the left hand side of the spectrum, for bends I to V. W2 bend waveguide geometries are similar to W1 except for the width of the waveguides. Black dashed-line corresponds to the W1 while red solid is for W2 bend waveguide. 214

7.3 Illustration of the wave propagation of a) bend V and b) improved bend V waveguides at 4.1 THz where transmission is improved with the design. Blue and red regions show the positive and negative parts of electric field distribution. The electromagnetic wave is confined and propagates perfectly within the guiding channel in improved bend design formed by removing two rows of rods. Geometry of this design can also be seen, in which circles correspond to the metallic cylinder rods. 218

7.4 Transmission spectra and frequency dependence of the phase shift for bend V (black dashed line) and improved bend V (red solid line) waveguides in the case of two rows of rods are removed from metallic band-gap structure. 219

7.5 Transmission spectra and frequency dependence of the phase shift for improved bend V (black dashed line) and same length linear (red solid line) waveguides in the case of two rows of rods are removed from metallic band-gap structure. 221

7.6 Schematic illustration of a) W1 and b) W3 photonic crystal bend waveguides in triangular lattice array. 222

7.7 a) Construction of a quadratic Bézier curve for 60° bend design. b) the rods on the sharp bending corner c) the rods positioned according to the Bézier curve. 225

7.8 a) Transmission and b) reflection spectra of 60° bend designs as a function of frequency, from 2 to 6 THz. The schematic illustrations of W1 bend waveguides are depicted on the right hand side of the transmission figure. Black dashed-line corresponds to the Bend I while red solid line is for Bend II waveguides. 226

7.9 Transmission spectra and frequency dependence of the phase shift for bend II (black dashed line) and W1 linear (red solid line) waveguides. 227

7.10 a) Transmission and b) reflection spectra of 60° bend designs as a function of frequency, from 2 to 6 THz. The schematic illustrations of W3 bend waveguides are depicted on the right hand side of the transmission figure. Black dashed-line corresponds to the Bend I while red solid line is for Bend II waveguides. 228

7.11 Illustration of the wave propagation of W3 bend waveguide at a) 1.5 THz and V and b) 2.5 THz. Blue and red regions show the positive and negative parts of electric field distribution. The electromagnetic wave is confined and propagates perfectly within the guiding channel in bend II design formed by removing three rows of rods. The circles correspond to the metallic cylinder rods. 229

7.12 Transmission and reflection spectra of T-splitter a) without any modification b) with one rod are removed from each corner. Schematic illustrations of T-splitters compared are given on the left hand side of each transmission/reflection spectra. 231

7.13 Transmission and reflection spectra of T-splitter where the corners are replaced with curved design a) without any additional rods, b) with one additional rods and c) four added rods Schematic illustrations of T-splitters compared are given on the left hand side of each transmission/reflection spectra. 232

7.14 Transmission and reflection spectra of T-splitter where the corners are replaced with curved design a) without any additional rods, b) with one additional rods and c) four added rods Schematic illustrations of T-splitters compared are given on the left hand side of each transmission/reflection spectra. 234

7.15 Transmission spectra of original T-splitter and the improved T-Splitter. 235

7.16 Transmission and reflection spectra of Y-splitters. Schematic illustrations of Y-splitters are given on the left hand side of each transmission/reflection spectra. Worth noting that the transmission corresponds to half of the total power transmitted. 236

List of Tables

5.1 Drude fitting parameters used in calculations for permittivity and conductivity (4; 10; 11). 97

5.2 Drude fitting parameters of used in calculations of permittivity and conductivity (4; 10; 11). 102

5.3 Symbols and wave vector directions for square and triangular lattices 110

6.1 The attenuation values calculated from the transmission results as a function of waveguide length for W1 square lattice waveguides made of copper, gold, silver and aluminium 182

6.2 The attenuation values calculated from the transmission results as a function of waveguide length for W1 triangular lattice waveguides made of copper, gold, silver and aluminium. 196

Chapter 1

INTRODUCTION

Photonics is a field that is growing fast in order to fulfill the need for higher bandwidth for developing technological applications. Current and developing technologies need even more bandwidth realized in ultra compact and cheap devices. Those devices can only be realized with photonic technology achieving data transmission at light speeds and also must be able to integrate to all optical devices. Due to the increasing hunger for bandwidth in communication systems, technological developments in optical systems are starting to shift from micro systems to nano systems. Optical properties of photonic crystals can be tailored in a way to create optical circuits in order to take advantage of the speed of light by utilizing photons rather than electrons. With the development of optical integrated circuits based on photonic crystals, it would be possible to design small and low power devices that carry the information at the speed of light and create ultra high-speed optical computers (1). THz frequencies bridge the gap between microwaves and infrared wavelengths. This part of the electromagnetic spectrum is where electronics and photonics meet. Devices that can carry THz radiation i.e. signals of thousands of GHz, make it possible to reach speeds much faster than today's fastest microprocessor (2). Besides which, THz radiation offers unique features and possible practical applications that

can be applied in a broad range of disciplines. Applications in medical and security imaging, tomography, sensing, spectroscopy, package inspection etc. can be given as examples (3).

Terahertz (THz) waves refer to electromagnetic radiation that has a frequency between 0.3 THz and 10 THz, occupying a large portion of the electromagnetic spectrum between the infrared and microwave bands. This part of the electromagnetic spectrum has remained unexplored until recently, mainly due to the difficulty of generating and detecting THz signals with traditional methods used for microwaves and optical frequencies. There is a great need for optical components operating efficiently in this range, such as THz sources, detectors, waveguides, cavities etc. Therefore, a growing interest has been focused on the THz electromagnetic wave and development for variety of possible application. There are a number of approaches used to generate THz radiation, each with their own individual challenges. The use of photonic crystals (PhC) in THz frequency range has gained a lot of interest in recent years. A photonic crystal as a waveguide in the THz region is one of the possible applications of these devices. In such systems the wave to be transmitted across the system in connection to other devices could be sent over a wide frequency range with a good performance. Design of such waveguides for THz applications is the focus of this research.

The purpose of this study is to design THz rectangular waveguides, based on the THz band-gap crystals (BGCs). The motivations are to guide and to manipulate the THz radiation in an efficient way in order to increase the performance of the actual THz devices. Photonic crystals are good candidates to construct wave guiding devices as they feature small size, low loss and flexibility of fabrication due to comparatively large THz wavelengths. Metallic photonic crystals have been used due to certain advantageous properties over dielectric crystals, which can be relevant for guiding THz radiations.

This thesis is divided into 8 chapters including the first chapter comprises this introduction and the remaining are organized with the following layout.

Chapter 2 Fundamentals of Photonic Crystals - A brief introduction to photonic crystals background is given. Macroscopic Maxwell's equations are discussed in order to understand the phenomenon of band-gap crystals and to model wave propagation in photonic crystals by Bloch waves and Brillouin zones. The scalability of Maxwell's equations and symmetry properties are also considered. Band-gap diagram of photonic crystals are also presented in this chapter.

Chapter 3 Modelling Tools - This chapter presents a brief overview of different types of methods used for photonic crystal study. These methods are used to understand photonic crystals behavior and also to design and simulate photonic crystal structures.

Chapter 4 THz Technology - In this chapter brief information is given for THz radiation, THz wave generation and THz applications. As a last point, the photonic crystal research is mentioned. The various applications of photonic crystals in THz range are covered.

Chapter 5 The Analysis of Metallic Photonic Crystals - Firstly, an introduction to metallic band gap and optical properties of metals is given to understand the idea of metallic photonic crystal structures and waveguides. Secondly, the FEM method for simulation is introduced and it is validated by comparing its output with case studies. Band-gap diagrams and transmission characteristics of metallic photonic crystals are presented. Some waveguide design parameters are obtained to create and to simulate high performance waveguides for THz frequency.

Chapter 6 Linear Defects in 2D Metallic Photonic Crystals - This chapter present 2D metallic photonic crystal waveguides formed by line defects. Transmission and dispersion characteristics and guided modes of metallic photonic crystal waveguides are discussed. The strong correlation between dispersion diagrams and transmission spectra are shown for metallic photonic crystal waveguides. The losses associated with modal behaviour of waveguides associated with interaction between the guided modes are discussed.

Chapter 7 Metallic Photonic Crystal Devices - This chapter present photonic crystal devices designed for THz waveguides using metallic photonic crystals. From the design parameters obtained in the previous chapters bend waveguides and power splitters are modelled and optimized in order to increase the transmission performances.

Chapter 8 Conclusions and Future Work - The thesis is concluded in this chapter with a brief analysis of the work presented in the previous chapters and future work.

Chapter 2

FUNDAMENTALS OF PHOTONIC CRYSTALS

In this chapter, brief information about the basic concepts and origin of photonic crystals and the photonic band-gap is given. The theory behind light (i.e. electromagnetic wave) propagation in a photonic crystal and how this can be utilized to implement a waveguide will be described. However, more detailed information about photonic crystals can be found in the reference book of the field given in Ref. (4)

Nature has been always a great source of inspiration to the scientist. Nature hides many mysteries to be solved, as underneath there are very complex structures and yet in perfect form. By carefully analysing and solving those mysteries, it becomes possible to apply it to real life and furthermore manipulate them to give new directions. Photonic crystals or photonic band gap materials are one of the optical systems that have counterparts in nature (5). Scientists have been studying different configurations of photonic crystals in order to create large band-gaps. One of the most optimal designs described by scientists is the one has the same crystal struc-

ture as carbon atoms in diamond. It was discovered that Brazilian beetles have the same crystal arrangement (6). Because of light cannot be transmitted or reflected at certain wavelength or angles due to their different reflection abilities, different colours can be observed in many biological systems, such as on natural opals, on the wings of some butterflies, or beetles as mentioned above, etc. (7; 8; 9).

Photonic crystals (PhC) are artificially periodic structures with the periodicity of the order of the wavelength of electromagnetic waves. Photonic crystals can be obtained by using at minimum two different materials that provide high and low index contrast. Because the periodicity of the structure is on the order of wavelength of light, electromagnetic waves cannot propagate inside the photonic crystals at certain frequency ranges and directions called photonic band gap (PBG). Photonic crystals, also known as photonic band gap (PBG) materials, are named by analogy with the periodic potential of material where electrons can only occupy some certain energy bands separated by forbidden gaps. In the PBG no propagation of electromagnetic radiation is possible. This effect provides a very important feature for confining the light in line or point defects introduced to the PBG structure in order to guide or localize the light. The photonic band structure depends on the crystal structure, lattice constant, geometry, dielectric constant of materials and the filling fraction.

The first experimental studies on electromagnetic waves in one-dimensional media were done by Rayleigh in 1887. However, the idea of artificially periodic structures having forbidden bands in two and three dimensions was first proposed by E. Yablonovitch. In 1987, he proposed the spontaneous emission of light could be prohibited by the electromagnetic band gap of light while S. John found that a disorder in a periodic medium can localize the light (10; 11). The existence of photonic band-gaps and the ability of photonic crystals to control and manipulate the flow of light have been theoretically and experimentally proven by some research groups in the following years. Photonic crystals have attracted a lot of attentions from

scientists of widely varying backgrounds rangeing from solid-state physics, semiconductor physics, quantum optics, to material science. The first demonstration of photonic band-gap effects of 2D photonic crystals at optical wavelengths was made in 1996 (12). Photonic crystals have been studied intensively for the last two decades and studies have demonstrated novel features and applications. In many applications, devices based on photonic crystals have started to be used, even taking places of traditional ones, such as in low threshold lasers (13) or low-loss photonic crystal fibers (14).

The photonic crystals can be classified as one-dimensional (1D), two-dimensional

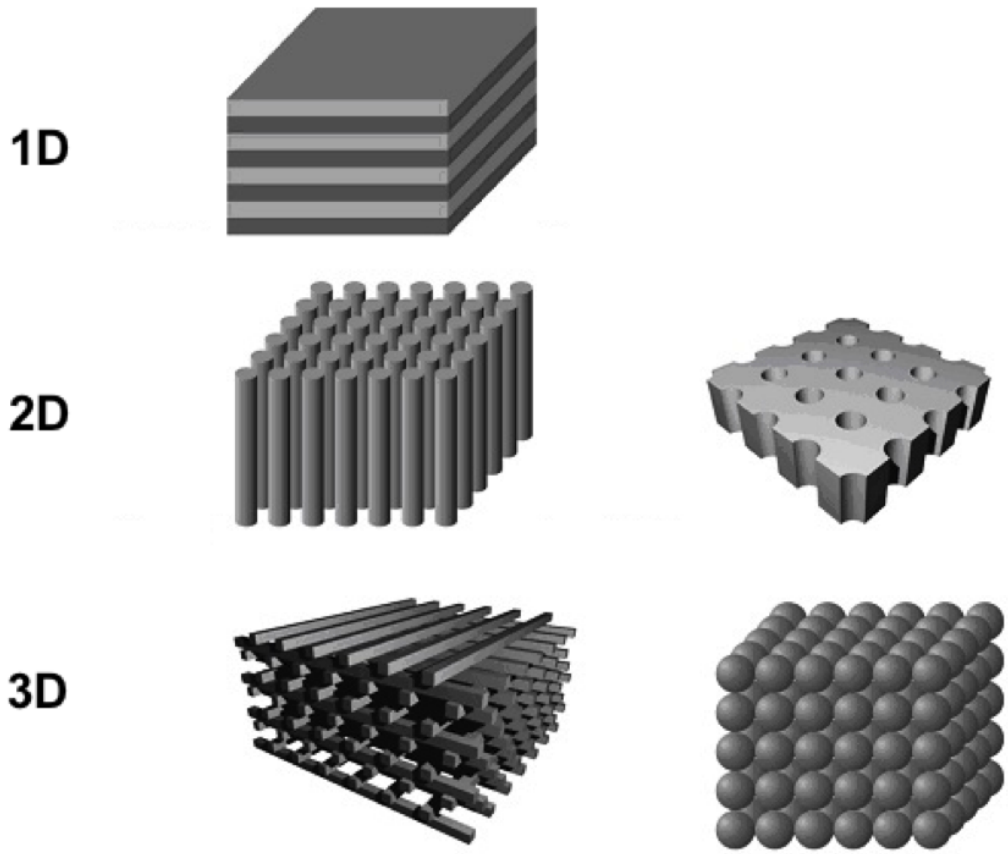

Figure 2.1: Schematic illustrations of one-, two-, and three-dimensional photonic crystals.

(2D) and three-dimensional (3D) structures where the periodicity variation is along one, two and three directions, respectively. Generally photonic crystals are composed of two different materials. Figure 2.1 shows some schematic pictures of 1D, 2D and 3D photonic crystal structures.

1-D photonic band gap crystals, also better known as Bragg reflectors or mirrors, are periodic in one dimension and are typically composed of two alternating layers constructed as multi-stack layers which are the simplest form of the photonic crystals (15). The allowed wavelengths can be controlled by changing refractive indices of high and low index layers and/or selecting the thicknesses to result in constructive or destructive interference of the reflected and transmitted waves. The alternating layers exhibit strong reflection for limited angle and wavelengths due to constructive interference between reflections at multiple interfaces. The reflectivity increases with the number of alternating layers.

1-D photonic crystals, i.e. Bragg reflectors have been widely used in optoelectronics for a long time. Due to their wavelength-selective reflection properties, they are used in a wide range of applications including high-efficiency mirrors, FabryProt cavities, optical filters and distributed feedback lasers. 2D photonic crystals have periodicity along two spatial directions (i.e. x,y) or two axes, and homogenous along the third direction (i.e. z). Typically, 2D photonic crystals are constructed in two different forms by either periodically arranged pillars/rods or holes in arrays within the material (see Figure 2.1). 2D photonic crystals have partial band-gaps where electromagnetic wave propagation is prohibited for a certain frequency range for any direction except but for a particular polarization, i.e. TE, TM.

In 3D photonic crystals, a complete band-gap exists where no electromagnetic wave can propagate within a photonic crystal structure for any direction or polarization for a certain frequency range. 3D photonic crystals are periodic along three axes and

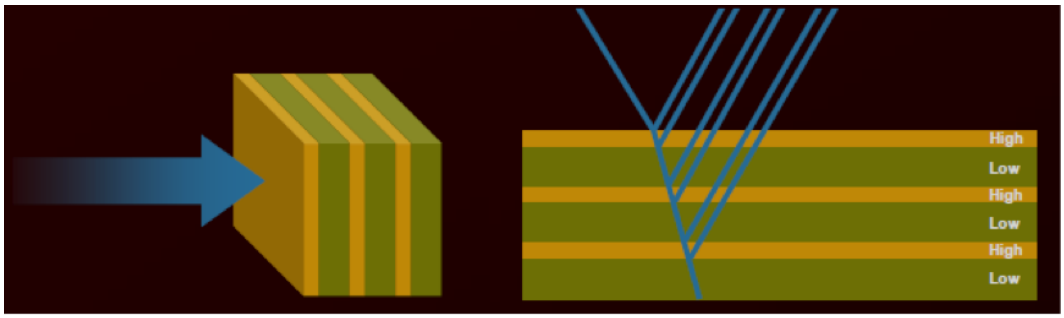

Figure 2.2: Schematic of an example of 1-D photonic crystal.

they have been studied extensively because of the possibility of exhibiting a complete photonic band-gap in various geometries including a diamond lattice structure, also known as Yablonovite (16), layer-by-layer (a wood pile type) (17) and face-centered-cubic (fcc), often called opal (18) and inverted opal (19). The schematics of layer-by-layer and opal type are shown in Figure 2.1.

3D photonic crystals have analogous structures to solid-state crystals, such as semiconductors. 2-D and 3-D photonic crystals have been intensively studied and great progress has been achieved in theory, applications and fabrication in just over a few decades. Applications of photonic crystals exist not only in the microwave and optical regions, but also extend to the infrared and far-infrared region, which includes the terahertz range.

2.1 Photonic Crystal Theory

In order to describe the principles of electromagnetic theory behind the wave propagation in photonic crystals, Maxwell's Equations are used. The master equation, which reduces the equations into a linear Hermitian eigenvalue problem, is derived from Maxwell's Equations to explain important properties, i.e. scalability,

orthogonallity.

2.1.1 The Macroscopic Maxwell's Equations

It is well-known that Maxwell's equations are used to describe electric field and magnetic field behaviour. All macroscopic Maxwell's equations can be applied for microscopic scale electromagnetism, including the propagation of light in photonic crystals. Since light consists of electromagnetic waves the propagation of light satisfies Maxwell's equations here expressed in SI units:(20)

$$\vec{\nabla} \cdot \vec{B} = 0 \tag{2.1}$$

$$\vec{\nabla} \times \vec{E} + \frac{\partial \vec{B}}{\partial t} = 0 \tag{2.2}$$

$$\vec{\nabla} \cdot \vec{D} = \rho \tag{2.3}$$

$$\vec{\nabla} \times \vec{H} - \frac{\partial \vec{D}}{\partial t} = \vec{J} \tag{2.4}$$

where $\vec{E}$ and $\vec{H}$ are the electric and magnetic fields respectively, and $\vec{D}$ and $\vec{B}$ are the electric flux density and magnetic flux density. ρ and $\vec{J}$ are the free charge and current densities, respectively. Generally, all these quantities are function of position vector $\vec{r}$ and time t. Here, the derivation of Maxwell's equations will be carried out in a medium has a spatially changing dielectric permittivity and no free

charges or currents. ($\rho = \vec{J} = 0$).

$$\vec{D} = \varepsilon_0 \varepsilon(\vec{r}) \vec{E} \tag{2.5}$$

$$\vec{B} = \mu_0 \mu(\vec{r}) \vec{H} \tag{2.6}$$

$$\vec{\nabla} \cdot \vec{H}(\vec{r}, t) = 0 \tag{2.7}$$

$$\vec{\nabla} \times \vec{E}(\vec{r}, t) + \mu_0 \frac{\partial \vec{H}(\vec{r}, t)}{\partial t} = 0 \tag{2.8}$$

$$\vec{\nabla} \cdot \Big(\varepsilon(\vec{r}) \vec{E}(\vec{r}, t) \Big) = 0 \tag{2.9}$$

$$\vec{\nabla} \times \vec{H}(\vec{r}, t) - \varepsilon_0 \varepsilon(\vec{r}) \frac{\partial \vec{E}(\vec{r}, t)}{\partial t} = 0 \tag{2.10}$$

where, ε_0 is the permitivity of the vacuum, $\varepsilon(\vec{r})$ is the relative permittivity of the material. Assuming that $\varepsilon(\vec{r})$ is not a function of frequency, so no material dispersion is taken into account. μ_0 is the vacuum permeability and relative magnetic permeability $\mu(\vec{r})$ is very close to unity for most materials and taken as unity for simplicity.

In general, $\vec{E}$ and $\vec{H}$ fields are dependent on both time and space. Since Maxwell's equations are linear, they can be expressed by the combination of time and space separately by expanding the field into a set of harmonic modes. $\vec{E}(\vec{r}, t)$ and $\vec{H}(\vec{r}, t)$ that can be written from Fourier analysis as:

$$\vec{E}(\vec{r}, t) = \vec{E}(\vec{r}) e^{-i\omega t} \tag{2.11}$$

$$\vec{H}(\vec{r}, t) = \vec{H}(\vec{r}) e^{-i\omega t} \tag{2.12}$$

Maxwell's equations are rewritten as a new set of equations using the above relation

$$\vec{\nabla} \cdot \vec{H}(\vec{r}) = 0 \tag{2.13}$$

$$\vec{\nabla} \cdot \left(\varepsilon(\vec{r})\vec{E}(\vec{r})\right) = 0 \tag{2.14}$$

$$\vec{\nabla} \times \vec{E}(\vec{r}) - i\omega\mu_0\vec{H}(\vec{r}) = 0 \tag{2.15}$$

$$\vec{\nabla} \times \vec{H}(\vec{r}) + i\omega\varepsilon_0\varepsilon(\vec{r})\vec{E}(\vec{r}) = 0 \tag{2.16}$$

$$\vec{\nabla} \times \left(\frac{1}{\varepsilon(\vec{r})}\nabla \times \vec{H}(\vec{r})\right) = \left(\frac{\omega}{c}\right)^2 \vec{H}(\vec{r}) \tag{2.17}$$

$$\underbrace{\vec{\nabla}\times\frac{1}{\varepsilon(\vec{r})}\vec{\nabla}\times\vec{H}(\vec{r})}_{Eigen-operator} = \underbrace{\left(\frac{\omega}{c}\right)^2}_{Eigen-value} \underbrace{\vec{H}(\vec{r})}_{Eigen-state} \qquad (Master Equation)$$

where $c = 1/\sqrt{\varepsilon_0\mu_0}$ is the speed of light in vacuum. The above equation is an eigenvalue equation, known as the master equation. It completely determines $\vec{H}$ and the corresponding frequencies of given structure $\varepsilon(\vec{r})$. It should be noted that the master equation is derived with the following restrictions only dealing with low-loss dielectrics: the material is macroscopic and isotropic and any explicit frequency dependence of the dielectric constant is ignored. The master equation is used to calculate the modes propagating in any photonic crystal by solving this equation for $\vec{H}$ and determining $\vec{E}$. The eigen-state $\vec{H}$ is the field patterns of the harmonic modes with the eigenvalue $(\omega/c)^2$ and an eigen-operator $\vec{\nabla} \times \frac{1}{\varepsilon(\vec{r})}\vec{\nabla}\times$ is Hermitian (4).

It is worth mentioning here that the linear operator $\hat{\Theta}$ acting on $\vec{H}(\vec{r})$ field,

$$\hat{\Theta}\vec{H}(\vec{r}) \;=\; \vec{\nabla} \times \left(\frac{1}{\varepsilon(\vec{r})} \vec{\nabla} \times \vec{H}(\vec{r}) \right) \tag{2.18}$$

gives the eigenvalues which are real and positive. However, the same operator acting on $\vec{E}(\vec{r})$ field is not Hermitian. For mathematical convenience, $\vec{E}(\vec{r})$ can be recovered by using the following equation.

$$\vec{E}(\vec{r}) \;=\; \frac{i}{\omega \varepsilon_0 \varepsilon(\vec{r})} \vec{\nabla} \times \vec{H}(\vec{r}) \tag{2.19}$$

The Hermitian operator, $\hat{\Theta}$, is a linear operator and positive-definite (for real $\varepsilon > 0$) and eigenfrequencies ω are real. Eigen-states are also complete and orthogonal (20). The same linear-algebraic theorems in quantum mechanics can be applied to the electromagnetic wave solutions. The Bloch Theorem (extended Floquet 1-D Theorem) states that waves can propagate in a periodic medium without scattering. Schrödinger's equation can be verified by arranging Maxwell's equations as an eigenvalue problem in which electrons are considered as waves. Details can be found in ref. (20). The Schrödinger's equation:

$$\hat{H}\psi(\vec{r}) \;=\; \left[\frac{\hbar}{2m} \nabla^2 + V(\vec{r}) \right] \psi(\vec{r}) \;=\; E\psi(\vec{r}) \tag{2.20}$$

The terms in the above equation correspond to kinetic and potential energy, where $\hat{H}$ is Hermitian Hamiltonian operator, $\psi(\vec{r})$ is eigenfunction for quantum mechanical wave and E is the total energy eigenvalue.

2.1.2 Scaling Properties of Maxwell's Equation

For photonic crystals the master equation is independent of the dimension of length unlike the quantum mechanic analogues where length scale is usually introduced with the Bohr radius.

Changing the variables in the master equation (Eq. 2.17) $r' = sr$ and $\nabla' = \nabla/s$. Here s is the scaling factor.The scalability of the equation can be shown as follows:

$$s\vec{\nabla}' \times \left(\frac{1}{\varepsilon(\vec{r'}/s)} s\vec{\nabla}' \times \vec{H}(\vec{r'}/s) \right) = \left(\frac{\omega}{c} \right)^2 \vec{H}(\vec{r'}/s) \tag{2.21}$$

But $\varepsilon(\vec{r'}/s)$ is actually $\varepsilon'(\vec{r'})$, so by dividing both sides by s, we will have,

$$\vec{\nabla}' \times \left(\frac{1}{\varepsilon'(\vec{r'})} \vec{\nabla}' \times \vec{H}(\vec{r'}/s) \right) = \left(\frac{\omega}{cs} \right)^2 \vec{H}(\vec{r'}/s) \tag{2.22}$$

If $\vec{H}(\vec{r})$ is a solution of the original master equation for the frequency ω, then $\vec{H}'(\vec{r'}) = \vec{H}(\vec{r'}/s)$ is a solution of the rescaled master equation for the frequency ω/s.

The solution of the problem at one scale determines the solutions at all other length scales. Therefore band-gap diagrams and corresponding frequencies are often represented as normalized to the lattice constant value (a/λ) in the case of dispersionless materials. Thus, scalability of Maxwell's equations is very important from a practical point of view. Photonic crystals can be tailored by the scaling of the periodicity and therefore lattice constant in order to operate in certain frequency ranges from microwave in millimeter scales to the optical part of the spectrum in micro/nanometer scales.

2.2 Theory of the Photonic Band-Gap

A band structure is expected when a material has spatially periodic structure (21). The range of wavelengths in which propagation of electromagnetic radiation is forbidden in a photonic band-gap depends on various factors. These factors controlling the presence as well as the size of band-gap depend on the refractive index contrast of the compounds of materials, the shape and the symmetry of lattice structure and the filling fraction, which is defined as the proportion of the material volume to background material in a unit volume. However, the incident wave on a photonic crystals structure is also important, as for a given structure waves are reflected or scattered through the structure and the band-gap can be only obtained for certain frequencies, directions and polarizations. By solving the eigenvalue problem given in the master equation form for all directions, allowed and forbidden frequencies can be determined for a given wave vector. The relation between ω and $\vec{k}$ is called the dispersion relation and defines the band structure of crystal.

The close resemblance of the master equation to Schrödinger's equation governing quantum mechanics helps us to understand the propagation of electromagnetic waves in a periodic medium. As a consequence to the dielectric function in a photonic crystal structure $\varepsilon(\vec{r})$ is analogous to the periodic potential $V(\vec{r})$ of electrons in a crystal structure. Similar to the electronic energy band-gap that states that certain electronic waves are forbidden in a crystal lattice, photonic crystal structures form photonic band-gaps as the dielectric function varies periodically, whereby electromagnetic wave propagation is forbidden. The direct analogy allows writing the photonic system in 'Bloch form', consisting of a plane wave modulated by a function arising from the periodicity of the lattice. This approach becomes particularly useful when considering the coupling of light into two and three-dimensional photonic crystals.

2.2.1 The Brillouin Zone and the Reciprocal Lattice

If a dielectric structure has symmetry, this can help to determine properties of electromagnetic system and classify the electromagnetic modes. By studying a certain region that fully characterizes the periodic structure due to the symmetry, the system behaviour can be obtained. This region in reciprocal space presents all the lattice symmetry of the structure and it is called the irreducible Brillouin zone (IBZ). If additional rotational symmetries are present the first Brillouin zone can be degraded to a fraction of the zone, which can represent all the modes, called irreducible Brillouin zone. Irreducible Brillouin zone is obtained by reducing the first Brillouin zone to the high-symmetry points, namely Γ, X, K and M for 2D photonic crystals where the dispersion characteristics are not related to symmetry. These terms are analogous to the concepts in the solid-state physics and will be explained here briefly.

Instead of searching for the solution for the whole structure which requires a solution of too many plane waves, the calculations are reduced to a primitive unit cell that presents a spatial domain defined by the Wigner-Seitz cell (22). A unit cell depends on the lattice structure, and represents the symmetry of structure. By regularly repeating the unit cell, the whole structure can be duplicated. In real space, everything is known about the solution if the field is known everywhere in the unit cell. Similarly, in reciprocal space everything is known when the solution to the eigen-value problem is obtained at every point within the Brillouin zone.

The Brillouin zone is particularly important for finding the solutions for a periodic system according to the Bloch-Floquet theorem. This is because, in the Brillouin zone, the eigenvalues obey the dispersion relation, which includes the frequency of an eigenfunction $\omega_n(\vec{k})$, where $\vec{k}$ is the Bloch wave vector associated the modes in the system. The dispersion relation defines the relation between the frequency and

wave number $\vec{k}$, $|\vec{k}| = \omega/c$ and shows the dispersive properties of a medium with respect to the frequency. When $\omega_n(\vec{k})$ is plotted as a function of $\vec{k}$ vectors, the resulting figure shows that k-vectors exist for certain frequency intervals or bands while for some other frequency intervals or bands there is no k-vector. These solutions are called band-gap. The band-gap frequencies are the stop band of the structure, and the $\vec{k}$ vectors with frequency solutions are called allowed band or pass band.

The complete information of all modes can be obtained for the values of $\vec{k}$ within the reciprocal lattice. The eigenfunctions of the master equation of a periodic structure correspond to eigenvalues of $(\omega/c)^2$.

$$\vec{H}_{\vec{k}}(\vec{r}) = e^{i\vec{k}\cdot\vec{r}}\vec{h}_{n,\vec{k}}(\vec{r}) \tag{2.23}$$

The above Hermitian eigenproblem over the Brillouin zone eigenvalues $\omega_n(\vec{k})$ at each Bloch wave vector $\vec{k}$ defines the dispersion relation, where $\vec{h}_{n,\vec{k}}(\vec{r})$ is a periodic function that satisfies the master equation. Because of discrete translational symmetry, $\omega_n(\vec{k})$ is characterized by wave vector and band index n.

The Bloch-Floquet theorem states that, in a periodic medium, the eigenfunctions of a Hermitian eigenvalue problem can be written as the product of plane wave $e^{i\vec{k}\cdot\vec{r}}$ and a periodic function $u(\vec{r})$ that has the same periodicity with the lattice vector $\vec{R}$.

$$\vec{H}_{\vec{k}}(\vec{r}) \;=\; e^{i\vec{k}\cdot\vec{r}}\vec{u}_{\vec{k}}(\vec{r}) \;=\; e^{i\vec{k}\cdot\vec{r}}\vec{u}_{\vec{k}}(\vec{r}+\vec{R}) \tag{2.24}$$

The spatial distribution of unit cell is defined by a set of basis vectors with discrete translational symmetry. The number of the vectors is equal to the number of dimensions. These vectors are called primitive lattice vectors. The lattice vector is any

linear combination of the primitive lattice vectors.

The lattice vector can be written in terms of the primitive lattice vectors as:

$$\vec{R} \;=\; l\vec{a}_1 + m\vec{a}_2 + n\vec{a}_3 \tag{2.25}$$

where (l, m, n) are the integers and $\vec{a}_1, \vec{a}_2, \vec{a}_3$ are the primitive lattice vectors.

The set of wave vectors exist in reciprocal lattice space, a concept that is fundamental to solid state physics (23). In order to work in the wave-vector space and derive dielectric function in wave vector representation, real lattice space transforms into reciprocal lattice space through integral transform.

When real-space lattice vectors $\vec{R}$ are known, the reciprocal lattice vectors $\vec{G}$ can be obtained. Since eigen solutions are also periodic functions of $\vec{k}$ and since $\vec{k}$ and $\vec{k} + \vec{G}$ are equivalent: $\vec{G} \cdot \vec{R} \;=\; 2\pi N$, where N is an integer. In a similar way, the reciprocal lattice vectors can be written as:

$$\vec{R} \;=\; l'\vec{b}_1 + m'\vec{b}_2 + n'\vec{b}_3 \tag{2.26}$$

Given the lattice vectors, the reciprocal lattice vectors can be calculated by:

$$\vec{b}_1 \;=\; 2\pi \frac{\vec{a}_2 \times \vec{a}_3}{\vec{a}_1 \cdot (\vec{a}_2 \times \vec{a}_3)} \tag{2.27}$$

$$\vec{b}_2 \;=\; 2\pi \frac{\vec{a}_3 \times \vec{a}_1}{\vec{a}_1 \cdot (\vec{a}_2 \times \vec{a}_3)} \tag{2.28}$$

$$\vec{b}_3 \;=\; 2\pi \frac{\vec{a}_1 \times \vec{a}_2}{\vec{a}_1 \cdot (\vec{a}_2 \times \vec{a}_3)} \tag{2.29}$$

satisfying the condition

$$\vec{a}_i \cdot \vec{b}_j \;=\; 2\pi\delta_{ij}, \quad \delta_{ij} \;=\; \begin{cases} 1, & i \;=\; j \\ 0, & i \;\neq\; j \end{cases} \tag{2.30}$$

with δ_{ij} denoting Kronecker symbol. Reciprocal lattices are the inverse transforms of their crystal lattices multiplied by 2π.

2.2.2 Dispersion relation

The relation between the wave vector $\vec{k}$ and the frequency ω is called dispersion relation. The dispersion of the light in an isotropic dielectric material is given by:

$$\omega(\vec{k}) \;=\; c\vec{k}/n \;=\; c\vec{k}/\sqrt{\varepsilon_r} \tag{2.31}$$

where c is the speed of light, $\vec{k}$ is a wave vector, ε is a dielectric constant, n is the refractive index and the relative permeability is $\mu_r \;\approx\; 1.$ $n = \sqrt{\mu_r \varepsilon_r} \;=\; \sqrt{\varepsilon_r}$
The dispersion relation is a measure of light propagation in a material in comparison to light propagation in vacuum. The speed of light c is reduced by a factor of n in a material defined by phase velocity, v_p.

$$\omega(\vec{k}) \;=\; v_p\vec{k} \tag{2.32}$$

The phase velocity is the gradient of a line passing through the origin, intersecting the point $(\vec{k}, \omega)$. The slope of the dispersion diagram yields the group velocity defined as:

$$v_g = \frac{\partial\omega}{\partial\vec{k}} \tag{2.33}$$

Due to the scalability of Maxwell's Equations, the units on the dispersion diagram

are often expressed in normalized form.

$$Normalised\,Frequency \;=\; \omega a/2\pi c \;=\; a/\lambda$$

where a is the period, namely lattice constant and k is expressed in units of π/a.

$$k \;=\; 2\pi n\lambda_0 \;=\; 2\pi\lambda \tag{2.34}$$

Dispersion relations can be calculated with many numerical techniques by solving the eigenvalue equation. In numerical methods like Finite Difference Time Domain (FDTD) method and Plane Wave Expansion (PWE) method the wave vector is an independent variable and the frequency is an eigenvalue. In Transfer Matrix Method (TMM), Eigen Mode Expansion (EME) method and Finite Element Method (FEM) the frequency is an independent variable and wave vector is an eigenvalue.

In the following section, Brillouin zones are constructed for 1D and 2D photonic crystals and band-gap diagrams are obtained by means of the PWE method, which will be discussed in detailed in the next chapter.

2.3 Band-Gap of 1D Photonic Crystals

For a 1D system has continuous a translational symmetry in the x direction, discrete translational symmetry in the y direction, the basic step length is the lattice constant a, and the basic step vector is called the primitive lattice vector, which in this case is $\vec{a} = a\hat{y}$. Because of this discrete symmetry, $\varepsilon(\vec{r}) = \varepsilon(\vec{r} \pm \vec{a})$, by repeating this translation, $\varepsilon(\vec{r}) = \varepsilon(\vec{r} + \vec{R})$ for any $\vec{R}$ that is an integral multiple of $\vec{a}$; that is, $\vec{R} = l\vec{a}$, where l is an integer. The *unit cell* is defined as the structure that is re-

peated regularly in the crystal. The unit cell of a 1D photonic crystal is a lattice period long line. $\vec{b} = \frac{2\pi}{a}\hat{y}$ is the primitive reciprocal lattice for 1D photonic crystal system.

The solution of the eigenstates $\vec{H}_{\vec{k}}(\vec{r})$ for each k wave vector and the solution for $k + 2\pi/a$ are the same. Therefore, instead of searching for all solutions for k, it is sufficient to solve the eigenvalue problem of finite k in the range of $-\pi/a \leq k \leq \pi/a$. This range is called the *first Brillouin zone*. All other wave vectors are equivalent to some points in this zone under translation by a multiple of the reciprocal lattice vector. The first Brillouin zone can be even further reduced since lattices generally possess additional symmetries. This symmetry reduced zone is called the *irreducible Brillouin zone*. The dispersion relation of the 1D photonic crystal is mirror symmetric with respect to the point 0 with a periodicity of $2\pi/a$. Therefore, the irreducible Brillouin zone is $0 \leq k \leq \pi/a$.

Figure 2.3 shows the dispersion of light propagating through a dielectric stack where different layers have different dielectric constants. The dielectric constants 13, 12, 1 represent the standard values for GaAs, GaAlAs and air respectively. Figure 2.3 a) shows that no photonic band-gap appears in the material because there is no contrast in dielectric constants, this is a homogeneous material structure. Both figure b) and c) shows the effect of index contrast. In Figure 2.3 c) between the first two bands there is a photonic band-gap where there is no wave propagation within the interval between normalised frequency 0.15 and 0.25. The periodicity of the crystal induces a photonic band-gap if there is a significant contrast in the refractive index of the layers. The stronger the contrasts in the refractive index the wider the band gap. For instance, there is a band-gap in Figure 2.3 b) but it is narrow as the difference between the dielectric constants is only 1. The figures exhibit a perfect match with the literature results (4).

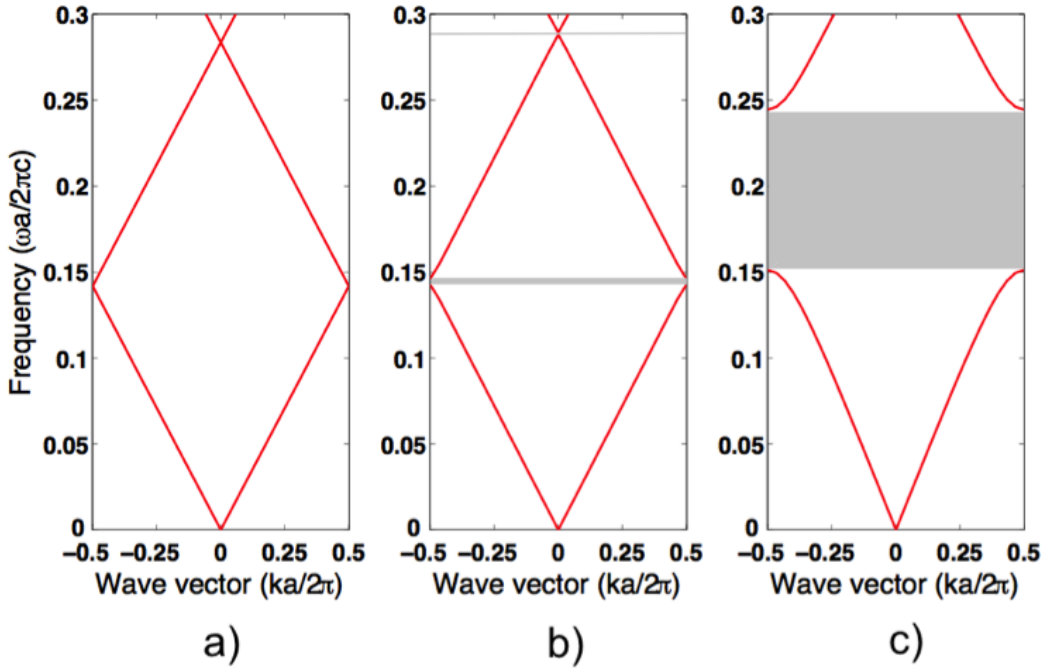

Figure 2.3: Photonic band structure of 1D photonic crystals, the ratio of the thickness of alternating layers is 0.5 where the dielectric constants are a) $\varepsilon_1 = 13$ and $\varepsilon_2 = 13$, b) $\varepsilon_1 = 13$ and $\varepsilon_2 = 12$, c) $\varepsilon_1 = 13$ and $\varepsilon_2 = 1$. The grey areas depict the photonic band-gaps.

2.4 Band-Gap of 2D Photonic Crystals

In this section, two types of lattice configuration are introduced to carry out a 2D analysis of photonic crystals: square lattice and triangular lattice. Firstly, Brillouin zones are obtained in order to plot band-gap diagrams of dielectric lattices by means of the PWE method based on calculating the eigenmodes. Band-gap diagrams and band-gap maps are obtained for different lattice configurations and polarizations.

In order to represent eigen modes of a periodic photonic crystal structure, Bloch vectors should be defined. Bloch states can be represented by a small volume of reciprocal phase space to label the modes called as first Brillouin zone. The first Brillouin zone is defined as the Wigner-Seitz primitive cell in the reciprocal lattice.

The cell is obtained by picking a point in the reciprocal lattice as a centre. Lines are drawn between this centre point and its nearest lattice points. Similarly, other lines are drawn perpendicularly, at the middle of each previously drawn line and the remained area gives the Wigner-Seitz cell (22).

If there is rotational symmetry in the lattice then the frequency bands $\omega_n(\vec{k})$ have additional redundancies in the Brillouin zone. This is also the case if the lattice has a mirror-reflection, or inversion symmetry. These collections of symmetry operations (rotations, reflections, and inversions) are called the point group of the crystal (4). From this point using the high symmetry points, i.e. for square lattice, high symmetry points are Γ, X, M, one can obtain the band-gap of the structure. The relation between eigen states of a 2D photonic crystal and frequency at these high symmetry points gives the dispersion relation in which the frequencies corresponding to the first Brillouin zone fall between the lowest and the highest frequencies at the Brillouin zone edges. The frequencies remaining between these lowest and highest points exhibit the band-gap frequencies.

2.4.1 Square Lattice

The construction of the first Brillouin zone for a two-dimensional square lattice is shown below.

The centre-to-centre spacing in the square lattice is a which is also known as the *lattice constant* when it is $2\pi/a$ for the reciprocal lattice. The diagram on the right (Figure 2.4 c)) shows the Brillouin zone of the square lattice centred at the origin (Γ). The points at the corner and face are known as M and X respectively. If the crystal has rotational symmetry, the crystal is invariant to a rotation, and it has the same properties. The lattice vectors and corresponding reciprocal lattice vectors for

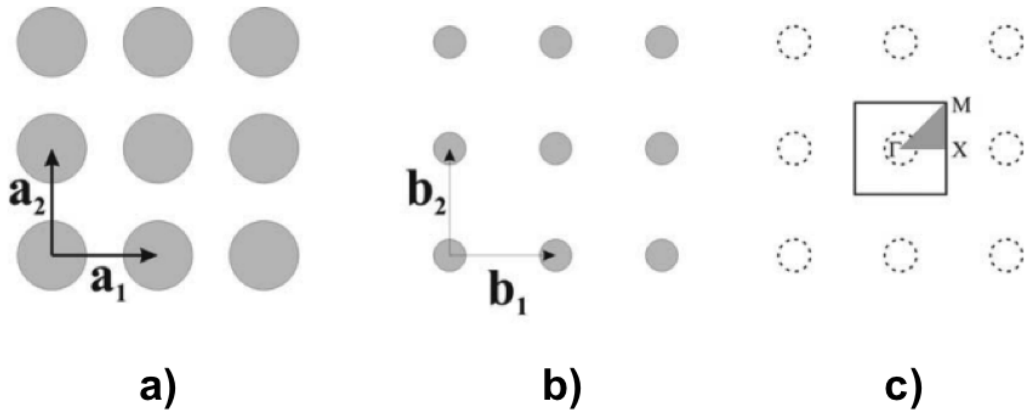

Figure 2.4: Square Lattice a) Lattice generated by the basis vectors b) The corresponding reciprocal lattice and reciprocal vectors c) First Brillouin zone (Wigner-Seitz primitive cell) and irreducible region denoted as square and triangle, respectively.

square lattice are as follows:

$$\vec{a}_1 = a(1,0) \qquad \vec{b}_1 = \frac{2\pi}{a}(1,0) \tag{2.35}$$

$$\vec{a}_2 = a(0,1) \qquad \vec{b}_2 = \frac{2\pi}{a}(0,1) \tag{2.36}$$

The coordinates of the symmetry point of the first Brillouin zone are:

$$\Gamma = (0,0), \qquad X = \left(\frac{\pi}{a}, 0\right), \qquad M = \left(\frac{\pi}{a}, \frac{\pi}{a}\right)$$

The filling fraction, f is the proportion of rod area to unit cell area, for square lattice

$$f = \pi\left(\frac{r_r}{a}\right)^2 \tag{2.37}$$

where r_r is the radius of rods and a is the lattice period.

2.4.2 Triangular Lattice

The construction of the first Brillouin zone for a two-dimensional triangular lattice is shown below.

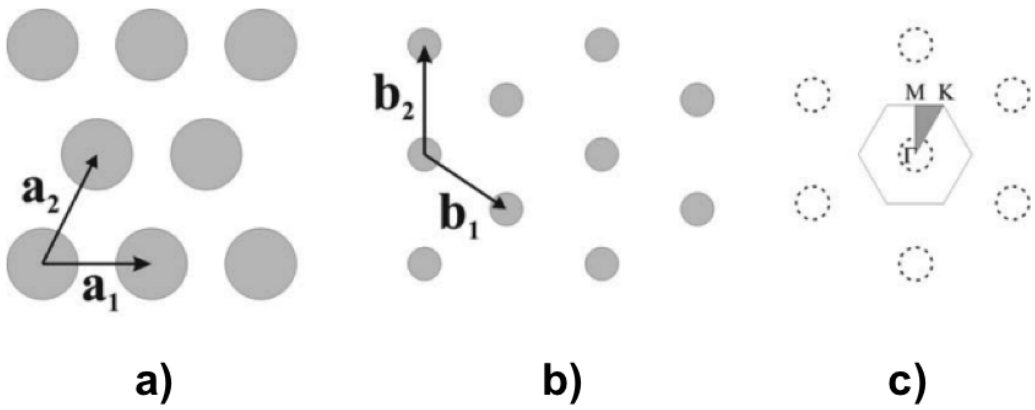

Figure 2.5: Triangular Lattice a) Lattice generated by the basis vectors b) The corresponding reciprocal lattice and reciprocal vectors c) First Brillouin zone (Wigner-Seitz primitive cell) and irreducible region denoted as hexagon and triangle, respectively.

The lattice vectors and corresponding reciprocal lattice vectors for triangular lattice are centred at the origin (Γ). The points at the corner and face are known as K and M respectively. The diagram on the right (Figure 2.5 c)) shows the Brillouin zone of the triangular lattice

$$\vec{a}_1 = a\left(\frac{1}{2}, \frac{\sqrt{3}}{2}\right) \qquad \vec{b}_1 = \frac{2\pi}{a}\left(\frac{\sqrt{3}}{2}, \frac{1}{2}\right) \tag{2.38}$$

$$\vec{a}_2 = a(\frac{1}{2}, -\frac{\sqrt{3}}{2}) \qquad \vec{b}_2 = \frac{2\pi}{a}\left(\frac{\sqrt{3}}{2}, -\frac{1}{2}\right) \tag{2.39}$$

The coordinates of the symmetry point of the first Brillouin zone are:

$$\Gamma = (0,0), \qquad M = \left(0, \frac{2\pi}{\sqrt{3}a}\right), \qquad K = \left(\frac{2\pi}{3a}, \frac{2\pi}{\sqrt{3}a}\right)$$

The filling fraction,

$$f = \frac{2\pi}{\sqrt{3}}\left(\frac{r_r}{a}\right)^2 \tag{2.40}$$

A 2D photonic crystal is periodic along two of its axes and homogeneous along the third axis. The multilayer film only reflects light at normal incidence but two-dimensional photonic crystals can reflect incident light from any direction in the plane. The modes propagating in photonic crystals can be classified as transverse electric, TE or transverse magnetic, TM according to their polarization directions. If we consider a photonic crystal that has discrete transitional symmetry in the xy-plane and continuous transitional symmetry in the z-direction, the TE or TM polarization can be distinguished from whether the electric field or magnetic field vectors are in line with the z-direction. The definition of TE and TM polarization is however different from the conventional definition. TM polarization defines the wave orientation where the electric field is parallel to the rod axis. The magnetic field oscillates transverse to the z-direction E_z, H_x, H_y are non-zero, in TM polarization. TE polarization defines the wave orientation where the electric field is perpendicular to the rod axis where H_z, E_x, E_y are non-zero.

There are two types of photonic crystals: high-index materials are grown in a low-index medium and low-index materials drilled in a high-index medium. We may distinguish these structures as pillar type and hole type crystals, respectively, since in most conditions the low-index material is the air. The most studied photonic crystals consist of arrays of cylindrical pillars (rods) or circular holes in air or dielectric in square and triangular (hexagonal) lattice configurations.

There are two most favourable and studied conditions: dielectric pillars in air in

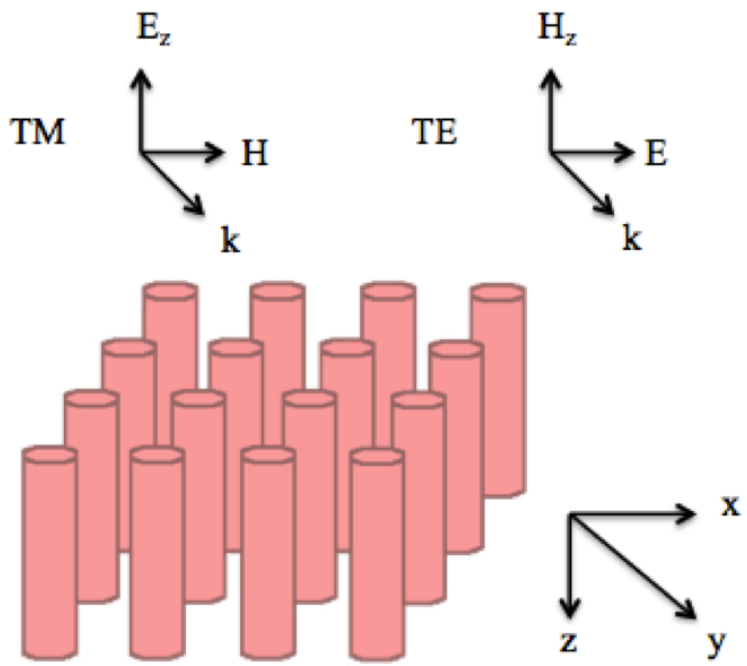

Figure 2.6: Directions and electromagnetic field vectors for TE and TM polarizations considered for 2D photonic crystals.

a square lattice array and air holes in dielectric medium in a triangular lattice array. In 2D photonic crystals, high-ε dielectric materials in a low-ε medium lead to large TM band-gaps because most of the energy is concentrated in high-ε. Therefore, pillar type crystals exhibit large TM, small TE band gaps with small filling factors. On the other hand low-ε material in a high-ε material lead to TE band-gaps in a connected lattice, therefore hole-type crystals exhibit both TE and TM bands when the size of radius is large enough.

The irreducible Brillouin zone is represented with special directions in a crystal structure called high symmetry points. These are used in order to characterize the dispersion of electromagnetic radiation inside the structure. In the band-gap diagrams for 2D and 3D photonic crystals, k-vectors are often expressed in Greek letters corresponding to the high symmetry points in the crystal. Usually computa-

tion starts from the centre of the Brillouin zone denoted by Γ and by scanning the all possible angles through the symmetry points, the contour is completed by returning to the centre where the k-vector is zero. For instance, for 2D photonic crystals in square array these symmetry points are Γ-X-M where in the interval Γ-X, k_x increases while k_y remains zero, $\omega = c\,k_x$, in the X-M interval, k_x remains constant while k_y increases, $\omega = c\sqrt{{k_x}^2 + {k_y}^2}$ and M-Γ both k_x and k_y are decreasing. $\omega = ck$, $\vec{k} = k_x\hat{x} + k_y\hat{y}$.

Silicon is one of the most commonly used materials in semiconductors and photonic crystals due to its high refractive index and low losses. The dielectric constant of silicon is 11.7 (24). Figure 2.7 shows the band-gap diagram of Silicon (Si) pillars of square lattice array in air. The radius of the rods is $0.2a$.

The polarization plays an important role on wave propagation in 2D photonic crystals. As can be seen from the band-gap diagrams in Figure 2.7, wave propagation is affected by the polarization of light. There are no TE gaps for square lattice in the frequency range displayed with the given ratio. However, there are two gaps clearly seen in the band structure for TM mode, as high-ε regions lead to TM gaps. In the reverse dielectric configuration where air holes are drilled in silicon medium, in triangular lattice array, the band diagrams are shown in Figure 2.8. A triangular lattice of air columns of radius r = $0.48a$ exhibits a band-gap for both polarizations for a short range of frequencies around $0.5(\omega a/2\pi c)$ whereas the TE and TM gaps overlap and encompass a complete band-gap.

A complete photonic band gap is a range of ω in which there are no propagating (real $\vec{k}$) solutions of Maxwell's equations for any $\vec{k}$, surrounded by propagating states above and below the gap. There are also incomplete gaps, which only exist over a subset of all possible wave vectors, polarizations, and/or symmetries. In order for a complete band gap to arise in 2D or 3D, an additional requirement must be

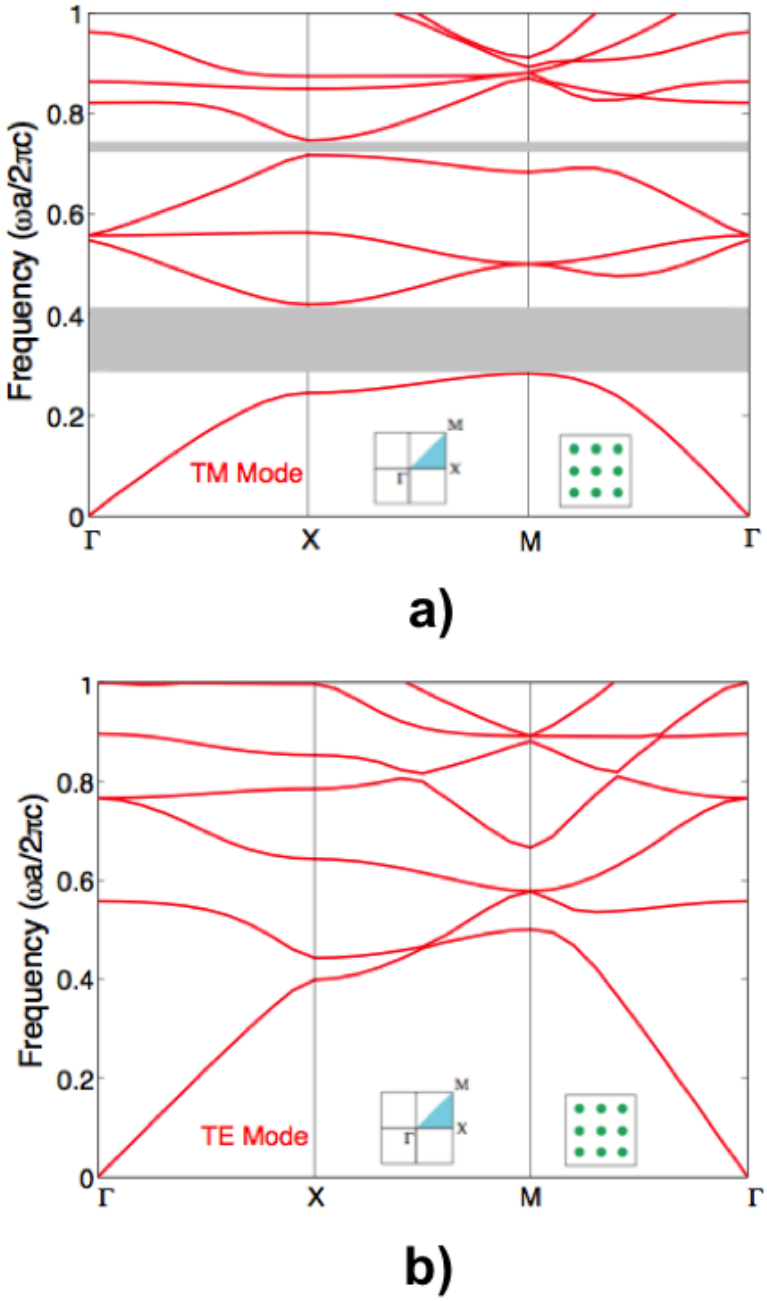

Figure 2.7: The photonic band structure for a square array of dielectric columns embedded in air, ε_1 = 11.7 and ε_2 = 1, with r = 0.2a. The photonic band gaps are shown by shaded areas a) TM polarization b) TE polarization.

met. In each symmetry direction of the crystal (and each k point) there may be band gaps. However, these band gaps do not necessarily overlap in frequency (or even lie

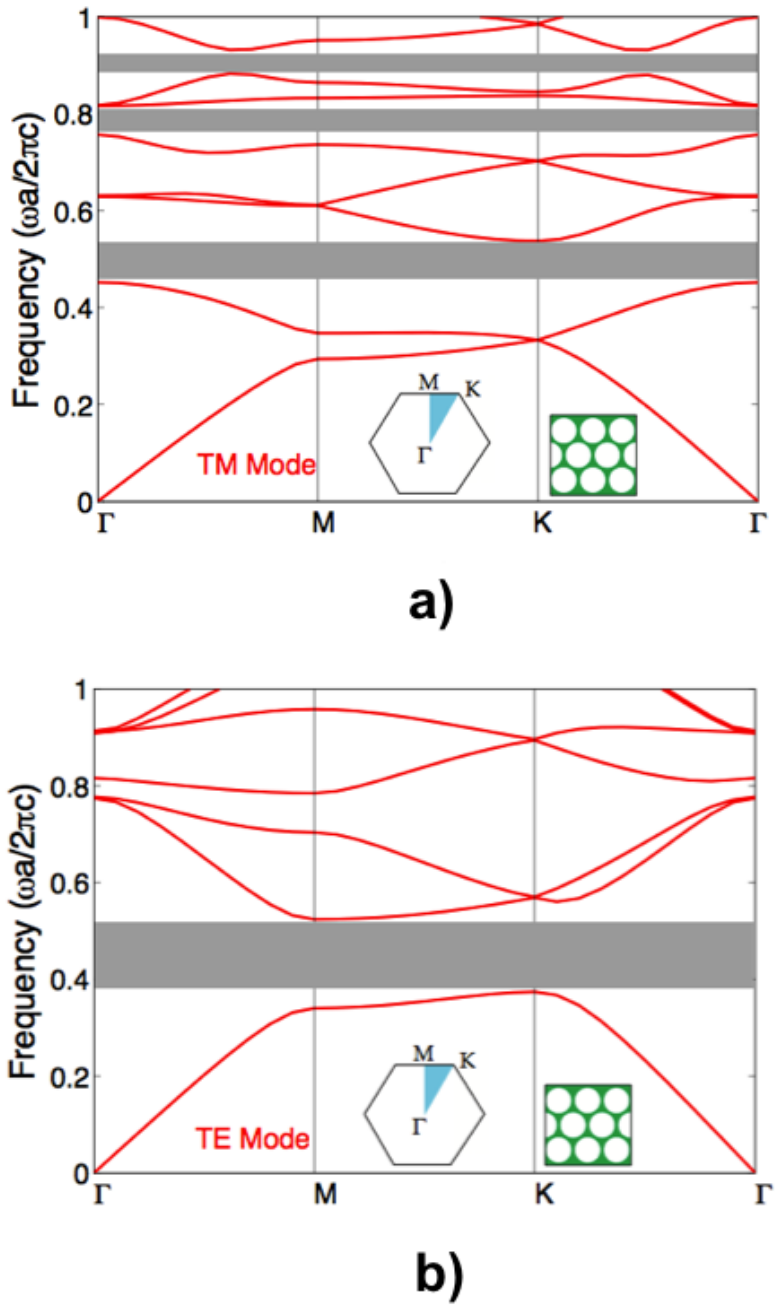

Figure 2.8: The photonic band structure for a triangular of dielectric columns embedded in air, ε_1 = 1 and ε_2 = 11.7, with r = 0.48a. The photonic band gaps are shown by shaded areas a) TM polarization b) TE polarization.

between the same bands) as seen in the diagram above. An overlap is more likely if a band-gap is sufficiently large, which implies a minimum ε contrast (typically

at least 4:1 in 3D structures). Since mid-gap frequency for 1D photonic crystals is $\approx c\pi/(a\sqrt{\varepsilon})$ and varies inversely with the period a, large band-gaps are obtained for the crystals whose periodicity is nearly constant in all directions. Therefore, the largest gaps typically arise for triangular lattices in 2D structures and face-centred cubic (fcc) lattices in 3D structures which have the most nearly circular/spherical Brillouin zones (4).

In order to have a clearer idea on the band-gap positions not only for a particular size of crystal but also for all possible sizes, we can utilize diagrams called *band-gap maps*. In these, diagram shows the size and positions of band-gaps of a 2D photonic crystal for a given lattice type and filling factor and dielectric contrast. Gap maps are generated from band gap figures, by determining the gaps for each r/a value. As holes/pillars overlap for $r/a \geq 0.5$ data for larger r/a are not shown in band-gap map figures. The x-axis of the diagram is the radius of rods or the holes in the inverse configuration, y-axis is the frequency; both are normalized to lattice constant. From the diagram, frequency interval of largest band-gap and corresponding r/a value can be determined. As the diagram is normalized by lattice constant, it must be scaled to the desired levels.

Here, we present band-gap maps for two photonic crystal structures: silicon pillars in air in square lattice array and air holes in silicon in triangular lattice array in Figure 2.9 and Figure 2.10, respectively. The locations of the band gaps are shown as a function of r/a for both TE and TM polarizations. In this study, both band-gap diagrams and band-gap maps are obtained by means of the PWE method, which implemented on a MATLAB platform.

TE gaps are very sparse, because the isolated patches of high-ε regions lead to the TM gaps and the connectivity of high dielectric constant regions. In square lattice structures it is difficult to produce the complete photonic band gaps because of

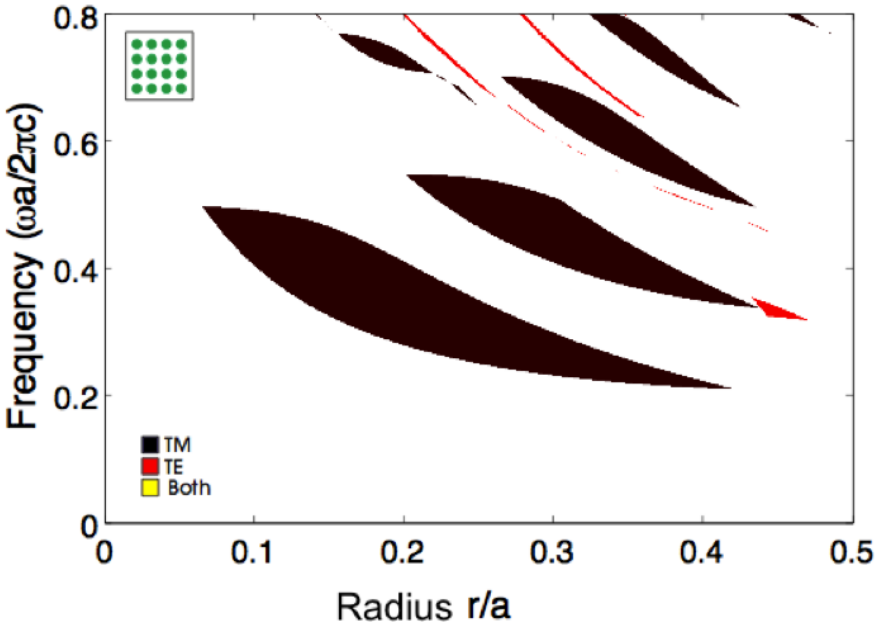

Figure 2.9: Band-gap map for a square array of silicon in air, red and black regions show band-gap islands of TE and TM modes, respectively.

high spatial symmetry. On the other hand, triangular lattice structures exhibit complete band-gaps. TE and TM bands overlap when the radii are large enough. Such overlap can be very desirable for some applications. Otherwise conditions lead to polarization selectivity, which is also important for many applications.

2.5 Devices Based on the Photonic Crystals

Photonic crystals are very promising candidates for building faster and smaller devices in order to fulfil the needs of bandwidth and high-speed switching. Photonic crystals can be engineered in order to meet requirements of an application. With a proper choice of design parameters (lattice type, filling factor, index contrast) photonic crystals can be utilized for many applications (25; 26; 27). Due to the fabrication difficulty of 3D photonic crystal structures, 2D photonic crystals have been studied intensively and many novel devices are developed.

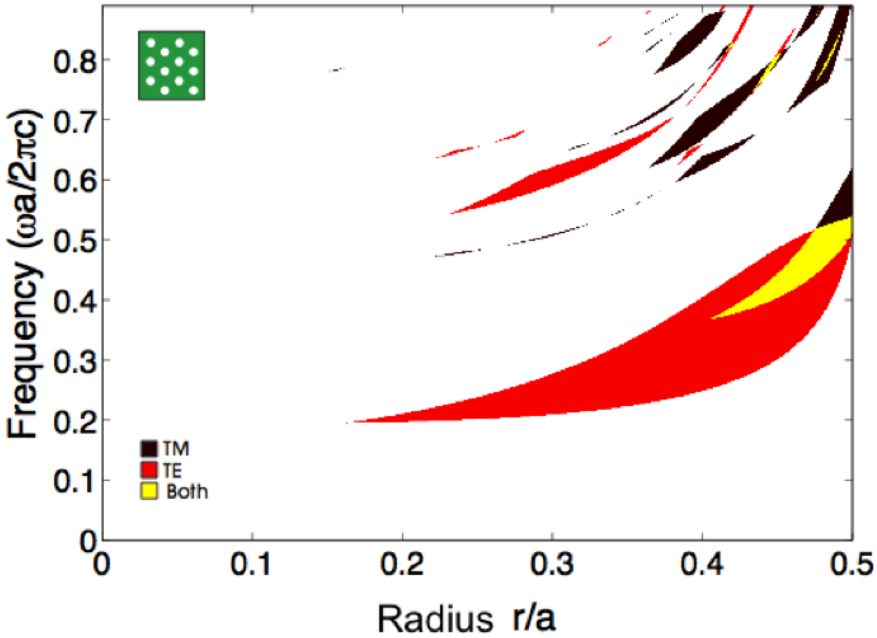

Figure 2.10: Band-gap map for triangular array of holes in silicon, red, black and yellow regions show band-gap islands of TE, TM modes and both, respectively.

The existence of the band gaps makes many applications possible. In a photonic crystal structure defects can be created by removing rods/holes. When a defect is introduced to the photonic crystal, this causes a new band state to appear in the band-gap diagram (4; 28). Depending on the defect and dimensions of the structures waves can be localised into a small volume around the defect or along the defect. This gives the ability to control propagation inside the defect, and also the possibility to design different devices.

We can roughly classify these devices into three categories:

- Point defect - If a point defect is introduced in a 2D photonic crystal; the electromagnetic wave can be trapped and confined in the defect, i.e. microcavities.

- Line defect - If a line defect is introduced, the electromagnetic waves are confined and forced to follow predetermined routes along the line defect, i.e. waveguides.

- Combination of point and line defects - with the integration of both point and line defect, waves propagating in the line defect waveguide can be trapped by a cavity formed by point defect placed close to waveguide in the structure, i.e. add-drop filters.

There are many promising devices which can be created based on the reflection properties of photonic crystals. For instance, omnidirectional mirrors are operated at band-gap frequencies since light cannot pass through the structure and all the radiation will be reflected completely from the photonic crystal surface (29; 30).

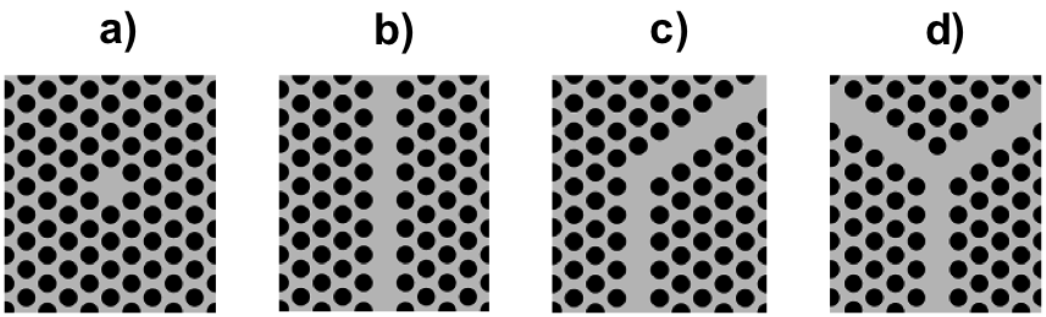

Figure 2.11: Schematics of two-dimensional photonic devices made of photonic crystals. a) a microcavity, b) a waveguide, c) a waveguide bend, d) a waveguide splitter. Here those circles can be considered as the air holes etched in a solid slab, or as rods/pillars standing in air.

In a high-Q microcavity, a point defect behaves like a cavity surrounded by reflecting walls, since the waves within the photonic band-gap cannot propagate in the crystal but in the defect, light is localized producing high quality factors. The quality factor, Q, can be increased up to tens of thousands. High-Q microcavities generate a narrow so-called defect mode within the photonic band gap, which can

be used to create high field intensity selective filters transmitting only a very narrow range of wavelengths or frequencies. In addition, microcavities can also be used as photonic crystal laser (31; 32; 33; 34). These types of lasers can reduce spontaneous emission effectively leading to a very low threshold (35) or thresholdless lasing (36). Light extraction efficiency can be increased using photonic crystals in light emitting diodes (LED) by overcoming the total internal reflection (TIR) in conventional LEDs and with lower effective refractive index (37).

Photonic crystal waveguides are utilized at the photonic band-gap frequencies in order to confine the light in the wave-guiding channel introduced by a line defect. Traditional hollow metal waveguides are used for guiding at microwave range as metals have relatively low absorption at those frequencies, and light can be reflected for any incident angles. Photonic crystal waveguides and the conventional dielectric waveguide differ from each other in confining and guiding the light. In the conventional waveguides, the guiding mechanism is based on total internal reflection. Conventional guiding takes place within large refractive index material (core) surrounded by a low refractive index media (cladding). In order to achieve total internal reflection the refractive index of the core needs to be larger than that of the cladding. On the other hand in photonic crystal structures guiding is based on Bragg reflection. However, in 2D photonic crystals Bragg reflection only applies to in-plane propagation, while out of plane propagation relies on total internal reflection. It is well known that photonic crystals have many advantages over conventional metal hollow and dielectric waveguides, especially for wave transmission in a sharp bend. 2D photonic crystal waveguides allow the carrying of electromagnetic waves through more compact, smaller bend radii sharp bends with high efficiency and low losses (38; 39). There are also variety of passive components which can be fabricated on the same principle such as power splitters (40; 41; 42), modulators and combiners (43), couplers (44; 45), optical switches (46), optical amplifiers (47), optical filters (48), polarizers (49), and channel drop filters (50; 51).

A channel drop filter is a device that can send multiple signals through the same waveguide but at different wavelengths (channels) by accessing one channel of a wavelength division, multiplexed signal while leaving other channels undisturbed. This is used for Wavelength Division Multiplexing (WDM) networks. Resonant filters are also attractive candidates for channel dropping, since they can potentially be used to select a single channel with a very narrow line width (52).

Photonic crystal fiber (PCF), is a novel device studied first by Russell providing important advantages over conventional fibers (14). The guiding mechanism in the conventional fibers is based on Total Internal Reflection (TIR) between high refractive index core and the low index cladding and has a drawback of light travelling at different speed for different wavelengths. In photonic crystal fibers light is confined by the band-gap effect and is able to propagate in low refractive index core, even in air (holey fiber)(53). Since no doping is required for the core, the fabrication of these fibers is less complex than that of conventional fibers. Photonic crystal fibers provide single mode operation over a wide wavelength and large waveguide dispersion (54).

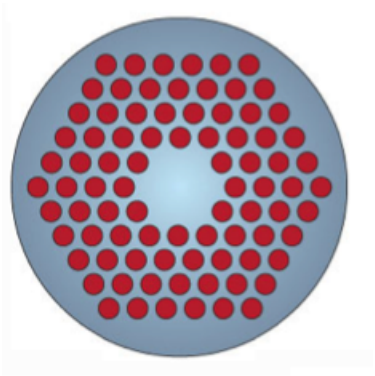

Figure 2.12: Schematic figure of photonic crystal fiber

Furthermore, photonic crystals also exhibit unusual dispersive properties. A dis-

tinctive example is the superprism, which provides very large angular deflection of light in the PhC by a slight change of the incident angle (55).

Metamaterials also know as left-handed materials (LHM), which posses negative permittivity and permeability, were first proposed theoretically by Veselago in 1967. LHMs had not been attracted attention for over thirty due to the lack of experimental verification until the study by Pendry et.al. in 1999 (56). Negative refraction is observed when a wave passes through an interface of left-handed materials and right-handed materials. With the use of 2D photonic crystals negative refraction can be controlled by the structure and allows the fabrication of a perfect lens (57; 58).

2.6 Conclusion

In this chapter, fundamentals of photonic crystals are mentioned and information on background is given. Macroscopic Maxwell's equations are discussed to understand the phenomenon band-gap crystals and model wave propagation in photonic crystals by Bloch waves and Brillouin zone. Band-gap diagram of photonic crystals are also presented for 1D and 2D photonic crystals. The chapter is concluded with brief information about photonic crystal based devices.

In this thesis, band-gap diagram and wave propagation are studied using finite element method (FEM). In the next chapter, FEM and the other most common numerical methods used in photonic crystal study will be mentioned.

References

[1] M. Johri, Y. A. Ahmed, and T. Bezboruah, "Photonic band gap materials: Technology, applications and challenges," *Current Science*, vol. 92, no. 10, pp. 1361–1365, 2007.

[2] P. H. Siegel, T. Loffler, D. Mittleman, K. Mizuno, and X. C. Zhang, "Guest EditorialTerahertz technology: Bridging the Microwave-to-Photonics gap," *IEEE Transactions on Microwave Theory and Techniques*, vol. 58, pp. 1901–1902, July 2010.

[3] M. Tonouchi, "Cutting-edge terahertz technology," *Nat Photon*, vol. 1, pp. 97–105, Feb. 2007.

[4] J. D. Joannopoulos, *Photonic crystals: molding the flow of light*. Princeton Univ Pr, 2008.

[5] A. R. Parker and H. E. Townley, "Biomimetics of photonic nanostructures," *Nature Nanotechnology*, vol. 2, no. 6, pp. 347 – 353, 2007.

[6] J. W. Galusha, L. R. Richey, J. S. Gardner, J. N. Cha, and M. H. Bartl, "Discovery of a diamond-based photonic crystal structure in beetle scales," *Physical Review E*, vol. 77, p. 050904, May 2008.

[7] J. V. Sanders, "Colour of precious opal," *Nature*, vol. 204, pp. 1151–1153, Dec. 1964.

[8] P. Vukusic and J. R. Sambles, "Photonic structures in biology," *Nature*, vol. 424, no. 6950, pp. 852 – 855, 2003.

[9] J. P. Vigneron, J. F. Colomer, M. Rassart, A. L. Ingram, and V. Lousse, "Structural origin of the colored reflections from the black-billed magpie feathers," *Physical Review E*, vol. 73, no. 2, p. 021914, 2006.

[10] S. John, "Strong localization of photons in certain disordered dielectric superlattices," *Physical Review Letters*, vol. 58, no. 23, pp. 2486 – 2489, 1987.

[11] E. Yablonovitch, "Inhibited spontaneous emission in solid-state physics and electronics," *Physical review letters*, vol. 58, no. 20, pp. 2059 – 2062, 1987.

[12] T. F. Krauss, R. M. Rue, and S. Brand, "Two-dimensional photonic-bandgap structures operating at near-infrared wavelengths," *Nature*, vol. 383, no. 6602, pp. 699 – 702, 1996.

[13] J. O'Brien, W. Kuang, J. R. Cao, M. H. Shih, P. T. Lee, M. Bagheri, A. Mock, and W. K. Marshall, "Photonic crystal microcavity lasers," *Journal of Physics D: Applied Physics*, vol. 40, p. 2671, 2007.

[14] P. Russell, "Photonic crystal fibers," *Science*, vol. 299, no. 5605, p. 358, 2003.

[15] K. Cho, T. Hirai, and T. Ikawa, "Propagating mode in the photonic gap of 1D resonant bragg reflector," *Journal of Luminescence*, vol. 100, pp. 283–289, Dec. 2002.

[16] E. Yablonovitch, T. J. Gmitter, and K. M. Leung, "Photonic band structure: The face-centered-cubic case employing nonspherical atoms," *Physical Review Letters*, vol. 67, p. 2295, Oct. 1991.

[17] E. Ozbay, G. Tuttle, M. Sigalas, C. M. Soukoulis, and K. M. Ho, "Defect structures in a layer-by-layer photonic band-gap crystal," *Physical Review B*, vol. 51, p. 13961, May 1995.

[18] S. Lin, J. G. Fleming, D. L. Hetherington, B. K. Smith, R. Biswas, K. M. Ho, M. M. Sigalas, W. Zubrzycki, S. R. Kurtz, and J. Bur, "A three-dimensional photonic crystal operating at infrared wavelengths," *Nature*, vol. 394, no. 6690, pp. 251 – 253, 1998.

[19] K. Busch and S. John, "Photonic band gap formation in certain self-organizing systems," *Physical Review E*, vol. 58, no. 3, p. 3896, 1998.

[20] S. G. Johnson and J. D. Joannopoulos, "Introduction to photonic crystals: Blochs theorem, band diagrams, and gaps (but no defects)," *Photonic Crystal Tutorial*, pp. 1 – 16, 2003.

[21] L. Rayleigh, "On the maintenance of vibrations by forces of double frequency, and on the propagation of waves through a medium endowed with a periodic structure," *Phil. Mag*, vol. 24, no. 147, p. 145159, 1887.

[22] R. M. Martin, *Electronic structure: basic theory and practical methods*. Cambridge Univ Pr, 2004.

[23] C. Kittel, *Introduction to Solid State Physics*. New York: John Wiley & Sons, Inc., 6th ed., 1986.

[24] F. Genereux, S. W. Leonard, H. M. van Driel, A. Birner, and U. Gsele, "Large birefringence in two-dimensional silicon photonic crystals," *Physical Review B*, vol. 63, p. 161101, Apr. 2001.

[25] D. Cassagne, C. Jouanin, and D. Bertho, "Hexagonal photonic-band-gap structures," *Physical Review B*, vol. 53, p. 7134, Mar. 1996.

[26] Z. Li, J. Wang, and B. Gu, "Creation of partial band gaps in anisotropic photonic-band-gap structures," *Physical Review B*, vol. 58, no. 7, p. 3721, 1998.

[27] Y. Kalra and R. K. Sinha, "Photonic band gap engineering in 2D photonic crystals," *Pramana*, vol. 67, pp. 1155–1164, Dec. 2006.

[28] K. Sakoda, *Optical properties of photonic crystals*. Springer, 2005.

[29] Y. Fink, J. N. Winn, S. Fan, C. Chen, J. Michel, J. D. Joannopoulos, and E. L. Thomas, "A dielectric omnidirectional reflector," *Science*, vol. 282, pp. 1679 –1682, Nov. 1998.

[30] E. R. Brown, O. B. McMahon, and C. D. Parker, "Photonic-crystal antenna substrates," *Lincoln Laboratory Journal*, vol. 11, no. 2, 1998.

[31] K. Inoue, M. Sasada, J. Kawamata, K. Sakoda, and J. W. Haus, "A Two-Dimensional photonic crystal laser," *Japanese Journal of Applied Physics*, vol. 38, pp. L157–L159, Feb. 1999.

[32] O. Painter, R. K. Lee, A. Scherer, A. Yariv, J. D. O'Brien, P. D. Dapkus, and I. Kim, "Two-Dimensional photonic Band-Gap defect mode laser," *Science*, vol. 284, pp. 1819 –1821, June 1999.

[33] S. Noda, M. Yokoyama, M. Imada, A. Chutinan, and M. Mochizuki, "Polarization mode control of Two-Dimensional photonic crystal laser by unit cell structure design," *Science*, vol. 293, no. 5532, pp. 1123 –1125, 2001.

[34] J. Vukovi, M. Lonar, H. Mabuchi, and A. Scherer, "Design of photonic crystal microcavities for cavity QED," *Physical Review E*, vol. 65, p. 016608, Dec. 2001.

[35] M. Loncar, T. Yoshie, A. Scherer, P. Gogna, and Y. Qiu, "Low-threshold photonic crystal laser," *Applied Physics Letters*, vol. 81, no. 15, p. 2680, 2002.

[36] H. Hirayama, T. Hamano, and Y. Aoyagi, "Novel surface emitting laser diode using photonic band-gap crystal cavity," *Applied Physics Letters*, vol. 69, no. 6, p. 791, 1996.

[37] M. Boroditsky, T. F. Krauss, R. Coccioli, R. Vrijen, R. Bhat, and E. Yablonovitch, "Light extraction from optically pumped light-emitting diode by thin-slab photonic crystals," *Applied Physics Letters*, vol. 75, no. 8, p. 1036, 1999.

[38] A. Mekis, J. C. Chen, I. Kurland, S. Fan, P. R. Villeneuve, and J. D. Joannopoulos, "High transmission through sharp bends in photonic crystal waveguides," *Physical Review Letters*, vol. 77, p. 3787, Oct. 1996.

[39] S. Lin, E. Chow, V. Hietala, P. R. Villeneuve, and J. D. Joannopoulos, "Experimental demonstration of guiding and bending of electromagnetic waves in a photonic crystal," *Science*, vol. 282, pp. 274 – 276, Oct. 1998.

[40] S. Fan, S. G. Johnson, J. D. Joannopoulos, C. Manolatou, and H. A. Haus, "Waveguide branches in photonic crystals," *Journal of the Optical Society of America B*, vol. 18, pp. 162–165, Feb. 2001.

[41] S. G. Johnson, C. Manolatou, S. Fan, P. R. Villeneuve, J. D. Joannopoulos, and H. A. Haus, "Elimination of cross talk in waveguide intersections," *Optics Letters*, vol. 23, pp. 1855–1857, Dec. 1998.

[42] S. Boscolo, M. Midrio, and T. F. Krauss, "Y junctions in photonic crystal channel waveguides: high transmission and impedance matching," *Optics Letters*, vol. 27, pp. 1001–1003, June 2002.

[43] S. Kim, I. Park, and H. Lim, "Proposal for ideal 3-dB splitters-combinersin photonic crystals," *Optics Letters*, vol. 30, pp. 257–259, Feb. 2005.

[44] A. Mekis, A. Dodabalapur, R. E. Slusher, and J. D. Joannopoulos, "Two-dimensional photonic crystal couplers for unidirectional light output," *Optics Letters*, vol. 25, pp. 942–944, July 2000.

[45] S. Boscolo, M. Midrio, and C. Someda, "Coupling and decoupling of electromagnetic waves in parallel 2D photonic crystal waveguides," *IEEE Journal of Quantum Electronics*, vol. 38, pp. 47–53, Jan. 2002.

[46] V. R. Almeida, C. A. Barrios, R. R. Panepucci, and M. Lipson, "All-optical control of light on a silicon chip," *Nature*, vol. 431, pp. 1081–1084, Oct. 2004.

[47] K. Sakoda, "Enhanced light amplification due to group-velocity anomaly peculiar to two- and three-dimensional photonic crystals," *Optics Express*, vol. 4, pp. 167–176, Mar. 1999.

[48] J. Chen, H. Haus, S. Fan, P. Villeneuve, and J. Joannopoulos, "Optical filters from photonic band gap air bridges," *Journal of Lightwave Technology*, vol. 14, pp. 2575–2580, Nov. 1996.

[49] D. R. Solli, C. F. McCormick, R. Y. Chiao, and J. M. Hickmann, "Photonic crystal polarizers and polarizing beam splitters," *Journal of Applied Physics*, vol. 93, no. 12, p. 9429, 2003.

[50] S. Fan, P. R. Villeneuve, J. D. Joannopoulos, and H. A. Haus, "Channel drop filters in photonic crystals," *Opt. Express*, vol. 3, no. 1, pp. 4 – 11, 1998.

[51] A. Chutinan, M. Mochizuki, M. Imada, and S. Noda, "Surface-emitting channel drop filters using single defects in two-dimensional photonic crystal slabs," *Applied Physics Letters*, vol. 79, no. 17, p. 2690, 2001.

[52] B. Min, J. Kim, and H. Y. Park, "Channel drop filters using resonant tunneling processes in two-dimensional triangular lattice photonic crystal slabs," *Optics Communications*, vol. 237, pp. 59–63, July 2004.

[53] J. Knight, J. Arriaga, T. Birks, A. Ortigosa-Blanch, W. Wadsworth, and P. Russell, "Anomalous dispersion in photonic crystal fiber," *IEEE Photonics Technology Letters*, vol. 12, pp. 807–809, July 2000.

[54] T. A. Birks, J. C. Knight, and P. S. Russell, "Endlessly single-mode photonic crystal fiber," *Optics Letters*, vol. 22, pp. 961–963, July 1997.

[55] H. Kosaka, T. Kawashima, A. Tomita, M. Notomi, T. Tamamura, T. Sato, and S. Kawakami, "Superprism phenomena in photonic crystals: Toward microscale lightwave circuits," *Journal of Lightwave Technology*, vol. 17, p. 2032, Nov. 1999.

[56] J. Pendry, A. Holden, D. Robbins, and W. Stewart, "Magnetism from conductors and enhanced nonlinear phenomena," *IEEE Transactions on Microwave Theory and Techniques*, vol. 47, pp. 2075–2084, Nov. 1999.

[57] J. B. Pendry, "Negative refraction makes a perfect lens," *Physical Review Letters*, vol. 85, p. 3966, Oct. 2000.

[58] E. Cubukcu, K. Aydin, E. Ozbay, S. Foteinopoulou, and C. M. Soukoulis, "Subwavelength resolution in a Two-Dimensional Photonic-Crystal-Based superlens," *Physical Review Letters*, vol. 91, p. 207401, Nov. 2003.

Chapter 3

MODELLING TOOLS

The problem of wave propagation in a photonic crystal is essentially an electromagnetic wave propagation problem. The behaviour of electromagnetic field in a photonic crystal is described by macroscopic Maxwell's equations. To simulate the wave propagation it is required to solve these equations with appropriate boundary conditions. Maxwell's equations are simply a group of partial differential equations. Except in a few cases, there are no analytical solutions for these equations. There are several numerical methods to solve Maxwell's equations and model photonic crystal structure. Maxwell's Equations can be expressed either in time domain or frequency domain form. Therefore, the numerical methods used to model photonic crystals, typically, can be classified as frequency or time domain methods. In time domain methods, time-dependent Maxwell's equations are solved directly on spatial grids and the solution has a time dependency. This is particularly advantageous for obtaining transient response and comparing with experimental results. On the other hand frequency domain methods provide the frequency response of the system assuming the harmonic time dependency, such as calculating eigenstates, studying band structures, or highly dispersive materials. The relation between time and frequency can be obtained by Fourier transformation.

In the previous chapter, the basic theory of band-gaps was discussed, Bloch modes were introduced and band-gap diagrams were obtained by means of the plane wave expansion method. The details of the plane wave method and other methods mostly used for analysing photonic crystals deeply in terms of transmission, loss and other aspects for modelling will be discussed.

All numerical methods have advantages and drawbacks; some are efficient for a given problem while the others are only efficient in limited cases. A single method is not enough for analysing all kinds of problems in photonic crystals since not all methods are suitable, flexible or efficient to analyse photonic crystals to all extents. Moreover, accuracy and computation time and sources are always factors one needs to consider.

Many numerical methods have been developed in order to study photonic crystals. Among them, the most used and accepted methods are Plane Wave Method (PWM), the Transfer Matrix Method (TMM), Finite Difference Time Domain (FDTD) method, the Finite Element Method (FEM). These will be discussed briefly.

3.1 Plane Wave Expansion Method

The PWE method is one of the most commonly used methods in photonic crystal study and is primarily used for obtaining band-gap diagrams of photonic crystals. In photonic crystals where the electromagnetic field distribution is periodic as well as the refractive index, the field can be represented as a sum of plane waves. PWE method is based on the Fourier expansion method to solve Maxwell's equations by super positioning the plane waves. The solution of problem results in an eigenvalue matrix of vectors where the matrix size is theoretically infinite, and it needs to be

truncated by numerical calculations. Ho, Chan and Soukoulis conducted the first theoretical demonstration of complete band-gap in 3D photonic crystals in 1990 (1). In their study, the band-gap of a diamond lattice of air spheres in a solid background was predicted correctly by means of PWE method (2). Soon after this study, it became possible to predict a complete band-gap in three-dimensional photonic crystals correctly before fabrication and experimental characterisation.

Here, it is shown how to derive Maxwell's equations as a set of plane waves using Fourier expansion. Fourier series are expanded for calculation of eigenvalues for electromagnetic fields using the periodicity and Bloch form with plane waves. As long as the periodicity is defined in reciprocal lattice by reducing the symmetry according to high symmetry points, the band gap structure of any type of crystal lattice can be calculated.

The periodic material with periodicity of lattice vector satisfies,

$$\varepsilon(\vec{r}) \;=\; \varepsilon(\vec{r}+\vec{R}) \tag{3.1}$$

where $\vec{R}$ the lattice vectors. By solving the Maxwell's equations for magnetic field considering the periodicity of the dielectric constant in the reciprocal space the Bloch theorem can be applied (3):

$$\nabla \times \left(\frac{1}{\varepsilon(\vec{r})} \nabla \times \vec{H}_{\vec{k}}(\vec{r}) \right) = \left(\frac{\omega}{c} \right)^2 \vec{H}_{\vec{k}}(\vec{r}) \tag{3.2}$$

$$\vec{H}_{\vec{k}}(\vec{r}) \;=\; \vec{h}_{n,\vec{k}}(\vec{r}) e^{i\vec{k}\vec{r}} \tag{3.3}$$

where $\vec{h}_{n,\vec{k}}(\vec{r})$ is the periodic function with periodicity of the lattice for wave vector $\vec{k}$ and discrete band index, n. Expanding the appropriate Fourier series and expan-

sions into the equation results in infinite matrix-eigenvalue problem and the number of basis function, $e^{i\vec{G}\vec{r}}$ needs to be truncated into N plane waves to numerically solve the problem.

$$\vec{h}_{n,\vec{k}}(\vec{r}) \;=\; \sum_{\vec{G}} \vec{h}_{\vec{G}} e^{i\vec{G}\vec{r}} \tag{3.4}$$

The magnetic field is expanded into plane waves of wave vector $\vec{k}$ with respect to the reciprocal lattice vector $\vec{G}$.

$$\vec{H}_{\vec{k}}(\vec{r}) \;=\; \sum_{\vec{G}\lambda} h_{\vec{G}\lambda} \hat{e}_{\lambda} e^{[i(\vec{k}+\vec{G})\vec{r}]} \tag{3.5}$$

$\vec{h}_{\vec{G}\lambda}$, the coefficients of the wave vector and can be written as :

$$\vec{h}_{\vec{G}\lambda} \;=\; \sum_{\lambda=1}^{2} h_{\vec{G}\lambda} \hat{e}_{\lambda} \tag{3.6}$$

where the polarization vectors $\hat{e}_{\lambda}$ characterize two independent polarizations λ, which are perpendicular to $\vec{k}+\vec{G}$. If the equation of superposition of plane waves for magnetic field is put into the master equation, we obtain

$$\sum_{\vec{G}'\lambda'} E^{\vec{k}}_{\vec{G}\lambda,\vec{G}'\lambda'} \vec{h}_{\vec{G}'\lambda'} \;=\; \left(\frac{\omega}{c}\right)^2 \vec{h}_{\vec{G}\lambda} \tag{3.7}$$

The matrix E in the eigenvalue equation is a $2N \times 2N$ Hermitian matrix, where N is the number of plane waves, given by:

$$E^{\vec{k}}_{\vec{G}\lambda,\vec{G}'\lambda'} \;=\; [(\vec{k}+\vec{G}) \times \hat{e}_{\lambda}][(\vec{k}+\vec{G}') \times \hat{e}_{\lambda'}]\varepsilon^{-1}(\vec{G},\vec{G}') \tag{3.8}$$

The Fourier transform of inverse dielectric constant depends on the difference of the reciprocal lattice vectors only

$$\varepsilon^{-1}(\vec{G},\vec{G}') \;=\; \varepsilon^{-1}(\vec{G}-\vec{G}') \tag{3.9}$$

The equation finally forms as follows:

$$\sum_{\vec{G}'} |\vec{k}+\vec{G}||\vec{k}+\vec{G}'|\varepsilon^{-1}(\vec{G}-\vec{G}') \begin{bmatrix} \hat{e}_2\cdot\hat{e}_2' & -\hat{e}_2\cdot\hat{e}_1' \\ -\hat{e}_1\cdot\hat{e}_2' & \hat{e}_1\cdot\hat{e}_1' \end{bmatrix} \begin{bmatrix} \vec{h}_1' \\ \vec{h}_2' \end{bmatrix} \;=\; \left(\frac{\omega}{c}\right)^2 \begin{bmatrix} \vec{h}_1 \\ \vec{h}_2 \end{bmatrix} \tag{3.10}$$

Given that the dielectric constant is periodic, its inverse $\varepsilon^{-1}(\vec{G},\vec{G}')$ can be expanded in Fourier series as

$$\frac{1}{\varepsilon(\vec{r})} \;=\; \sum_{\vec{G}} \hat{\kappa}(\vec{G})e^{i\vec{G}\vec{r}} \tag{3.11}$$

where $\hat{\kappa}(\vec{G})$ are the Fourier coefficients obtained through an integration over the primitive unit cell and Ω is the volume of the unit cell.

$$\hat{\kappa}(\vec{G}) \;=\; \frac{1}{\Omega}\int_{\Omega} \varepsilon^{-1}(\vec{r})e^{-i\vec{G}\vec{r}}d^3(\vec{r}) \tag{3.12}$$

By using sufficient a number of plane waves, this standard eigenvalue problem can be solved numerically and the photonic band-gap structure is obtained. The size of the coefficient matrix depends on whether electric field or magnetic field is used in the equation. Due to the transversality of the magnetic field ($\nabla\cdot\vec{H} = 0$), it is possible to write wave vector coefficients for only two polarizations resulting in $2N\times 2N$ matrix, instead of the $3N\times 3N$ matrix that would have been if the equation was solved for electric field. When Fourier transform is performed, the selection of the integration region, the unit cell, becomes important. If inversion symmetry

is provided, the Fourier transform matrix will be real. However, the real part of complex Fourier coefficients does not provide the full solution. For instance, if we consider a 2D photonic crystal in cylindrical rods in square lattice configuration, the Fourier coefficients are given by (4):

$$\hat{\kappa}(\vec{G}) = \begin{cases} \frac{1}{\varepsilon_r} f + \frac{1}{\varepsilon_b}(1-f) & |\vec{G}| = 0 \\ \\ \left(\frac{1}{\varepsilon_r} - \frac{1}{\varepsilon_b}\right) f \frac{2J_1(\vec{G}r_r)}{\vec{G}r_r} & |\vec{G}| \neq 0 \end{cases} \tag{3.13}$$

where, ε_r, ε_b are the dielectric constants of rods and the background, respectively. r_r is the radius of rods and J_1 is the first-order Bessel function. The filling fraction, f is the proportion of rod area to unit cell area and is equal to $\pi\left(\frac{r_r}{a}\right)^2$ for a square lattice, where a is the lattice period.

When the equation is solved, the photonic band-gap diagram is obtained for two-polarizations: transverse electric, TE and transverse magnetic TM polarization. The plane wave equations can be rewritten for TE and TM polarization by assuming wave propagation along the xy-plane. The unit vector $\hat{e}_1$ is in the xy-plane and $\hat{e}_2 = \hat{a}_z$. The polarization vectors are simplify as follows:

$$\hat{e}_1 = [\cos\theta, \sin\theta, 0] \tag{3.14}$$

$$\hat{e}_2 = [0, 0, 1] \tag{3.15}$$

In a TM wave, H component is along $\hat{e}_1$ and has no components along $\hat{e}_1 = \hat{a}_z$. In a TE wave, H component is along $\hat{e}_2 = \hat{a}_z$ and E has no component along $\hat{a}_z$ (5).

TM

$$\sum_{\vec{G}} |\vec{k}+\vec{G}||\vec{k}+\vec{G}'|\varepsilon^{-1}(\vec{G}-\vec{G}')\vec{h}_1(\vec{G}') = \left(\frac{\omega}{c}\right)^2 \vec{h}_1(\vec{G}) \tag{3.16}$$

TE

$$\sum_{\vec{G}} |\vec{k}+\vec{G}||\vec{k}+\vec{G}'|\varepsilon^{-1}(\vec{G}-\vec{G}')\vec{h}_2(\vec{G}') \;=\; \left(\frac{\omega}{c}\right)^2 \vec{h}_2(\vec{G}) \tag{3.17}$$

The accuracy of the method relies on the number of plane waves used in the calculations. The method is very effective for rather simple cases where the dielectric contrast is not too large and unit cell is less than a wavelength. In order to analyse photonic crystal cavities and waveguides where either point or line defects are introduced the structure, the super cell approach can be used (6; 7). Computation time and number of plane wave required to solve the problem accurately will increase depending on the size of super cell. The super cell approach cannot be applied to the cases such as bends and splitters where periodicity is not kept through out the whole structure.

Conditions that require using large amount of plane waves results not only in large dimensions of matrix equations but also in some instabilities related to slow convergence due to the Gibb's phenomena that occurs when Fourier series are applied to a periodic function with discontinuities. The convergence problem has been studied to improve results (8; 9; 10; 11).

PWE method is one of the most popular methods for calculating dispersion diagrams for photonic crystals and has being used to plot band gap-map atlas. This method is easy to implement and straightforward as well as it gives reliable results in most circumstances. Although PWE method precisely indicates the band gap positions, it is hard to observe how much power is transmitted from the structures, PWE has some limitations and it can only be applied to lossless and dispersion free materials which means that the method cannot consider losses. PWE method searches for frequencies at a fixed wave vector each time. When the dielec-

tric constant is frequency dependent this method becomes inefficient. Therefore, a band-gap diagram of photonic crystals with a frequency-dependent dielectric function, i.e. metallic photonic crystal, cannot be calculated accurately. However, there are some studies of studying metallic band-gap calculations in which the dielectric function is expressed in different forms to solve the eigenvalue problem (12; 13; 14; 15; 16). Using a plane wave solution it is possible to obtain allowed or forbidden frequencies of a periodic structure, which is especially important to control the confinement of the electromagnetic radiation. The dielectric photonic crystal structures without loss are easy to apply in the PWE method. For lossy and dispersive materials and more complex structures, other methods i.e. transfer matrix method (TMM) is better choice.

3.2 Transfer Matrix Method

Transfer matrix method for photonic crystal calculations was first introduced by Pendry and MacKinnon (17; 18). This method is developed to calculate the band structure of photonic crystals as well as the transmission and reflection coefficients. The method is a combination of FDTD and multilayer scattering analysis methods in which the approach represents the Finite Difference Frequency Domain (FDFD) method. In TMM method, first, the total computational domain is divided into set of layers, and then by using a uniform Cartesian grid each layer is discretized. Instead of transforming to the Fourier space, TMM uses discretized Maxwell's equations on a discrete lattice of real space points for time harmonic electromagnetic field to obtain the scattering matrix of a single layer of system. These discrete equations can be arranged to form a transfer matrix of the wave fields in adjacent layers, which are connected via a layer-to-layer transfer matrix. Once the transfer matrix of individual layers is obtained, the overall matrix can be obtained by taking the products of individual layer transfer matrices. Here the idea is to prevent numerical

instabilities, using multiple scattering formulas for combining the transmission and reflection coefficients of the individual layers rather than multiplying the individual layer transfer matrices. The output field is then calculated from the input field by the transfer matrix of the system. This enables the electric and magnetic fields to be found at any point in the system. Since the transmission and reflection coefficients of a given structure can be obtained, the comparison of transmission spectrum with experimental data can be directly achieved with TMM methods. The transmission spectrum is obtained directly, so that comparison with experimental data is possible.

In a similar way, Bloch wave vectors and so the dispersion relation of infinite periodic structures can be obtained via the eigenvalues of the transfer matrix. TMM is able to calculate the band structure of PC based structures including structures of complex or frequency dependent dielectric functions as in the case of metallic structures.

The main advantage of TMM is that the calculation is from a given frequency to find the field and corresponding coefficients. In TMM method, transfer matrix is calculated for a single frequency and searches for all possible values of wave vector as oppose to PWE method. By introducing a complex-valued relative permittivity into calculations, material dispersion can be taken into account. Losses in a medium are expressed through the imaginary part of relative permittivity. Moreover, frequency dependency can also be considered since the dielectric constant is fixed at a given frequency. These features make calculations of metallic structures possible.

TMM method can handle most photonic crystal structures; however it has a limitation for calculations of structures with disorders. Defect structures with a considerable disorder can be treated using a super cell approach with periodic boundary conditions. Nevertheless, as in PWE method, for the cases that super cell approach

cannot be applied such as bend, splitters, couplers etc. TMM cannot be used. In addition, TMM method cannot provide information about the field inside the photonic crystals. While a band-gap diagram can be obtained easily, to obtain a band-gap map is almost impossible, unlike with the PWE method.

This method has been reviewed by Pendry and computer codes implemented and published (19). TMM program is freely available under the name Translight .The original computer code developed by the group of John Pendry has been rewritten by Andrew Reynolds who added a graphical user interface to the program (20).

3.3 Finite Difference Time Domain Method

Finite-difference time-domain (FDTD) method is one of the widely used computation technique for modelling many scientific and engineering problems, especially dealing with electromagnetic problems. It is extensively used for photonic crystal calculations to study their dynamic behaviour.

Time-dependent Maxwell's equations are solved to obtain numerical solution by discretization of the structure and electromagnetic field both spectrally and temporally. As all the calculations are in real space, unlike PWE, time domain pulses (i.e. Gaussian pulse, point source), are used as source pulses, which is very useful as a broadband frequency response can be obtained in one simulation.

Electromagnetic fields are related to each other in time and space. Electric and magnetic field components are described as spatial variation depending on temporal variations of the other and vice versa. Discretization is made using the well-known Yee algorithm (21). The description of FDTD method based on Yee algorithm and FDTD as an acronym were first introduced by Taflove in 1980 (22). The methodo-

logy and computational schemes for a variety of electromagnetic problems can be found in Taflove's books (23; 24; 25). Yee's algorithm is based on lattice cell representation of electric and magnetic field components that satisfy Maxwell's Equations in both differential and integral forms. The cell, known as Yee cell, is shown in Figure 3.1

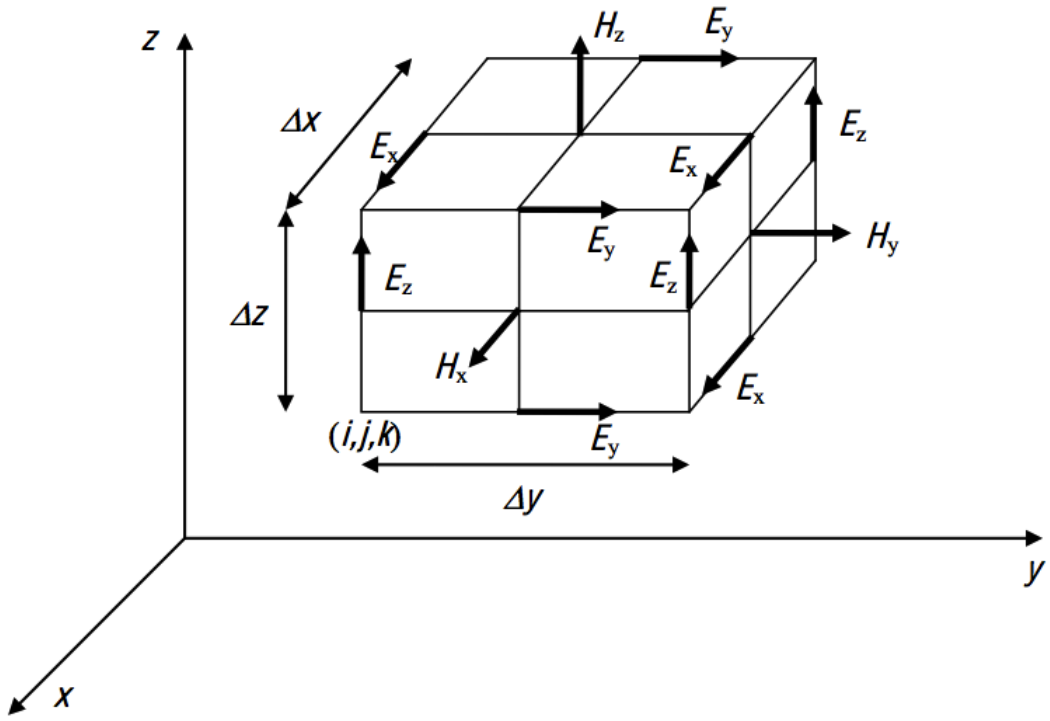

Figure 3.1: Illustration of Yee cell for a 3D case where a cubic voxel is used representing E and H fields. On the Yee cell, E field components are arranged to form the edges of the cube while the H fields are normal to the face of the cube.

Maxwell's equations for linear, isotropic non-dispersive source free medium can be written as:

$$\nabla \times \vec{E}(\vec{r},t) \;=\; -\frac{\partial \vec{H}(\vec{r},t)}{\partial t} \tag{3.18}$$

$$\nabla \times \vec{H}(\vec{r},t) \;=\; \varepsilon(\vec{r})\frac{\partial \vec{E}(\vec{r},t)}{\partial t} \tag{3.19}$$

where $E = (E_x, E_y, E_z)$ and $H = (H_x, H_y, H_z)$ are vector quantities and $\varepsilon(\vec{r}) \;=\; \varepsilon_0$ is the dielectric permittivity. The electromagnetic field components can be written in six scalar equations, E_x field component is:

$$\frac{\partial E_x(\vec{r},t)}{\partial t} \;=\; \frac{1}{\varepsilon(\vec{r})}\left(\frac{\partial H_z(\vec{r},t)}{\partial y} - \frac{\partial H_y(\vec{r},t)}{\partial z}\right) \tag{3.20}$$

and other five components can be written similarly.

According to the Yee algorithm, the temporal evolution of the electromagnetic field is calculated by means of discretization based on shifting E and H fields in Cartesian coordinates by half a spatial and half a time step, repeatedly. The spatial derivatives are approximated at each lattice point by a corresponding centred difference; as a result, each value of a component of a field is calculated by the difference of the fields at neighbouring points by following a so-called *leapfrog* scheme. The electric field at a time $n+1/2$ is computed from the stored value of the electric field at $n-1/2$ and the curl of the local magnetic fields at n. The magnetic field at $n+1$ is then evaluated from the stored value of the magnetic field at n and the curl of the local electric field at $n+1/2$, and so on. This method results in six equations that can be used to compute the electromagnetic field at any given mesh point. The spatial grid is defined by the coordinates $(i,j,k) \;=\; (i\Delta x, j\Delta y, k\Delta z)$, where $\Delta x, \Delta y$ and Δz are the space increments along the x, y and z axis, respectively. Similarly, time is broken up into discrete steps of Δt. E_x field component can be written in terms of central differences as (26):

$$\frac{E_x|^{n+1/2}_{i,j+1/2,k+1/2} - E_x|^{n-1/2}_{i,j+1/2,k+1/2}}{\Delta t} = \frac{1}{\varepsilon_0 \varepsilon_{1,j+1/2,k+1/2}}$$

$$\left(\frac{H_z|^n_{i,j+1,k+1/2} - H_z|^n_{i,j,k+1/2}}{\Delta y} - \frac{H_y|^n_{i,j+1/2,k+1} - H_y|^n_{i,j+1/2,k}}{\Delta z} \right) \tag{3.21}$$

and the corresponding equations for E_y, E_z, H_x, H_y, H_z can be written similarly.

For basic FDTD problem, a finite domain, a boundary condition, and spatial and temporal grids are defined and material properties are specified before the simulations. The entire computational domain must be gridded. The size of the spatial grid affects the accuracy of the results. The denser the grid points in the FDTD problem, the more accurate the solutions that can be obtained. In order to ensure accuracy and numerical stability both the spatial and temporal grid size must be fine enough to resolve well the smallest wavelength and the smallest region in the geometry. Typically, the grid spacing should be set to less than one tenth of the wavelengths in the materials (27). The stability of the simulation depends on the relationship between the spatial and temporal grids, called the Courant condition:

$$\Delta t \leq \frac{1}{c\sqrt{\frac{1}{(\Delta x)^2} + \frac{1}{(\Delta y)^2} + \frac{1}{(\Delta z)^2}}} \tag{3.22}$$

where, c is the speed of light in vacuum.

In FDTD simulations, Perfectly Matched Layers (PML) is one of the most effective and used boundary conditions, actually absorbing boundary layers that surround the computational domain, to prevent any reflection back to the domain (28; 29) (see Figure 3.2). However, when analysing periodic structures, i.e. band-gap calculations, periodic boundary conditions are often used as an equivalent to infinite

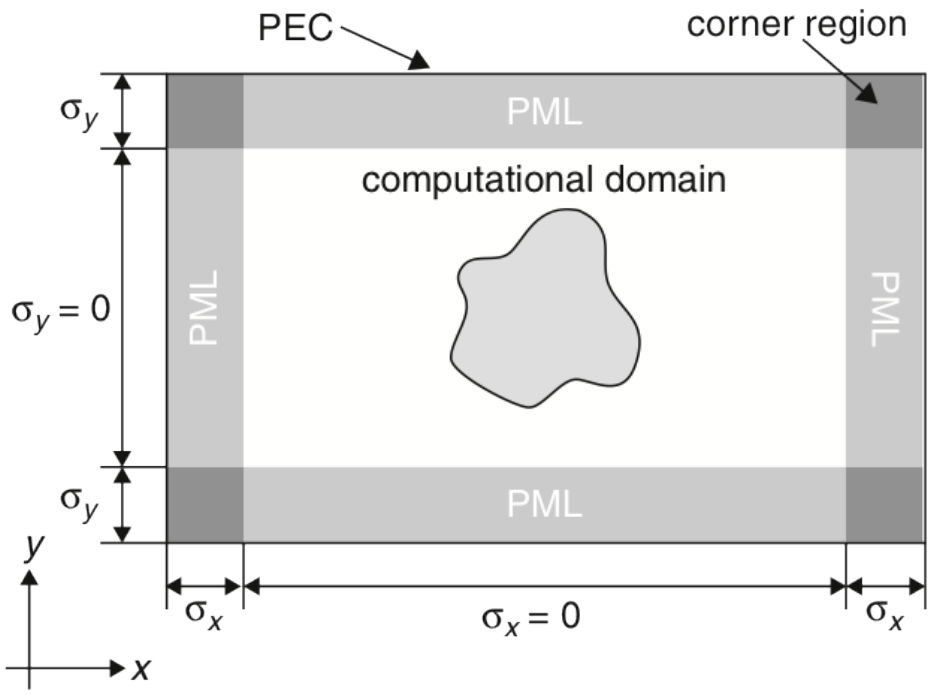

Figure 3.2: Schematic illustration of PML boundary layers surrounds a 2D computational domain.

repeated sections.

As FDTD is a time-domain method, it is advantageous for time dependent problems, i.e. simulated pulse propagation through an optical device, frequency domain response can also be obtained by using a Fourier transform of the solution in time domain. However, for very large computational domains, 3D simulations or structures with high aspect ratio, i.e. wire, FDTD simulations can be very demanding of computational time and memory. Because of its discretization type i.e. rectangular grid, FDTD algorithms use staircase approximation and become inefficient in resolving curved surfaces (30; 31).

3.4 Finite Element Method

Finite element method is a widely used numerical method to solve partial differential equations for engineering and mathematical physical problems. FEM was originally developed for simulations in civil engineering to use in structural analysis in 1940 by Richard Courant (32). Now it is used in a variety of engineering disciplines, including electromagnetics.

FEM discretizes the complex system by dividing it into simple components called finite elements so that the computation domain can be represented by a number of subdomains. The idea of this method is to be able to obtain the solution of complex problems by combining the results of a number of simple calculations on those small portions of the problem in which the unknown function is represented by simple interpolation functions with unknown coefficients (33).

In FEM, Maxwell's equations are transformed into a set of linear equations that approximates the electromagnetic field over an element. These approximations are usually based on interpolation functions and their coefficients are the unknown variables. Once the function is chosen, the function coefficients are computed for every element, and these are saved in individual arrays as element matrices. In order to generate the element matrices, elemental equations are derived as a function of the chosen interpolation order and the governing differential equation and boundary conditions. Generally, there are two methods used to derive the element matrix corresponding to the solution of the PDE (partial differential equations), namely, variational method and weighted residual method minimizing the error (34). The individual arrays are assembled to form a global matrix eigenvalue problem whose size depends on the total number of elements. The equations system is solved for unknown values using techniques of linear algebra or nonlinear numerical schemes.

The resulting eigenvalues are the frequencies of the allowed modes and the corresponding eigenvectors representing the field strength at the nodes (35; 36). The number of degrees of freedom is proportional to the total number of nodes, showing the complexity of the system.

FEM is a differential equation method where Helmholtz's equation is solved by scattered time harmonic electric field and boundaries. The wave propagation characteristics of a waveguide can be calculated by describing the boundary value problem in terms of electromagnetic field equations.

$$\nabla \times \left(\frac{1}{\mu_r} \nabla \times \vec{E} \right) - k_0^2 \varepsilon_r \vec{E} \; = \; 0 \qquad in\, \Omega \tag{3.23}$$

$$F(\vec{H}) \; = \; \frac{1}{2} \iint_{\Omega} \left[\frac{1}{\mu_r} (\nabla \times \vec{E}) \cdot (\nabla \times \vec{E}^*) - k_0^2 \varepsilon_r \vec{E} \cdot \vec{E}^* \right] d\Omega \tag{3.24}$$

where the asterisk denotes the complex conjugate. This equation can be discretized as follows:

$$[A] \left\{ \begin{array}{c} E_x \\ E_y \\ -jE_z \end{array} \right\} \; = \; k_0^2 [B] \left\{ \begin{array}{c} E_x \\ E_y \\ -jE_z \end{array} \right\} \tag{3.25}$$

This form of the wave equation can then be used to solve Maxwell's equation at a specified frequency, with the propagation constants of the modes as the eigenvalues.

The main factors to consider in selecting one numerical method over others are the ability to carry out most of the analysis with the selected method as well as to obtain high accuracy results. FEM is very well suited for calculations related to photonic crystals studies. Not only the transmission characteristics but also bandgap analysis can be achieved considering material dispersion and losses as well as the frequency dependence which is particularly important for metallic photonic

crystal study. Finite element method is based on frequency domain analysis even though time dependency can be considered with certain required settings. The main advantage of FEM especially to the grid based methods i.e FDTD is the way of discretization (37).

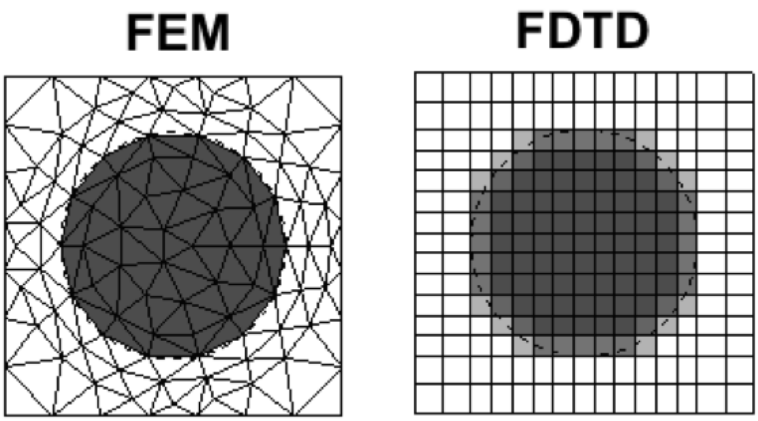

Figure 3.3: The computational domain of the photonic crystal discretized with triangular mesh in FEM and rectangular grid in FDTD method. The figure shows that a circle, which represents rods or holes, resolved well than uniform Cartesian grid. FEM mesh converge using triangular mesh without staircase approximation on the boundaries as in the grid based meshing.

In grid based methods, depending on the geometry, a dense/fine rectangular mesh is usually enough to converge the computational geometry, however, especially for complex geometries, FEM converges more effectively. FEM uses unstructured mesh for discretization the computational domain, composing many elements of simple shape, size and arrangements (i.e. triangular shape for 2D and tetragonal in 3D). FEM mesh resolves complex or arbitrary and small geometry better than rectangular mesh. FEM algorithm adapts the mesh sizes according to geometry of the system. In a given geometry, it uses fine mesh sizes for key areas while using coarser meshes for large areas in the geometry. The density of the nodes increases in narrow or small areas of high refractive index. These types of mesh characteristics provide better approximation of the material boundaries. Moreover, the

non-uniform nature of discretization in FEM is more suited to circular geometry representing the rods or holes in photonic crystal study as depicted in Figure 3.3.

In our simulation we have used COMSOL Multiphysics based on FEM method. It is very fast, effective and reliable software for modelling various physics and engineering problems. COMSOL 3.5a (38) has been run using the RF module for 2D simulations of photonic crystal structure. The module solves problems in the general field of electromagnetic waves, such as RF and microwave applications, optics, and photonics.

Modelling steps start with setting the application mode according to the analysis type: static, time-harmonic, transient, mode analysis, eigenfrequency analysis. After designing the geometry, physical conditions need to be set, i.e. boundary conditions, subdomain settings. FEM method allows the user to specify the equation parameters and the appropriate boundary conditions such as scattering, periodic, matched, impedance boundary conditions and PML in order to solve the E and H fields anywhere in the computational domain. A wide variety of linear and nonlinear dielectric and magnetic materials can also be modelled.

The following step is the discretization of the whole geometry. As was mentioned before, the FEM algorithm sets mesh dimensions automatically according to geometry where finer mesh is generated in small area/volumes. The discretization is an important issue to solve problem accurately. The accuracy can be improved by refining the mesh. As a rule of thumb, the maximum length of the edge of triangles should be less than one tenth of the operating wavelength, which means ten elements for 2D and five-six elements for 3D models per wavelength are needed to be applied. In this thesis, this rule is considered in every calculation; even finer meshes are applied to the geometries to ensure the accuracy of the results. After these settings, the solution step can be done by choosing the type of numerical

solver and then running the solver (linear solvers UMFPACK, SPOOLES, PARDISO, GMRES, FGMRES etc.). After the solution is calculated, results can be displayed via post processing.

The accuracy of the problem is strongly related to the discretization. Smaller mesh sizes or smaller grids give a good approximation to the exact solution but a high order interpolation function requires a large number of degrees of freedom. When the computational domain is large both FDTD and FEM become costly in terms of time and memory consumption. To overcome memory problem, if symmetries or periodicity exist symmetry planes or periodic boundary conditions can be used or the solver type can be changed: for instance, the iterative solver GMRES reaches solutions without memory problems but it is not as fast as direct solvers.

Traditionally, plane wave techniques have been applied to photonic crystal modelling. These have the disadvantages of being slow to converge. They are also computationally and memory intensive. The motivation for applying finite element techniques to the computation of photonic crystal spectra is to allow for flexible, efficient and accurate modelling of crystal structures.

In Figure 3.4 and Figure 3.5, we show the comparison between PWE and FEM methods for calculating the band-gap diagram of 2D photonic crystal in square lattice configuration with silicon rods in air for TM and TE modes, respectively. In the figures, the solid black lines represent the bands calculated using PWE method and red dots represent the bands calculated using FEM method. The PWE result can be comparable with the published result given in Ref. (39). As can be seen from Figure 3.4, there is a large band-gap for TM mode in the frequency range between 0.28 ($\omega a/2\pi c$) - 0.42 ($\omega a/2\pi c$) in terms of normalised frequencies and a small band-gap between 0.72 ($\omega a/2\pi c$) - 0.75 ($\omega a/2\pi c$). In TE mode, no band-gap appears for this configuration (see Figure 3.5). For both band-gap calculation in TM and TE mode

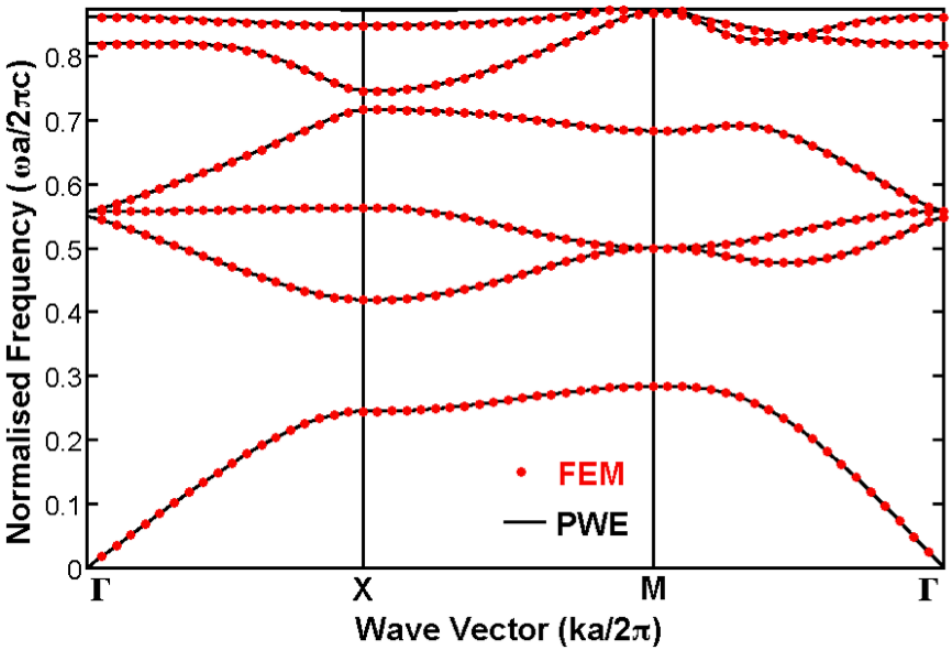

Figure 3.4: TM band structure of 2D photonic crystal in square lattice of silicon rods in air, radius $r = 0.2a$. Solid black lines represent the bands calculated using the PWE method. The bands calculated using FEM are represented with red dots.

FEM results matches almost perfectly with the results with PWE method. FEM method was studied for calculations of band gap calculation of dielectric photonic crystals using an adaptive scheme in Ref. (40), however results showed some discrepancies with PWE results. It is evident that our FEM results show almost no discrepancies PWE results.

Band-gap simulations are done with an eigenvalue solver in COMSOL using periodic boundary conditions and are able to solve and find eigen wave vectors accurately. PWE method is restricted only to infinite periodic structures and from simulation field patterns and losses cannot be obtained. The key advantage of FEM is that, unlike PWE, FEM has no convergence problems. FEM can simulate a wider range of designs even the complex structures with material dispersion and losses taken into account, by using a complex dielectric constant/refractive index. This will be widely used in this body of work.

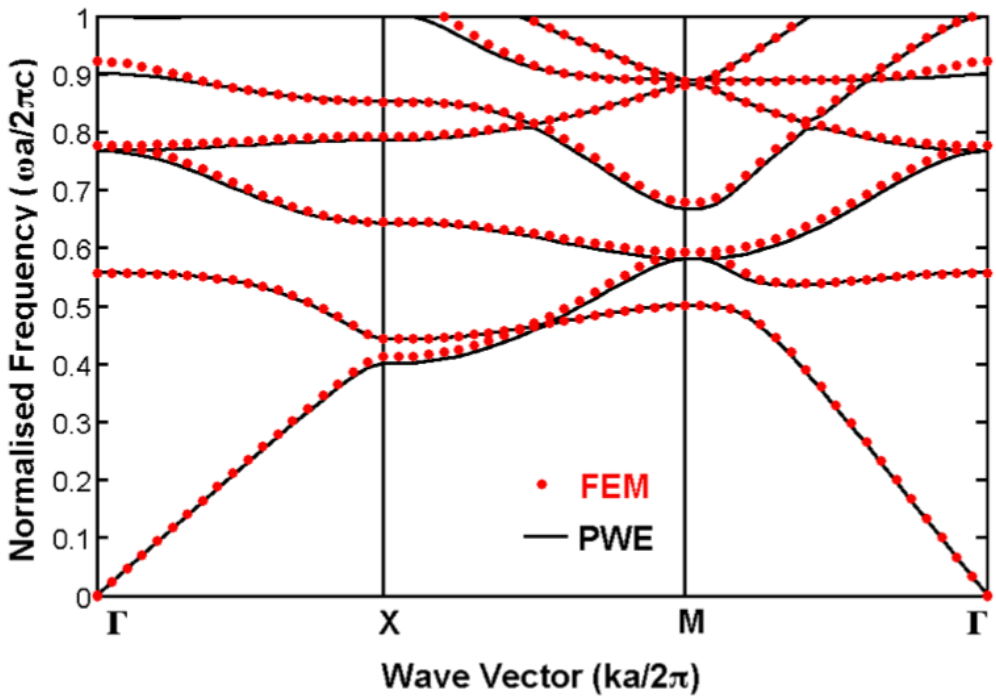

Figure 3.5: TE band structure of 2D photonic crystal in square lattice of silicon rods in air, radius $r = 0.2a$. Solid black lines represent the bands calculated with the PWE method. The bands calculated with FEM are represented with red dots..

3.5 Conclusion

This chapter aimed to give a brief overview on some of the most commonly used numerical methods in photonic crystal study, such as TMM, FEM, PWE and FDTD methods. Throughout this study, FEM method has been selected to study photonic crystal behaviour and also design and simulate photonic crystal structures. In the later chapters, FEM will be used to calculate band diagrams and to analyse the transmission characteristics of metallic photonic crystal structures.

References

[1] K. M. Ho, C. T. Chan, and C. M. Soukoulis, "Existence of a photonic gap in periodic dielectric structures," *Physical Review Letters*, vol. 65, p. 3152, Dec. 1990.

[2] K. Leung and Y. Liu, "Full vector wave calculation of photonic band structures in face-centered-cubic dielectric media," *Physical Review Letters*, vol. 65, pp. 2646–2649, Nov. 1990.

[3] N. W. Ashcroft and N. D. Mermin, *Solid state physics*. Holt, Rinehart and Winston, 1976.

[4] D. W. Prather, A. Sharkawy, and S. Shi, *Photonic crystals: theory, applications, and fabrication*. John Wiley and Sons, May 2009.

[5] I. A. Sukhoivanov and I. V. Guryev, *Photonic Crystals: Physics and Practical Modeling*. Springer, Oct. 2009.

[6] R. D. Meade, K. D. Brommer, A. M. Rappe, and J. D. Joannopoulos, "Photonic bound states in periodic dielectric materials," *Physical Review B*, vol. 44, p. 13772, Dec. 1991.

[7] M. M. Sigalas, "Elastic wave band gaps and defect states in two-dimensional composites," *The Journal of the Acoustical Society of America*, vol. 101, p. 1256, Mar. 1997.

[8] H. S. Sozuer, J. W. Haus, and R. Inguva, "Photonic bands: Convergence problems with the plane-wave method," *Physical Review B*, vol. 45, p. 13962, June 1992.

[9] T. Minami, K. Sekine, H. Ajiki, and K. Cho, "Inverse matrix diagonalization for photonic band calculation," *Journal of Luminescence*, vol. 87-89, pp. 378–380, May 2000.

[10] L. Shen and S. He, "Analysis for the convergence problem of the plane-wave expansion method for photonic crystals," *Journal of the Optical Society of America A*, vol. 19, pp. 1021–1024, May 2002.

[11] Y. Cao, Z. Hou, and Y. Liu, "Convergence problem of plane-wave expansion method for phononic crystals," *Physics Letters A*, vol. 327, pp. 247–253, June 2004.

[12] V. Kuzmiak, A. A. Maradudin, and F. Pincemin, "Photonic band structures of two-dimensional systems containing metallic components," *Physical Review B*, vol. 50, p. 16835, Dec. 1994.

[13] V. Kuzmiak and A. A. Maradudin, "Distribution of electromagnetic field and group velocities in two-dimensional periodic systems with dissipative metallic components," *Physical Review B*, vol. 58, no. 11, p. 7230, 1998.

[14] K. Sakoda, N. Kawai, T. Ito, A. Chutinan, S. Noda, T. Mitsuyu, and K. Hirao, "Photonic bands of metallic systems. i. principle of calculation and accuracy," *Physical Review B*, vol. 64, p. 045116, July 2001.

[15] A. J. Gallant, M. A. Kaliteevski, D. Wood, M. C. Petty, R. A. Abram, S. Brand, G. P. Swift, D. A. Zeze, and J. M. Chamberlain, "Passband filters for terahertz radiation based on dual metallic photonic structures," *Applied Physics Letters*, vol. 91, no. 16, p. 161115, 2007.

[16] J. M. Shainline and J. Xu, "Slow light and band gaps in metallodielectric cylinder arrays," *Optics Express*, vol. 17, no. 11, p. 88798891, 2009.

[17] J. B. Pendry and A. MacKinnon, "Calculation of photon dispersion relations," *Physical Review Letters*, vol. 69, p. 2772, Nov. 1992.

[18] J. B. Pendry, "Photonic band structures," *Journal of Modern Optics*, vol. 41, pp. 209–229, Feb. 1994.

[19] P. M. Bell, J. B. Pendry, L. M. Moreno, and A. J. Ward, "A program for calculating photonic band structures and transmission coefficients of complex structures," *Computer Physics Communications*, vol. 85, pp. 306–322, Feb. 1995.

[20] A. L. Reynolds, "Translight software," *University of Glasgow, UK*, 2000.

[21] K. S. Yee, "Numerical solution of initial boundary value problems involving maxwell's equations in isotropic media," *Antennas and Propagation, IEEE Transactions on*, vol. 14, pp. 302–307, May 1966.

[22] A. Taflove, "Application of the Finite-Difference Time-Domain method to sinusoidal Steady-State Electromagnetic-Penetration problems," *Electromagnetic Compatibility, IEEE Transactions on*, vol. EMC-22, pp. 191–202, Aug. 1980.

[23] A. Taflove, *Advances in computational electrodynamics: the finite-difference time-domain method*. Artech House, 1998.

[24] A. Taflove and S. C. Hagness, *Computational electrodynamics: the finite-difference time-domain method*. Artech House, June 2005.

[25] S. C. Hagness, A. Taflove, S. D. Gedney, W. Schilders, and E. ter Maten, "Finite-Difference Time-Domain methods," in *Numerical Methods in Electromagnetics*, vol. Volume 13, pp. 199–315, Elsevier, 2005.

[26] S. Obayya, *Computational Photonics*. John Wiley and Sons, Dec. 2010.

[27] RSoft Photonics, *CAD Layout v5.1.1 User Guide*. Rsoft Design Group, Inc, 2009.

[28] J. Berenger, "A perfectly matched layer for the absorption of electromagnetic waves," *Journal of Computational Physics*, vol. 114, pp. 185–200, Oct. 1994.

[29] J. P. Berenger, "Perfectly matched layer for the FDTD solution of wave-structure interaction problems," *IEEE Transactions on Antennas and Propagation*, vol. 44, pp. 110–117, Jan. 1996.

[30] E. Popov, M. Nevire, B. Gralak, and G. Tayeb, "Staircase approximation validity for arbitrary-shaped gratings," *Journal of the Optical Society of America A*, vol. 19, pp. 33–42, Jan. 2002.

[31] T. Noda, R. Yonezawa, S. Yokoyama, and Y. Takahashi, "Error in propagation velocity due to staircase approximation of an inclined thin wire in FDTD surge simulation," *IEEE Transactions on Power Delivery*, vol. 19, pp. 1913– 1918, Oct. 2004.

[32] R. Courant, "Variational methods for the solution of problems of equilibrium and vibrations," *Lecture Notes in Pure and Applied Mathematics*, p. 1, 1994.

[33] J. Jin, *The finite element method in electromagnetics*. Wiley, 2002.

[34] D. B. Davidson, *Computational Electromagnetics for RF and Microwave Engineering*. Cambridge University Press, Nov. 2010.

[35] M. J. Fagan, *Finite element analysis: theory and practice*. Longman Scientific & Technical, 1992.

[36] O. C. Zienkiewicz and R. L. Taylor, *The finite element method: Basic formulation and linear problems*. McGraw-Hill, Feb. 1989.

[37] R. Garg, *Analytical and computational methods in electromagnetics*. Artech House, June 2008.

[38] COMSOL, *COMSOL Multiphysics ver. 3.5a*. Sweden: COMSOL AB, 2009.

[39] T. Yamashita and C. J. Summers, "Evaluation of self-collimated beams in photonic crystals for optical interconnect," *IEEE Journal on Selected Areas in Communications*, vol. 23, pp. 1341– 1347, July 2005.

[40] M.-C. Lin and R.-F. Jao, “Finite element analysis of photon density of states for two-dimensional photonic crystals with in-plane light propagation,” *Opt. Express*, vol. 15, pp. 207–218, Jan 2007.

Chapter 4

TERAHERTZ TECHNOLOGY

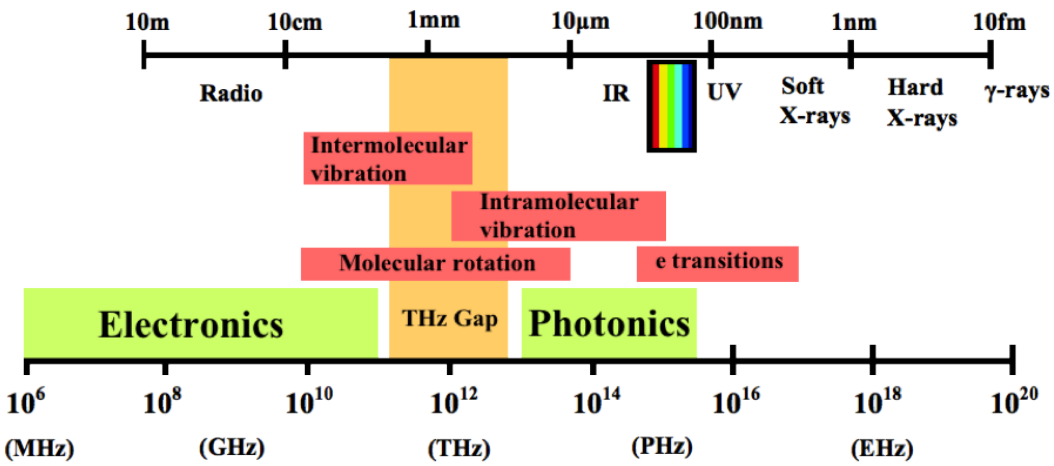

Figure 4.1: The THz gap in the electromagnetic spectrum.

Terahertz (THz) waves refer to electromagnetic radiation that has a frequency between 0.3 THz and 10 THz, occupying a large portion of the electromagnetic spectrum between microwave and infrared bands. THz radiation lies between microwave and infrared regions and corresponds to the submillimeter and far infrared wavelength range between 30 μm and 1 mm and for wave numbers: 10 cm^{-1} and 333.33 cm^{-1}.

This frequency range covers the spectrum from millimeter waves to far-infrared

waves. This part of the electromagnetic spectrum is also known as the THz gap, and even though it offers significant scientific and technological potential for many fields, it remains the least explored region mainly due to the technological difficulties of making efficient and compact sources and detectors suitable for THz radiation. After improving convenient devices to generate THz waves, this region has become scientifically available and attracted a lot of attention for its potential and promising applications (1; 2; 3).

This chapter aims to give brief information about THz waves and radiation. THz technologies are in the early stages of their development. Applications of THz radiation as well as the THz generation and detection techniques will be mentioned. With the development of THz wave generation and detection systems in order to develop current THz applications further and for possible future applications, efficient THz wave guiding components are required. Several approaches have been applied for guiding THz waves. Later in this chapter, an overview of THz wave guiding solutions will be given.

4.1 Applications of THz

THz radiation has important characteristic features that can be used in new applications or as a better alternative to existing ones. In many areas such as in medical and security imaging, spectroscopic measurements, biological sensing, quality control in a production system, ultra-fast communications, astronomy etc., utilization of THz technology based devices has been begun. Most of the studies in THz technology are focused toward more practical, commercial valued applications (4).

THz radiation is non-ionizing. The photon energy corresponding to THz wavelengths is between 1.8×10^{-22} - 60×10^{-22} J and this is much lower than X-rays and γ

rays. Therefore, it is not expected to damage tissues and DNA, unlike X-rays (5). Some THz frequencies can penetrate within several millimeters of organic tissues with low water content and be reflected back. THz radiation can be used to detect the density of tissues from the water absorption. This can be exploited to image and diagnose some cancer types, i.e. skin cancer in a safer way (6; 7). Another important feature of THz waves used in biotechnology for sensing chemical and biochemical compounds is that biological structures including DNA exhibit characteristic motions such as, rotation, vibration or twisting at THz frequencies. It is possible to detect the presence of mutation in a DNA sequence using THz (8).

THz pulses are also interesting to study due to their absorption and reflection properties. THz radiation is transparent to most of the materials such as, paper, plastic, clothing, wood etc. and THz waves can penetrate through these materials except water and metal (9). THz radiation is strongly attenuated by water. Metals are highly reflective to THz radiation due to their high conductivity.

Water absorbs the THz radiation strongly, and this feature can be used in biomedical imaging as an advantage. On the other hand, in the area of biological sensing this is a problem still under study, since biological molecules use water. Moreover, due to the water vapour in atmosphere, the transmission of THz radiation in free space is very poor except for some frequency ranges.

In security screening i.e. at airports, due to their penetration characteristics, THz waves (T-rays) have begun to be exploited for detection of threat objects in baggage, packages and especially on people since using T-rays of a few meV of photonic energy is much safer than using X-rays (keV) (10). In addition, the current x-ray systems are effective in detecting metals but they cannot detect many explosives such as plastic explosives, illegal drugs or non-metal weapons etc. which can be hidden in same packing or under clothing.

One of the most important features of THz radiation in terms of practical application to commercial systems is that when THz radiation is applied to different materials, THz radiation causes materials to exhibit spectral characteristics, such as resonant peaks due to vibrational motions and inter-molecular interactions in organic and biological molecules, interband transitions in semiconductors etc. (11). Different molecular motion corresponds to different absorption behaviour. THz waves leave spectral fingerprints on exposed materials which are specific to them. With careful spectroscopic investigation this helps to identify materials and detect if there are any anomalies without any contact to the material.

There are many types of known explosive materials and illicit drugs. An investigation involves careful analysis of the interaction between these materials and THz radiation. THz spectroscopy has demonstrated that explosive materials could be identified since these materials have exhibited different characteristic of their spectral behaviour. When these behaviours are known those materials can be easily identified at security screening (12).

In a similar fashion many materials can be identified from the scattering of THz radiation. For example the identification of the content of bottled liquids can be achieved by THz scattering(13). In quality control of pharmaceutical products to test whether the product meets specifications (14) or to check the integrity of coatings (15), as well as the moisture content of the product (16; 17), these can be achieved by THz radiation scattering. Another application is in production line, which can be applied to many areas such as simple packing processes of a product or manufacturing of an integrated circuit device (18). The quality of product or packing can be increased using THz imaging systems in order to find the faults or device failure without touching or opening the randomly selected product/packets from the production line which in general is not a very effective way to find faults.

In communication systems at THz frequencies a very large bandwidth is available, it offers transmission of broadband signals and to carry large amount of information and reduced size antenna and equipment. Due to the water vapour in atmosphere, free space communication is limited to short distances which is suitable for short distance wireless communications and networking very promising for future communication systems with more faster speeds (10 Gbps) than current UWB (Ultra-wideband) technology (19; 20). On the other hand at high altitudes, THz wave transmission is almost lossless and makes aircraft-satellite or satellite-satellite communication possible.

In astronomical studies THz spectroscopy has been in use for a number of years. Various objects, such as stars, emit THz radiation; THz spectroscopy is used to identify spectral traces of molecules such as oxygen, carbon monoxide, nitrogen, and water in distant galaxies (21; 22). THz radiation is also studied in atmospheric research such as environmental protection, monitoring the ozone layer for example (23).

In this section, distinctive properties of THz radiation and applications in various disciplines are discussed briefly. In the following section THz radiation and detection techniques are presented.

4.2 THz Radiation

4.2.1 THz Generation

In the past decades, THz region has attracted a lot of attention. In order to operate at THz frequencies many electrical and optical techniques have been developed.

These are mainly due to the inefficient generation of THz pulses with traditional electronic and optical methods. THz radiation is located at a higher frequency range than microwave electronics and at a lower frequency range than light sources, therefore either THz pulses cannot be generated fast enough or in the desired low frequency level. Moreover, THz waves have low photon energy ($\sim$ meV), which is difficult to detect. For the applications that would utilise the THz frequency range, high power, tuneable and portable sources working at room temperature, sensitive detectors, and efficient, compact and easy to integrate components are required.

Solid-state electronic devices such as transistors, Gunn oscillators and Schottky diode and multipliers become very inefficient for frequencies higher than 0.1 THz. Higher frequencies may be achieved with frequency multipliers but it results in considerable power losses (1). On the other hand, optical lasers that emit THz radiation require cryogenic temperatures to operate at low energy levels (1 - 40 meV). The techniques that have been developed to generate THz radiation above 1 THz can be classified into three groups: up conversion from microwave, down conversion from optical regime and THz lasers.

Generation of low power THz radiation with up conversion technique can be done through multiplication of microwave oscillators using chains of Schottky doublers or triplers with low efficiency (24). Frequencies up to 2.7 THz have been demonstrated (25). One of the two approaches for generation of THz radiation with down conversion techniques is nonlinear photo mixing. A tuneable continuous wave (CW) THz beam can be generated by the difference frequency mixing of two lasers with adjacent wavelengths. This is achieved by the excitation of photocurrent pulses in a semiconductor modulated at the lasers detuning frequency, resulting in a narrow-band and tunable THz signal and also providing high spectral resolution (26; 27). The other approach is using photoconductivity by applying femtosecond ultra-short optical pulses for generation of THz radiation (1). The combination of

femtosecond lasers and a semiconductor antenna acts as a THz emitter and is used to obtain pulsed THz waves. When femtosecond pulses are incident on semiconductor, they generate free-charge carriers that may be accelerated in the presence of an electrical bias field (28). Commercially available systems based on femtosecond lasers i.e. Ti:sapphire laser to generate THz radiation are bulky and costly, and typically cover a frequency range up to 3 THz (29). Femtosecond lasers are used mainly for THz time domain spectroscopy (THz-TDS) (30).

Optically pumped molecular gas lasers, free electron lasers (FEL), and quantum cascade lasers (QCL) are the most promising examples of THz lasers. In optically pumped lasers sources, a carbon dioxide laser pumps a low-pressure gas cavity, which lases at the gas molecule's emission-line frequencies (31). Methanol and hydrogen cyanide are the widely used gases. These sources are line-tuneable in the range 0.3 - 5 THz, and typically require large cavities and kilowatt power supplies, however they can provide high output powers up to 100 mW (32). These types of sources are ideal for applications such as heterodyne spectroscopy and plasma diagnostics where no tuneability is required.

Free electron lasers (FELs) can generate powerful and narrow-band tunable THz coherent radiation with brightness levels several orders higher than other sources (32). FELs are based on the idea of sending electron bunches that are accelerated to relativistic speed, through a magnetic field, which causes the electrons to oscillate and emit photons. This produces coherent radiation up to kilowatt level power (25). These systems, however, are huge in size and costly, and require a dedicated facility, which makes them highly impractical for many kinds of experiments and applications. Table-top, free electron based backward wave oscillators (BWO) can operate in THz range at moderate power levels (1 - 100 mW) (33; 34).

Quantum cascade lasers (QCLs) were first demonstrated in 1994 (35). THz quantum

cascade lasers are compact photonic sources, which can generate high power THz waves up to tens of mW in the frequency range 1.2 - 5 THz, have a very narrow linewidth, and are suitable for applications in spectroscopy (36). With a voltage applied across the device, THz waves are emitted by few coupled quantum wells and barriers of a few nanometers thickness formed by alternating layers of GaAs and $Al_xGa_{1-x}As$, forcing the electrons to cascade through each layer. The main back draw of these systems is that they require low temperatures to operate; increasing temperature results in limited tuneability and low output power. Room temperature operation is still challenging, and 164 K is one of the highest working temperature at 3 THz (35).

One another method, which is used in our laboratories, is to generate THz radiation using a DC-biased passively mode-locked laser. This laser is multimode, and all modes are synchronised. The beating of these modes generates a THz signal if the free spectral range is in the THz spectrum. Using a photo-mixer it is therefore possible to filter out the optical carriers and to retrieve the THz radiation (37).

4.2.2 THz Detection

Detection of low energy THz signals requires highly sensitive detection methods. THz detection systems can be classified into two main categories: direct detection (non-coherent) and heterodyne (coherent) detection. Direct detection systems measure signal intensity and are characterized by broadband spectral response. Direct detection methods are more suitable for applications where high sensitivity is more important than the spectral resolution as these systems cannot provide high-resolution performance. For broadband detection, direct detection based thermal sensors such as bolometers, Golay cells and pyroelectric devices are commonly used (11). These sensors are based on thermal absorption and use different schemes

to measure temperature increase in the absorber attached to their heat sinks. Most of these sensors require cooling to reduce thermal background.

Heterodyne detection schemes are widely used because of their high sensitivity, and ability to measure narrow bandwidth high frequency signals. They are useful in applications that require very high sensitivity and spectral resolution. Heterodyne detection systems measure both amplitude of the signal and the phase of the field. A frequency down-conversion takes place in heterodyne detection systems. A narrow band THz source such as gas laser or QCL acting as a local oscillator is required in order to achieve an intermediate frequency in the RF range. By using nonlinear mixer i.e. Schottky diode mixer, a THz signal and a reference radiation from a local oscillator at a fixed frequency are combined. The mixer produces an output signal at the difference frequency in which the amplitude is proportional to the THz amplitude (38). Coherent detection techniques are limited by the THz generation technique as the same light source is utilised for generation and detection.

4.3 Terahertz Waveguides

The demand for effective THz wave guiding schemes has drawn considerable attention as THz generation and detection techniques have developed. Compact THz devices with low attenuation loss and low dispersion are highly desired and essential for the development of THz applications. Basic THz components such as THz waveguides, mirrors, spectral filters and cavities are required to build compact THz devices.

Due to the wavelengths in the THz range, some solutions available in microwave or optical ranges cannot be adequate in THz region, such as metallic waveguides for the microwave region or dielectric fibres for optical ranges. Because of high

loss from the finite conductivity of metals or high absorption of dielectric materials neither of them can guide THz wave for longer distances (39).

Waveguides are very important devices not only used for transferring/guiding light from input to output but also for allowing to control of light which enables the creation of other devices such as couplers, junctions or lasers for example.

Waveguide propagation of THz waves has been investigated by several research groups. The coupling of freely propagating THz waves into a waveguides with circular metal tubes using quasi-optical methods (40; 41), sapphire fibers (42) and planar ribbon waveguides (43) are examples of the early THz waveguides demonstrated by Grischkowsky and his co-workers. These waveguides suffer greatly with the problem of pulse broadening and spectral oscillations in the frequency domain. Dispersion is a serious issue for broadband THz pulses. The first low-loss, non-dispersive wave propagation for THz pulses was achieved by using parallel metal plates as waveguides (44; 45). Parallel metal plate waveguides propagating ultra-wideband THz pulses in the TEM-mode with very low-loss and negligible group velocity dispersion (GVD) are one of the most promising THz waveguides. However, they lead to losses due to beam diffraction for longer waveguides. To develop this further, optical components for THz are needed to control THz waves inside the waveguide. Some guided wave components such as metallic mirrors (46), dielectric lenses (47), sensors (48) are realized inside the parallel plate waveguide.

The ability to manipulate waves is key for developing integrated THz optoelectronics and potential applications of THz waves. Optical components that can manipulate THz waves inside a waveguide are urgently required. For that reason photonic crystals have been studied in THz with the aim of constructing many optical components that can manipulate the THz radiation.

The initial research on THz photonic crystals is conducted to understand the transmission, and dispersion behaviour and electromagnetic field distribution. Several THz photonic crystal structures have been studied in 1D (49; 50), in 2D dielectric (51; 52) and metallic (53; 54) for wave guiding (55), filtering (56; 57) purposes and for other applications such as biochemical sensing (58).

Photonic crystals embedded in parallel plate waveguides have also been studied. By sandwiching the photonic crystal structure between two parallel metal plates, dielectric photonic crystal slabs (59; 60) and metallic photonic crystal structure (61; 62) and waveguides (63) are realized and characterized by using terahertz time domain spectroscopy (THz-TDS) (64; 65).

Metal wires are another wave guiding solution for THz radiation, which can support a surface-guided wave with low attenuation and relatively little dispersion (39; 66; 67). However, the coupling efficiency between free-space THz waves and the surface of wire is very low due to the fact that metal wire is radially polarized while free-space waves are linearly polarized (39).

Enhanced THz transmission is obtained through subwavelength hole arrays (68), corrugated metal wires (69), because the modes consist of surface-plasmon polariton modes localized at the metal surface. There are many proposals for novel waveguides for terahertz applications reported by several research groups including photonic crystal fibers (70; 71) low index discontinuity wave-guides (72), metallic slits (73), and metamaterials (74; 75).

In this section, an overview was given on THz wave guiding solutions. Several approaches have been applied for guiding THz waves, starting from the early waveguides to the latest waveguide solutions, and these were discussed briefly. With the rise of THz frequency based technology, developments in generating THz radiation

and guiding THz waves efficiently with low loss and high performance has become a key objective.

4.4 Conclusion

THz technology is already in use mainly for medical and security related applications. However, THz technologies are still in the early stages of their development. THz development of THz technologies is limited to the point where the THz frequencies can be generated and detected. Depending on the generation scheme, currently it is possible to generate broadband radiation ranging from 0.2 to 5 THz with commercial THz based lasers. So far, most of the studies have been conducted in low frequency range up to 3 THz. However, it is important to reach frequencies above 3 THz for chemistry, spectroscopy applications and high power applications.

On the other hand, it is also important to be able to manipulate THz signals with effective components. Low cost, low loss and compact devices such as filters, waveguides, polarizers and resonant cavities are highly desirable. Photonic crystal structures offer design flexibility for wave guiding devices such as filters and cavity resonators as well as the integration with the sources and detectors.

In this study, metallic photonic crystals are exploited in order to design a variety of waveguiding components, such as filters, waveguides, bend and splitters, which will be introduced in the following chapters. Metallic photonic crystals have been selected due to certain advantages over dielectric photonic crystals such as wider band-gaps and smaller sizes, which will be detailed in the next chapter.

References

[1] P. H. Siegel, "Terahertz technology," *IEEE Transactions on Microwave Theory and Techniques*, vol. 50, pp. 910–928, Mar. 2002.

[2] M. Tonouchi, "Cutting-edge terahertz technology," *Nat Photon*, vol. 1, pp. 97–105, Feb. 2007.

[3] R. E. Miles, P. Harrison, and D. Lippens, *Terahertz sources and systems*. Springer, 2001.

[4] "Applications of terahertz technology - TeraNova IST." http://www.teranova.info/science/applications.

[5] D. Arnone, C. Ciesla, and M. Pepper, "Terahertz imaging comes into view," *Phys. World*, vol. 13, no. 4, p. 3540, 2000.

[6] R. M. Woodward, B. E. Cole, V. P. Wallace, R. J. Pye, D. D. Arnone, E. H. Linfield, and M. Pepper, "Terahertz pulse imaging in reflection geometry of human skin cancer and skin tissue," *Physics in Medicine and Biology*, vol. 47, pp. 3853–3863, Nov. 2002.

[7] Y. Bai and H. Qi, "A new perspective on terahertz image reconstruction based on linear spectral unmixing," in *15th IEEE International Conference on Image Processing, 2008. ICIP 2008*, pp. 2996–2999, IEEE, Oct. 2008.

[8] P. H. Bolivar, M. Brucherseifer, M. Nagel, H. Kurz, A. Bosserhoff, and R. Bttner, "Label-free probing of genes by time-domain terahertz sensing," *Physics in Medicine and Biology*, vol. 47, pp. 3815–3821, Nov. 2002.

[9] C. Jansen, S. Wietzke, M. Scheller, N. Krumbholz, C. Jrdens, K. Baaske, T. Hochrein, M. Koch, and R. Wilk, "Applications for THz systems," *Optik & Photonik*, vol. 3, pp. 26–30, Dec. 2008.

[10] "TeraView terahertz technology for 3D imaging and spectroscopy." http://www.teraview.com/terahertz/index.html.

[11] Y. Lee, *Principles of terahertz science and technology*. Springer, Dec. 2008.

[12] H. Zhong, A. Redo-Sanchez, and X. C. Zhang, "Identification and classification of chemicals using terahertz reflective spectroscopic focal-plane imaging system," *Opt. Express*, vol. 14, no. 20, p. 91309141, 2006.

[13] U. Moller, D. G. Cooke, K. Tanaka, and P. U. Jepsen, "Terahertz reflection spectroscopy of debye relaxation in polar liquids [Invited]," *Journal of the Optical Society of America B*, vol. 26, no. 9, pp. A113–A125, 2009.

[14] V. P. Wallace, P. F. Taday, A. J. Fitzgerald, R. M. Woodward, J. Cluff, R. J. Pye, and D. D. Arnone, "Terahertz pulsed imaging and spectroscopy for biomedical and pharmaceutical applications," *Faraday Discussions*, vol. 126, p. 255, 2004.

[15] H. Wu, E. J. Heilweil, A. S. Hussain, and M. A. Khan, "Process analytical technology (PAT): quantification approaches in terahertz spectroscopy for pharmaceutical application," *Journal of Pharmaceutical Sciences*, vol. 97, pp. 970–984, Feb. 2008.

[16] H. S. Chua, P. C. Upadhya, A. D. Haigh, J. Obradovic, A. A. Gibson, and E. H. Linfield, "Terahertz time-domain spectroscopy of wheat grain," in *Conference Digest of the 2004 Joint 29th International Conference on Infrared and Millimeter Waves, 2004 and 12th International Conference on Terahertz Electronics, 2004*, pp. 399– 400, IEEE, Oct. 2004.

[17] D. Banerjee, W. Von Spiegel, M. D. Thomson, S. Schabel, and H. G. Roskos, "Diagnosing water content in paper by terahertz radiation," *Opt. Express*, vol. 16, no. 12, p. 90609066, 2008.

[18] T. Kiwa, M. Tonouchi, M. Yamashita, and K. Kawase, "Laser terahertz-emission microscope for inspecting electrical faults in integrated circuits," *Optics Letters*, vol. 28, pp. 2058–2060, Nov. 2003.

[19] M. Koch, "Terahertz communications: A 2020 vision," in *Terahertz Frequency Detection and Identification of Materials and Objects* (R. E. Miles, X. Zhang, H. Eisele, and A. Krotkus, eds.), pp. 325–338, Dordrecht: Springer Netherlands, 2007.

[20] B. Zhu, Y. Chen, K. Deng, W. Hu, and Z. S. Yao, "Terahertz science and technology and applications," *PIERS Proceedings, Beijiing, China*, pp. 1166–1170, 2009.

[21] M. Swain, "Options for studying star formation at high redshift," *Publications of the Astronomical Society of the Pacific*, vol. 110, pp. 991–994, Aug. 1998.

[22] J. Lamarre, "FIRST (far-infrared and submillimeter space telescope): a major scientific project of ESA," in *Proceedings of SPIE*, (San Diego, CA, USA), pp. 267–274, 1993.

[23] A. Quema, H. Takahashi, M. Sakai, M. Goto, S. Ono, N. Sarukura, R. Shioda, and N. Yamada, "Identification of potential estrogenic environmental pollutants by terahertz transmission spectroscopy," *Jpn J Appl Phys Part 2*, vol. 42, no. 8A, pp. L932–L934, 2003.

[24] A. Maestrini, J. Ward, G. Chattopadhyay, E. Schlecht, and I. Mehdi, "Terahertz sources based on frequency multiplication and their applications," *Frequenz*, vol. 62, pp. 118–122, June 2008.

[25] G. L. Carr, M. C. Martin, W. R. McKinney, K. Jordan, G. R. Neil, and G. P. Williams, "High-power terahertz radiation from relativistic electrons," *Nature*, vol. 420, no. 6912, p. 153156, 2002.

[26] T. Lffler, K. J. Siebert, H. Quast, N. Hasegawa, G. Loata, R. Wipf, T. Hahn, M. Thomson, R. Leonhardt, and H. G. Roskos, "All-optoelectronic continuous-wave terahertz systems," *Philosophical Transactions of the Royal Society of London. Series A: Mathematical, Physical and Engineering Sciences*, vol. 362, pp. 263 –281, Feb. 2004.

[27] C. Baker, I. Gregory, M. Evans, W. Tribe, E. Linfield, and M. Missous, "All-optoelectronic terahertz system using low-temperature-grown InGaAs photomixers," *Optics Express*, vol. 13, pp. 9639–9644, Nov. 2005.

[28] J. Shan and T. F. Heinz, "Terahertz radiation from semiconductors," *Ultrafast Dynamical Processes in Semiconductors*, p. 20832083, 2004.

[29] F. Pozzi, C. C. Renaud, D. Rogers, I. Lealman, and A. J. Seeds, "Photonics integration for THz generation," *London Communications Symposium Proceedings, University College London, London, UK*, 2009.

[30] C. Fattinger and D. Grischkowsky, "Terahertz beams," *Applied Physics Letters*, vol. 54, pp. 490–492, Feb. 1989.

[31] M. Inguscio, G. Moruzzi, K. M. Evenson, and D. A. Jennings, "A review of frequency measurements of optically pumped lasers from 0.1 to 8 THz," *Journal of Applied Physics*, vol. 60, pp. R161–R192, Dec. 1986.

[32] G. P. Gallerano, S. Biedron, *et al.*, "Overview of terahertz radiation sources," in *Proceedings of the 2004 FEL Conference*, p. 216221, 2004.

[33] F. Lewen, E. Michael, R. Gendriesch, J. Stutzki, and G. Winnewisser, "Terahertz laser sideband spectroscopy with backward wave oscillators," *Journal of Molecular Spectroscopy*, vol. 183, pp. 207–209, May 1997.

[34] L. Ives, J. Neilson, M. Caplan, N. Chubun, C. Kory, M. Read, S. Schwartzkopf, and R. Witherspoon, "Development of backward wave oscil-

lators for terahertz applications," in *Proceedings of SPIE*, vol. 5070, (Orlando, FL, USA), pp. 71–82, 2003.

[35] J. Faist, F. Capasso, D. L. Sivco, C. Sirtori, A. L. Hutchinson, and A. Y. Cho, "Quantum cascade laser," *Science*, vol. 264, pp. 553 –556, Apr. 1994.

[36] B. S. Williams, "Terahertz quantum-cascade lasers," *Nat Photon*, vol. 1, no. 9, pp. 517–525, 2007.

[37] S. Latkowski, F. Surre, and P. Landais, "Terahertz wave generation from a dc-biased multimode laser," *Applied Physics Letters*, vol. 92, p. 081109, 2008.

[38] H. Hubers, "Terahertz technology: Towards THz integrated photonics," *Nat Photon*, vol. 4, no. 8, pp. 503–504, 2010.

[39] K. Wang and D. M. Mittleman, "Metal wires for terahertz wave guiding," *Nature*, vol. 432, pp. 376–379, Nov. 2004.

[40] R. W. McGowan, G. Gallot, and D. Grischkowsky, "Propagation of ultrawide-band short pulses of terahertz radiation through submillimeter-diameter circular waveguides," *Optics Letters*, vol. 24, pp. 1431–1433, Oct. 1999.

[41] G. Gallot, S. P. Jamison, R. W. McGowan, and D. Grischkowsky, "Terahertz waveguides," *Journal of the Optical Society of America B*, vol. 17, pp. 851–863, May 2000.

[42] S. P. Jamison, R. W. McGowan, and D. Grischkowsky, "Single-mode waveguide propagation and reshaping of sub-ps terahertz pulses in sapphire fibers," *Applied Physics Letters*, vol. 76, p. 1987, 2000.

[43] R. Mendis and D. Grischkowsky, "Plastic ribbon THz waveguides," *Journal of Applied Physics*, vol. 88, p. 4449, 2000.

[44] R. Mendis and D. Grischkowsky, "Undistorted guided-wave propagation of subpicosecond terahertz pulses," *Optics Letters*, vol. 26, pp. 846–848, June 2001.

[45] R. Mendis and D. Grischkowsky, "THz interconnect with low-loss and low-group velocity dispersion," *IEEE Microwave and Wireless Components Letters*, vol. 11, pp. 444–446, Nov. 2001.

[46] S. Coleman and D. Grischkowsky, "A THz transverse electromagnetic mode two-dimensional interconnect layer incorporating quasi-optics," *Applied Physics Letters*, vol. 83, p. 3656, 2003.

[47] J. Dai, S. Coleman, and D. Grischkowsky, "Planar THz quasioptics," *Applied Physics Letters*, vol. 85, p. 884, 2004.

[48] M. Nagel, P. H. Bolivar, and H. Kurz, "Modular parallel-plate THz components for cost-efficient biosensing systems," *Semiconductor Science and Technology*, vol. 20, pp. S281–S285, July 2005.

[49] N. Amer, W. C. Hurlbut, B. J. Norton, Y. Lee, S. L. Etringer, and B. K. Paul, "Terahertz wave propagation in one-dimensional periodic dielectrics," *Applied Optics*, vol. 45, pp. 1857–1860, Mar. 2006.

[50] H. Nemec, P. Kuel, F. Garet, and L. Duvillaret, "Time-Domain terahertz study of defect formation in One-Dimensional photonic crystals," *Applied Optics*, vol. 43, pp. 1965–1970, Mar. 2004.

[51] N. Jukam and M. S. Sherwin, "Two-dimensional terahertz photonic crystals fabricated by deep reactive ion etching in si," *Applied Physics Letters*, vol. 83, p. 21, 2003.

[52] H. Kitahara, N. Tsumura, H. Kondo, M. W. Takeda, J. W. Haus, Z. Yuan, N. Kawai, K. Sakoda, and K. Inoue, "Terahertz wave dispersion in two-

dimensional photonic crystals," *Physical Review B*, vol. 64, p. 045202, June 2001.

[53] C. Jin, B. Cheng, Z. Li, D. Zhang, L. Li, and Z. Zhang, "Two dimensional metallic photonic crystal in the THz range," *Optics Communications*, vol. 166, pp. 9–13, Aug. 1999.

[54] S. Wang, W. Lu, X. Chen, Z. Li, X. Shen, and W. Wen, "Two-dimensional photonic crystal at THz frequencies constructed by metal-coated cylinders," *Journal of Applied Physics*, vol. 93, p. 9401, 2003.

[55] C. Lin, C. Chen, G. Schneider, P. Yao, S. Shi, A. Sharkawy, and D. Prather, "Wavelength scale terahertz two-dimensional photonic crystal waveguides," *Optics Express*, vol. 12, pp. 5723–5728, Nov. 2004.

[56] B. Shew, H. Li, C. Pan, and C. Ko, "X-ray micromachining SU-8 resist for a terahertz photonic filter," *Journal of Physics D: Applied Physics*, vol. 38, pp. 1097–1103, Apr. 2005.

[57] T. D. Drysdale, G. Mills, S. M. Ferguson, R. J. Blaikie, and D. R. S. Cumming, "Metallic tunable photonic crystal filter for terahertz frequencies," *Journal of Vacuum Science & Technology B: Microelectronics and Nanometer Structures*, vol. 21, p. 2878, 2003.

[58] H. Kurt and D. S. Citrin, "Photonic crystals for biochemical sensing in the terahertz region," *Applied Physics Letters*, vol. 87, p. 041108, 2005.

[59] Z. Jian, J. Pearce, and D. M. Mittleman, "Two-dimensional photonic crystal slabs in parallel-plate metal waveguides studied with terahertz time-domain spectroscopy," *Semiconductor Science and Technology*, vol. 20, pp. S300–S306, July 2005.

[60] T. Prasad, V. L. Colvin, Z. Jian, and D. M. Mittleman, "Superprism effect in a metal-clad terahertz photonic crystal slab," *Optics Letters*, vol. 32, pp. 683–685, Mar. 2007.

[61] A. Bingham, Y. Zhao, and D. Grischkowsky, "THz parallel plate photonic waveguides," *Applied Physics Letters*, vol. 87, p. 051101, 2005.

[62] Y. Zhao and D. R. Grischkowsky, "2-D terahertz metallic photonic crystals in Parallel-Plate waveguides," *IEEE Transactions on Microwave Theory and Techniques*, vol. 55, pp. 656–663, Apr. 2007.

[63] A. L. Bingham and D. R. Grischkowsky, "Terahertz 2-D photonic crystal waveguides," *IEEE Microwave and Wireless Components Letters*, vol. 18, pp. 428–430, July 2008.

[64] P. R. Smith, D. H. Auston, and M. C. Nuss, "Subpicosecond photoconducting dipole antennas," *IEEE Journal of Quantum Electronics*, vol. 24, pp. 255–260, Feb. 1988.

[65] M. van Exter and D. R. Grischkowsky, "Characterization of an optoelectronic terahertz beam system," *IEEE Transactions on Microwave Theory and Techniques*, vol. 38, pp. 1684–1691, Nov. 1990.

[66] K. Wang and D. M. Mittleman, "Guided propagation of terahertz pulses on metal wires," *Journal of the Optical Society of America B*, vol. 22, no. 9, pp. 2001–2008, 2005.

[67] T. Jeon and D. Grischkowsky, "Direct optoelectronic generation and detection of sub-ps-electrical pulses on sub-mm-coaxial transmission lines," *Applied Physics Letters*, vol. 85, p. 6092, 2004.

[68] H. Cao and A. Nahata, "Resonantly enhanced transmission of terahertz radiation through a periodic array of subwavelength apertures," *Optics Express*, vol. 12, pp. 1004–1010, Mar. 2004.

[69] S. A. Maier, S. R. Andrews, L. Martn-Moreno, and F. J. Garca-Vidal, "Terahertz surface Plasmon-Polariton propagation and focusing on periodically corrugated metal wires," *Physical Review Letters*, vol. 97, p. 176805, Oct. 2006.

[70] H. Han, H. Park, M. Cho, and J. Kim, "Terahertz pulse propagation in a plastic photonic crystal fiber," *Applied Physics Letters*, vol. 80, p. 2634, 2002.

[71] M. Goto, A. Quema, H. Takahashi, S. Ono, and N. Sarukura, "Teflon photonic crystal fiber as terahertz waveguide," *Japanese Journal of Applied Physics*, vol. 43, pp. L317–L319, Feb. 2004.

[72] M. Nagel, A. Marchewka, and H. Kurz, "Low-index discontinuity terahertz waveguides," *Optics Express*, vol. 14, pp. 9944–9954, Oct. 2006.

[73] M. Wachter, M. Nagel, and H. Kurz, "Metallic slit waveguide for dispersion-free low-loss terahertz signal transmission," *Applied Physics Letters*, vol. 90, p. 061111, 2007.

[74] T. J. Yen, W. J. Padilla, N. Fang, D. C. Vier, D. R. Smith, J. B. Pendry, D. N. Basov, and X. Zhang, "Terahertz magnetic response from artificial materials," *Science*, vol. 303, pp. 1494 –1496, Mar. 2004.

[75] H. Chen, J. F. O'Hara, A. K. Azad, A. J. Taylor, R. D. Averitt, D. B. Shrekenhamer, and W. J. Padilla, "Experimental demonstration of frequency-agile terahertz metamaterials," *Nat Photon*, vol. 2, pp. 295–298, May 2008.

Chapter 5

THE ANALYSIS OF METALLIC PHOTONIC CRYSTALS

In this chapter, a study of dispersion and transmission characteristics of metallic photonic crystal structures is presented. In the study, 2D metallic photonic crystals consist of metallic cylinders in air arranged by two types of lattice structures: square and triangular lattice structures are considered. Both the photonic band structure and transmission calculations for THz frequencies are carried out using the finite element method (FEM). Band-gap diagrams and transmission, reflection and absorption spectra are obtained for both E- and H-polarizations. A comparison is made between dispersion and transmission results. Results show perfect match and internal consistency between the presented results and previous studies. In both square and triangular lattice arrays, transmission spectra show that the size of the band-gap increases with increasing rod radius. Transmission characteristics are studied in many aspects, such as effect of number, size and layers of metallic rods, dependency of incident angle and photonic band-gap map. In the calculations, frequency-dependency and losses are considered by specifying the material properties within the Drude model.

This chapter starts with a short introduction to the optical properties of metals and the Drude model. Frequency-dependent metallic properties such as dielectric function, conductivity, reflectivity, and skin depth of metals are calculated for THz range. The dispersion and transmission properties of metallic photonic crystals are presented in the following sections.

5.1 Optical Properties of Metals

In this section, a model for predicting the frequency-dependent relative permittivity of metals, known as the Drude model is presented. The dielectric function and the bulk properties of metals are discussed.

In the THz domain, particularly in longer waveguides, the metallic losses are expected to be important, with respect to the wavelength of the transmitted signal. This can be attributed to the finite conductivity of metallic materials and their absorption property in the THz domain. In these structures, materials are characterized by their dielectric properties; moreover dielectric functions are frequency dependent and have a non-negligible imaginary part. In general terms, metallic conductivity, permittivity and magnetic permeability are frequency dependent. This can be accounted for by calculating the frequency response of the dielectric constant, while other properties can be considered constant over the spectral region of interest. For THz study, it is crucial to use frequency dependent models in order to precisely estimate these values.

The dielectric constant is necessary to analyse the properties of dielectric and metallic photonic crystals. Any material has a frequency and temperature dependent dielectric constant. In order to identify dispersive properties of metallic photonic

crystals and calculate the permittivity accurately, the well-known frequency-dependent Drude model can be used. The Drude model was proposed by Paul Drude in 1900 (1) Transport properties of electrons in materials and their response to an optical field are described in order to explain the dispersive properties of materials. Metals contain large densities of free electrons that originate from the valance electrons of the metals. The Drude model takes into account the optical interactions of free electrons in metals to determine the optical properties of good metals and can be applicable to free-electron metals (e.g. aluminium, gold, silver, copper). The Drude model is as follows (2; 3):

$$\varepsilon_c(\omega) \;=\; \varepsilon_\infty - \frac{\omega_p^2}{\omega^2 + i\omega\omega_\tau} \tag{5.1}$$

Here $\varepsilon_c(\omega)$ is the complex relative permittivity of the metal; ε_∞ is the permittivity of the metal at the limit of infinite frequency it considers the contribution of the bound electrons. For a non-transitional metal, ε_∞ is considered as 1 (4). ω is the incident frequency of the electromagnetic radiation, ω_p is the bulk plasma frequency, ω_τ is the damping frequency due to the electron scattering events, it is equal to $1/\tau$, where τ is the electron lifetime. Plasma frequency is a measure of the free electron density present which represents the natural frequency of the oscillations of free conduction electrons. The plasma frequency can be expressed as:

$$\omega_p \;=\; \sqrt{\frac{Ne^2}{m^*\varepsilon_0}} \tag{5.2}$$

where N is the free electron density, m^* is the effective electron mass, e is the fundamental unit of electric charge and ε_0 is the free-space permittivity.

If we rearrange the frequency-dependent complex relative permittivity where, ε_r

is the real part of the permittivity; ε_i is the imaginary part of the permittivity.

$$\varepsilon_c(\omega) \;=\; \varepsilon_r + i\varepsilon_i \tag{5.3}$$

$$\varepsilon_r \;=\; \varepsilon_\infty - \frac{\omega_p^3}{\omega(\omega^2 + i\omega_\tau^2)} \tag{5.4}$$

$$\varepsilon_i \;=\; \frac{\omega_p^2\omega_\tau^2}{\omega(\omega^2 + \omega_\tau^2)} \tag{5.5}$$

In a conducting medium (i.e. metals), some of the electrons are bound to the atoms, like in dielectrics; some of them are not bound to the atoms and move randomly, and they are called free electrons. When an external electric field is applied, electrons acquire additional velocity and move in a more orderly manner; this induces a current flow (5). In this model this motion is explained with the existence of two opposite forces: the force $e\vec{E}$ and a damping force $-\vec{v}/\tau$ associated with the electric field itself and the collisions occurring between the electron and the atoms of the metallic lattice, respectively (6). The damping time τ is typically of the order of 10^{-14} s.

The equation of motion of an electron with velocity $\vec{v}$ in a material can be written as (6)

$$m\frac{\partial\vec{v}}{\partial t} + m\vec{v}\omega_\tau \;=\; -e\vec{E} \tag{5.6}$$

$$\vec{J}(\omega) \;= \sigma(\omega)\vec{E} \;=\; \frac{Ne^2}{m(\omega_\tau - i\omega)}\vec{E} \;=\; \frac{Ne^2(\omega_\tau + i\omega)}{m(\omega_\tau^2 + \omega^2)} \tag{5.7}$$

where m and e are the mass and the charge of electron, and $\omega_\tau(1\tau)$ is the damping constant N is the electron density in the metal. The instantaneous current density can be expressed as $\vec{J} = -Ne\vec{v}$.

The complex permittivity due to the finite conductivity is defined as (7):

$$\varepsilon_c(\omega) \;=\; \varepsilon_\infty + i\frac{\sigma}{\omega\varepsilon_0} \;=\; \varepsilon_\infty - \frac{\omega_p^2}{(\omega^2 + i\omega\omega_\tau)} \tag{5.8}$$

$$\sigma(\omega) \;=\; \frac{i\sigma_0\omega_\tau}{(\omega + i\omega_\tau)} \;=\; \frac{i\varepsilon_0\omega_\tau}{(\omega + i\omega_\tau)} \tag{5.9}$$

$\sigma(\omega)$ is the complex conductivity and σ_0 is the conductivity measured with DC electric field. The above expression for conductivity $\sigma(\omega)$ is known as the Drude model, and any material that this method is applicable to is called a Drude-like material (2; 8).

As can be seen from the equations, the complex permittivity equation includes the complex conductivity.

$$\varepsilon_c(\omega) \;=\; \varepsilon_\infty - \frac{\sigma_0\omega_\tau}{\omega\varepsilon_0(\omega + i\omega_\tau)} \;=\; \varepsilon_\infty + \frac{i\sigma_0}{\omega\varepsilon_0(1 - i\omega/\omega_\tau)} \tag{5.10}$$

In a simple Drude model, the interband transitions are not taken into account to obtain the dielectric function of the metal. For the THz range interband transitions can be ignored, however, it is important at optical frequencies and in the near infrared region. The influence of these interband transitions can be covered with the Drude-Lorentz model where the complex relative permittivity can be expressed as

Table 5.1: Drude fitting parameters used in calculations for permittivity and conductivity (4; 10; 11).

Metal	$\omega_p/2\pi$ THz	$\omega_\tau/2\pi$ THz	DC Conductivity ($10^{-7}\ S \cdot m^{-1}$)
Copper	1914	8.4	5.959
Silver	2175	4.35	6.301
Gold	2175	6.5	4.517
Aluminium	3570	19.4	3.774

the sum of the intra-band effect with Drude model and the interband effect with Lorentz model (9).

In Table 5.1, Drude parameters used for calculations of the metals of interest, i.e. copper, silver, gold, and aluminium are listed. These parameters are used to produce the frequency dependent complex dielectric functions at THz frequencies. The corresponding conductivities are also calculated from the permittivity.

Figure 5.1 shows the real and imaginary part of the complex frequency dependent dielectric constant of four metals used throughout the study. Clearly, the dielectric constant of these metals is very high with the imaginary part of the dielectric constant being orders of magnitude higher than the absolute value of the real part of the dielectric constant at THz. The dielectric constant of copper, silver, gold, and aluminium are represented by square, triangle, cross and circle, respectively. The frequency dependent conductivities of copper, silver, gold, and aluminium are shown in Figure 5.2.

In the low frequency region, the real part of the conductivity is an order of magnitude higher than the imaginary conductivity. In optics, materials are analysed with their refractive indices, which are related to the dielectric constant, $\varepsilon_c = \varepsilon_r + i\varepsilon_i$ where $\varepsilon < 0$,

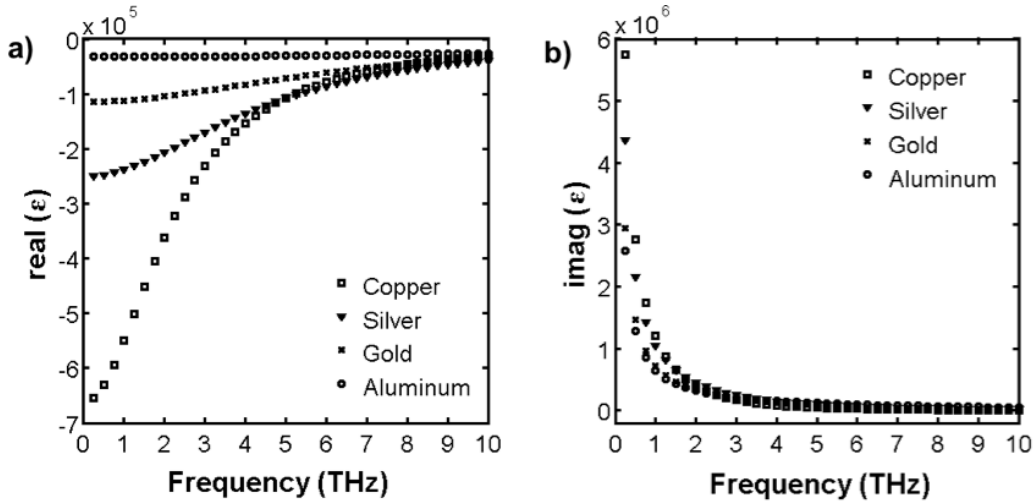

Figure 5.1: a) Real part and b) imaginary part of the relative permittivity of copper, silver, gold, and aluminium calculated using frequency-dependent Drude model for THz frequencies, represented by square, triangle, cross and circle, respectively.

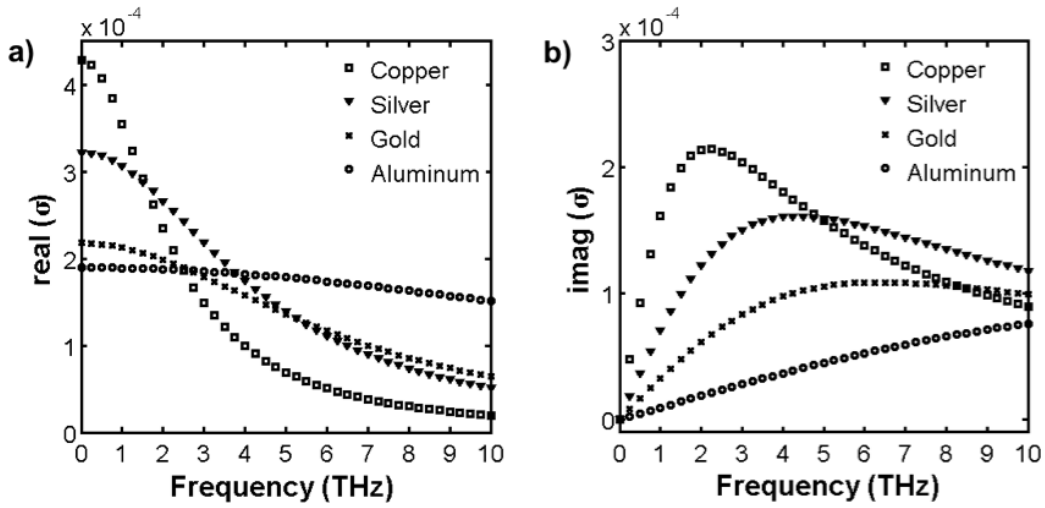

Figure 5.2: a) Real part and b) imaginary part of the conductivity of copper, silver, gold, and aluminium calculated using frequency-dependent Drude model for THz frequencies, represented by square, triangle, cross and circle, respectively.

$$\eta_c = \eta + i\kappa = \sqrt{\varepsilon_c} \tag{5.11}$$

where η_c is the complex refractive index, η is the refractive index, κ is the extinction index. When an electromagnetic wave incident on the interface of the reflectivity of a material in vacuum at normal incidence can be expressed as follows:

$$R = \frac{(1-\eta)^2 + \kappa^2}{(1+\eta)^2 + \kappa^2} \tag{5.12}$$

For most metals, the plasma frequency is in the ultraviolet region. In the infrared and visible regions as well as in THz region, the EM frequency and the relaxation frequency are usually significantly lower than the plasma frequency $\omega_p \gg \omega_\tau$. Below the plasma frequency metals behave as good reflectors while they are transparent above it (6). Just above the plasma frequency metal rapidly changes from a good reflector to a transparent material. Since the plasma frequency term is predominant in the Drude model equation, the permittivity of the metal is a negative real number with a large modulus compared to unity and the refractive index is a purely imaginary number of large magnitude. In other terms, metals remain good reflectors in these regions.

Figure 5.3 shows the reflectivity of copper, silver, gold, and aluminium at the normal incidence in the THz range up to 10 THz. The reflectivity of metallic surfaces in THz is close to unity. Copper has the highest reflectivity among other three high conductivity metals.

Currents accumulate at the surface of the conductor. In the presence of metallic losses, the electromagnetic field decays exponentially at the surface, also known as skin effect of metals due to their finite conductivity. The imaginary part of the permittivity relation describes the losses. The metallic losses are frequency dependent.

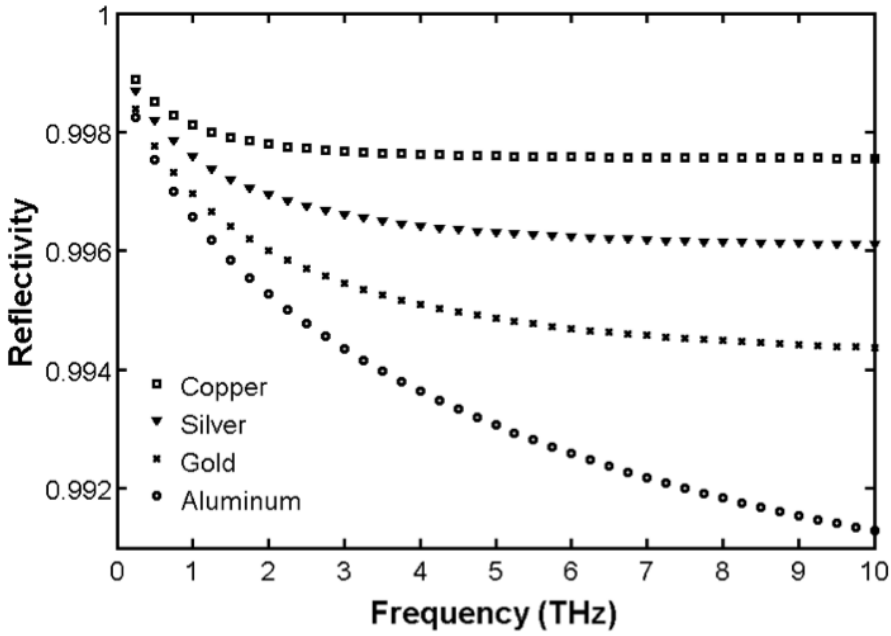

Figure 5.3: Reflectivity as a function of frequency described by Drude model for copper, silver, gold, and aluminium in the THz frequency range represented by square, triangle, cross and circle, respectively.

As frequency increases, conductivity decreases making the imaginary part of the permittivity larger in the relation.

The complex propagation constant is given by:

$$\gamma \;=\; \alpha + i\beta \;=\; i\omega\sqrt{\mu\varepsilon_0\varepsilon_c(\omega)} \tag{5.13}$$

Since $\omega/\omega_\tau \ll 1$ for THz frequencies, metals are mainly absorbing with an absorption coefficient expressed as follows:

$$\alpha \;=\; \left(\frac{2\omega_p^2\omega}{\omega_\tau c^2}\right)^{1/2} \tag{5.14}$$

The dc-conductivity can be written as $\sigma_0 \;=\; \frac{ne^2}{m\omega_\tau} \;=\; \frac{\varepsilon\omega_p^2}{\omega_\tau}$. The above equation

can be expressed as:

$$\alpha = \sqrt{2\sigma_0\omega\mu_0} \tag{5.15}$$

where μ_0 is the permeability of vacuum. The power falls off as $e^{-2z\delta}$, as the field strength varies as $e^{-z\delta}$ where z denoting the distance z from the surface (7).

The skin depth can then be calculated analytically using the dc-conductivity values given in Table 5.1 as:

$$\delta = \frac{2}{\alpha} = \sqrt{\frac{2}{\omega\mu_0\sigma_0}} \tag{5.16}$$

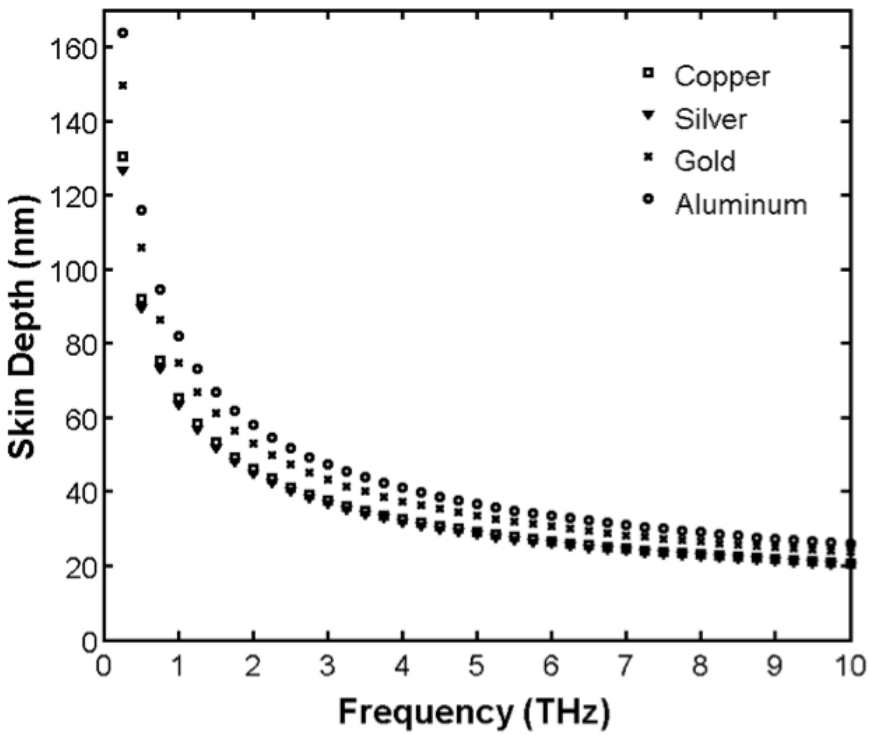

Figure 5.4: Skin depth as a function of frequency for copper, silver, gold, and aluminium in the THz frequency range represented by square, triangle, cross and circle, respectively.

Table 5.2: Drude fitting parameters of used in calculations of permittivity and conductivity (4; 10; 11).

	Copper	Silver	Gold	Aluminium
Skin Depth at 1 THz (nm)	65.1979	63.4038	74.8850	81.9255
Skin Depth at 3 THz (nm)	37.6420	36.6062	43.2349	47.2997

In THz region the skin depth of metals are very small, on the order of nanometers (Figure 5.4). The skin depth is less than 100nm at 1 THz and decreases as the frequency increases. Skin depth values for high conductivity metals at 1 THz and 3 THz are given in Table 5.2.

A limited number of fabrication techniques are available for manufacturing metallic photonic crystals. Developments in fabrication techniques for photonic crystals are favoured to dielectric or semiconductor based materials since they are used most often. The skin depth of metals for THz range is small enough to built metallic photonic crystals by coating. Metal-coated photonic crystal structures show the same properties as the pure metallic photonic crystals.

In this section, we introduced the optical properties of metals and the frequency-dependent Drude model. Throughout the thesis, frequency-dependent complex dielectric constant of metals is calculated by using the Drude model. The following section is dedicated to 2D metallic photonic crystals. Band-gap and transmission analysis of metallic photonic crystals presented. Copper, which shows the highest reflectivity in the THz range, will be used as a metallic material in the following section.

5.2 2D Metallic Photonic Crystals

In this thesis, metallic photonic crystals are studied for wave guiding applications for the THz frequency range. Only 2D photonic crystals are considered. There are many ways to construct optical components. With their small sizes, photonic crystals are good candidates to start to build a variety of components. In this part of the study, the main aim is to present some of our results achieved with photonic crystal design to fulfil the wave guiding demand in the THz range. We investigate photonic crystal structures with metal rods, and simulate results using FEM method. FEM has proven to be a very reliable and effective numerical method for modelling and simulating a wide range of physics and multi-physics problems especially for complex structures. FEM is also able to resolve and describe wave propagation as well as the dispersion diagrams of PhC structures (12; 13; 14).

As mentioned earlier, without depending on scaling, photonic crystal structures can be built from micrometer to millimetre dimensions, from optical frequencies to microwaves (15). Photonic crystals can be classified into two groups: dielectric and metallic photonic crystals. In photonic crystals, mostly dielectrics or semiconductor materials are used. The metallic photonic crystals have been mainly studied in the microwave range since in this range these structures are easy to fabricate and absorption is considerably less than in optical ranges (16; 17; 18; 19; 20; 21; 22). In THz range, photonic crystals can be studied in a similar way to microwave frequencies. However, in the transitions from longer to the shorter wavelengths, the frequency dependency of the material needs to be considered. In microwave, the conductivity of metals is considered frequency-independent and equal to its dc-value. In THz frequencies, the conductivity losses are comparatively less than optical ranges. The skin depth is smaller than microwave frequencies.

In photonic crystal structures, lattice type, filling factor, and dielectric contrast of the constituent materials are the main design parameters. By proper choice of these parameters the size of photonic band-gaps can be enlarged or formed to suit the needs of the design. In 2D photonic crystal systems, the structure consists of arrays of pillars/rods or holes in various lattice configurations; most common ones are square and triangular lattice.

5.2.1 Properties of Metallic Photonic Crystals

In this study, metallic photonic crystals are preferred to dielectric photonic crystals due to their very promising advantages. Compared to dielectric photonic crystals, metallic photonic crystals offer much wider photonic band gaps which leads to wider frequency ranges (16; 23; 24). Metallic photonic crystals are more reflective their dielectric counterparts (25; 26). Therefore, it is possible to design more compact and lighter devices since with metallic photonic crystals fewer periods are required (27; 28). Moreover, metallic photonic crystals are more suited to coping with higher energy THz signals than dielectric photonic crystals.

Metallic photonic crystals exhibit important features when their band-gap characteristics are investigated. Metallic photonic crystals have wide band-gaps for E-polarization (TM mode) where the incident wave is polarized parallel to the rod axis. On the other hand, metallic photonic crystals exhibit a very small band-gap for H-polarization (TE mode) where the incident wave is polarized perpendicular to the rod axis. Band-gap for E-polarization starts from zero frequencies to cut-off frequency (29; 30).

The effect of absorption is considered as loss of the signal. Even though the level of absorption is lower than optical frequencies, the absorption of light is the main

disadvantage of metallic structures in THz range. However, with photonic crystal design, due to the periodicity, redistribution of the photon wave field prevents metal from absorbing the light (31).

5.2.2 Metallic Band-Gap

The optical properties of photonic crystals rely on the dielectric constant of the constituting materials, the geometry of the structure and the direction of polarization. In order to calculate the band-gap structure of a photonic crystal system that contains metallic components, the dielectric constant of the metal is introduced to calculations in three ways by assuming: i) the metal as a perfect conductor, ii) as dispersive materials modelling the dielectric function with free-electron form ($\varepsilon(\omega) = 1 - \omega_p^2\omega^2$, where ω is the frequency and ω_p is the plasma frequency of metals) or iii) the refractive index of the metal can be described by the Drude model.

Metallic photonic crystals have been theoretically studied by many methods that consider photonic crystals with frequency-dependent permittivities. Transmission spectra of metallic photonic crystals were calculated by using TMM method (TMM) by Pendry *et al.* in 1992 (32). The photonic band gap of a square lattice array of metal or semiconductor cylinders, and of an fcc array of metal or semiconductor spheres, have been computed numerically using the PWE method (25). An important study on the band structure of 2D arrays of infinitely long metallic cylinders embedded in vacuum was carried out by Kuzmiak *et al.* in 1994 (29). The modified PWE method was utilized calculating the eigenvalues to study the band-gap diagrams of metallic photonic crystals with dielectric constant in free-electron form arranged in square and triangular patterns. The permittivity is real valued so the absorption is not taken into account. This study showed the significant differences in the band structures for E- and H-polarization. For E-polarization, where electric

field is parallel to the rod axis, metallic photonic crystals exhibit a broad photonic band-gap between zero frequency and their cut-off frequency. On the other hand for H-polarization, where electric field is perpendicular to the rod axis, metallic photonic crystals produce flat bands with very low group velocities. Another study was carried out by using the generalized Rayleigh identity method to calculate band diagrams of two-dimensional arrays of perfectly conducting cylinders (33). Later, the photonic bands of metallic systems were calculated by means of the numerical simulation of the dipole radiation based on the finite-difference time-domain method (FDTD), in 2001 by Sakoda *et al.* (34; 35). The results were in agreement with Kuzmiaks study moreover, the flat bands with very low group velocities seen in H-polarization were explained by the existence of plasmon resonances. For these modes, wave propagation is provided with plasmon resonances, rather than a band-gap mechanism. Some other approaches are used to calculate the photonic band-gap of metallic photonic crystals. They include transfer matrix method (36) and finite-difference time domain method (23; 37); finite difference method, (26; 38), multiple multipole method (39), and order-N method(40). Most of the studies on metallic photonic crystals are limited to vacuum background. Metallic photonic crystals, when the background is a dielectric material instead of vacuum, have also been studied by using PWE (41)and FDTD (42) methods.

The following sections focus on the dispersion and transmission characteristics of 2D metallic photonic crystals. Electromagnetic wave propagation within metallic photonic crystals is investigated in order to better understand the scattering behaviour. Firstly, a single rod is studied to achieve the band-gap diagram. Then, a set of four layers of metallic rods is studied. The transmission and reflection are calculated as a function of frequency by changing rods' sizes at a fixed lattice period of a = 50 μm. In these simulations FEM is used in order to calculate the eigen-modes of square and triangular lattice structures for E- and H-polarizations. Band-gap maps and transmission spectra are obtained for various metals and lattice configurations.

5.3 Dispersion Analysis of Metallic Photonic Crystals

A band-gap diagram, namely a dispersion diagram, is calculated by solving the eigenvalue problem. Dispersion diagram are important for determining band-gaps and pass bands of periodic structures. To achieve band-gap diagrams of periodic photonic crystal structures, the PWE method is the most used and reliable method. However this approach has a limitation when it comes to metallic photonic crystal structures. The equations for the PWE method are valid for real-valued dielectric constant. Therefore, PWE method cannot deal with lossy materials since the loss in a material is incorporated into the model through the imaginary part of the dielectric constant.

Calculations are performed for dispersion in metallic 2D photonic crystals. In this approach, metals exhibit dissipative and dispersive properties where the dielectric function is frequency dependent. The non-linear eigenvalue problem is solved for wave vectors at a given frequencies. FEM is used in order to compute the dispersion of metallic photonic crystal structures. Mostly for simplicity, for computation of band diagrams, loss free photonic crystals are used since the most used methods have limitations in the treatment of losses. Using the free electron expression for metals, frequency dependency is taken into account however, the imaginary part of the dielectric constant is ignored, and so are the losses. Therefore, most of the publications dealing with band-gap calculations of metallic photonic crystals do not take the losses into account.

For most computation methods, eigen frequencies are calculated by scanning over a real-valued wave vector. Unlike those methods, for dispersion calculations FEM searches for wave vectors, for given frequencies. Eigen values may be complex-

valued. The propagating modes in a photonic crystal are described by a real-valued wave vector, while the imaginary part of the complex wave vector exhibits the evanescent modes. Results of eigen-modes and band-gap calculations are presented in the following sections.

5.3.1 Square Lattice

Firstly we calculate the band-gap diagram for photonic crystal lattice structures for a square lattice array and similarly for a triangular lattice array. Quadratic eigenvalue calculations are performed over a unit cell of a photonic crystal lattice. This is sufficient because of their repeated pattern. In order to analyse the whole structure in a single cell, periodic boundary conditions with Floquet periodicity are applied. Periodic boundary conditions extend the structure to the infinity.

Floquet periodicity is a periodic boundary condition that uses a complex phase factor to relate fields at different locations within a periodic structure. The phase shift is determined by a complex wave vector and the distance between the source and destination. At the source boundary, the field is extracted and the predetermined phase difference between the boundaries is enforced before equating the fields at source and destination boundaries (43).

$$E_{dest} = E_{source} e^{-ik(r_{dest} - r_{source})} \tag{5.17}$$

The 2D photonic crystal is a medium described in terms of the underlying Bravais lattice. The medium is characterized by a permittivity ε, with the periodicity of the lattice. We use a square lattice with the lattice constant a and consider E-polarized waves in the crystal. In the E-polarization case, where the electric field is in the z-direction, the electric field satisfies the equation

$$-\Delta E_z(x,y) \;=\; \frac{\omega^2}{c^2}\varepsilon(x,y,\omega)E_z(x,y) \tag{5.18}$$

The non-zero solution is of the form

$$E_z(x,y) \;=\; e^{i(k_x x + k_y y)}u(x,y) \tag{5.19}$$

where u is a periodic function and $\vec{k} = (k_x, k_y)$ is the Floquet-Bloch wave vector. Eigenfunctions of periodic media can be obtained by solving the eigenvalue problem. The translational symmetry of the permittivity implies that Bloch waves are determined from a problem over one cell in the lattice array. For a fixed frequency ω, the Bloch waves can be determined from an eigenvalue problem in $\vec{k}$. This eigenvalue is nonlinear, which complicates the numerical computations. However, in order to determine the band structure and modal fields of a photonic crystal, a nonlinear eigenvalue problem has to be solved. Instead of searching eigen frequencies for a given wavevector, complex eigen wavevectors are computed for a given frequency. In fact for lossy materials in calculations both frequency and the wave vector become complex. Complex frequencies lead to mode decaying in time and complex wave vectors describe attenuation in wave propagation along the propagation direction. This consideration is especially important for analysing photonic crystal waveguides.

First, we calculate the photonic band structure of a system consisting of a square lattice array of copper cylinders embedded in air for E-polarization. The radius of the rods is $r = 0.2a$, where a is the lattice constant of the square pattern set at 50 μm. The complex eigenvalue problem is solved for wave vector $\vec{k}$, for a given frequency ω, in the unit cell of square lattice by setting periodic boundary conditions. Since the dielectric function is complex, the calculated eigen-wavevectors found are

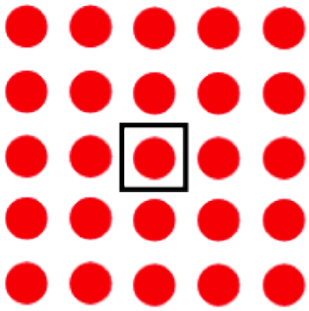

Figure 5.5: The unit cell of a square lattice

Table 5.3: Symbols and wave vector directions for square and triangular lattices

Square Lattice		Triangular Lattice	
Symbol	Reciprocal Lattice	Symbol	Reciprocal Lattice
Γ	$\vec{k} = 0$	Γ	$\vec{k} = 0$
X	$\vec{k} = \frac{\pi}{a}\hat{a}_x$	M	$\vec{k} = \frac{2\pi}{\sqrt{3}a}\hat{a}_y$
M	$\vec{k} = \frac{\pi}{a}\hat{a}_x + \frac{\pi}{a}\hat{a}_y$	K	$\vec{k} = \frac{2\pi}{3a}\hat{a}_x + \frac{2\pi}{\sqrt{3}a}\hat{a}_y$

also complex. This provides not only the guided modes but also the lossy modes in the system.

The photonic bands of a photonic crystal are obtained by solving an eigenvalue problem in the unit cell for a discrete set of wave-vectors of the irreducible Brillouin zone. In the dispersion diagram below, photonic bands that have the lowest frequencies in THz range are drawn.

At the boundary of the Brillouin zone as depicted in Figure 5.6, there are regions where the dispersion curves are separated by gaps, i.e. stop-bands in which propagation along the specified direction is forbidden for a given range of frequencies. Stop-bands are usually localized by the upper frequency and the lower frequency limit of the stop-band described by the stop-band edges. For some specific frequency ranges, the stop-bands are overlapped forming a band-gap where propagation along the photonic crystal for any given angle is forbidden. In order

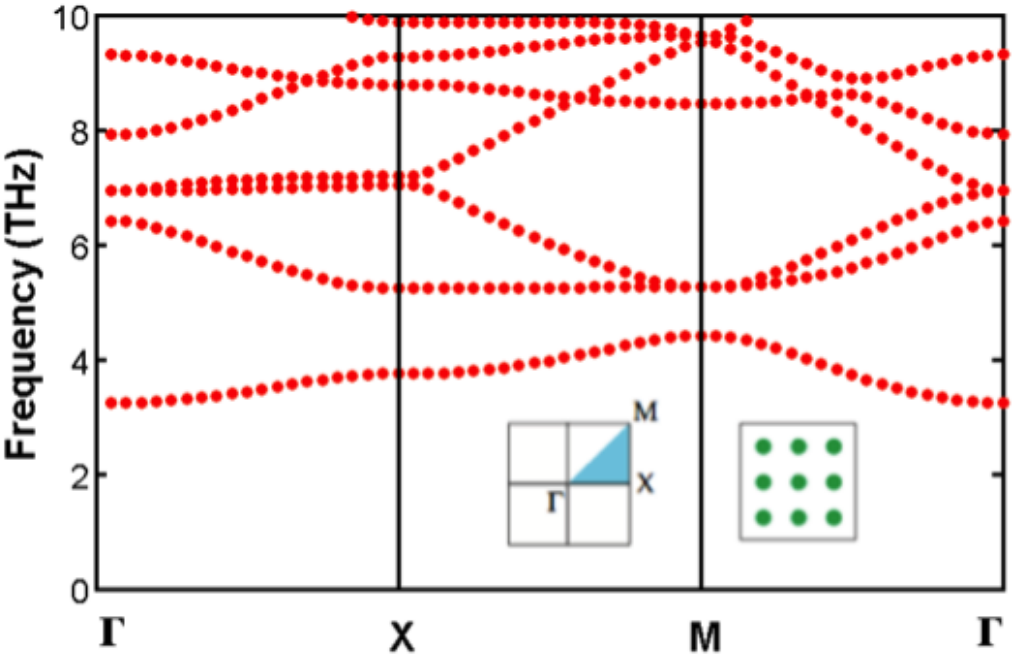

Figure 5.6: The photonic band structure of a square lattice of metal cylinders in vacuum for E-polarization. The PhC is characterized by a 50 μm lattice period in square lattice pattern with a radius of $0.2a$. The left inset shows the high symmetry points at the corners of the irreducible Brillouin zone, the right inset the square lattice pattern.

to specify frequencies where photonic band-gaps appear, high symmetry points are used.

The calculated dispersion curves are plotted along high symmetry directions Γ, X, M as depicted in Figure 5.6 and Figure 5.7 for E-polarization and H polarization respectively. The high symmetry points are set Γ(0, 0), X(π/a, 0), and M($\pi/a, \pi/a$) from centre to near and far edge of the Brillouin zone.

For E-polarization, the band diagram in Figure 5.6 shows that there are two band-gaps for metallic photonic crystal. The first band-gap is wider which extends from 0 to 3.244 THz and the second band is between 4.413 and 5.242 THz correspond-

ing to 0 - 0.5407 $(\omega a/2\pi c)$ and 0.734 - 0.8778 $(\omega a/2\pi c)$, respectively, in terms of normalized frequencies. Between these two bands there is a region where photonic crystals become transparent to wave propagation. This region can be called the pass-band of the crystal. These results are in good agreement with previously published results (29; 38; 44).

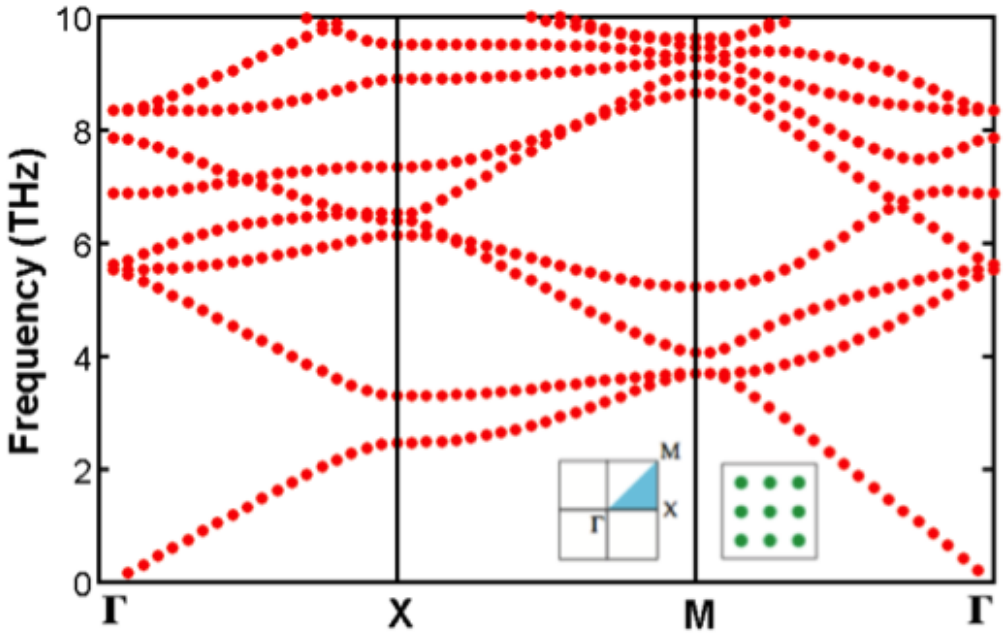

Figure 5.7: The photonic band structure of a square lattice of metal cylinders in vacuum for H-polarization. The PhC is characterized by a 50 μm lattice period in square lattice pattern with a radius of $0.2a$. The left inset shows the high symmetry points at the corners of the irreducible Brillouin zone, the right inset the square lattice pattern.

In dispersion diagrams, the frequency axis is usually represented by normalised frequencies. The frequency is normalised by the period of the lattice constant, as dispersion does not depend on the scale of the system. This approach is convenient for the systems that have frequency-independent dielectric functions. However this is not the case with metallic materials, thus we have represented the frequencies without any normalisation. Within the band-gap, the photonic crystal waveguides

support guided modes. No wave can propagate through the structure for frequencies falling within the photonic band-gap (PBG), as opposed to the pass band of the structure where it becomes transparent to the waves. The region between 3.244 THz and 4.414 THz is the pass-band of the metallic structure; this is where the losses are expected to occur. On the other hand, for H-polarization there is no band-gap as can be seen in Figure 5.7. Therefore, in the following chapters, only E-polarization is considered for wave guiding structures.

Figure 5.8 shows the electric field distribution of eigenmodes of the 6 lowest photonic bands of a square lattice of metallic cylinders at Γ point. The E-field is plotted for the modes with in order from lowest frequency to higher, labelled as a) 3.244 THz, b) 6.415 THz c) 6.933 THz d) 6.933 THz e) 7.918 THz and f) 9.308 THz. As a result of spatial symmetry of the lattice structure, all the eigenmodes are symmetric. The first mode (Figure 5.8 a) corresponds to the cut-off frequency and therefore most of the energy is concentrated in the metallic lattice unlike the other modes shown in the figure. The cut-off corresponds to the lowest mode of the Γ point in k-space. 3rd and 4th modes appear at the same frequency and their electric field distributions have the same field distribution with a mirror symmetry.

A finite cut-off frequency occurs only for E-polarization, because the modes can couple to longitudinal oscillations of charge along the length of cylinders (45). Since, in metallic photonic crystals, the material is spatially spread, these oscillations, which normally do not occur at bulk plasma frequencies, occur at an effective plasma frequency proportional to the average electron densities. For H-polarization, on the other hand, a number of flat, low dispersion bands are produced, which are explained by excitations associated with isolated cylinders, and very low group velocities related to plasmon resonances.

For a given value of the lattice constant, as the radius of rods increases, the posi-

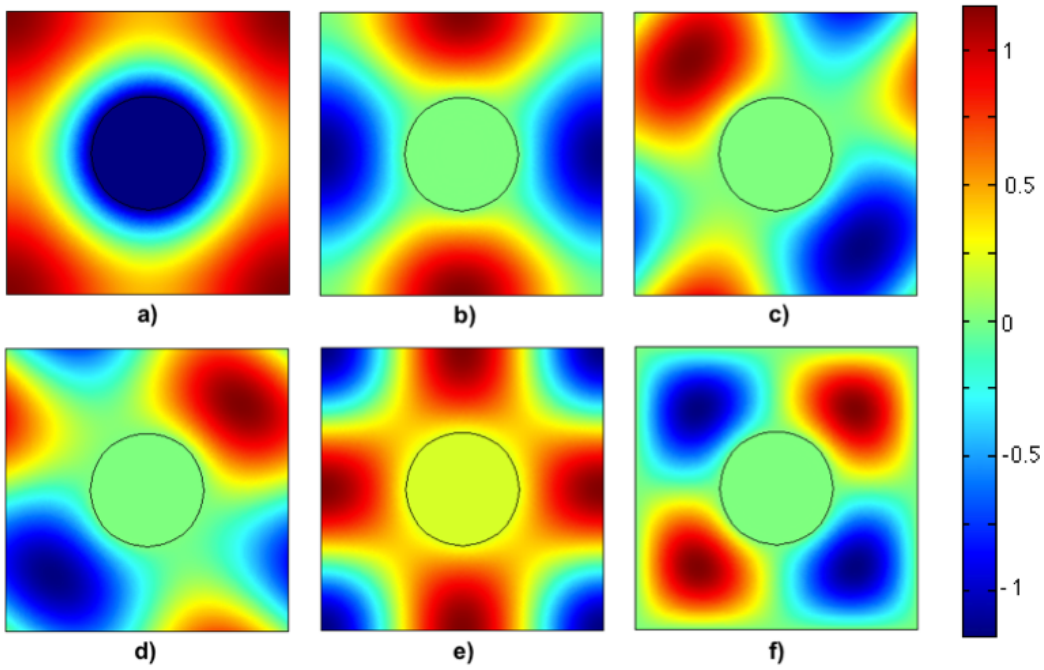

Figure 5.8: Electric field distribution of first 6 eigenmodes at Γ point of a square lattice of metallic circular cylinders for E-polarization. In the figures the maximum of electric field is normalized to unity.

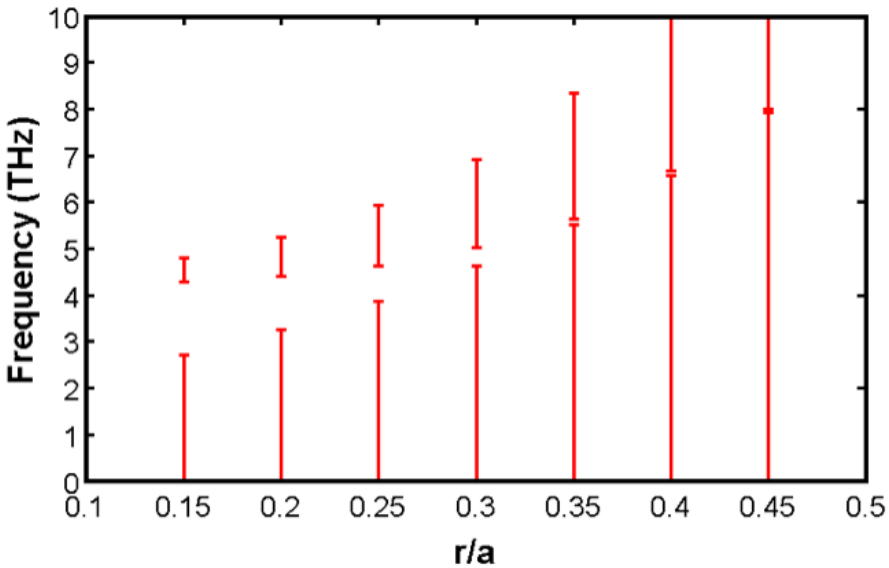

Figure 5.9: The spectral range and position of band-gaps for E-polarization for varying rod sizes.

tion of cut-off frequency shifts to higher frequencies, 2.715 THz, 3.244 THz, 3.874 THz, 4.629 THz, 5.524 THz, 6.582 THz and 7.957 THz for r/a equals to 0.15, 0.2, 0.25, 0.3 0.35, 0.4 and 0.45, respectively. Figure 5.9 shows the position and the spectral range of band gaps for varying rod sizes. There are two band-gaps that appear for metallic photonic crystals in square lattice pattern for E-polarization within the THz range. The frequency range between zero frequency and the cut-off frequency defines the first band-gap. The second band-gap is located between the maximum of the first band and the minimum of the second band. The size of first band gap increases while the size of pass band decreases. The size of second band also increases with increasing rod radius.

Unlike E-polarization, in H-polarization, metallic photonic crystals do not possess a non-zero cut-off frequency. Moreover, no band-gap appears for small rod radii, i.e. $r < 0.3a$. A small band-gap appears for $r = 0.35a$ for frequency range between 3.343 THz and 3.658 THz, and $r = 0.4a$ from 2.982 THz to 3.814 THz.

5.3.2 Triangular Lattice

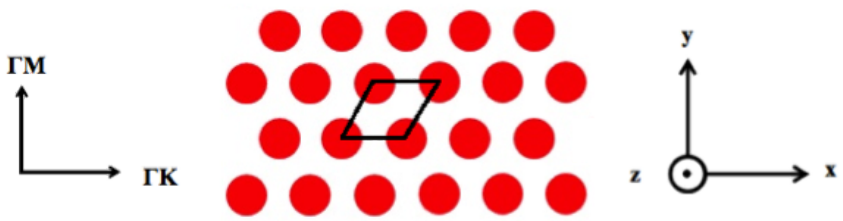

Figure 5.10: Schematic of triangular lattice pattern; the unit cell of a triangular lattice is highlighted. Cartesian coordinates and the lattice directions used for calculations i.e. Γ - M and Γ - K are also depicted.

In triangular lattice pattern, the metallic cylinders are arranged periodically, the separation between rods is equal to the lattice constant, a, in Γ - K direction, while rods are $\sqrt{3}$ a apart from each other in Γ - M direction. The complex eigenvalue

problem is solved for wave vector $\vec{k}$, for a given frequency ω in the unit cell of triangular lattice array of copper cylinders embedded in air by setting periodic boundary conditions. In the dispersion diagram calculations, metallic photonic bands for triangular lattice are obtained over the unit cell, the region indicated by the black frame in Figure 5.10. The radius of the rods is $r = 0.2a$, where a is the lattice constant of the triangular pattern and is set at 50 μm.

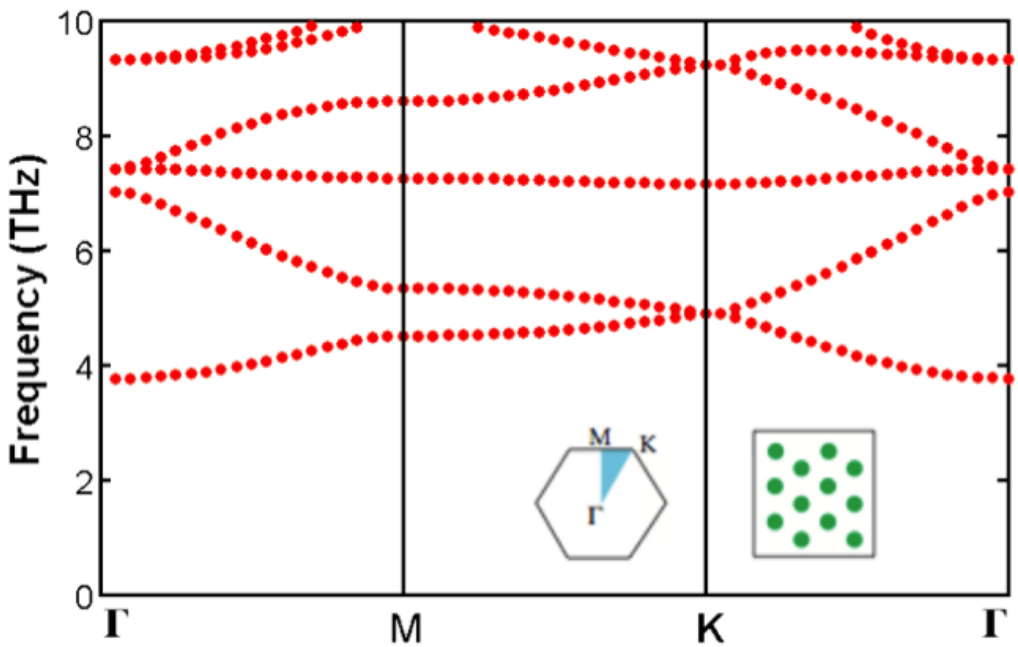

Figure 5.11: The photonic band structure of a triangular lattice of metal cylinders in vacuum for E-polarization. The PhC is characterized by a 50 μm lattice period in triangular lattice pattern with a radius of $0.2a$. The left inset shows the high symmetry points at the corners of the irreducible Brillouin zone, the right inset the triangular lattice pattern.

The calculated dispersion curves are plotted along high symmetry directions Γ, M, K as depicted in Figure 5.11 and Figure 5.12 for E-polarization and H-polarization respectively. In the dispersion diagram, the lowest frequency bands in THz range are drawn. The high symmetry points Γ, M and K from centre to near and far edge of the Brillouin zone are set as in Table 5.3.

The band diagram depicted in Figure 5.11, shows that there are two band-gaps for metallic photonic crystals. Similar to the square lattice case for E-polarization a cut-off frequency is observed. The first band-gap is wider than the second one and extends from 0 to 3.764 THz while the second band is very narrow and spans from 7.019 to 7.157 THz, corresponding to 0 - 0.673 $(\omega a/2\pi c)$ and 1.1698 - 1.928 $(\omega a/2\pi c)$, respectively. The width of this gap increases with increase in rod radius. In the band-gap diagram for H-polarization, neither band-gap nor cut-off frequency is observed as shown in Figure 5.12. The lowest frequency bands tend to zero at Γ point. A very small band-gap appears along the H-polarization direction for rod radius $r > 0.2a$.

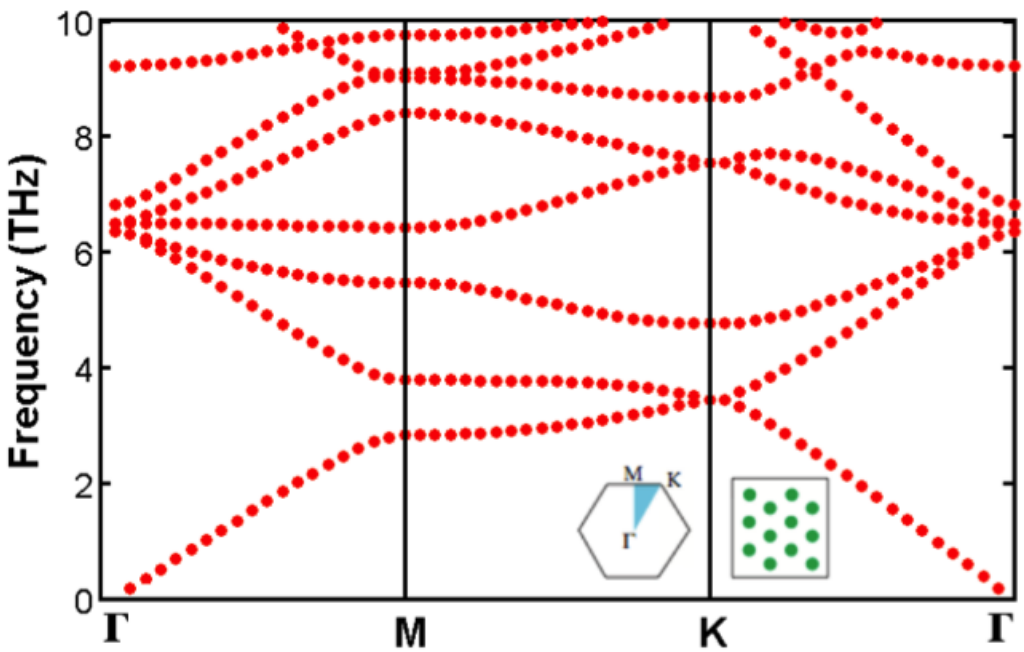

Figure 5.12: The photonic band structure of a triangular lattice of metal cylinders in vacuum for H-polarization. The PhC is characterized by a 50 μm lattice period in triangular lattice pattern with a radius of $0.2a$. The left inset shows the high symmetry points at the corners of the irreducible Brillouin zone, the right inset the triangular lattice pattern.

Figure 5.13 shows the electric field distribution of eigenmodes of the 6 lowest photonic bands of a triangular array of metallic cylinders at Γ point. The E-field is plotted for the modes from lowest frequency to highest labelled as a) 3.764 THz, b) 7.019 THz c) 7.415 THz d) 7.415 THz e) 9.313 THz and f) 9.313 THz. Similar to the square lattice eigenmodes, most of the electromagnetic field is concentrated between the metallic cylinders. As can be seen from the eigenmodes in the figure, a triangular lattice pattern supports symmetric (even) and anti-symmetric (odd) modes. Anti-symmetric modes appear for higher eigenfrequencies.

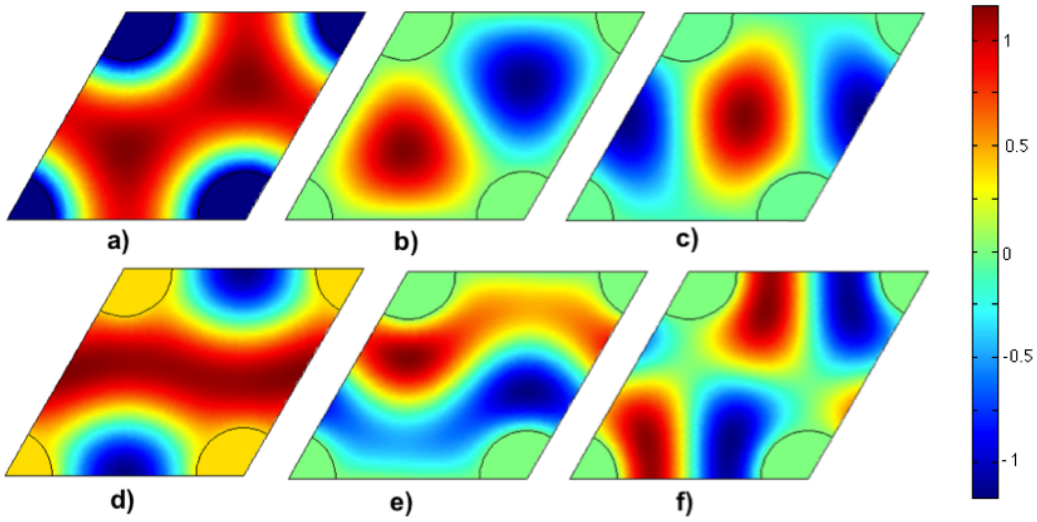

Figure 5.13: Electric field distribution of first 6 eigenmodes at Γ point of a triangular lattice of metallic circular cylinders for E-polarization. In the figures the maximum of electric field is normalized to unity.

We may distinguish the parity of modes whether even or odd from the electric field distribution of the bands. This helps in understanding the transmission characteristics of the metallic lattice structure which will be analysed in detail in the following section.

5.4 Transmission Characteristics of Metallic Photonic Crystals

After completing and validating the study for band-gap diagrams for metallic cylinders in square and triangular lattice, transmission and reflection spectra of square and triangular lattice arrays of copper cylinders embedded in air will be discussed in this section.

Transmission and filtering characteristics of 2D metallic photonic crystals without defects, and with point defect and Fabry-Perot type defects have been studied experimentally using THz-TDS and these experimental results have been compared with simulation results achieved by TMM results by Zhao and Grischkowsky (46). In this study, 5 columns of gold-coated SU-8 polymer cylinders embedded in air in square lattice with lattice constant of 160 μm and rod radius of $r = 0.22a$, and height of 80 μm have been exposed to a signal in the range of 0.5 - 3 THz. The structure is confined between a parallel plate waveguide separated by the height of the rods. We have carried out a series of simulations in order to obtain transmission characteristics of THz wave propagation within metallic structures in a similar manner to this work (46) with the lattice constants of 50, 75 and 100 μm and compared results for different rod sizes. It is necessary to determine the transmission properties of the band-gap crystal lattice, before characterizing the metallic crystal waveguides. For this task, both square lattice and triangular lattices are studied and transmission characteristics are obtained for each case and compared to the band-gap characteristics.

The following equation is solved to simulate wave propagation in 2D metallic

photonic crystals using Finite Element Method.

$$\nabla \times (\nabla \times E_z) - n^2 k_0 E_z \;=\; 0 \tag{5.20}$$

$$\varepsilon_r \;=\; n^2, \qquad \mu_r \;=\; 1, \qquad \sigma \;=\; 0$$

where n is the complex refractive index and k_0 is the free-space wave number. In this equation the dielectric function of metal is represented by permittivity instead of refractive index. As it is shown earlier, the conductivity is already taken into account through the Drude model relation; therefore in the equation conductivity is set to 0 to prevent any redundancy. In THz range, the metals such as copper, silver, gold, and aluminium have a relative permeability that is very close to unity (11).

Scattering parameters are utilized in order to obtain transmission and reflection coefficients. S-parameters are complex-valued, frequency dependent matrices describing the transmission and reflection of electromagnetic energy measured at different ports of devices like filters, antennas, waveguide transitions, transmission lines, etc. which are very well known in design and analysis of miccrowave components. S-parameters were originally introduced in transmission line theory and are defined in terms of transmitted and reflected voltage waves. All ports are assumed to be connected to matched loads, i.e. there is no reflection directly at a port.

For a device with n ports, S-parameters can be expressed as:

$$S = \begin{vmatrix} S_{11} & \cdots & S_{1n} \\ \vdots & \ddots & \vdots \\ S_{n1} & \cdots & S_{nn} \end{vmatrix}$$

where S_{11} is the voltage reflection coefficient at port 1, S_{12} is the voltage transmission coefficient from port 1 to port 2 etc. The time average power reflec-

tion/transmission coefficients are obtained as $|S_{ij}|^2$.

S-parameters used regarding reflection and transmission can be described as follows:

$$S_{11} = \sqrt{\frac{Power\ reflected\ from\ input\ 1}{Power\ incident\ on\ output\ 1}}$$

$$S_{21} = \sqrt{\frac{Power\ delivered\ to\ output\ 2}{Power\ incident\ on\ output\ 1}}$$

The incident and delivered powers are calculated using the $Poynting\ vector$. The Poynting vector defines the energy transported by an electromagnetic wave, which is expressed as:

$$\vec{S} = \vec{E} \times \vec{H} \tag{5.21}$$

The time average of the power flux for time harmonic fields is given by the Poynting vector:

$$\vec{S}_{av} = \frac{1}{2}\{\vec{E} \times \vec{H}^*\} \tag{5.22}$$

The amount of power flowing through a boundary is given by the normal component of the Poynting vector expressed as:

$$\vec{n} \cdot \vec{S}_{av} = \frac{1}{2}Re\{\vec{E} \cdot n \times \vec{H}^*\} \tag{5.23}$$

In order to obtain the outflow power at outputs, the Poynting vector can be directly

integrated along the boundary. Since only the electric field values are defined for the input wave, special considerations have to be taken for magnetic field. The normal vector is directed in negative z-direction in this study. So, for TM waves the following equality can be written,

$$\vec{E} \cdot n \times \vec{H}^* \;=\; -E_z H_y^* \tag{5.24}$$

TM waves also satisfy Faradays equation:

$$-j\beta E_z - j\omega\mu H_y \;=\; 0 \tag{5.25}$$

where ω is the angular frequency, μ is the permeability and β is the propagation constant. The electric field E_z is integrated at the input line of the waveguide. The incident power at input is therefore,

$$-\vec{n} \cdot \vec{S}_{av} \;=\; \frac{1}{2} Re\left(\frac{\beta}{\omega\mu} {E_z}^2\right) \tag{5.26}$$

To specify the absorbing boundary condition the propagation constant, β, of the wave needs to be considered by entering the correct propagation constant and to eliminate all the waves with their wave number in the propagating direction.

In order to calculate the modulus of the transmission or the reflection coefficient of the square lattice, four layers/periods of rods, and of the triangular lattice, five layers/periods of rods are used respectively.

Perfectly matched layers (PML) are used in order to prevent any reflections from the boundaries. A PML is not a boundary condition but an additional domain, where computational geometry is surrounded, absorbs incident electromagnetic waves

without any reflections. PML parameters are set to yield an impedance, where artificial absorbing material's anisotropic permittivity and permeability match the adjacent medium's material properties, so that no reflection occurs. In order to define a PML an absorbing layer with anisotropic material parameters are introduced (43).

$$\mu = \mu_0 \mu_r L \tag{5.27}$$

$$\varepsilon = \varepsilon_0 \varepsilon_r L \tag{5.28}$$

where L is a diagonal two rank tensor

$$L = \begin{bmatrix} L_{xx} & 0 & 0 \\ 0 & L_{yy} & 0 \\ 0 & 0 & L_{zz} \end{bmatrix} \tag{5.29}$$

where

$$L_{xx} = \frac{s_y s_z}{s_x} \tag{5.30}$$

$$L_{yy} = \frac{s_z s_x}{s_y} \tag{5.31}$$

$$L_{zz} = \frac{s_x s_y}{s_z} \tag{5.32}$$

A PML that absorbs waves traveling in a particular direction can be created by assigning suitable values to the complex-valued coordinate scaling parameters s_x, s_y, and s_z. For a PML that attenuates a wave traveling in the x direction these parameters are set as:

$$s_x = a - ib \tag{5.33}$$

$$s_y = 1 \tag{5.34}$$

$$s_z = 1 \tag{5.35}$$

where a and b are arbitrary positive real numbers.

The wave traveling some distance Δx through the PML will experience some loss in electric field intensity due to the presence of evanescent waves. The field value can be calculated using the equation $|E| = |E_0|e^{-bk_x\Delta x}$, where b is the imaginary s_x component, k_0 is the wave number, and Δx is the PMLs thickness in the direction the wave is traveling. To ensure a high enough electric field propagates through the PML, the user must ensure that the PML width is of the same order of magnitude as the wavelength being used.

The THz wave is incident from one side of the structure and transmission is calculated from the other side, in order to understand how much power is transmitted through or reflected by the structure. The direction of incident wave corresponds to Γ - X direction in crystal symmetry. The results should match with the band-gap diagram of corresponding lattice structure, since the band-gap diagrams are also another way of studying a structures reflectivity or transparency for a given direction. It is worth noting that the transmitted, reflected power or loss cannot be determined from band-gap diagrams.

In the following sections, the transmission, reflection and absorption of a square lattice and a triangular lattice are obtained for different lattice period and rod sizes.

5.4.1 Square Lattice

Transmission and reflection spectrum calculations of a metallic photonic crystal structure consisting of copper rods are carried out over a geometry shown in Figure 5.15. The computational domain is surrounded by PML boundaries. The left boundary in the computational domain where the wave is introduced to the structure

is considered as both an absorbing boundary and as the input boundary conditions. This boundary is set as an identity boundary pair in order to use single boundary for two sets of boundaries as source and destination domains. When there is an incoming field through the structure, multiple reflections back to the source boundary occur; therefore a PML boundary is set behind a source boundary to prevent the possibility of multiple reflections from the structure.

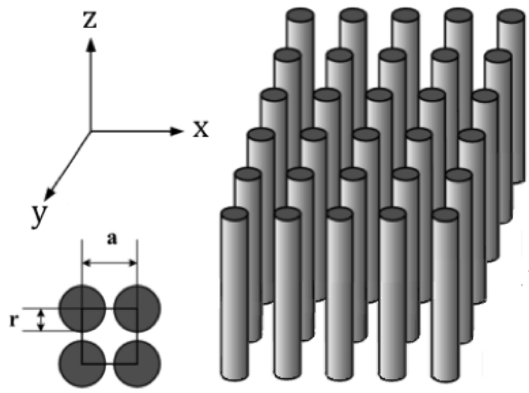

Figure 5.14: Schematic illustration of photonic crystal rods in square array, showing the lattice parameters r and a.

The input field expression can be written in terms of the coordinate variables and the k- vectors which are all dependent on the input angle variable as:

$$E_z = E_0 e^{i(k_x x + k_y y)} \tag{5.36}$$

$$k_x = k \cos\theta \tag{5.37}$$

$$k_y = k \sin\theta \tag{5.38}$$

where, E_0 is the amplitude of incident electric field, $k = 2\pi/\lambda$ is the wave number.

Using the electric field equation for E-polarization and similarly magnetic field for

H-polarization excitations can be solved for incident angle, θ, varying from 0° to 90°. The incident angle is defined as the angle between incident wave and the surface of the structure, so at the normal incident the incident angle is 90°.

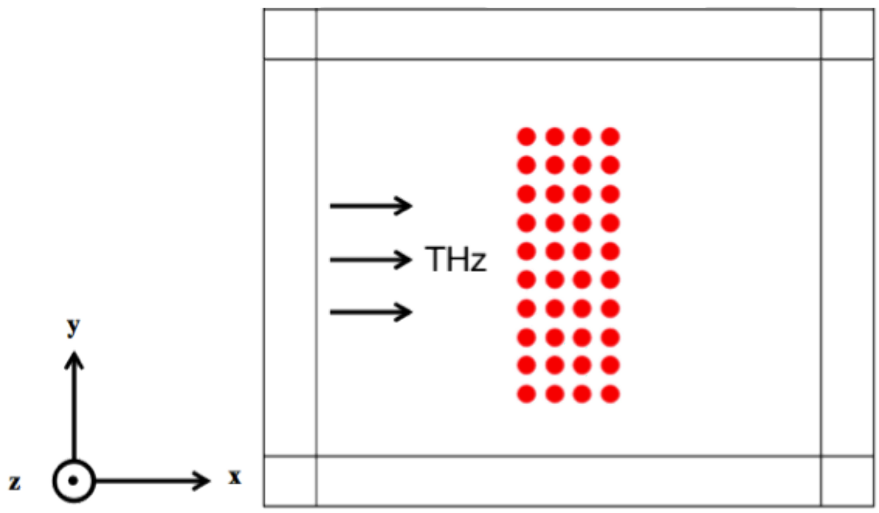

Figure 5.15: Schematic illustration of the geometry used in calculations. Red circles correspond to metallic cylinders. Perfectly matched layers are used to surround computational area in order to prevent reflections.

In order to validate our dispersion results, a transmission spectrum is calculated for transmission along Γ - X direction. Figure 5.16 a) shows the transmission spectra of 4 layers of rods in Γ - X lattice direction, b) band-gap diagram of square lattice structure in Γ - X direction. As seen from these figures, the dispersion figure and the transmission spectra figures are in good agreement. In the photonic band-gap diagram, the shaded areas show the band-gaps. The transmission is calculated for Γ - X direction and it exhibits the band characteristics in the given direction. These are the regions where propagation encounters stop-bands and pass-bands only for given direction. However, the band-gaps are defined as the stop-bands where propagation in any crystal direction is prohibited.

The position of transmission dips follows the same pattern with the band-gap dia-

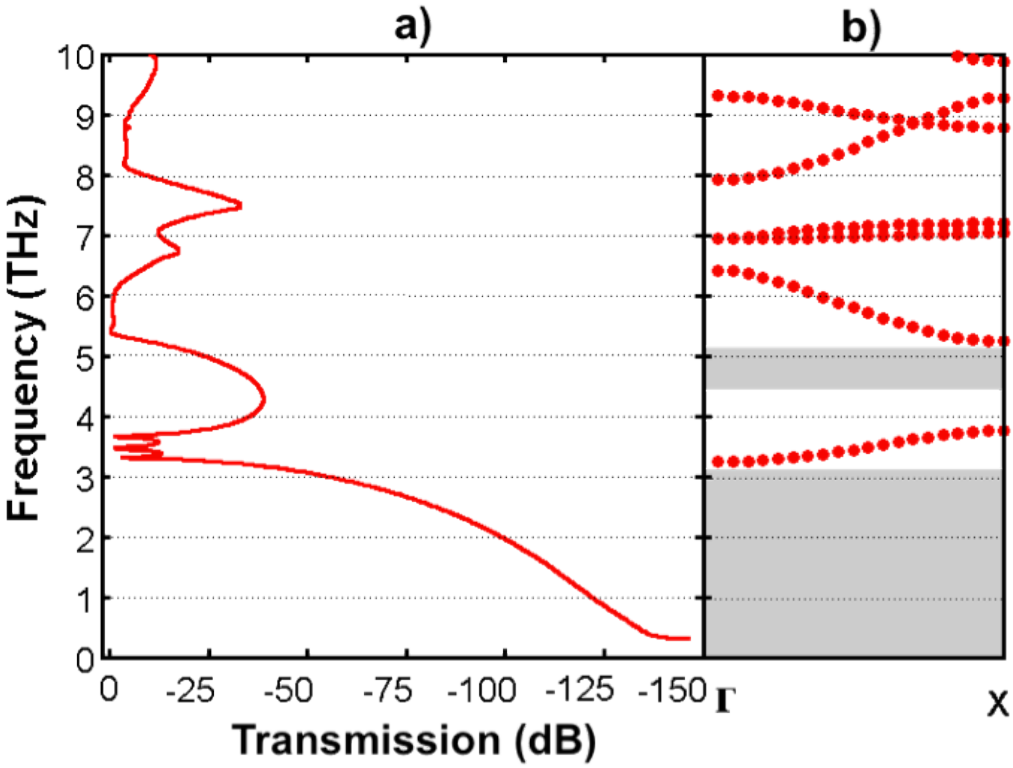

Figure 5.16: a) Transmission spectra are calculated for 4 layers of square lattice structure in Γ - X direction. b) Photonic band structure of a square lattice of metallic rods in Γ - X direction. The rods radius is $r = 0.2a$ where a = 50 μm. Shaded areas represent common photonic band-gaps for any crystal direction.

gram in Figure 5.16. Transmission occurs only at the frequencies where there are eigenmodes with wave vectors in the direction of the incident radiation Γ - X and in the band-gaps, transmission is very low. The position of dips corresponds to the point on Γ direction as the wave is at normal incidence. In the band gap the structure is reflective, therefore the transmission of the incident wave to other side of the crystal structure is very low. In the first band-gap range between 0 - 3.244 THz the transmission is as low as -150 dB. The frequency ranges where there is a wave transmission correspond to the pass-bands of square lattice structure for a given direction. The first pass-band is between 3.244 and 3.751 THz. The second band-gap in the given direction is between 3.751 THz and 5.236 THz, there are also two other

small band-gaps in the range of THz frequencies are between 6.415 THz and 6.933 THz and between 7.188 THz and 7.918 THz. The corresponding positions of the dips and peaks of the transmission results are in good agreement with the band-gap diagram.

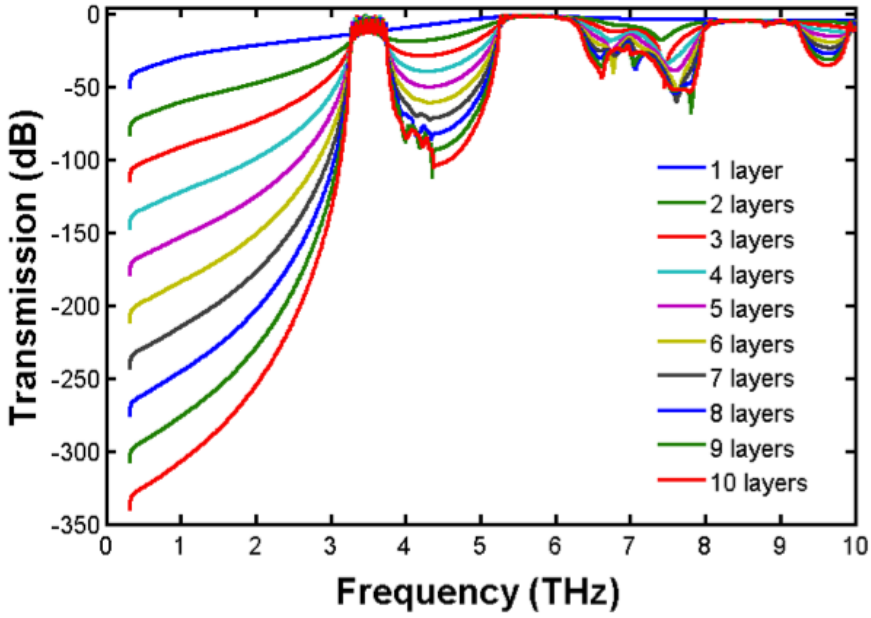

Figure 5.17: Transmission spectra of E-polarization of metallic photonic crystals in square lattice array for number of layers along the Γ - X direction.

The dependence of the number of layers on the module of the transmission is presented in Figure 5.17. The incidence of the wave is set in the Γ - X direction of the crystal, which corresponds to a normal incidence. As the number of layers increases, the wave transmission decreases. However this statement is only true for the band-gap of the structure. As the structure is transparent to the incident wave, transmission is not affected by the number of layers for the frequency ranges corresponding to the pass-band of the structure. As the number of layers increases, it affects the transmission level, not the bandwidth. This also explains why the bandwidth of the transmission is only linked to the band-gap characteristics of the structure. The change in the transmission level is negligible for a number of layers

greater than 5, even if the wave is incident at a right angle.

Figure 5.18 gives an illustration of the electric field propagation at normal incidence to square lattice crystal for two frequencies at 3 THz and 3.5 THz. Wave incidence corresponds to Γ - X direction of the structure. If the frequency is within a photonic band-gap as at 3 THz, the E-field rapidly decays inside the crystal otherwise it propagates through the array as depicted at 3.5 THz. In the figure the red and the blue parts show the positive and negative parts of the electric field. The scale on the right hand side shows the electric field value.

As it is shown in Figure 5.16, in transmission figures, high transmission corresponds to pass-band and transmission dips to the band-gaps of a photonic structure. conversely, in reflection figures high rejection obtained for frequencies correspond to the band-gap. For a complementary analysis, absorption is also calculated. In the figures, transmission and reflection are expressed in dB levels following the common use.

To complete the study of transmission spectrum for the square lattice structure, the frequency dependence of the reflection and the absorption is treated. When a wave is incident on a metallic photonic crystal structure, there are three possibilities. The incident wave is transmitted, reflected or absorbed by the structure. Some of the wave may be scattered in the structure but not necessarily inside the metallic rods; this condition is taken into consideration by the absorption. By expressing the transmission and reflection in linear scale the absorption is obtained from the following relation:

$$Absorption \; = \; 1 - T - R$$

where T is the transmission and R is the reflection. Absorption is expressed in linear scale.

First, transmission, reflection and absorption are obtained for a square lattice structure with lattice period of 50 μm and rod radii equal to $0.2a$, $0.3a$ and $0.4a$; in another words for rod radii of 10 μm, 15 μm and 20 μm. Figure 5.19 represents the transmission and reflection spectra along Γ - X direction, black dash line show results for H-polarization while red solid line shows the E-polarization.

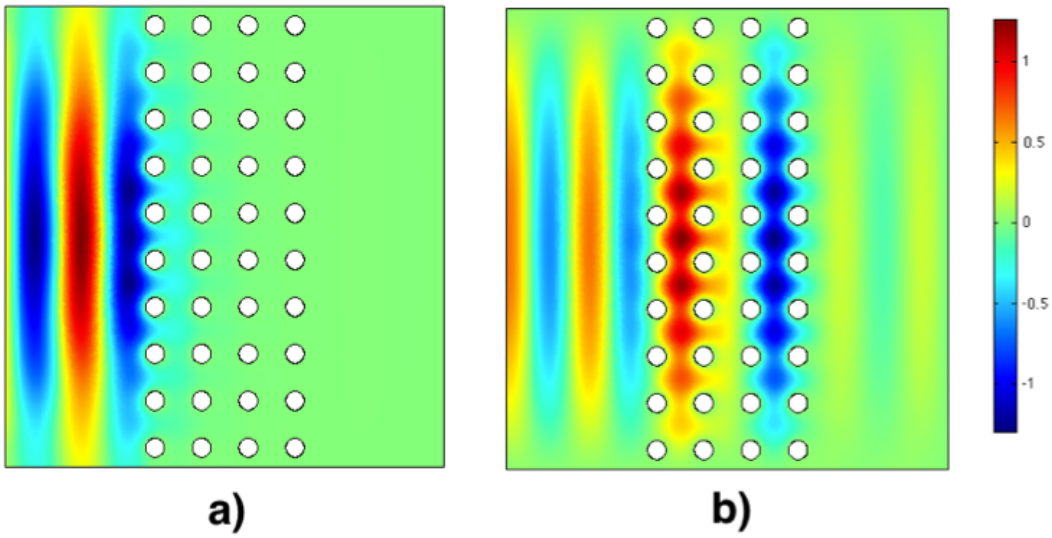

Figure 5.18: Electric field distribution in metallic photonic structure in square lattice array with rod radius is $0.2a$, where lattice constant a = 50 μm at a) 3 THz and b) 3.5 THz

In Figure 5.19 a) $r = 0.2a$, b) $r = 0.3a$ and c) $r = 0.4a$ the transmission of H-polarization is very low, around -50 dB, and decreases with the increase of rod size. Since transmission and reflection are both very low, absorption is very high for almost the whole range, and is equal to 1. In E-polarization, the transmission and reflection figures give a complementary view. The peaks in the transmission figure correspond to dips in the reflection figure, or vice versa. The absorption is

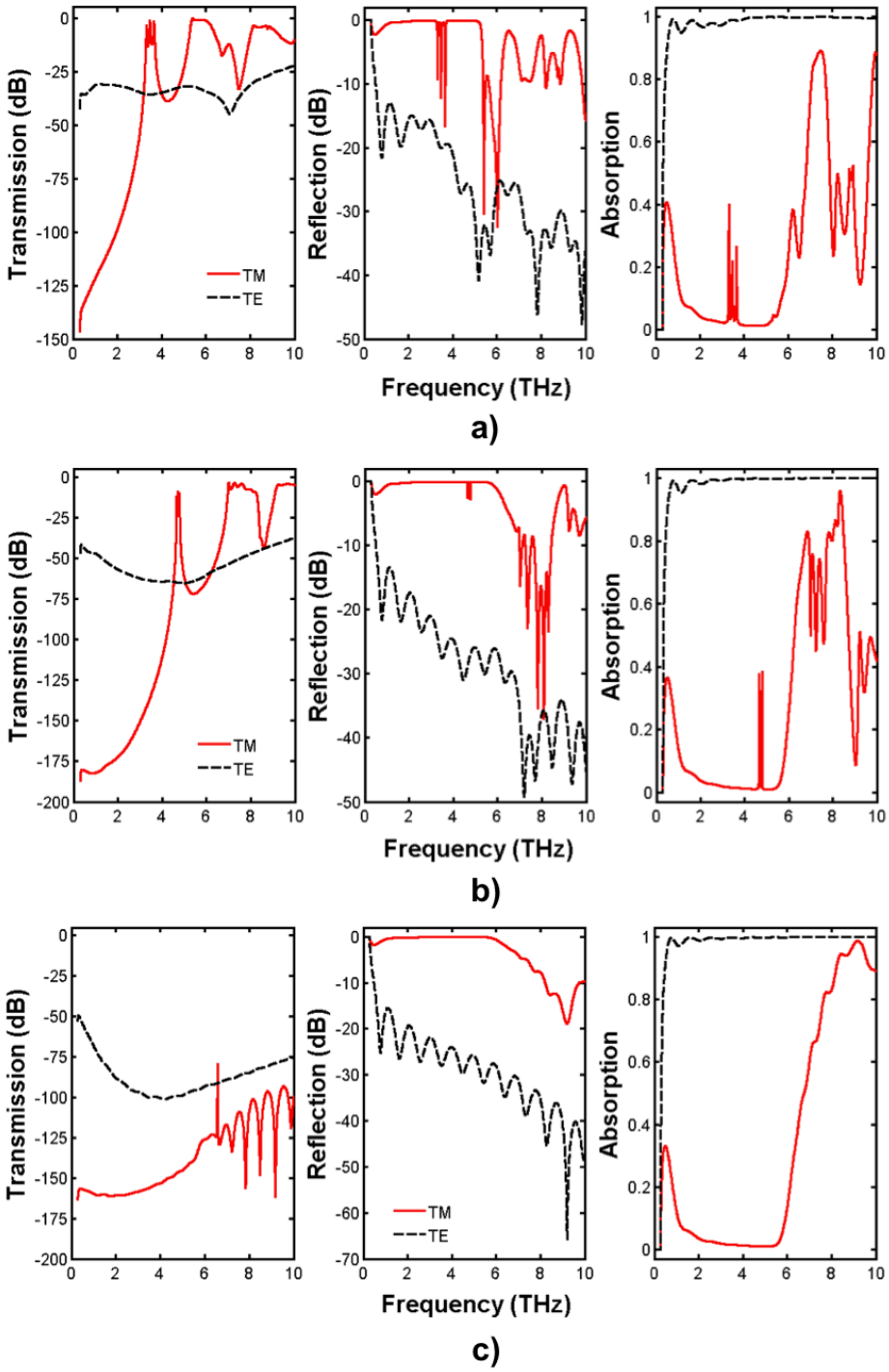

Figure 5.19: Transmission, reflection and absorption spectrum of E- and H-polarizations for 4 layers of metallic photonic crystal structure in square lattice array with lattice constant of 50 μm for different rod sizes along Γ - X direction. Transmission, reflection in dB scale and absorption in linear scale. Black dash line shows results for H-polarization while red solid line shows the E-polarization for a) $r = 0.2a$, b) $r = 0.3a$ and c) $r = 0.4a$

very low, below 10 % in the range between 1 - 5.7 THz, and beyond this point the absorption raises abruptly. This indicates either that waves penetrate inside the metallic material of the crystal or they are lost in the structure. If a threshold is set to -30 dB, the lowest transmissions are obtained between 0 and 3.227 THz and 0 - 4.635 THz for r/a equals to 0.2 and 0.3, respectively, which agrees with cut-off frequencies obtained in dispersion analysis. For r/a equals 0.4, transmission is very low, below -100 dB for almost whole the range except the peak at 6.58 THz, which corresponds to the small band opening between first and second band-gaps as previously seen in Figure 5.9. From the band-gap results, for this given ratio of 0.4, there is a broad band-gap including the whole THz range between 0 and 10.18 THz except the small pass-band between 6.582 and 6.595 THz. In Figure 5.19 a) in the reflection figure, there is a dip between 5.314 and 6.376 THz, after a high rejection. Absorption is quite low, below 5 % in the range between 1.887 and 3.277 THz, where minimum absorption of 1.203 % is obtained at 4.76 THz, and 3.696 - 5.524. The maximum absorption, 99.95 % is obtained at 7.78 THz. In Figure 5.19 b) the structure shows almost full rejection in the range of up to 6 THz, and on the transmission figure there is a small pass band in the 4.635 - 4.802 THz when -30 dB taken as a threshold. Another pass-band is between 6.807 and 8.385 THz, and 8.808 THz and higher. The corresponding positions of the dips and peaks of the transmission results are in good agreement with the band-gap diagram. The reflection decreases in the range of 6-9 THz with a minimum of -49.32 dB at 7.2 THz. The absorption is below 5 % between 1.807 and 4.64 THz except the narrow stop-band between 4.64 and 4.79 THz. In Figure 5.19 c) the transmission is very low. The range up to 6 THz is very suitable for wave guiding since most of the input signal is reflected from the structure and in this range absorption is also very low, below 5 % between 1.729 - 5.76 THz. The photonic crystal acts as almost a perfect reflector. On the other hand, for frequencies over 6 THz, despite the low transmission and decreasing reflection, absorption increases dramatically, even reaching a maximal absorption of 98.7 % for 9.2 THz.

We have examined the transmission characteristics of 4 layers of photonic crystal in square lattice pattern for E- and H-polarization. As expected from the band diagrams, while the crystal structure is completely transparent for H-polarization, it is reflective for E-polarization. This feature is very important to design certain devices like polarization filters. Within the frequency range of the pass-band of the structure with $r = 0.2a$ and $0.3a$ (Figure 5.19 a), Figure 5.19 b)) shows more than 30 dB transmission difference between E- and H-polarization.

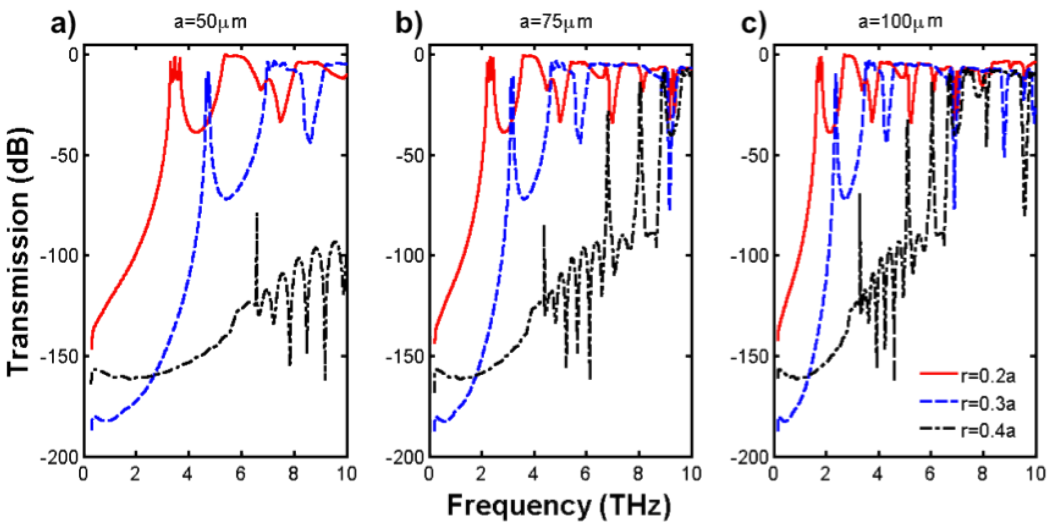

Figure 5.20: Transmission spectra of 4 layers of metallic photonic crystal structure in square lattice array for E-polarization Γ - X direction. Transmission is calculated for different lattice period a) 50 μm b) 75 μm c) 100 μm for rod radii equal to $0.2a$ (red solid line), $0.3a$ (blue dash line), $0.4a$ (black dash dot line).

According to scaling law, a photonic crystal structure can be scaled independently of their lattice period, and for this reason the dispersion diagram is often expressed in normalised frequencies. The size of pass- and stop-bands is inversely proportional to the lattice constant. Therefore, structure shows the same band-gap trend independent of the lattice period, but the size of gaps become smaller and the cut-off frequency for metallic structure decreases accordingly with the lattice constant

increase. These can be seen in Figure 5.20, for transmission spectra calculated with various lattice periods a) 50 μm b) 75 μm c) 100 μm for rod radii $r = 0.2a$ (red solid line), $r = 0.3a$ (blue dash line), and $r = 0.4a$ (black dash dot line). These figures show that the size of band-gaps decreases as the lattice constant value increases and the cut-off frequency is shifted to the lower frequencies. For instance, when -30 dB is taken as a threshold, the cut-off frequency of rod radius $r = 0.2a$, is 3.224 THz, 2.151 THz and 1.614 THz, when lattice constant is fixed to 50 μm, 75 μm, and 100 μm, respectively. Similarly, for $r = 0.3a$, the cut-off frequencies become 4.634 THz, 3.091 THz, and 2.319 THz.

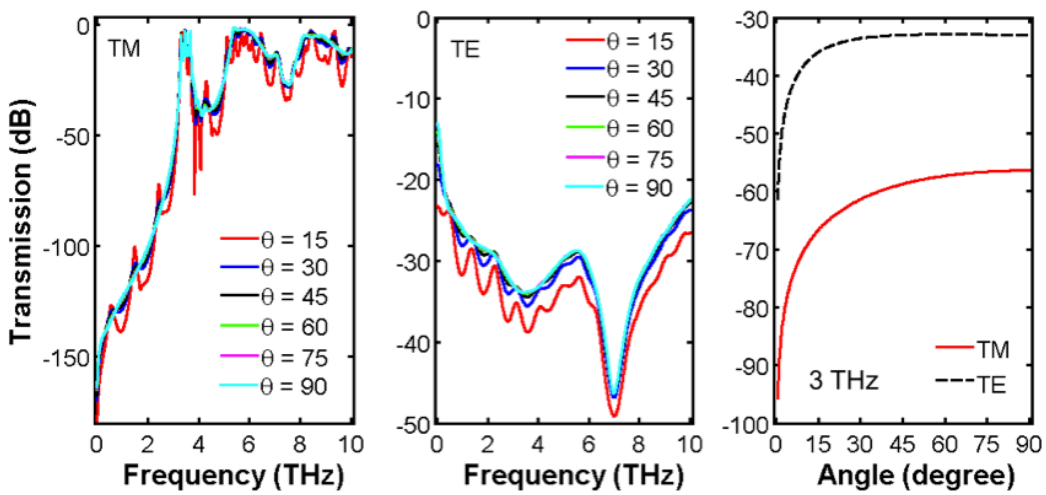

Figure 5.21: Transmission spectra of 4 layers of metallic photonic crystal structure in square lattice array with rod radius is 0.2a, where lattice constant a = 50 μm for a) E- and b) H-polarizations in Γ - X direction for various incident angles. c) Transmission is as function of incident angles for E- and H-polarizations at 3THz.

As seen in Figure 5.21, transmission spectra are calculated for various incident angles for E- and H-polarizations. Transmission is lower for small incident angles and shows some oscillations. In both E- and H-polarizations, transmission increases with increasing incident angles. Transmission takes its highest value when the wave is incident on the structure at a normal incidence as in Figure 5.21 c), where trans-

mission is calculated as a function of incident angle at 3 THz. At the normal incidence the incident angle is 90°. No transmission is calculated when angle between incident wave and the surface of the structure is 0°.

5.4.2 Triangular Lattice

In order to verify dispersion results, a transmission spectrum is calculated for transmission along Γ - M and Γ - K directions for E-polarization. Comparison has been carried out in a similar way to square lattice structures. Figure 5.22 a) shows the transmission spectra of a triangular lattice array consisting of 5 layers with lattice constant of 50 μm and rod radius of $0.2a$ along Γ - M and Γ - K lattice directions, and b) shows the dispersion diagram of a triangular lattice for the same size metallic photonic crystal along high symmetry points. The dispersion figure and the transmission spectra figures are matching, and positions of the dips and peaks of the transmission spectra can be followed from the dispersion diagram in Figure 5.22 b). In the dispersion diagram, the shaded areas show the band-gap for any crystal direction. The transmission is calculated for Γ - M and Γ - K directions and it exhibits the band characteristics in the given direction. The positions of transmission dips follow the same pattern as the band-gap diagram. In the band gap, the structure is reflective; therefore the transmission of incident wave to the output side of the crystal structure is very low. The dispersion diagram represents the 6 lowest bands for metallic cylinders in triangular lattice array in the THz range. It can be seen from the transmission spectra that transmission occurs only at the frequencies where there are eigen-modes with wave vectors in the direction of the incident radiation. However, as mentioned earlier, for this structure not all the modes are symmetric. For instance, in Γ - M direction the 3rd mode and in Γ - K direction 2nd and 4th modes are anti-symmetric. The symmetric (even) modes are represented by red dots while anti-symmetric (odd) modes are represented by red open dots. When

two modes are intersecting at the high symmetry points, mode crossing occurs. The two modes intersecting at a symmetry point have group velocities of different sign. One of the modes is symmetric and the other one is anti-symmetric. The symmetric (or anti-symmetric) input field can only couple with symmetric mode (or anti-symmetric). The uncoupled modes lead to low transmission (47).

Both in Γ - M and Γ - K directions, the first band-gap range between 0-3.764 THz has a transmission as low as -175 dB. The frequency ranges where there is a wave transmission correspond to the pass-bands of triangular lattice structure for given direction. In Γ - M direction, the first pass-band is between 3.764 and 4.507 THz. The second band-gap in the given direction is between 4.507 THz and 5.311 THz, and there are also two other small band-gaps in the range of THz frequencies between 7.019 THz and 7.253 THz and between 8.594 - 9.313 THz. In the range between 7.253 THz and 7.415 THz low transmission is due to anti-symmetric modes. In Γ - K direction, the first pass-band is between 3.764 and 4.901 THz. Even though modes appear in 4.901 - 7.019 THz and 7.157 - 9.288 THz ranges, there are dips in transmission spectra, since the input field cannot couple with these anti-symmetric modes with respect to the Γ - K direction. The peak between 7.019 and 7.157 THz in the transmission figure corresponds to the small pass-band in the dispersion figure.

In Figure 5.23 transmission spectra are shown for an electromagnetic polarization along the rods in Γ - M direction and an incidence angle normal to the direction of the metallic rods. The transmission decreases for frequencies falling within the stop-band of the structure as the number of layers increases. On the other hand, as the structure is completely transparent in pass-band frequencies, these ranges are not affected by the number of layers as shown for square lattice.

Transmission, reflection and absorption spectra of 2D metallic photonic crystals

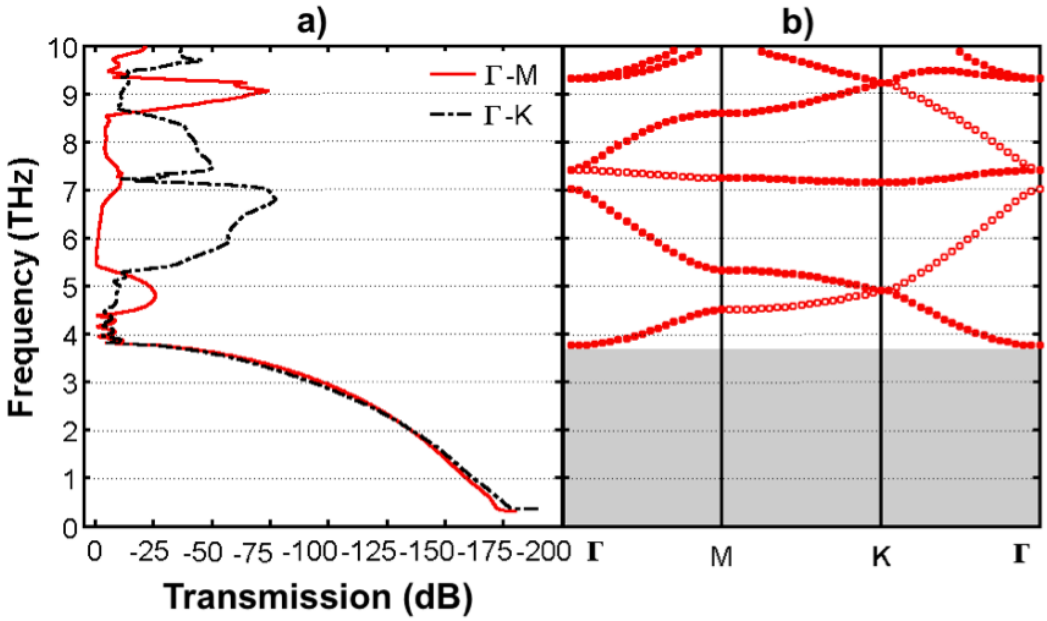

Figure 5.22: a) Transmission spectra are calculated for 5 layers of triangular lattice structure in Γ - M and Γ - K directions. b) Photonic band structure of a triangular lattice of metallic rods in E-polarization. The rod radius is $r = 0.2a$ where a = 50 μm. Shaded areas represent common photonic band-gaps in any crystal direction for E-polarization.

in triangular lattice array with respect to two lattice directions are shown in Figure 5.24 and Figure 5.25 for Γ - M direction, and Figure 5.26 and Figure 5.27 for Γ - K direction. The wave propagation direction is normal to the interfaces and two polarizations have been considered, H-polarization and E-polarization. Transmission, reflection and absorption are obtained for triangular lattice structure with lattice period, a, of 50 μm and rod radius 0.2a, 0.3a and 0.4a; in another words for rod radii of 10 μm, 15 μm and 20 μm. Calculations have been carried out in two lattice directions. The transmission, reflection and absorption spectra along Γ - M direction are represented in Figure 5.24, Γ - K represented in Figure 5.25. Black dash line shows results for H-polarization while red solid line shows the E-polarization.

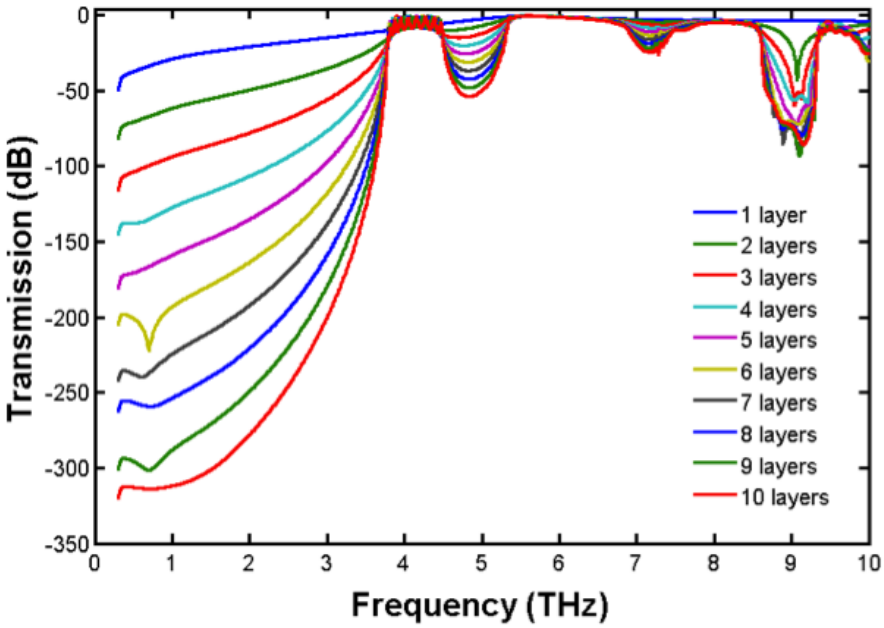

Figure 5.23: Transmission spectra of E-polarization of metallic photonic crystals in triangular lattice array for number of layers along the Γ - M direction. The rods radius is $r = 0.2a$ where lattice constant, a = 50 μm.

The cut-off frequencies increase and the bandwidth of pass-band becomes narrower with the radius of metallic rods. When the rod radius is large enough, the structure has a broad band-gap that covers the whole THz frequency range.

Similar to the square lattice case, the transmission of H-polarization is very low in triangular lattice case, as seen in Figure 5.24 and Figure 5.25, for rod radius $r = 0.2a$. It ranges between -25 dB and -50 dB in Γ - M and slightly lower in Γ - K direction, and as the rod size increases transmission decreases. Similarly absorption is very high, almost 1 for the whole THz range. As expected the reflection is very low and decreases as the frequency increases.

For E-polarization, in Figure 5.24 a) the absorption is below 10 % between 1.153 and 5.617, except for the interval between 3.794 and 4.413 THz which corresponds to the pass-band of the structure. This can be observed from transmission and re-

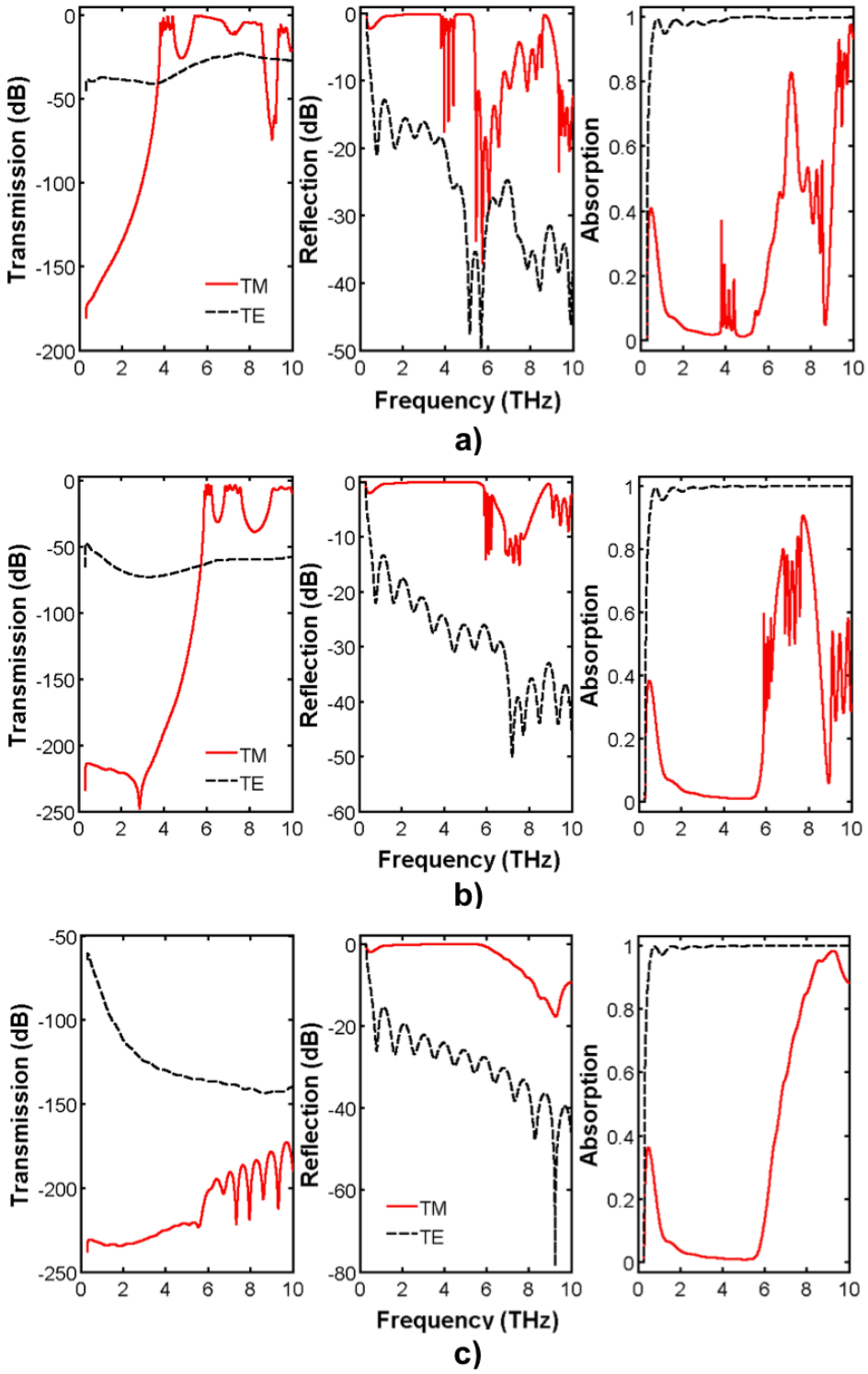

Figure 5.24: Calculated transmission, reflection in dB scale and absorption in linear scale for 5 layers of triangular lattice structure in Γ - M direction for E- and H-polarizations for rod radii a) $r = 0.2a$, b) $r = 0.3a$ and c) $r = 0.4a$, where lattice constant $a = 50\mu m$.

flection spectra. In transmission spectra, the first band-gap is between 0 - 3.803 THz, and this range corresponds to a high reflection between 0 - 3.802 THz. These values match well with the cut-off frequency 3.764 THz obtained from the dispersion diagram earlier. There are two other band-gaps from 4.443 THz to 5.28 THz and from 9.06 THz to 9.363 THz. In Figure 5.24 b) a broad band-gap is seen from the transmission spectrum between 0-5.946, which fits 5.873 THz, the cut-off frequency obtained from dispersion figure. Very high reflection is obtained in the range between 1.02 THz and 5.881 THz. In the broad band-gap, the absorption is very low, below 10 % in the range between 1.116 THz and 5.758 THz and even below 5 % between 1.842 THz and 5.643 THz. In Γ - M direction for rod radius $r = 0.4a$, and the lattice constant a = 50 μm, from the dispersion diagram the cut-off frequency is calculated as 10.53 THz, which means the whole THz range is within the band-gap of the triangular lattice. The transmission varies between -170 dB and -240 dB in Figure 5.24 c). The absorption is very low, below 10 % in the range between 1.05 - 5.915 THz and below 5 % between 1.794 - 5.768 THz. In this range, the absorption and transmission is very low, and the structure acts as almost a perfect reflector showing very high reflectivity. Beyond 6 THz the absorption abruptly rises as in the previous cases and reaches the maximum 98.26 % at 9.3 THz. The total absorption increases and the reflection is reduced as most of the waves are absorbed/lost in the structure.

The characteristics of triangular lattice structure in Γ - K direction are slightly different from those in Γ - M direction. The transmission spectra for E-polarization shows that stop bands are formed for waves incident along the Γ - K direction, while in the Γ - M direction the structure exhibits pass-bands. For instance when Figure 5.24 a) and Figure 5.25 a) are compared, in Γ - K direction there is a broad stop-band between 5.27 and 8.68 THz except for the peak at 7.22 THz. In the Γ - M direction on the other hand there is abroad pass-band in the same interval at the peak. The transmission in Γ - M direction is slightly lower. Moreover, as seen from

Figure 5.25, the absorption is always low in the interval 1 - 3 THz, instead of very low absorption in 1 - 6 THz, followed by a peak. The peaks correspond to the high transmission and low reflection. The transmission for rod radius $r = 0.4a$ is lower in Γ - K direction than that in Γ - M direction. As distinct from the square lattice, for lattice periods of 75 and 100 μm transmission increases abruptly and pass-bands appear.

In Γ - K direction, the transmission spectra show important characteristics: the pass-bands corresponding to the intervals between 3.737 and 5.396 THz in Figure 5.25 a) and between 5.875 and 6.813 THz in Figure 5.25 b) are separated distinctively by the neighboring regions in terms of transmission level. At least 50 dB difference is observed between the pass and stop bands. The structure can be used as a band-pass filter with the advantage of small size and weight.

In Figure 5.25 a) reflection is lower in the range between 3.569 and 5.411 THz corresponding to the frequency range of the first pass-band, and in this range the absorption increases up to 80 % from 3 THz to 5.974 THz. Similarly, in Figure 5.25 b) reflection is lower in the range between 3.58 and 5.197 THz corresponding to the frequency range of the first pass-band, and in this range the absorption increases up to 80 % from 3.251 THz to 5.76 THz, however, in this range the transmission is very low. The first pass-band occurs later in frequency and in this range absorption is relatively lower, mostly below 40 %. In Figure 5.25 c) the drop in reflection between 3.634 and 5.57 THz corresponds to the high absorption between 3.298 and 6.266 THz where transmission is very low.

In Figure 5.26 transmission spectra in Γ - M direction for E-polarization are calculated for several lattice periods a) 50 μm b) 75 μm c) 100 μm for rod radii $r = 0.2a$ (red solid line), $r = 0.3a$ (blue dash line), and $r = 0.4a$ (black dash dot line). These figures show that the size of band-gaps decreases as the lattice constant value

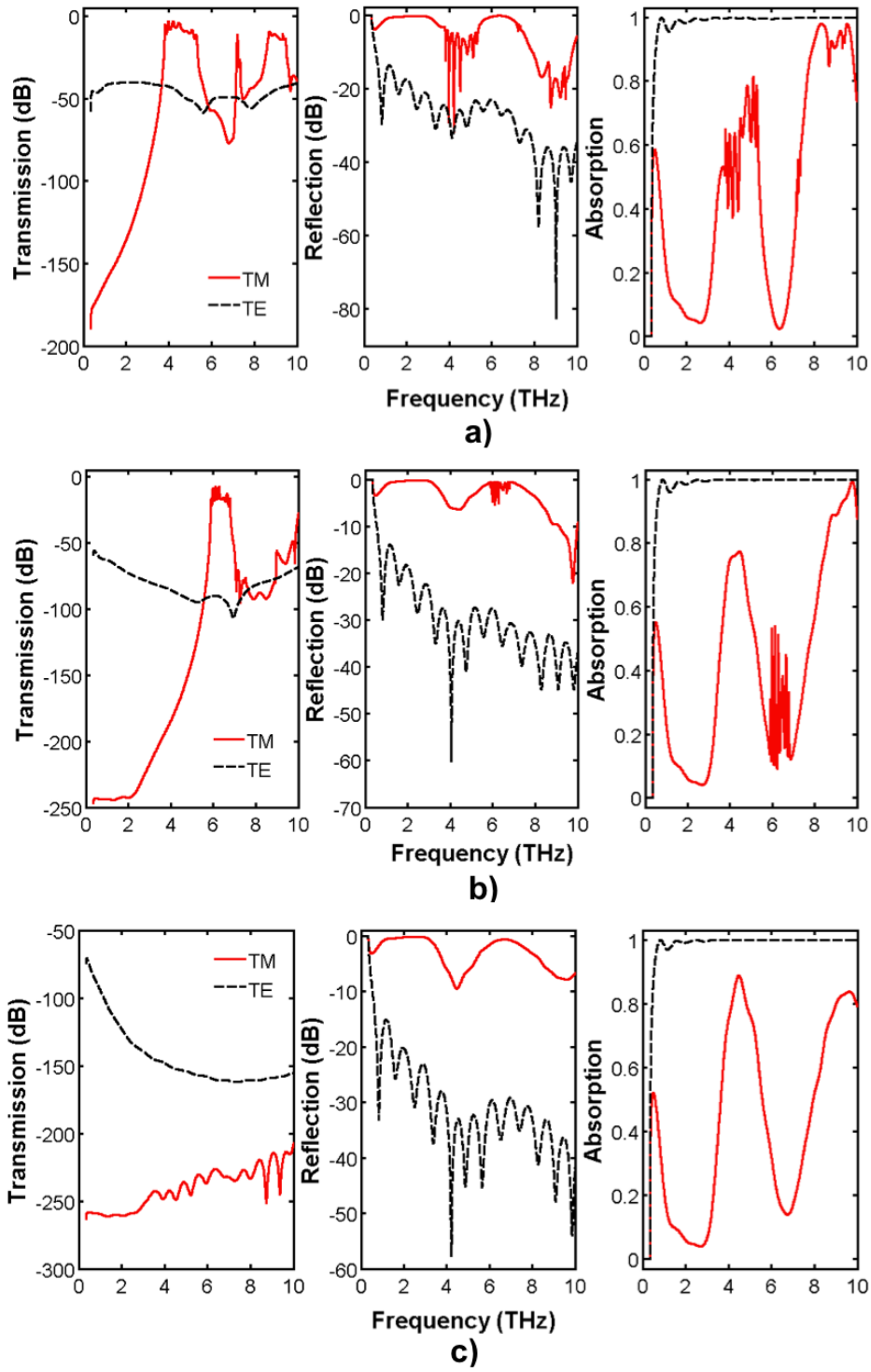

Figure 5.25: Calculated transmission, reflection in dB scale and absorption in linear scale for 5 layers of triangular lattice structure in Γ - K direction for E- and H-polarizations for rod radii a) $r = 0.2a$, b) $r = 0.3a$ and c) $r = 0.4a$, where lattice constant a = 50 μm.

increases and the cut-off frequency value is shifted to the lower frequencies. For instance, when 30 dB is taken as a threshold, the cut-off frequency for rod radius $r = 0.2a$, is 3.746 THz, 2.499 THz and 1.875 THz, when the lattice constant is fixed to 50 μm, 75 μm, and 100 μm, respectively. Similarly, for $r = 0.3a$, the cut-off frequencies become 5.858 THz, 3.908 THz, and 2.932 THz. This result is different from the square lattice case, where the cut-off frequency obtained for $r = 0.4a$, was 7.018 THz for a = 75 μm and 5.271 THz for a = 100 μm.

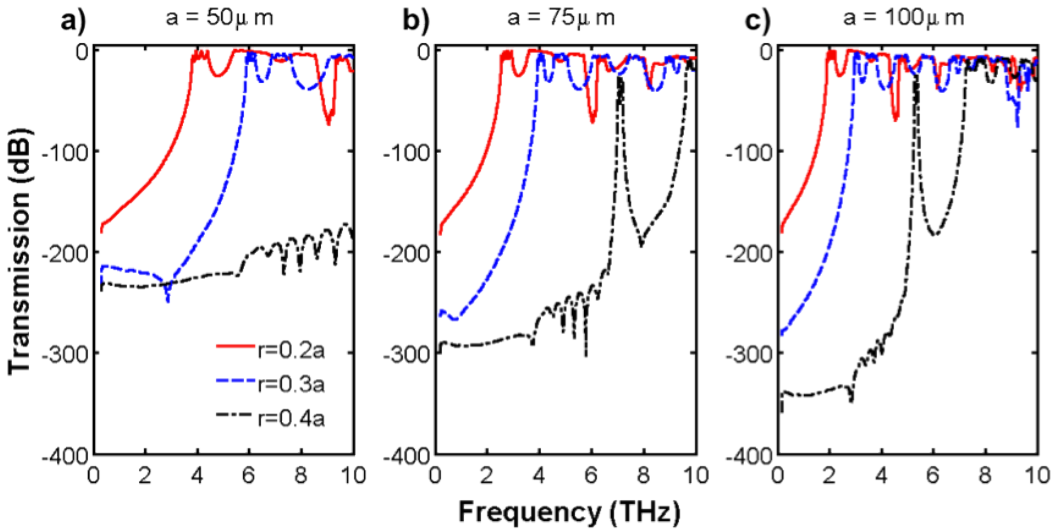

Figure 5.26: Transmission spectra of 5 layers of metallic photonic crystal structure in triangular lattice array for E-polarization $\Gamma - M$ direction. Transmission is calculated for different lattice period a) 50 μm. b) 75 μm. c) 100 μm with rod radii 0.2a (red solid line), 0.3a (blue dash line), 0.4a (black dash dot line).

Figure 5.27 shows the transmission spectra in Γ - K direction for E-polarization for several lattice periods of a) 50 μm b) 75 μm c) 100 μm with $r = 0.2a$ (red solid line), $r = 0.3a$ (blue dash line), and $r = 0.4a$ (black dash dot line). When -30 dB is taken as a threshold, the cut-off frequency of rod radius $r = 0.2a$, is 3.737 THz, 2.493 THz and 1.871 THz, when lattice constant is fixed to 50 μm, 75 μm, and 100 μm, respectively. Similarly, for $r = 0.3a$, the cut-off frequencies become

5.875 THz, 3.92 THz, and 2.941 THz. As distinct from the square lattice case, for $r = 0.4a$, a cut-off frequency appears within THz frequency range for a = 75 μm and a = 100 μm at 7.04 THz and 5.3 THz, respectively. The centre frequency of pass-band as well as the position of the cut-off is shifted to the lower frequency and the size of bandwidth become narrower. For instance, for $r = 0.3a$, the centre frequencies of pass-bands are 6.344 THz, 4.2325 THz and 3.1750 THz for a) 50 μm b) 75 μm and c) 100 μm, respectively. The corresponding bandwidths taken at -30 dB-threshold are 0.9380, 0.6250 and 0.4680 THz. By adjusting the rod radius and the lattice period the band edges can therefore be tuned.

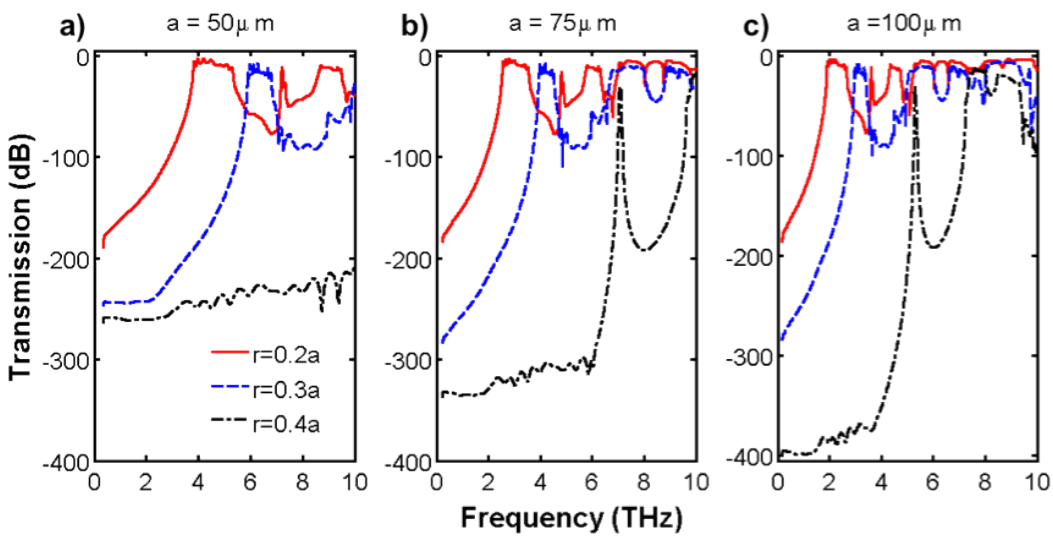

Figure 5.27: Transmission spectra of 5 layers of metallic photonic crystal structure in triangular lattice array for E-polarization Γ - K direction. Transmission is calculated for different lattice period a) 50 μm. b) 75 μm. c) 100 μm with rod radii $0.2a$ (red solid line), $0.3a$ (blue dash line), $0.4a$ (black dash dot line).

In Figure 5.28 a) and b) the transmission spectra are obtained at various incident angles and in Figure 5.28 c) the transmission is presented as a function of incident angles at 3 THz for triangular lattice structure in Γ - M and Γ - K directions. The incident angle θ is varied in steps of 15° to 90° and for each value of θ the transmis-

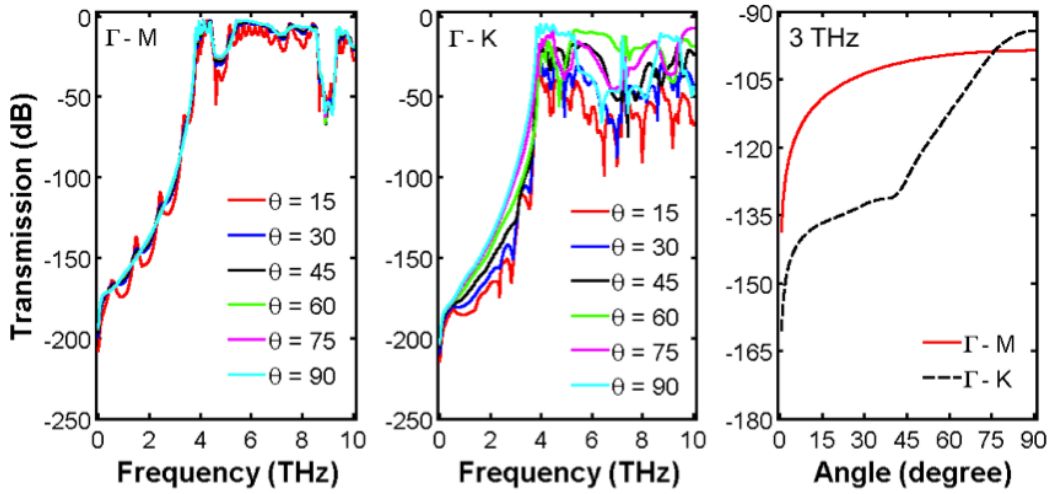

Figure 5.28: Transmission spectra of 5 layers of metallic photonic crystal structure in triangular lattice array with rod radius is $0.2a$, where lattice constant a = 50 μm for E-polarization in a) Γ - M and b) Γ - K directions for various incident angles. c) Transmission is as function of incident angles for Γ - M and Γ - K directions at 3 THz.

sion spectrum is calculated. At different incident angles, the transmission spectra in Γ - M direction are close to each other, however, at small incident angles the transmission figures show some ripples. In Γ - K direction, the transmission is more sensitive to incident angle than Γ - M direction. The transmission increases as the incident angle gets closer to normal incidence as seen in Figure 5.28 c). However, in the range from 5.3 to 8.6 THz, at 60° incident angle, the structure has a higher transmission than at normal incidence.

In this section the transmission, reflection and absorption behaviour of square and triangular lattice arrays of copper rods in air for E- and H-polarization for THz frequencies has been discussed and compared to band-gap diagrams that were obtained in the previous section. Photonic crystal waveguides confine and guide the wave within the band-gap frequencies of the structure. To be able to understand the band-gap behaviour of the structure is important for waveguide analysis. In the

next section, for THz frequencies, we calculate the transmission spectra of metallic photonic crystals by varying the rod size to obtain a map that shows transmission spectra as a function of both frequency and rod size. These maps help to determine optimum parameters to design a waveguide device.

5.5 Band-Gap Maps

As presented previously, the width of band-gap and its position in the spectrum depends on many parameters, i.e. lattice pattern, polarization, refractive index of constituent materials and angle of incidence. Photonic band-gap maps provide visual information about the band-gap size and positions in order to determine optimal geometrical lattice parameters. Band-gap maps are simply obtained by plotting the band-gap positions found within a dispersion diagram as a function of rod radius, r/a, and the dimensionless frequency $\omega a/2\pi c$. The optimal lattice parameters and frequency range that gives the largest band-gap can be obtained by replacing the lattice constant with the real value for the structure. By following the photonic band-gap maps, devices based on photonic crystals can be designed and engineered to suit the needs of the optical applications.

In order to obtain a photonic band-gap map, instead of computation of the band structure, transmission spectra of square and triangular lattice array structures are calculated for various values of rod radii r/a (Figure 5.29, Figure 5.30). Ins this way, frequency dependency and metallic losses are taken into account. These band-gap maps provide information regarding the possibility of determining metallic photonic crystal parameters at which the photonic crystal has maximum reflection or partially transmits the radiation within the THz frequencies. The photonic band-gap map of the 2D metallic photonic crystals with rods arranged in square lattice or triangular lattice array with lattice constant a = 50 μm is obtained by changing

the rod radius' value and calculating the corresponding transmission spectrum. The band gap-map is obtained only for E-polarization since metallic photonic crystals have much wider band-gaps for E-polarization than H- polarization, as previously demonstrated.

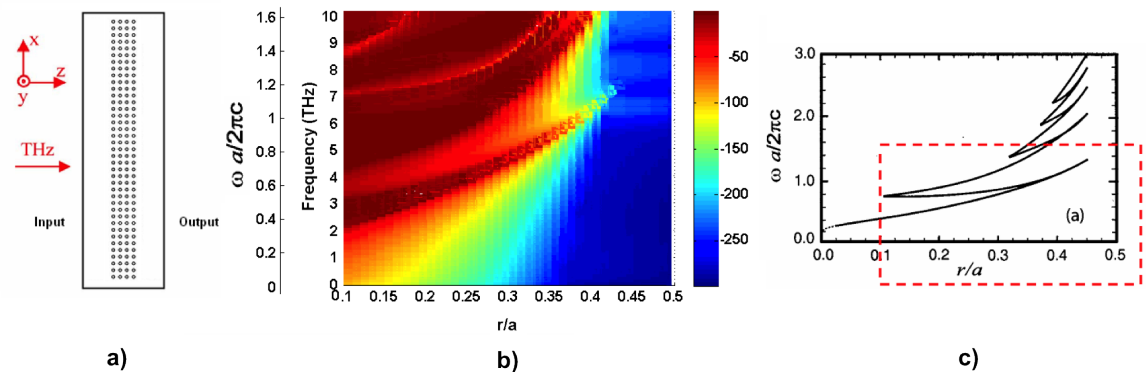

Figure 5.29: a) The schematic illustration and direction of incoming wave of simulated structure, b) band-gap map of metallic photonic crystal structure in square lattice pattern, c) the gap-map for metallic photonic crystal in square lattice, courtesy of Smirnova *et al.* (38).

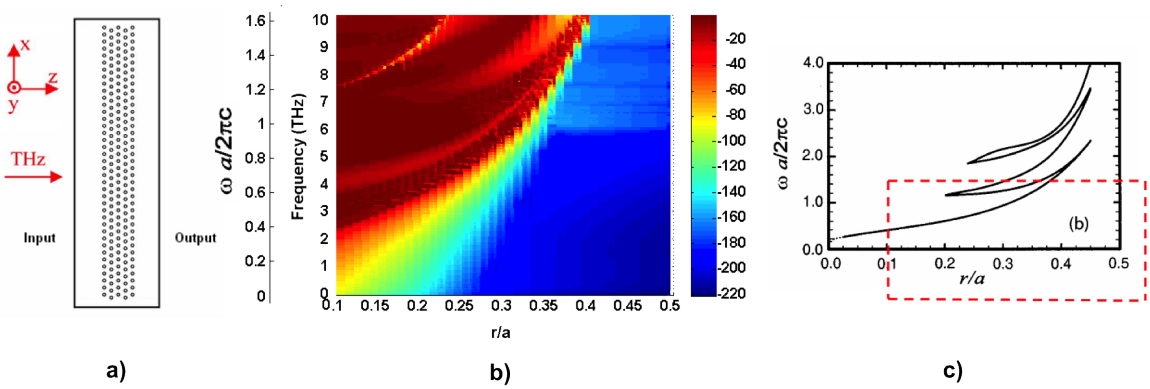

Figure 5.30: a) The schematic illustration and direction of incoming wave of simulated structure, b) band-gap map of metallic photonic crystal structure in triangular lattice pattern, c) the gap-map for metallic photonic crystal in triangular lattice, courtesy of Smirnova *et al.* (38).

The band-gap maps using the transmission spectra of 2D metallic photonic band-

gap structures formed by 5-layers of square lattice array in Γ - X and 5 layers of triangular lattice in Γ - M directions are obtained by varying the radii between $0.1a$ (5 μm) and $0.49a$ (24.5 μm).

For a triangular lattice the Γ - M direction is preferred for calculation of band-gap maps. The positions of stop- and pass-bands calculated in the transmission spectra of Γ - M direction gives much closer results to actual band-gap characteristics than transmission in Γ - K direction.

Figure 5.29 and Figure 5.30 b) show the band-gap map of square lattice and triangular lattice structure with a colour scale on the right side showing the transmission levels in dB. On the y-axis of the figure, both frequencies and the normalised frequencies are shown to compare our results with the published results in (38). Figure 5.29 and Figure 5.30 c) present the band-gap map of metallic photonic crystals calculated by using finite difference method (38). The band-gap map figures that we have obtained with transmission spectra using FEM show an excellent agreement with the band-gap maps studied previously (38; 48). If we take -30 dB as the threshold, we can obtain band-gap maps of metallic structures similar to the highlighted part in figures represented in Figure 5.29 c) and Figure 5.30 c). In the regions, transmission is below threshold value and the structure is highly reflective, corresponding to the band-gaps.

When investigating the band-gap map in Figure 5.29 b), it is seen that such a photonic crystal has more than one photonic band-gap in the range of radius from $0.1a$ to $0.4a$. On the other hand, in Figure 5.30 b) the photonic band-gap map exhibits more than one band-gap in the range of radius from $0.2a$ to $0.4a$. In both figures, the structures have a band-gap that exists for the whole THz frequency range for radius $r > 0.4a$. Hence, in order to achieve high reflection with a small number of columns, using a square or triangular lattice the ratio r/a must be greater or equal

to 0.4.

5.6 Conclusion

In summary, we employ FEM to calculate the transmission, reflection, absorption and dispersion characteristics of 2D metallic photonic crystals arranged in square and triangular lattice form for E- and H-polarization. There is a strong correlation between the key features i.e. positions of the dips and peaks of a transmission spectra and the corresponding photonic-band structure. In our study, a comparison between dispersion and transmission results show perfect match and consistency internally and with previous studies. The modal field symmetry characteristics have been discussed. The position and width of the photonic band gap are well reproduced in transmission spectra. Wave polarization, incidence direction and the size of rods affect the transmission. In both square and triangular lattice arrays, transmission spectra show that the size of the band-gap increases with increasing rod radius. As expected from the band diagrams, while the crystal structure is completely transparent for H-polarization, it is reflective for E-polarization. Metallic photonic crystal system are very sensitive to polarization direction. This kind of structure can be used as a polarization filter. Between E- and H-polarization there is more than 30 dB transmission difference for the structure is consisting of 4 - 5 layers of metallic cylinders, in which E- and H-polarization waves are discriminated perfectly. Both square and triangular lattice structures show large photonic band gaps in the THz band. The transmission spectra of triangular lattice structures for E-polarization in Γ - K direction show pass-bands separated distinctively by the adjacent stop-bands. The width and the position in terms of frequency of pass-bands can be tuned by lattice period and rod radius. The structure can be used as a band-pass filter. These filters possess the advantages of high performance, low weight, small size and low cost.

The major challenges in studies of THz systems are the generation of THz signals at high power levels and low-loss and the development of low-dispersion waveguides in order to transmit THz waves efficiently. For some other applications that require high power, metals become the more reasonable choice since they have high melting points. Given the absorption level and dispersion that metallic photonic crystals have in optical ranges, they may not be suitable to built optical devices. In the THz range, absorption and dispersion levels are not as high as in optical ranges and this makes metallic structures more attractive for high power THz applications. Using the optimized number of layers and lattice parameters for metallic structures studied in this chapter, effective metallic photonic crystal waveguides can be formed by introducing a line defect for the use of THz applications. A detailed analysis will be presented in the next chapter.

References

[1] P. Drude, *The Theory of Optics, translated by CR Mann and RA Millikan*. Longmans, Green, and Co., 1902.

[2] M. A. Ordal, R. J. Bell, J. Alexander, L. L. Long, and M. R. Querry, "Optical properties of fourteen metals in the infrared and far infrared: Al, co, cu, au, fe, pb, mo, ni, pd, pt, ag, ti, v, and w.," *Applied Optics*, vol. 24, pp. 4493–4499, Dec. 1985.

[3] C. F. Bohren and D. R. Huffman, *Absorption and scattering of light by small particles*. Wiley, 1983.

[4] M. A. Ordal, L. L. Long, R. J. Bell, S. E. Bell, R. R. Bell, J. Alexander, and C. A. Ward, "Optical properties of the metals al, co, cu, au, fe, pb, ni, pd, pt, ag, ti, and w in the infrared and far infrared," *Applied Optics*, vol. 22, pp. 1099–1119, Apr. 1983.

[5] M. Born and E. Wolf, *Principles of Optics: Electromagnetic Theory of Propagation, Interference and Diffraction of Light*. CUP Archive, Feb. 2000.

[6] J. Lourtioz, H. Benisty, D. Pagnoux, V. Berger, J. Gerard, and D. Maystre, *Photonic crystals: towards nanoscale photonic devices*. Springer, 2008.

[7] A. M. Fox, *Optical properties of solids*. Oxford University Press, May 2010.

[8] K. Inoue and K. Ohtaka, *Photonic crystals: physics, fabrication, and applications*. Springer, 2004.

[9] A. D. Rakic, A. B. Djuriic, J. M. Elazar, and M. L. Majewski, "Optical properties of metallic films for Vertical-Cavity optoelectronic devices," *Applied Optics*, vol. 37, no. 22, pp. 5271–5283, 1998.

[10] I. El-Kady, M. M. Sigalas, R. Biswas, K. M. Ho, and C. M. Soukoulis, "Metallic photonic crystals at optical wavelengths," *Physical Review B*, vol. 62, p. 15299, Dec. 2000.

[11] S. Lucyszyn, "Investigation of anomalous room temperature conduction losses in normal metals at terahertz frequencies," *Microwaves, Antennas and Propagation, IEE Proceedings* -, vol. 151, pp. 321– 329, Aug. 2004.

[12] Y. Tsuji and M. Koshiba, "Finite element method using port truncation by perfectly matched layer boundary conditions for optical waveguide discontinuity problems," *Journal of Lightwave Technology*, vol. 20, pp. 463–468, Mar. 2002.

[13] W. J. Kim and J. D. O'Brien, "Optimization of a two-dimensional photonic-crystal waveguide branch by simulated annealing and the finite-element method," *Journal of the Optical Society of America B*, vol. 21, pp. 289–295, Feb. 2004.

[14] N. Kono and Y. Tsuji, "A novel Finite-Element method for nonreciprocal Magneto-Photonic crystal waveguides," *Journal of Lightwave Technology*, vol. 22, p. 1741, July 2004.

[15] J. D. Joannopoulos, *Photonic crystals: molding the flow of light*. Princeton University Press, Feb. 2008.

[16] E. R. Brown and O. B. McMahon, "Large electromagnetic stop bands in metallodielectric photonic crystals," *Applied Physics Letters*, vol. 67, p. 2138, 1995.

[17] D. F. Sievenpiper, M. E. Sickmiller, and E. Yablonovitch, "3D wire mesh photonic crystals," *Physical Review Letters*, vol. 76, p. 2480, Apr. 1996.

[18] J. S. McCalmont, M. M. Sigalas, G. Tuttle, K. . Ho, and C. M. Soukolis, "A layerbylayer metallic photonic bandgap structure," *Applied Physics Letters*, vol. 68, pp. 2759–2761, May 1996.

[19] E. Ozbay, B. Temelkuran, M. Sigalas, G. Tuttle, C. M. Soukoulis, and K. M. Ho, "Defect structures in metallic photonic crystals," *Applied Physics Letters*, vol. 69, pp. 3797–3799, Dec. 1996.

[20] A. Kao, K. A. McIntosh, O. B. McMahon, R. Atkins, and S. Verghese, "Calculated and measured transmittance of metallodielectric photonic crystals incorporating flat metal elements," *Applied Physics Letters*, vol. 73, p. 145, 1998.

[21] C. Jin, B. Cheng, B. Man, D. Zhang, S. Ban, B. Sun, L. Li, X. Zhang, and Z. Zhang, "Two-dimensional metallodielectric photonic crystal with a large band gap," *Applied Physics Letters*, vol. 75, p. 1201, 1999.

[22] M. M. Sigalas, R. Biswas, K. M. Ho, C. M. Soukoulis, and D. D. Crouch, "Waveguides in three-dimensional metallic photonic band-gap materials," *Physical Review B*, vol. 60, no. 7, p. 4426, 1999.

[23] S. Fan, P. R. Villeneuve, and J. D. Joannopoulos, "Large omnidirectional band gaps in metallodielectric photonic crystals," *Physical Review B*, vol. 54, p. 11245, Oct. 1996.

[24] Z. Li, I. El-Kady, K. Ho, S. Y. Lin, and J. G. Fleming, "Photonic band gap effect in layer-by-layer metallic photonic crystals," *Journal of Applied Physics*, vol. 93, p. 38, 2003.

[25] A. R. McGurn and A. A. Maradudin, "Photonic band structures of two- and three-dimensional periodic metal or semiconductor arrays," *Physical Review B*, vol. 48, p. 17576, Dec. 1993.

[26] D. R. Smith, S. Schultz, N. Kroll, M. Sigalas, K. M. Ho, and C. M. Soukoulis, "Experimental and theoretical results for a twodimensional metal photonic bandgap cavity," *Applied Physics Letters*, vol. 65, pp. 645–647, Aug. 1994.

[27] M. M. Sigalas, C. T. Chan, K. M. Ho, and C. M. Soukoulis, "Metallic photonic band-gap materials," *Physical Review B*, vol. 52, p. 11744, Oct. 1995.

[28] E. Ozbay and B. Temelkuran, "Reflection properties and defect formation in photonic crystals," *Applied Physics Letters*, vol. 69, p. 743, 1996.

[29] V. Kuzmiak, A. A. Maradudin, and F. Pincemin, "Photonic band structures of two-dimensional systems containing metallic components," *Physical Review B*, vol. 50, p. 16835, Dec. 1994.

[30] M. Bayindir, E. Cubukcu, I. Bulu, T. Tut, E. Ozbay, and C. M. Soukoulis, "Photonic band gaps, defect characteristics, and waveguiding in two-dimensional disordered dielectric and metallic photonic crystals," *Physical Review B*, vol. 64, p. 195113, Oct. 2001.

[31] A. J. Ward, J. B. Pendry, and W. J. Stewart, "Photonic dispersion surfaces," *Journal of Physics: Condensed Matter*, vol. 7, pp. 2217–2224, Mar. 1995.

[32] J. B. Pendry and A. MacKinnon, "Calculation of photon dispersion relations," *Physical Review Letters*, vol. 69, p. 2772, Nov. 1992.

[33] N. A. Nicorovici, R. C. McPhedran, and L. C. Botten, "Photonic band gaps for arrays of perfectly conducting cylinders," *Physical Review E*, vol. 52, p. 1135, July 1995.

[34] K. Sakoda, N. Kawai, T. Ito, A. Chutinan, S. Noda, T. Mitsuyu, and K. Hirao, "Photonic bands of metallic systems. i. principle of calculation and accuracy," *Physical Review B*, vol. 64, p. 045116, July 2001.

[35] T. Ito and K. Sakoda, "Photonic bands of metallic systems. II. features of surface plasmon polaritons," *Physical Review B*, vol. 64, July 2001.

[36] O. Takayama and M. Cada, "Two-dimensional metallo-dielectric photonic crystals embedded in anodic porous alumina for optical wavelengths," *Applied Physics Letters*, vol. 85, p. 1311, 2004.

[37] M. Qiu and S. He, "A nonorthogonal finite-difference time-domain method for computing the band structure of a two-dimensional photonic crystal with dielectric and metallic inclusions," *Journal of Applied Physics*, vol. 87, pp. 8268–8275, June 2000.

[38] E. I. Smirnova, C. Chen, M. A. Shapiro, J. R. Sirigiri, and R. J. Temkin, "Simulation of photonic band gaps in metal rod lattices for microwave applications," *Journal of Applied Physics*, vol. 91, p. 960, 2002.

[39] E. Moreno, D. Erni, and C. Hafner, "Band structure computations of metallic photonic crystals with the multiple multipole method," *Physical Review B*, vol. 65, p. 155120, Apr. 2002.

[40] J. Arriaga, A. J. Ward, and J. B. Pendry, "Order-N photonic band structures for metals and other dispersive materials," *Physical Review B*, vol. 59, p. 1874, Jan. 1999.

[41] L. Khee Lam, M. Mat Jafri, and S. Aziz Khan, "Dielectric slab photonic crystals containing metallic components for e polarization mode," *Applied Physics Research*, vol. 2, no. 2, p. p17, 2010.

[42] M. Ustyantsev, L. Marsal, J. Ferr-Borrull, and J. Pallars, "Effect of the dielectric background on dispersion characteristics of metallo-dielectric photonic crystals," *Optics Communications*, vol. 260, pp. 583–587, Apr. 2006.

[43] COMSOL Multiphysics, 3.5a, *User's Guide and RF Module User's Guide*. COMSOL AB, 2009.

[44] M. Qiu and S. He, "Guided modes in a two-dimensional metallic photonic crystal waveguide," *Physics Letters A*, vol. 266, pp. 425–429, Feb. 2000.

[45] A. Ward, *Transfer Matrices Photonic Bands and Related Quantities*. PhD thesis, Imperial College, University of London, 1996.

[46] Y. Zhao and D. R. Grischkowsky, "2-D terahertz metallic photonic crystals in Parallel-Plate waveguides," *IEEE Transactions on Microwave Theory and Techniques*, vol. 55, pp. 656–663, Apr. 2007.

[47] Z. Jian, J. Pearce, and D. M. Mittleman, "Two-dimensional photonic crystal slabs in parallel-plate metal waveguides studied with terahertz time-domain spectroscopy," *Semiconductor Science and Technology*, vol. 20, pp. S300–S306, July 2005.

[48] Y. Kokubo, T. Kawai, and I. Ohta, "Photonic crystal waveguides with inner metal coated posts at millimeter-wave frequency range," in *Microwave Conference, 2004. 34th European*, vol. 3, pp. 1137–1140, IEEE, Oct. 2004.

Chapter 6

LINEAR DEFECTS IN 2D METALLIC PHOTONIC CRYSTALS

This chapter is focused on the study of guided modes and on the transmission properties of two-dimensional metallic photonic crystal waveguides realized by introducing line defects in 2D metallic photonic crystals. A line defect along the structure can be achieved by removing row(s) of rods (1). The main objective is to have a better understanding of transmission losses in order to design an optimal waveguide structure that gives the lowest transmission loss. We numerically investigate the band structure and guided modes for metallic photonic crystal waveguides based on square and triangular lattice arrangements of cylindrical rods in air. Following the guided modes in dispersion diagrams, and comparing the transmission results, the optimal design parameters are obtained. We show that the guided modes appear in the band-gap of structure and can be used to guide waves within the waveguide. All the calculations are carried out by using FEM. As discussed in the previous chapter, copper crystals have shown highest reflectivity compared with various high

conductivity metals such as gold, silver and aluminium. Transmission spectra results show that copper gives the highest transmission with less attenuation for longer waveguides. The attenuation is as low as 0.057774 dB/mm for square lattice waveguides and 0.10007 dB/mm for triangular lattice waveguides.

By examining the guided modes in the dispersion diagram, we may find some explanations for the trend of losses in the transmission spectra and find an optimal design for 2D metallic photonic crystal waveguide for THz range.

6.1 Introduction

In our computational investigation, Maxwells equations are solved in order to simulate wave propagation in a given waveguide design surrounded with non-reflecting boundary conditions. This waveguide channel is considered to only allow transmission of light in TM mode (E-polarization), in which the electric field is parallel to the rod axis. The EM wave confinement is provided using the contrast between metal and vacuum permittivities. In addition, metallic rods in the analysed waveguide arrays exhibit a frequency dependent dielectric constant. In order to calculate the frequency dependent complex dielectric constant of metallic materials, based on the Drude model, which was explained in detail in the previous chapter, is used. Dispersion characteristics as well as the transmission characteristics are investigated. We show how a simple structure of metallic photonic crystals can be used to guide broadband THz radiation with very high performance, including low loss and negligible group velocity dispersion. The attenuation due to the conductivity losses is low for frequencies up to 6 THz. The behaviour of the wave propagation on a metallic photonic crystal shows high reflectance on metal surface rather than absorption. Copper has the highest reflectivity among metals such as gold, silver and aluminium at THz frequencies.

As already known for the band-gap frequencies of the lattice, wave propagation is prohibited inside the photonic crystal structure. Using this, waveguides can be formed that work with a high transmission for the band-gap frequencies. The wave is simply confined in the gap separating the photonic crystal structure.

Waveguides are one of the most used optical integrated circuit components. Waveguides are used to transfer electromagnetic waves from one component to another providing the interconnection in the system. In a photonic crystal waveguide, line defects exhibit waveguide modes in the band gap of photonic crystal. As no wave will be propagated through the photonic crystal structure, waves can be confined in a waveguiding channel where the wall of the waveguide is formed by the photonic crystal. As a result, if the frequencies fall within the photonic band-gap of photonic crystal, waves can be guided with minimal losses. The line defect waveguides are named after the number of rows removed from the photonic crystal structure as WN waveguides, where N represents the number of rows missing, i.e. W1, W2, W3 etc.

In this chapter, waveguide structures based on metallic cylinders in air formed in square and triangular lattice patterns are introduced. For both square lattice and triangular lattice waveguides we have carried out two studies: dispersion and transmission analysis of waveguides. In the dispersion analysis, dispersion diagrams for waveguides are obtained and guided modes are discussed. In transmission analysis, transmission, reflection and absorption spectra are obtained for each case and results are compared with the dispersion diagrams to determine the waveguide modal properties. Numerical simulations are carried out on commercially available software based on the Finite Element Method (FEM) in 2D and 3D. Only the E-polarization (TM modes) band gap is considered here since there are no band gaps found for the H-polarization (TE modes).

6.2 Dispersion Analysis

In the previous chapter, photonic band-gaps for metallic photonic crystals were discussed. To study the properties of photonic band gap materials it is important to find the bands of frequencies where the propagation of the electromagnetic waves is prohibited in all the directions. A band-gap diagram is obtained solving the eigen-value problem for wavevectors, at fixed frequencies. 2D photonic crystals are structures with a transverse periodicity (x-y plane) and a longitudinal uniformity (z-axis). The calculations are carried out over a unit-cell, which represents the symmetry of the periodic photonic crystal structure. When a line-defect is introduced to the photonic crystal structure, a waveguide is formed and modes may localize in the gap formed by the line-defect. Guided modes propagate inside the line defect since electromagnetic waves cannot penetrate into the photonic crystal. A guided mode is characterized by an evanescent wave in the direction perpendicular to the Bloch vector. The dispersion relation $\omega(\vec{k})$ gives the information on the guiding modes along the propagation direction, and this can be compared with the mode profiles and transmission characteristics.

The dispersion diagrams of the guided modes of photonic crystal waveguides is obtained by supercell approach (2). The smallest region in the photonic crystal waveguide that repeats throughout the structure is selected as a supercell, which is a layer of photonic crystal waveguide that contains the defect. The supercell represents the symmetry of waveguide structure and this approach is used in the dispersion diagram calculations, in a similar way to the unit cell used in band gap diagram calculations for photonic crystal. The size of the supercell should be large enough in order to ensure that the coupling between adjacent supercells is negligible. The dispersion relation is calculated by means of FEM, for the given supercell, using the reciprocal primitive vectors and the Bloch vectors described in earlier chapters.

In this section, guided modes in a two-dimensional metallic photonic crystal waveguide formed with two types of lattice pattern, square lattice and triangular lattice waveguides, are discussed. In a square lattice structure waveguide line defects are introduced along the Γ - X direction, while in a triangular lattice the waveguide lies along the Γ - K direction. Dispersion characteristics of square lattice waveguides are investigated for two conditions: when one and two rows of rods are removed to form W1 and W2 waveguide, respectively. On the other hand, triangular lattice waveguides will be considered for two conditions: W1 and W3 waveguides, where one and three rows of rods are omitted, respectively.

We avoid presenting the dispersion diagram in normalised frequencies where frequencies are scalable with respect to the lattice constant value. Since our interest is focused only on THz frequencies and due to the frequency dependence of material which may result in some discrepancies, the dispersion diagram is presented in real frequency values. For the dispersion diagrams the computations are carried out with the following parameters: the lattice constant is 50 μm, the rods radius r = 10 μm (0.2a). Since the refractive index contrast of high conductivity metals such as gold, silver, aluminium and copper and air is on the order of 10^5, the dispersion diagram is not sensitive to the refractive index difference. In the calculation we have characterized the waveguide dispersion diagram based on copper rods embedded in air.

6.3 Square Lattice Waveguide

Two types of metallic photonic crystal waveguide based on square lattice arrangement are considered here: W1 and W2 waveguides. The width of a WN waveguide in square lattice array is $w = (N + 1)a - 2r$, where N is the number of removed

rows. Therefore, the main difference between W1 and W2 geometries is the width of the waveguide. In the W2 waveguide, the waveguide width is a lattice constant wider than that of the W1 waveguide. On the other hand, removing more rows results in multimode guiding.

Computation of the dispersion diagram of a 2D photonic crystal waveguide is carried out over a supercell to determine modal properties of the waveguide. We consider a supercell of the geometry in the x-y plane as highlighted in Figure 6.1 to represent the symmetry of the periodic waveguide section including the defect. The dimensions of the supercell are as follows: the width is 11 or 12 lattice constant long for W1 and W2 waveguides, respectively, where the rod(s) in the middle is(are) omitted. There are 5 rods on each side of the defect and the height of the supercell is equal to lattice constant.

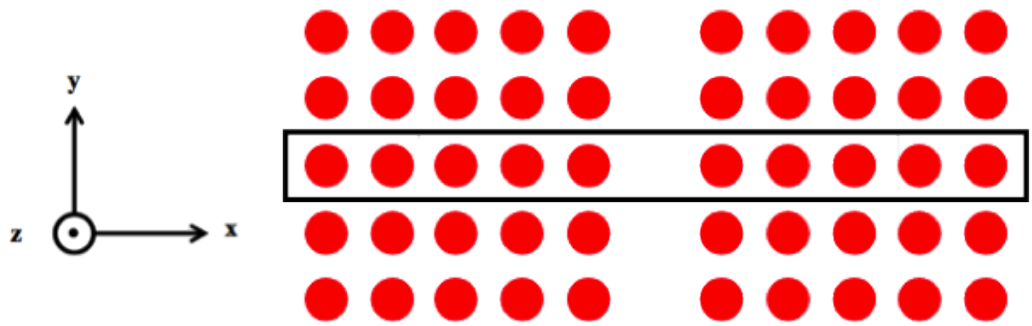

Figure 6.1: Schematic illustration of single line defect (W1) photonic crystal waveguide in square lattice array. The defect breaks the periodicity in the x-axis while it is still periodic in the y-axis. The supercell used in dispersion calculations is highlighted.

The most common way to run eigenvalue calculations over a supercell is setting periodic boundary conditions at all boundaries. However, in order to reflect more realistic results, periodic boundary conditions are only used for the boundaries along the x-axis. For the boundaries in the y-axis, absorbing boundary conditions

are used in order to take radiation losses into account by following the so-called open supercell approach (3).

To obtain the dispersion characteristics, eigenvalue calculations are carried out by means of FEM for E-polarization of the photonic crystal waveguide consisting of square lattice array of copper cylinders embedded in air. The eigenvalue problem for waveguide is solved along the (1,1) direction, namely Γ - M direction of the square lattice. Modes in a metallic photonic crystal waveguide are studied considering the dispersive properties and frequency dependence. The periodicity is broken in the x-direction since one and two rows of rods are removed in 2D photonic crystal to form the wave-guiding channel. However, it is still periodic along the line defect on the y-axis. The dispersion diagrams are achieved for THz frequencies and presented in Figure 6.2 and Figure 6.3 for W1 and W2 linear waveguides, respectively, as shown by the inset at the right-bottom side of the figures.

M. Qiu and S. He calculated the guided modes of W1 and W2 metallic photonic crystal waveguides in square lattice arrays of copper rods in air with rod radius of $0.2a$ using FDTD method (4).The conductivity of copper is taken as σ=5.80=10^7 S/m. It is found that the guided modes in the photonic crystal waveguide are related to those in a conventional metallic waveguide. Our calculations based on FEM for dispersion diagrams of W1 and W2 waveguides, which are shown Figure 6.2 and Figure 6.3, are in very good agreement with their study as shown in Figure 6.4 a) and b) respectively.

In the previous chapter, the photonic band structure of a square lattice was calculated. The complex eigenvalue problem was solved for wave vector $\vec{k}$, for a given frequency ω in the unit cell of square lattice by setting periodic boundary conditions. The calculated band-gap diagram showed that there are two band-gaps for a square lattice of metallic photonic crystal. The first band-gap extends from 0 to

3.244 THz and the second band is between 4.413 and 5.242 THz corresponding to 0 - 0.5407 ($\omega a/2\pi c$) and 0.734 - 0.8778 ($\omega a/2\pi c$), respectively, in terms of normalized frequencies. The band structure of metallic square lattice Γ - M direction is shown in blue solid lines as a guideline. No wave can propagate through the structure for frequencies falling within the photonic band-gap (PBG), as opposed to the pass band of the structure where it becomes transparent to the waves. Within the band-gap, the photonic crystal waveguide supports guided modes. For the regions corresponding to the pass-band of the metallic structure, losses are to be obtained.

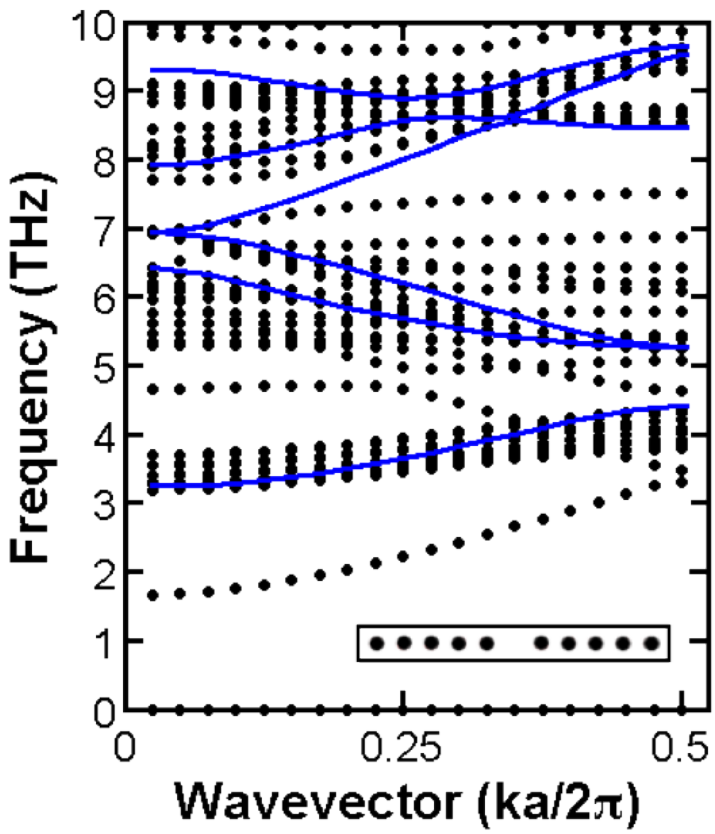

Figure 6.2: Dispersion diagram of a W1 waveguide where one row of rods is removed from square lattice composed of metal cylinders in air. Dispersion curves for waveguide are obtained in the Γ - M (1,1) direction of the square lattice. Blue solid lines show the photonic band-gap structure of square lattice in the same direction. Inset shows the supercell used in the dispersion calculations of W1 waveguide.

Line defects lead to guided or evanescent modes in the band-gap structure. Depending on the width of waveguide or how many row of rods are omitted from the structure single or multi modes propagate. As seen in Figure 6.2, in the first band-gap of the photonic crystal, there is one guided mode, a single mode, that lies between 1.652 and 3.316 THz. In this range the waveguide operates only in single mode. This mode is folded at the edge of the Brillouin zone. As the waveguide is symmetric with respect to its axis, guided modes can be classified as even or odd mode. The parity of lowest defect mode is even. The modes can be distinguished from the field distribution, where even mode has even number of maxima in transverse direction while odd mode has odd number of maxima. It is worth mentioning that even modes usually have lower group velocity than odd modes (5). Dispersion diagrams also clearly indicate the position of a cut-off frequency of s W1 waveguide. The effective width of a W1 waveguide is expected to be in the range between 80 - 100 μm $(2a - 2r < w < 2a)$. The width of the waveguide corresponding to the cut-off frequency is 90.79 μm, which gives good approximation of effective width and also matches with a published study where the effective width calculated as $1.8a$ (4).

When a guided mode is folded at the edge of the Brillouin zone, it exhibits a very narrow band called a mini stop-band. This can be explained with the periodic boundaries of the waveguiding channel acting as a 1D periodic structure that results in a narrow gap in the dispersion relation. If two modes have same symmetry with respect to the waveguide axis, these modes may interact with each other. When one mode couples with a higher order mode, two bands repel each other instead of intersecting and this leads to a condition called anti-crossing of the modes. This condition can be observed from dispersion diagrams. The anti-crossing causes a narrow band-gap to open in the waveguide called the mini stop-band where the wave propagation is suppressed (6; 7; 8). The mini stop-bands manifests transmission loss as a dip in the transmission spectrum of the guided mode as its energy is transferred to the higher-mode (9).

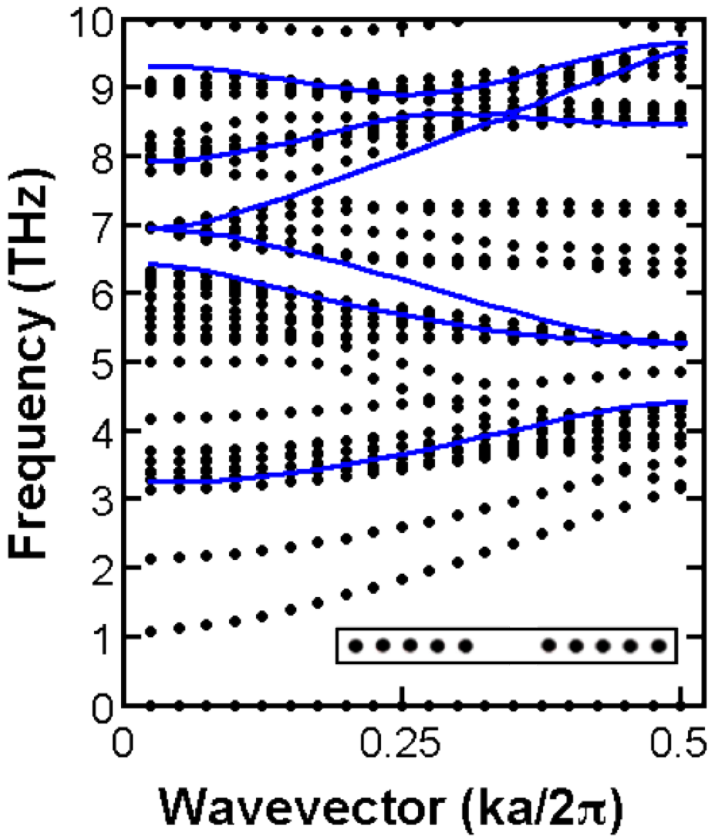

Figure 6.3: Dispersion diagram of a W2 waveguide where two rows of rods are removed from the square lattice composed of metal cylinders in air. Dispersion curves for waveguide are obtained in the (1,1) direction of the square lattice. Blue solid lines show the band-gap structure of metallic square lattice in Γ - M direction. Inset shows the supercell used in the dispersion calculations for W2 waveguide.

In Figure 6.2, the fundamental mode is folded back at the Brillouin zone edge at around 3.4 THz creating a narrow band between 3.316 and 3.484 THz. The fundamental mode continues to propagate in the second band-gap, this mode couples with a higher order even mode with the same group velocity but opposite sign and in the dispersion curve this is seen as the anti-crossing of modes. A mini stop-band occurs in the range between 4.715 and 4.954 THz where a transmission dip is expected in the transmission spectrum due to the anti-crossing at around 4.8 THz. The fundamental mode couples to another even mode instead of the odd mode since

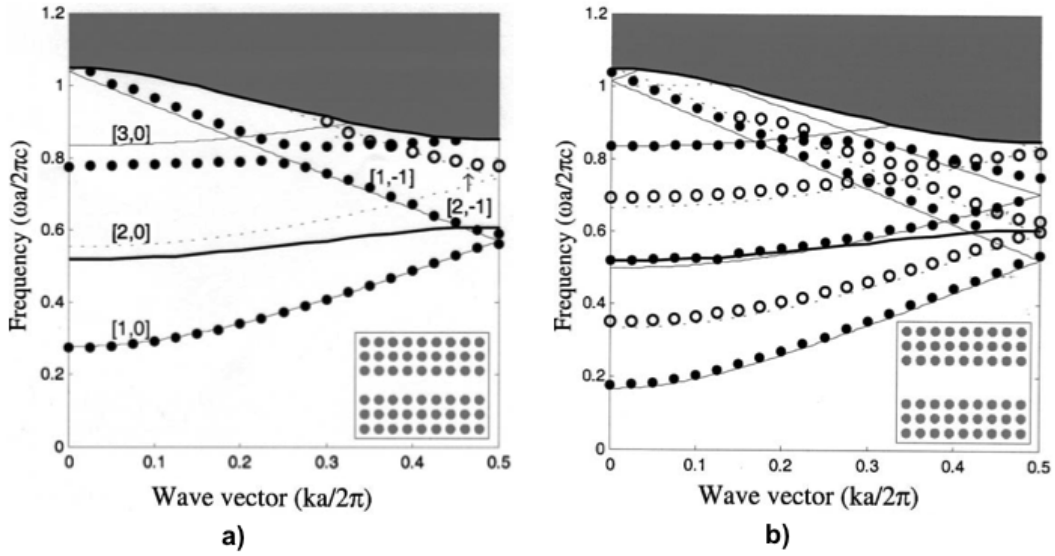

Figure 6.4: Dispersion diagram of a) W1 and b) W2 metallic photonic crystal waveguides in a square array of copper rods in air; the radius of the rods is $r = 0.2a$. The dots show even modes while open dots show odd. The thick lines show the band diagram of the perfect photonic crystal. Eigen frequencies of the guided modes are calculated with FDTD method, courtesy of Qiu *et al.* (4).

modes only couple with modes of the same parity. The higher order guided modes of the waveguides are especially strongly influenced by mode coupling.

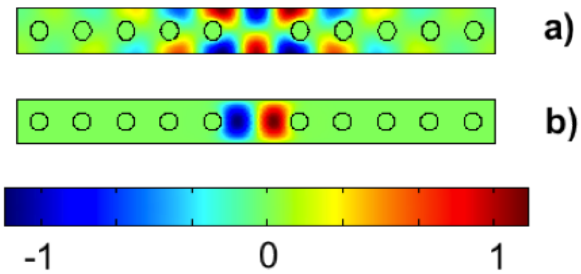

Figure 6.5: Visualisation of E-field distribution of guided modes in a W1 line defect waveguide a) even mode at 5.071 THz b) odd mode at 4.642THz for $k = 0.5$, illustrating the difference in symmetry.

Electric-field distribution of the even and odd mode modes in the second band-gap at $k = 0.5$ is shown in Figure 6.5. The difference in symmetry of modes can be

seen clearly. The even mode lies between 6.216 - 5.071 THz for $k = 0$ and $k = 0.5$, respectively, while the odd mode lies between 5.293 THz ($k = 0$) - 4.642 THz ($k = 0.5$).

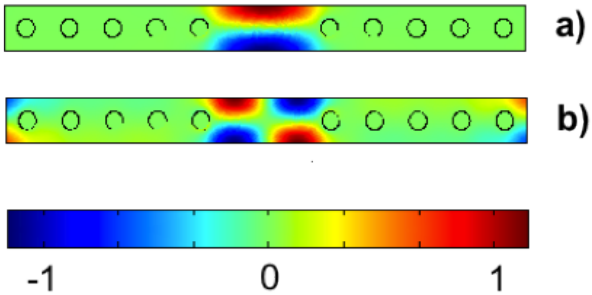

Figure 6.6: Visualisation of E-field distribution of guided modes in a W2 line defect waveguide a) even mode at 3.15 THz b) odd mode at 3.55 THz for $k = 0.5$, illustrating the difference in symmetry.

Increasing the width of the waveguide causes an increase of the number of guided modes in the photonic crystal band-gap and transmission becomes multimode as seen in Figure 6.3. Within the first band-gap of the photonic crystal, there are two guided modes; an even and an odd mode lie below the lowest band. The even mode lies between 1.064 and 3.15 THz and the odd mode lies between 2.12 and 3.55 THz. Electric-field distribution of these modes at $k = 0.5$ are shown in Figure 6.6. The difference in symmetry of modes can be seen clearly.

If the input wave is an even mode, the input wave couples only with the even mode. The first guided mode, which is an even mode, is the fundamental mode. This mode indicates the cut-off frequency at 1.064 THz, which is close to cut-off frequency corresponding to the width of W2 waveguide, 1.15 THz. The second guided mode, an odd mode, starts to operate at 2.12 THz. In the range between cut-off frequency and 2.125 THz, W2 waveguide operates as a single mode waveguide, whereas for higher frequencies it becomes multimode. The fundamental mode is folded back at the edge of the Brillouin zone around 3.2 THz. This folding can be

considered as a mode splitting and therefore this creates a narrow gap.

An undisturbed crossing is observed when symmetric and anti-symmetric modes intersect in the dispersion diagram. As can be seen in the dispersion diagram of W2 waveguide in Figure 6.3, in the second band-gap, a mode crossing occurs between the fundamental mode and the odd mode at 4.43 THz for $k = 0.28$. As only the modes that have same parity couple to each other, this crossing does not create a mini stop-band. On the other hand, a coupling between the fundamental mode and a higher order even mode creates a mini stop-band at around 5.2 THz. This results in a frequency range without a waveguide mode as modes repel each other, and a mini stop-band occurs in the range between 4.98 and 5.37 THz that affects the transmission spectrum, creating a dip for frequencies within this mini stop-band.

6.4 Triangular Lattice Waveguide

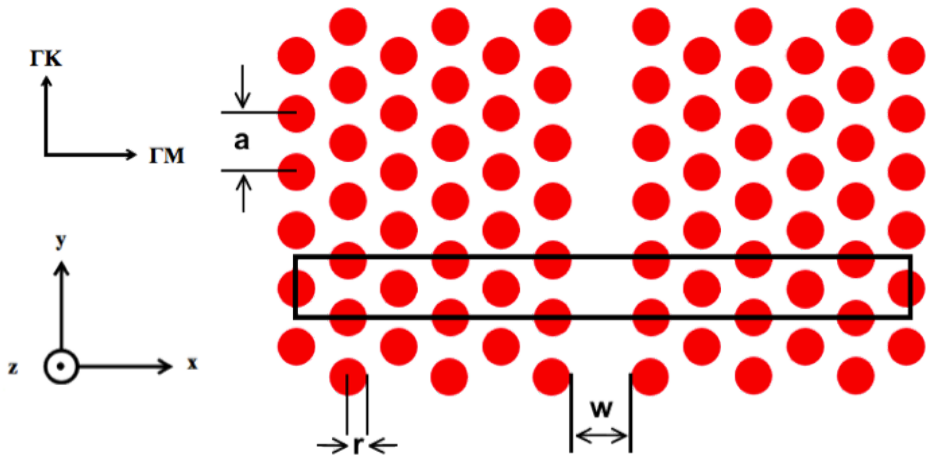

Figure 6.7: Schematic illustration of a photonic crystal waveguide (W1) formed by introducing a line defect along the Γ - K direction of a triangular lattice of metallic rods in air. The defect breaks the periodicity in the x-axis while it is still periodic in the y-axis. The supercell used in dispersion calculations is highlighted. The width of W1 waveguide, $w = a\sqrt{3} - 2r$, a is the lattice constant and r is the rod radius.

We consider a line defect consisting of a missing row of rods along the Γ - K direction of the triangular lattice. The line defect breaks the symmetry in the Γ - M direction, but the structure is still symmetric along the Γ - K direction, where the lattice period is a. The dispersion diagram is obtained using FEM with a combination of periodic boundary conditions and absorbing boundary conditions over a supercell. In the supercell, the line defect consists of certain number of layers separated by a missing rod in the middle. The height of the supercell is a lattice period long. Similar to the square lattice waveguide, the Bloch wave vector along the waveguide axis represents the guided mode wave-vectors. In a triangular lattice structure the line defect is introduced along the Γ - K direction rather than the Γ - M direction, since the waveguide walls are smoother. The width of waveguide in triangular lattice array is $w = a\sqrt{3}(N+1)/2 - 2r$ for the so-called WN waveguide where N is the number of removed rows.

The dispersion diagram is defined by the frequency of eigenmodes as a function of wavevector along the central axis of the waveguide. The dispersion diagram is represented by band-diagrams of mode frequencies as a function of the Bloch vector. Bloch vectors for a triangular lattice waveguide were given in earlier chapters. To obtain the dispersion characteristics, eigenvalue calculations are carried out by means of FEM for E-polarization of the photonic crystal waveguide consisting of a triangular lattice array of copper cylinders embedded in air. The eigenvalue problem for the waveguide is solved along the (1,1) direction, namely the Γ - K direction, of the triangular lattice. The radius of the rods is $r = 0.2a$, where a is set to 50 μm. W1 and W3 waveguides are considered. In W3 waveguide 3 rows of rods are removed in order to ensure the symmetry. Even though there are studies for dispersion calculations and the guided modes of metallic photonic crystal waveguides in square lattice pattern, there very are few studies conducted on dispersion relations of metallic photonic crystal waveguides with triangular lattice pattern (10).

In the previous chapter, the photonic band structure of a triangular lattice was calculated. The complex eigenvalue problem was solved for wave vector $\vec{k}$, for a given frequency ω in the unit cell of triangular lattice by setting periodic boundary conditions. The calculated band-gap diagram showed that there are two band-gaps. The first band-gap is wider extends from 0 to 3.764 THz and the second band is very narrow between 7.019 and 7.157 THz corresponding to 0 - 0.673 ($\omega a/2\pi c$) and 1.1698 - 1.928 ($\omega a/2\pi c$), respectively, in terms of normalized frequencies.

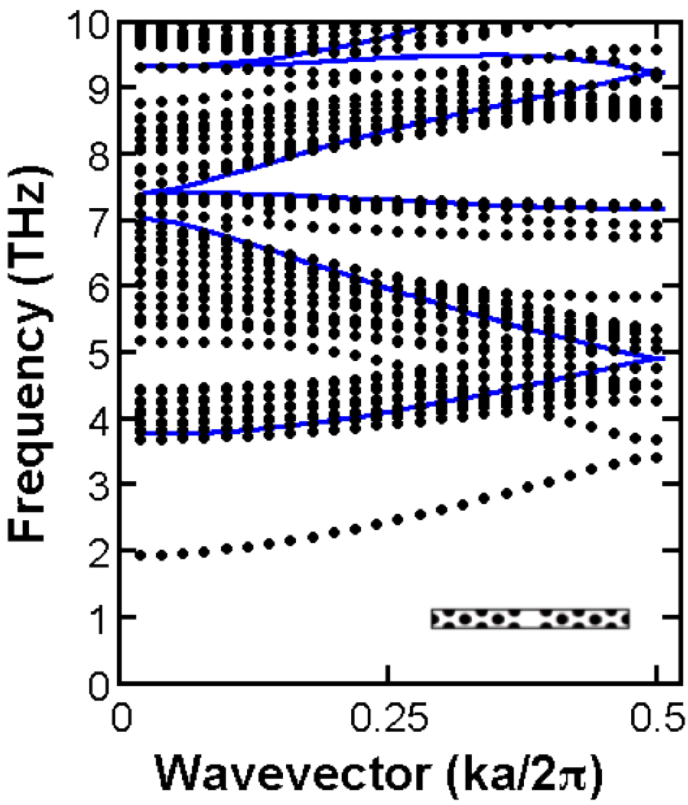

Figure 6.8: Photonic band structure of a W1 waveguide where a row of rods is removed from the triangular lattice composed of metal cylinders in air. Dispersion curves for waveguide are obtained in the in the Γ - K (1,1) direction of the triangular lattice. Blue solid lines show the band-gap structure of metallic triangular lattice in the same direction. Inset shows the supercell used in the dispersion calculations for W1 waveguide.

The dispersion diagrams are achieved and presented in Figure 6.8 and Figure 6.9

for W1 and W3 linear waveguides, respectively, while the inset at the right-bottom side of the figures indicates the supercell used in the calculation. The guided modes and leaky modes are depicted with black dots. The band structure of the triangular lattice in the Γ - K direction is shown in the figures with blue lines as guideline.

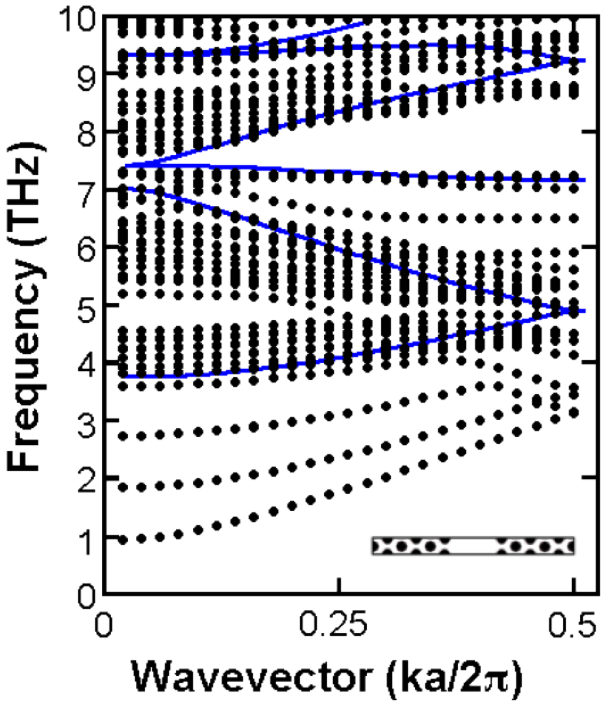

Figure 6.9: Photonic band structure of a W3 waveguide where a row of rods is removed from the triangular lattice composed of metal cylinders in air. Dispersion curves for waveguide are obtained in the Γ - K (1,1) direction of the triangular lattice. Blue solid lines show the band-gap structure of metallic triangular lattice in the same direction. Inset shows the supercell used in the dispersion calculations for W3 waveguide.

As is expected from the dispersion diagram of W1 waveguide, there is only one mode in the wider band-gap of the crystal. The parity of this mode is even, which can be seen from Figure 6.10 depicting the field distribution of waveguide cross-section within the supercell. This guided mode exists from cut-off frequency (1.926 THz) to nearly the band-gap at the edge of the Brilllouin zone at 3.412 THz.

From the dispersion diagram of the W1 waveguide in Figure 6.8, the fundamental mode is folded at around 3.5 THz and creates a mini stop-band between 3.412 THz and 3.666 THz. Below the first band indicated by a blue line, the even mode which extends from 3.804 to 3.666 THz crosses with the odd mode, which extents from 3.674 to 4.27 THz at 4.136 THz for $k = 0.38$. Another mode crossing occurs between an even and an odd mode at 4.747 THz for $k = 0.3$. The odd mode lies between 4.426 and 5.048 THz, while the even mode extends from 5.16 to 4.748 THz.

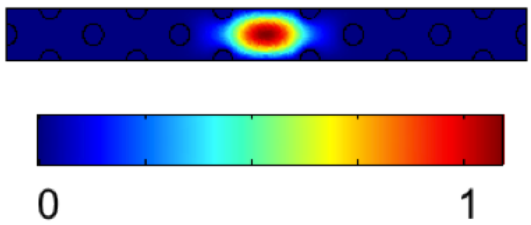

Figure 6.10: Visualisation of E-field distribution of guided modes in a W1 line defect waveguide for the lowest order mode which is an even mode at 3.412 THz for $k = 0.5$.

The dispersion diagram of the W3 waveguide, with the same lattice parameters as that of the W1 case, clearly shows the multi-mode behaviour of the waveguide. There are several even and odd modes within the band-gap of the triangular lattice. The number of allowed guided modes increases as the width of the waveguide increases. As can be seen from the dispersion diagram of the W3 waveguide in Figure 6.9, there are three guided modes in the photonic band-gap of the structure. The first mode, an even mode, lies between the cut-off frequency (0.914 THz) and 3.115 THz. This mode is a fundamental mode and is folded back at the edge of Brilllouin zone at 3.115 THz and constitutes the third mode, which extends from 2.722 to 3.145 THz. The second mode is an odd mode between 1.824 and 3.436 THz. The waveguide operates in single mode within the frequency range of 0.914 - 1.824 THz.

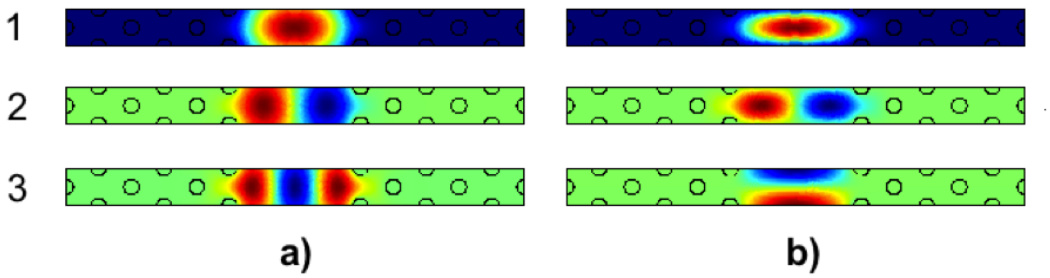

Figure 6.11: Electric field distributions of the guided modes within the band-gap of the W3 waveguide. a) for $k = 0.25$, for frequencies corresponding to 1.755, 2.357, 3.097 THz and b) for $k = 0.5$ at frequencies 3.115, 3.436 and 3.145 THz respectively for the first three lowest order guided modes, starting from the one which has the lowest frequency.

The electric field distribution of modes appears in the W3 waveguide within the band-gap. Two even and one odd mode are shown in Figure 6.11 for a) $k = 0.25$ and b) $k = 0.5$, respectively. The symmetry of the modes can be clearly distinguished from the figure. In the band-gap of the lattice structure, the guided mode has its energy confined inside the defect and interacts with the first row of rods that forms the wall of the waveguide.

In the dispersion diagram of the triangular W3 waveguide in Figure 6.9, the lowest order mode is also the fundamental mode and is folded around 3.1 THz and creates a very narrow band, between 3.115 and 3.145 THz. Modes having the same symmetry avoid crossing and form mini stop-bands.

6.5 Transmission Analysis

In the previous chapter, we calculated the photonic band structure of lattice and compared them with the transmission characteristics of lattice arrays. After study-

ing dispersion diagrams of 2D metallic photonic crystal waveguides in the previous section, propagation and transmission characteristics will be discussed in this section. We will also compare the calculated the dispersion diagrams of waveguide structures with their transmission characteristics.

For a waveguide, our interest is to investigate the amount of reflected energy, and wave distribution. The losses of metals are included by implementing a complex expression for material properties. Here, we investigate the losses for different metals. As it mentioned earlier, we will compare four highly conductive metals for use in photonic crystal structures for high transmission performance in the THz range. The THz frequency range will be scanned for transmission of wave-guiding structures.

The spectral behaviour of the waveguides depends on the dispersion characteristics and can be tuned by the rod radius and the lattice constant. As discussed in the previous chapter, increasing the size of the lattice constant resulted in a decrease in the size of the band-gap of the photonic crystal lattice structure. This simultaneously results in a decrease in the transmission bandwidth and total transmission of the photonic crystal waveguides. Therefore, in the following calculations and design, the lattice constant is set to 50 μm.

In the transmission analysis of the lattice array, PML boundaries were used in the calculations to prevent reflection in any directions since multiple scattering occurs when a wave is incident on the metallic structure. The PML regions need to be included in the computational area. Enlargement of the computation domain results in an increase of mesh elements. Therefore, for a large frequency sweep, the implementation of the calculations is slower as it requires more CPU time and memory. This issue becomes a significant problem for 3D simulations. To analyse transmission characteristics of metallic photonic crystal waveguides, the calculations are

carried out by replacing PML boundaries with absorbing boundary conditions.

For input and output boundaries, a type of absorbing boundary condition is called matched boundary condition is used that also make S-parameter calculations possible.The matched boundary condition is mainly used at boundaries that do not represent a physical boundary. If the electric field is an eigenmode of the boundary the boundary is exactly non-reflecting (11).

$$\hat{e}_z \cdot \vec{n} \times (\nabla \times E_z \hat{e}_z) - i\beta E_z = -2i\beta E_{0z} \quad (TM\ waves) \tag{6.1}$$

$$\hat{e}_z \cdot \vec{n} \times (\nabla \times H_z \hat{e}_z) - i\beta H_z = -2i\beta H_{0z} \quad (TE\ waves) \tag{6.2}$$

where β is the propagation constant of the electromagnetic wave.

Calculations from the previous chapter have shown that the first row of photonic crystals at each side of the waveguiding channel is the most important for minimizing in-plane scattering losses. Therefore, the absorbing boundary condition at the boundaries at each side of the waveguide is enough to prevent reflections.

The purpose of this section is to validate the modelling of waveguiding structure for designing the desired functionality. FEM is well suited for resolving photonic crystal geometry and is used for calculating the transmission spectra, displaying wave propagation and analysing the reasons for propagation losses. It is used for wave propagation in linear defects and translating the general concepts of dispersion relation and of mini stop-bands as seen in the following section transmission spectra.

In the following sections, dispersion diagrams and the transmission spectra of square lattice waveguides (W1, W2) and triangular lattice waveguides (W1, W3) are compared. The transmission of waveguides is interrupted by the transmission dips. The

reasons for these dips are discussed by analysing the dispersion diagram in parallel to the transmission spectra of waveguides.

Since our interest is on the waveguiding devices in the THz range, in order to design low loss waveguiding devices, we calculated the transmission, reflection and absorption of each waveguides. Waveguide attenuations are calculated for square and triangular lattice W1 waveguides for different materials.

6.5.1 Validation of the Two-Dimensional Approximation

In the following sections, transmission characteristics of photonic crystals made of metallic rods in air are considered. Before proceeding with the transmission calculation of metallic photonic crystal waveguides, in order to validate our 2D numerical simulations for waveguiding structures a comparison has been conducted between 2D and 3D simulations. A W1 square lattice waveguide is modelled in 3D and transmission and reflections results are compared with the 2D simulation results. In 3D simulations the metallic rods are sandwiched between two parallel metallic plates of a perfect conductivity, separated by the height of the rods of 50 μm. The 2D simulation is based on the same photonic crystal pattern except the structure is projected in the plane defined by the direction of propagation and direction perpendicular to the direction of the electric field. Transmission and reflection spectra in range of 1 - 6 THz are calculated for a simple waveguide. A W1 waveguide in a 10x10 rod square lattice photonic crystal is tested and results are presented in Figure 6.12. Black lines represent the transmission spectra, while red lines represent the reflection results. 3D transmission and reflection spectra are represented with black and red solid lines, respectively. Similarly, dashed lines represent the results for 2D simulations.

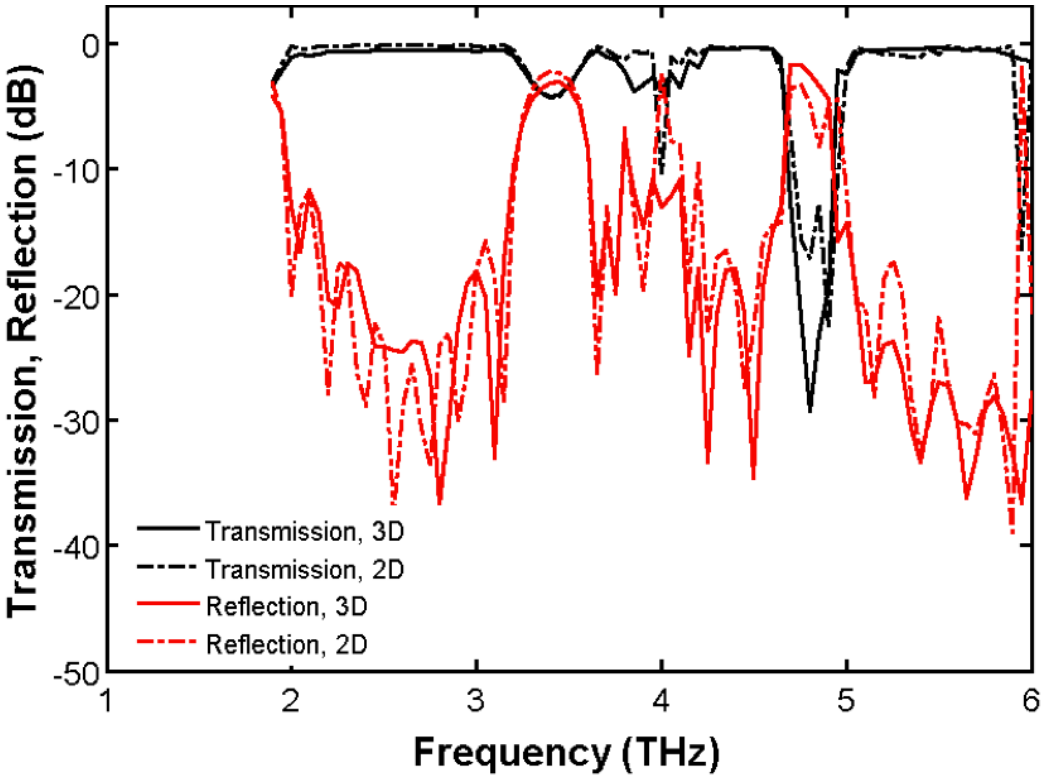

Figure 6.12: Transmission/reflection spectrum simulated in 3D (black/red solid line) and in 2D (black/red dash line) for a linear waveguide formed by removing one row of rods from a metallic PhC. The PhC is characterized by a 50 μm lattice period in square lattice pattern of 50 μm height rods, with a radius of $0.2a$.

As can be seen in Figure 6.12 the transmission spectrum of 2D geometry coincides with that of the 3D geometry and is comparable to band-gap diagram results and reported works (4; 12; 13). The transmission characteristic of a waveguide matches the band-gap and dispersion characteristics of W1 and W2 waveguides. The losses in linear waveguides are caused by the band-gap characteristics of the metallic photonic crystals, as the frequencies where losses are occur appear in dispersion characteristics of metallic photonic crystals (14). As long as the height is kept as small as half of the wavelength, which is the case for the remaining results of this study, 2D and 3D simulations give very similar results. It is worth noting that the positions and width of the photonic band-gap are well reproduced by 2D

approximation and results fit with the results of 3D calculation. For larger sizes of heights, drastic divergences appear. For instance, at 3 THz, the transmission calculated in 3D is -0.566 dB, -0.576 dB, -0.569 dB and -24.575 dB when the height of rods set at 25 μm, 50 μm, 75 μm and 100 μm respectively.

Naturally, for larger geometries, numerical calculations become complex, therefore, 3D simulations take much longer to calculate than 2D simulations and yet consume large amounts of memory. For instance, the 2D simulation features oscillations that are not resolved in 3D simulation. As a reasonable choice, we prefer running simulation in 2D instead of 3D. Hence, one can obtain more accurate results by using computer sources for finer mesh sizes to converge the geometry better and save time. On the other hand, the third dimension should not be ignored completely as long as the height is larger than 50 μm, which is not the case in this work. Therefore, we are only interested in metallic photonic crystal waveguides with third dimension size of 50 μm, since they can be efficiently simulated in 2D.

In the calculations in the following section and chapter, we focus mostly on 2D PhC waveguides and numerical simulations which are carried out in 2D for practical reasons. A 2D photonic crystal waveguide is periodic in the x-y plane. The z-direction has a finite length, i.e. a lattice constant length, in order to provide transmission independent from vertical confinement. A waveguide system consists of a square or triangular lattice array of cylindrical rods in air, where rods are made of metal. For these configurations, metallic photonic crystals have a large band-gap for E-polarization while there is no band-gap for H-polarization. Therefore, this study is mostly concerned with calculations for E-polarization.

6.5.2 Square Lattice Waveguide

Our previous study was mainly focused on the comparison of the transmission characteristics of lattice arrays within their band-gap. We have used copper as a metallic material, however, since our calculations are focused on the band-gap calculations and the verification of our calculations, we could have used another high conductivity metal. In this section we also compare the transmission characteristics of lattice arrays with their dispersion diagrams and show the agreement between them. For this comparison, the level of transmission and how much power is lost are not the concern.

However, in order to determine the optimum parameters that give high transmission performance with low attenuation, we will study transmission reflection and absorption spectra of waveguide structures with the material that gives the lowest possible attenuation in the THz region. We consider W1 and W2 waveguides with a length of 25 periods with 7 layers on each side of the line defect, made of metallic rods in air. The boundary conditions are set as previously described. The transmitted and reflected power is calculated as a function of THz frequencies.

In order to calculate the attenuation of a square lattice waveguide with different metallic materials, we compare the transmission spectrum of a waveguide in a square lattice array made of 4 different metals as a function of waveguide length. This comparison gives the attenuation of the waveguide for different metals. The waveguides in which the computations are carried out have the following parameters: the lattice constant is 50 μm, the rods radius r = 10 μm (0.2a). The guiding area is formed by removing a row of rods along the propagation axis.

The transmission in the W1 waveguide made of gold, silver, copper and aluminium cylinders in air in square lattice pattern is calculated at 3 THz. The length of the

waveguide varies from 10 to 100 periods long. The length of waveguide is increased by adding one layer of rods to the length of waveguide at each step. The computation results show the attenuation of waveguide as a function of waveguide length, presented in Figure 6.13.

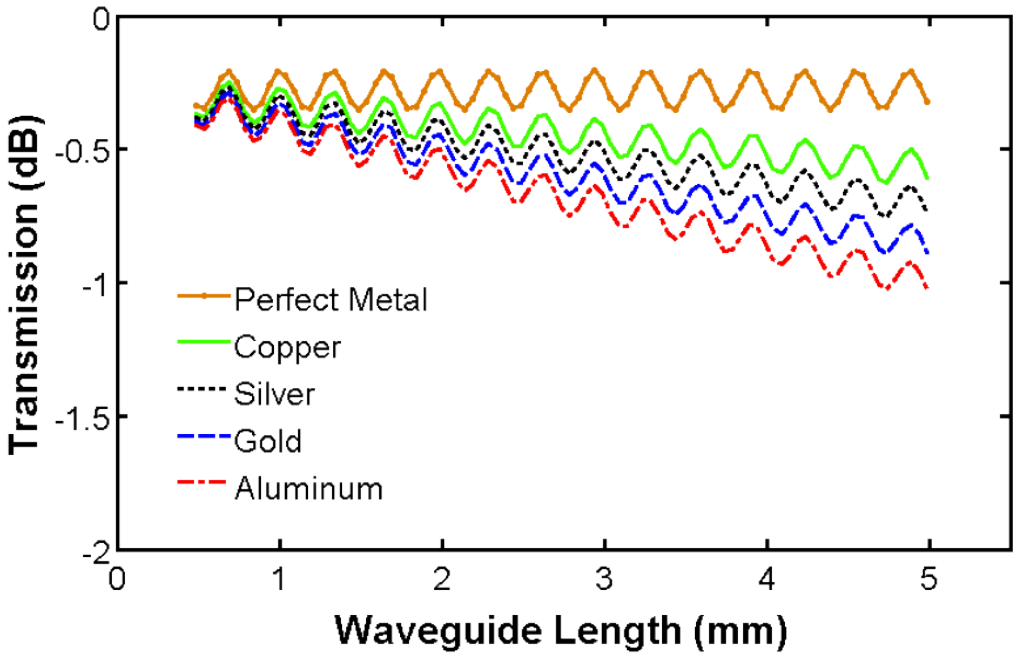

Figure 6.13: The transmission spectra of W1 square lattice waveguide as a function of waveguide length for perfect metal, copper, silver, gold and aluminium.

In the THz domain, particularly for longer waveguides, the metallic losses are expected to be important with respect to the wavelength of the transmitted signal. This can be attributed to the finite conductivity of metallic materials and their high absorption properties in this range. For some models, the imaginary part of permittivity is set to zero to make the calculations easier and with separate study metallic losses are included later (15). With this approximation one cannot obtain information about lossless conditions.

Table 6.1: The attenuation values calculated from the transmission results as a function of waveguide length for W1 square lattice waveguides made of copper, gold, silver and aluminium

	Attenuation (dB/mm)
Metals	W1 Waveguide
Copper	0.05774
Gold	0.11406
Silver	0.08472
Aluminium	0.14244

Therefore, in order to have a clear picture on the attenuation, we have included a photonic crystal waveguide by using perfect conductor rods. By setting *perfect electric conductor* boundary conditions for rods, we ensure that the electric field inside the rods is zero. In the simulation of a perfect conductor case, no attenuation is observed as expected however the level of transmission is below zero, indicating that some of the energy is kept in the photonic crystal structure and not inside the rods. The reason for the sinusoidal behaviour is attributed to the equidistant arrangement of rods.

The transmission is calculated at 3 THz, since the photonic crystal is highly reflective at this frequency. The waveguide is provided by the photonic band-gap and the level of transmission is high. Transmission results for different metals are very similar, but the transmission level changes slightly. As the length increases, the differences in transmission of the metals become apparent. However, copper shows better transmission performance than other highly conductive metals (aluminium, silver and gold). The linear curve fitting values for W1 square lattice waveguide attenuation values are given in Table 6.1. As can be seen from the Table 6.1, the lowest attenuation values are obtained with copper rods both for W1 waveguide, and the highest attenuation values are obtained with aluminium.

In order to study transmission characteristics, considering attenuation/propagation

losses in a waveguide are important when designing low loss waveguide. We will continue to analyse copper rods for which the attenuation is 0.05774 dB/mm for a W1 waveguide. The attenuation for same size copper rectangular waveguide is 0.06279 dB/mm.

6.5.2.1 W1 Waveguide

The modes in the photonic band-gap are considered as guided modes from the point-of-view of the waveguide. However, there are some dips observed in the transmission spectra within the photonic band-gap spectral range. To have a better understanding of the transmission characteristics the dispersion diagram of the waveguides should be compared. A W1 metallic photonic crystal waveguide in square lattice array with rod radius of $0.2a$, a = 50 μm, is considered.

The guided mode dispersion relation and corresponding transmission spectra for a W1 square lattice photonic crystal waveguide is shown in Figures 6.14 a) and b) respectively. In the dispersion figure, along with calculated modes, the band-gap structure of a square lattice in the Γ - M direction is shown with blue solid lines. The shaded areas correspond to the frequency ranges of the photonic band-gaps independent from the lattice direction. The dispersion curves of the modes are shown with black dots, except the guided modes within the photonic band-gap of the lattice structure which are shown with red dots or red open dots for even and odd modes, respectively. Due to the symmetrical boundary of the waveguide, the modes can be classified according to their symmetry with respect to the axis in the centre of the waveguide along its propagation direction as symmetric (even) and anti-symmetric (odd). In the transmission spectra, the transmission of the W1 waveguide is shown with a red line. Within the range of photonic band-gap frequencies, high transmission is obtained except for some frequencies where transmission dips are seen. The

corresponding dips are due to the mini stop-band at the edge of the Brillouin zone and the anti-crossing with a higher order mode, which were explained earlier.

As the length of the waveguide increases, transmission level decreases slightly,and the transmission level of dips drops dramatically, which also causes an increase of the width of mini stop-band. Therefore, the width of transmission dips corresponding to the mini stop-bands may differ.

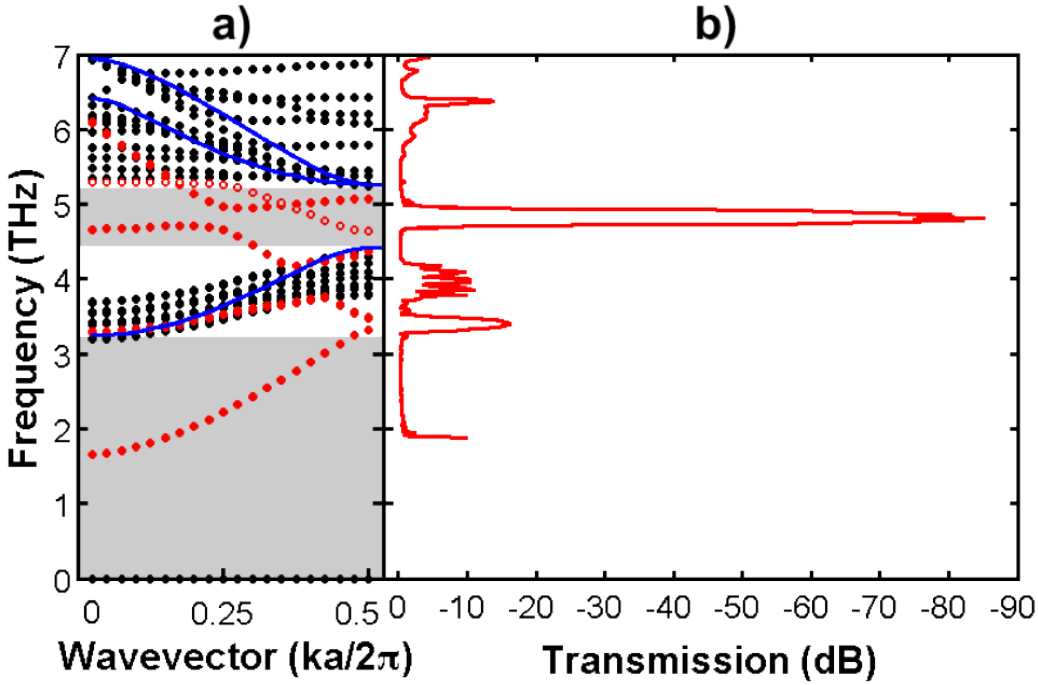

Figure 6.14: a) Dispersion diagram, b) transmission spectrum of W1 waveguide of copper rods in air in square lattice pattern for E-polarization. The radius of rods is $0.2a$, with lattice constant of 50 μm.

The fundamental mode is an even mode. The cut-off frequency obtained from the transmission spectra is in good agreement with the cut-off frequency from the dispersion diagram. The transmission behaviour of the fundamental mode can be followed from the transmission spectra as well as the dispersion diagram. In Fig-

ure 6.14, as expected in the single mode region high transmission is observed. The first transmission dip is observed where the fundamental mode is folded back at the edge of the Brillouin zone. The dip corresponds to the frequency range between 3.27 and 3.53 THz, corresponding to the mini stop-band between 3.16 - 3.484 THz obtained from eigenmode calculations. The range between 3.71 and 4.22 THz can be considered as a transmission dip where the transmission is degraded since this range is outside of the photonic band-gap frequency range. However, transmission is provided not with guided modes but bulky modes. The sharp dip in the frequency range between 4.69 and 4.98 THz corresponds to the anti-crossing due to the coupling between fundamental mode and a higher order even mode in the dispersion diagram. The mini stop-band as a result of anti-crossing occurs between 4.715 and 4.956 THz.

As can be seen from Figure 6.14, there is a strong correlation between the transmission spectra of the W1 waveguide and the corresponding dispersion diagram. The comparison between them helps to gain a better understanding of the trend in transmission and the losses of waveguide structures. From this comparison, we can state that our 2D simulations for the dispersion diagram and the transmission spectra are valid for metallic photonic crystal waveguide analysis.

In order to understand the modal behaviour of a W1 waveguide in square lattice array with rods radius $r = 0.2a$, wave propagation in the waveguide is shown for several frequencies in Figure 6.15. We observe that the lowest order guided mode has an even mode parity in the range between cut-off frequency and 3.316 THz from Figure 6.14 a). It is a guided mode within the first band-gap, and in this range the waveguide operates in single mode. Figure 6.15 a) shows the electric field distribution of the W1 waveguide at 2.5 THz. At this frequency, single mode operation results in perfect confinement and a high transmission level of -0.38 dB. Figure 6.15 b) shows the electric field distribution corresponding to the frequency

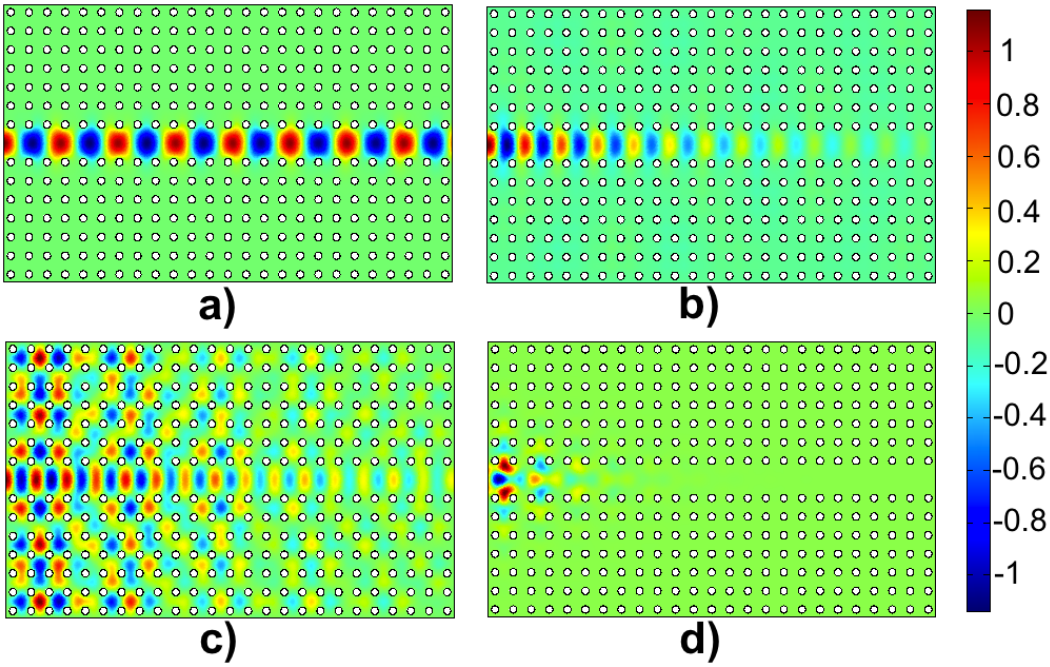

Figure 6.15: The electric field distribution of square lattice W1 waveguide for the frequencies corresponding to a) single mode propagation in the first band gap at 2.5 THz, and transmission dips at b) 3.38 THz, c) 4 THz and d) 4.81 THz, respectively.

where the first transmission dip is obtained, at 3.38 THz. This dip is associated with the mini stop-band in the dispersion diagram in Figure 6.14 a). Figure 6.15 c) and Figure 6.15 d) show the electric field distribution at 4 and 4.81 THz, the second and third transmission dips. At 4 THz, as seen from the electric field distribution while some of the energy is confined in the waveguide, some of the energy is scattered through into the photonic crystal structure. The main reason for energy loss is that this frequency is outside the photonic band-gap frequencies. Since the input wave is not confined by the photonic band-gap effect, metallic photonic crystals become transparent, and energy leaks through the photonic crystal walls. On the other hand, some of the energy is confined in the waveguiding channel almost perfectly with an even mode; however, due to the modes couple with bulk modes, transmission is degraded. At 4.81 THz within the mini stop-band between 4.7 and 4.9 THz, the electric field decays as the field propagates along the waveguide. The field pattern

shows the wave propagation of mode coupling between the fundamental mode and the higher order mode. The decay is stronger than the case in the mini stop-band due to the mode folding.

In Figure 6.16 a) transmission, b) reflection and c) absorption spectra of the W1 waveguide consisting of a square lattice array of copper rods in air with lattice period of 50 μm and rod radii equal to $0.2a$ (10 μm), $0.3a$ (15 μm) and $0.4a$ (20 μm), are compared. The solid red line shows the transmission, reflection and absorption of W1 waveguide with rod radius $0.2a$ while blue dash and black dash-dot line show that of W1 waveguide with rod radius $0.3a$ and $0.4a$, respectively.

From the transmission spectra in Figure 6.16, the cut-off frequencies obtained for the waveguides with rod radius of $0.2a$, $0.3a$ and $0.4a$ are 1.88, 2.15 and 2.5 THz, respectively. These values are in good agreement with the cut-off frequencies calculated for same size rectangular waveguide, which are 1.875, 2.143 and 2.5 THz respectively. In the figure, transmission and reflection are expressed in dB levels following the common use while absorption is expressed in linear scale.

In order to capture clearly the transmission difference between $r = 0.2a$, $r = 0.3a$ and $r = 0.4a$ cases, the transmission spectra are cropped at -50 dB in Figure 6.16 a). Below -50 dB where the transmission dips reach -83.96 dB at 4.82 THz for $0.2a$, at -115dB at 5.47 THz for $0.3a$ and at -63.35 dB at 9.73 THz for $r = 0.4a$ are not shown in the figure.

For the transmission, reflection and absorption analysis, we compare waveguides with three rods sizes, $0.2a$, $0.3a$ and $0.4a$. In order to express these waveguides easily, we numbered the waveguides according to how many row of rods are missing and the rod size. For instance, for W1 waveguides they are named as W1_0.2, W1_0.3 and W1_0.4.

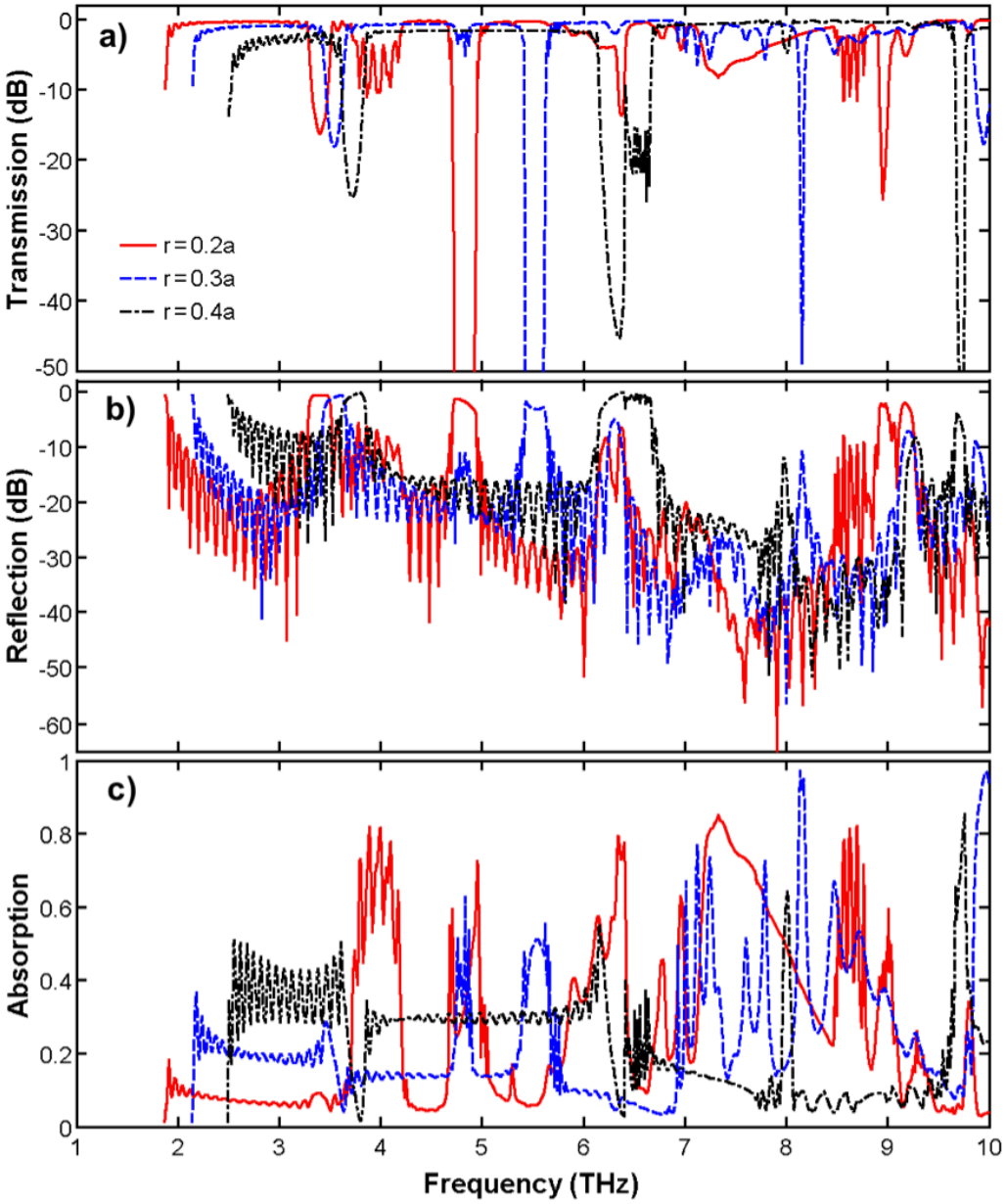

Figure 6.16: a) Transmission, b) reflection and c) absorption spectra different W1 waveguides in square lattice array with rod sizes $0.2a$ (red solid line), $0.3a$ (blue dash line), $0.4a$ (black dash dot line) with lattice constant of 50 μm. Transmission, reflection in dB scale and absorption is calculated in linear scale.

The positions of the dips are shifted to the higher frequency as the size of rods

is increased. In the single mode region, for W1_0.4 waveguide (from cut-off frequency to the first transmission gap) not only the transmission level is lower but also the 3-dB bandwidth is smaller than W1_0.2 and W1_0.3 waveguides. If we compare the transmission performance of the square lattice W1 waveguide in the single mode regions, the W1_0.2 waveguide has a higher transmission level than the others. In the single mode region range, 1.392 THz 3 dB-bandwidth is obtained between 1.897 and 2.289 THz, and transmission reaches up to 94% for the W1_0.2 waveguide. For W1_0.3, the 3 dB-bandwidth is between 2.17 and 3.431 THz, with transmission reaching 83%. On the other hand the W1_0.4 waveguide exhibits transmission around 3-dB with fluctuations in the range between 2.73 and 3.6 THz. We can consider separately the transmission characteristic below and above 6 THz. For instance, below 6 THz, except for the frequencies of the dips, the W1_0.2 waveguide has the highest transmission level while the W1_0.4 waveguide has the lowest levels; above 6 THz this is reversed. The reflection and absorption spectra give a complimentary picture of the transmission spectra. The cut-off frequencies and the positions of the transmission dips can be clearly seen. In Figure 6.16 c) in the range between 1.19 and 3.4 THz the lowest absorption (below 5%) is obtained for the W1_0.2 waveguide. For frequencies below 6 THz, except for the frequencies of the transmission dips where the absorption reaches to high values the absorption is around 10% for the W1_0.2 waveguide. Above 6 THz, the absorption for the W1_0.2 waveguide increases. The absorption of the W1_0.2 waveguide decreases nearly linearly in the range between 7.33 and 8.44 THz, where transmission increases in a similar way.

As opposed to what would be expected from the band-gap diagram of a square lattice where the photonic band-gap covers the whole THz range, The W1_0.4 waveguide does not exhibit the best transmission characteristics. In particular for frequencies below 6 THz the transmission level is lower than that of W1_0.2 and W1_0.3. The broadness of the largest 3-dB bandwidth is 2.23 THz, between 3.86

and 6.09 THz, where this waveguide exhibits a constant transmission level of 70% with almost no fluctuation. The transmission level of the W1_0.4a waveguide reaches up to 96% in the frequency range between 6.68 and 9.66 THz except for the small dip at around 8 THz, the transmission level is better than the preceding frequencies, mostly over 90%. The transmission of the W1_0.3 waveguide reaches up to 96.5%, and the largest bandwidth is obtained between 5.68 and 7 THz, and below 6 THz it is between 2.22 and 3.43 THz. The transmission of the W1_0.2 waveguide reaches up to 97% at 9.92 THz.

6.5.2.2 W2 Waveguide

In this paragraph, the transmission characteristics of W2 waveguides are analysed. Firstly, a comparison takes place between the transmission and the corresponding dispersion diagram of W2 waveguide in square lattice pattern with rod radius is equal to $0.2a$, where lattice constant a = 50 μm. Secondly, transmission, reflection and absorption spectra of W2 are obtained waveguide with several rod sizes.

In the dispersion diagram of the W2 waveguides in Figure 6.17 a) the modes propagating in the waveguide are shown. The photonic band structure of square lattice in the Γ - M direction is shown with blue solid lines. The photonic band-gap independent of the lattice directions is indicated with shaded areas. The dispersion curves of the modes are depicted with black dots. This waveguide carries even and odd modes, and since they have different symmetry, these modes cannot couple to each other. The guided modes are plotted depending on symmetry either with red dots or red open dots for even or odd modes, respectively.

The transmission spectrum of the waveguide linked to the dispersion diagram is shown in Figure 6.17 b) with a red solid line. The high transmission in W2 wave-

guide is occasionally interrupted by transmission dips. From the direct comparison between the dispersion and the transmission spectrum, we have a better understanding of both the modal behaviour of guided modes and the transmission and transmission dips for W2 waveguide. Within the frequency of the photonic band-gap of the lattice structure, the transmission dips correspond to the mini stop-bands that can be observed from the dispersion diagram of the waveguide. The transmission dips of the W2 waveguide are not as deep as in the W1 waveguide as seen in Figure 6.16.

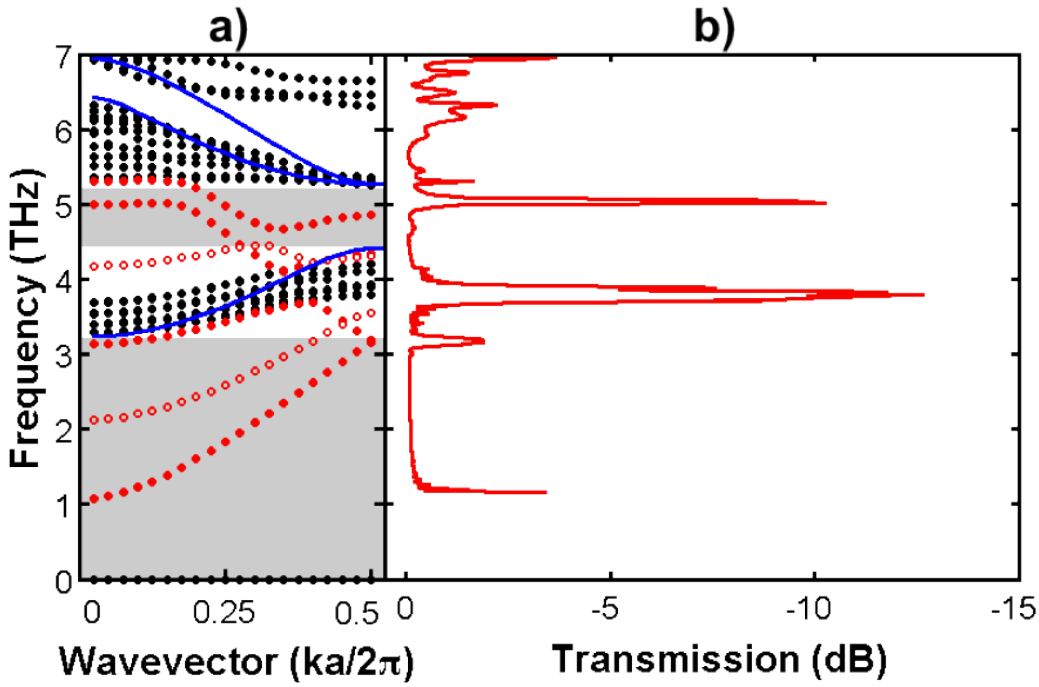

Figure 6.17: a) Dispersion diagram, b) transmission spectrum of W2 waveguide of copper rods in air in square lattice pattern for E-polarization. The radius of rods is $0.2a$, with lattice constant of 50 μm.

The lowest order mode is the fundamental mode, indicated in red dots in the first band-gap. The wave propagates inside the waveguide with high transmission, starting from the cut-off frequency to the edge of Brillouin zone. Since the input wave

is even mode, odd mode is not transmitted. In the transmission spectra the first transmission dips is are obtained in the range between 3.1 and 3.25 THz, which agrees well with the dispersion diagram where a mini stop-band exists in the range between 3.15 and 3.2 THz. Using eigenmode calculations carried out with FEM, not only the guided modes but also the bulk modes are obtained. The second dip is observed between 3.67 and 3.93 THz. As can be seen from the dispersion diagram, since the guiding mechanism does not rely on the photonic band-gap, the fundamental mode cannot couple to other modes in the range between 3.68 and 4.124 THz. A sharp dip is observed in the transmission spectra due to the anti-crossing of the fundamental mode with a higher order mode in the range between 4.92 and 5.19 THz corresponding to the mini stop-band between 4.885 and 5.296 THz. As pointed out earlier, the dip is associated with the mini stop-band, which results from the mode anti-crossing, since it is deeper than the dip resulting from the mode folding. As can be seen from the dispersion diagram, a crossing of even and odd modes takes place at 3.42 THz for $k = 0.45$. This, however, does not affect the transmission spectrum.

Figure 6.18 shows the a) transmission, b) reflection and c) absorption spectra of W2 waveguides in square lattice array for rod radius of $0.2a$, $0.3a$ and $0.4a$, where the lattice constant a = 50μm. For this waveguide the waveguide width is a lattice constant wider than the W1 waveguide, and consequently its cut-off frequencies are obtained at lower frequencies. The cut-off frequencies of W2_0.2, W2_0.3 and W2_0.4 waveguides are 1.16, 1.25 and 1.37 THz, respectively. The positions of cut-off frequencies show good agreement with the same width rectangular waveguide cut-off frequencies, which are 1.1538, 1.25 and 1.3636 THz in the same order. In Figure 6.18 a) the transmission spectrum is cropped at -20 dB, therefore the transmission dip at -49.08 dB, at 6.22 THz is not seen in the figure. In the spectral region between the cut-off frequencies and frequencies where the sharp transmission dips are obtained at 4THz, the transmission is over -3 dB for all three waveguides. This

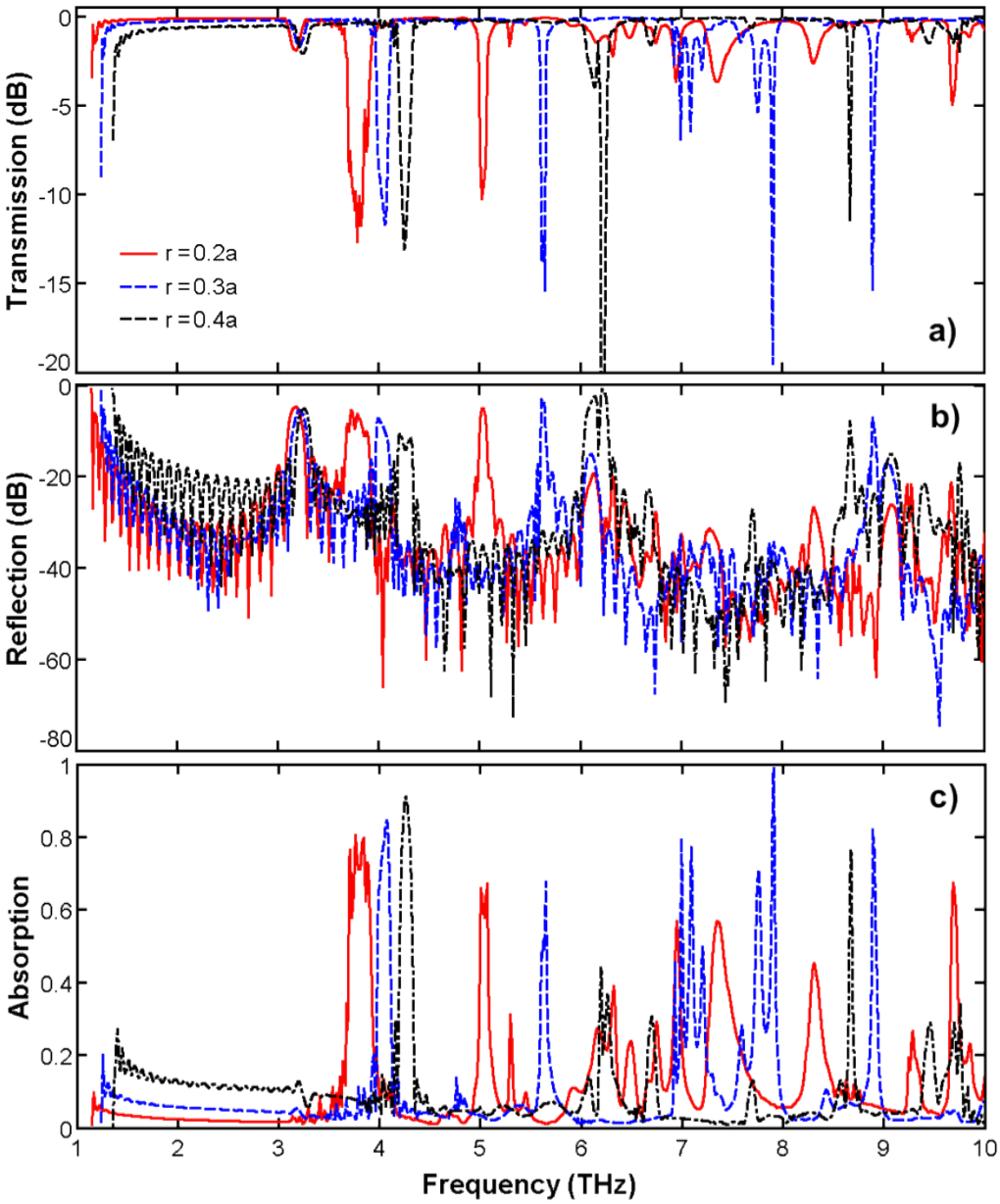

Figure 6.18: a) Transmission, b) reflection and c) absorption spectra different W2 waveguides in square lattice array with rod sizes $0.2a$ (red solid line), $0.3a$ (blue dash line), $0.4a$ (black dash dot line) with lattice constant of 50 μm. Transmission, reflection in dB scale and absorption is calculated in linear scale.

region includes a small dip at $\sim$ 3.2 THz. The largest bandwidths are observed in this range compared to the rest of the THz frequency range with transmission levels

over 90% for all the waveguides compared. The best transmission is obtained with the W2_0.2 waveguide in the range between 1.17 and 3.96 THz. In this range the reflection and the absorption take the lowest values as can be seen in Figure 6.18 b) and c). 3-dB bandwidths are obtained in the ranges between 1.26 and 3.97 THz, and between 1.39 and 4.19 THz for W2_0.3 and W2_0.4 waveguides.

The transmission of W2 waveguides is generally is better than the W1 waveguide shown in Figure 6.16, for both transmission bandwidth and level of transmission. The transmission level of W2 waveguide reaches up to 98% or over. The transmission characteristics of W2 waveguides changes roughly for frequencies above 6 THz, similarly to W1 waveguides, where W2_0.2 and W2_0.3 waveguides become more lossy than the W2_0.4 waveguide as opposed to frequencies below 6 THz. Above 6 THz, the absorption of W2_0.4 waveguide is lower than other W2 waveguides compared.

6.5.3 Triangular Lattice Waveguide

In this paragraph, we consider the properties of the two waveguides in a triangular lattice, namely, W1 and W3 waveguides which are formed by removing one and three row of rods in Γ - K direction, respectively. The considered W1 and W3 waveguides are 25 lattice periods long with 7 layers at each side of the line defect made of metallic rods in air. The lattice constant is set to 50 μm. The boundary conditions are set as those for studies of square lattice waveguides.

In the following subsections, a comparison takes place between the transmission and the corresponding dispersion diagram of W1 and W3 waveguide in triangular lattice pattern with rod radius equal to 10 μm ($0.2a$). Transmission, reflection and absorption spectra of W1 and W3 waveguides are calculated.

The attenuation of a triangular lattice waveguide with different metallic materials is simulated in a similar way as that of the square lattice waveguide. The transmission of W1 waveguides consisting of gold, silver, copper, aluminium and perfect conductor cylinders in air at 3 THz is calculated. The length of waveguide varies from 10 to 100 periods long. The length of the waveguide is increased by adding one layer of rods to the length of waveguide at each step. The computation results showing the attenuation of the waveguide as a function of waveguide length are presented in Figure 6.19.

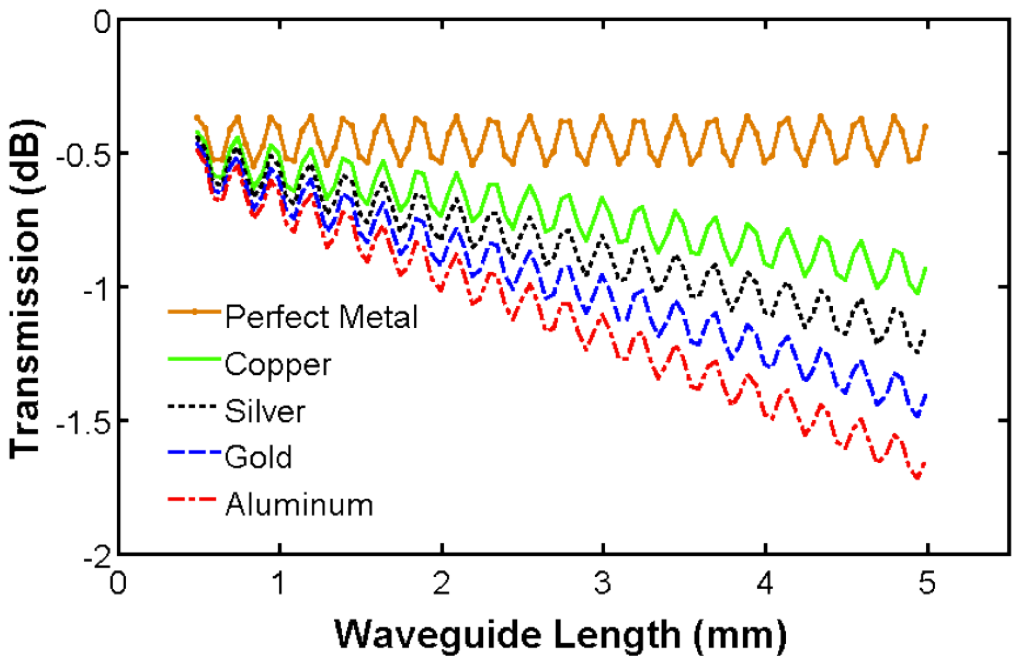

Figure 6.19: The transmission of triangular lattice waveguide as a function of waveguide length.

Because of the equidistant arrangement of rods with the period of half wavelength, the resulting transmission figure as a function of wavelength length has a sinusoidal waveform. In triangular lattice array due to the arrangement of rods, the sinusoidal waveform as not uniform as the square lattice array.In order to have a clear picture

Table 6.2: The attenuation values calculated from the transmission results as a function of waveguide length for W1 triangular lattice waveguides made of copper, gold, silver and aluminium.

	Attenuation (dB/mm)
Metals	W1 Waveguide
Copper	0.10007
Gold	0.19580
Silver	0.14553
Aluminium	0.24341

of the attenuation, the loss condition is included in the comparison. We calculate the transmission of the perfect metal by setting *perfect electric conductor* boundary conditions for rods. Thus, we ensure that the electric field inside the rods is zero. In the simulation of the perfect conductor case, no attenuation is observed as expected however the level of transmission is below zero, indicating that some of the energy is kept in the photonic crystal structure. As can be seen from the figure, the difference in transmission for even 100 rods-long waveguide for different metals, i.e. copper, gold, silver, aluminium is very small. Therefore, the difference will not be very clear when the transmission is plotted as a function of frequency. The difference in transmission will only become clear if the transmission spectra are viewed at smaller scales. However, it is clear in the figure that transmission is decreasing, as the length of waveguide increases. Copper gives the best transmission while aluminium is the most lossy metal in the THz range among these metals.

The linear curve fitting values for W1 triangular lattice waveguide attenuation values are given in Table 6.2. As can be seen from the table, the lowest attenuation values are obtained with copper rods both for W1 waveguides, and the highest attenuation values are obtained with aluminium.

In the calculations for transmission characterisation of triangular lattice waveguides copper rods will be used in which the attenuation is 0.10007 dB/mm for W1 wave-

guide. The attenuation for same size copper rectangular waveguide is 0.12839 dB/mm.

6.5.3.1 W1 Waveguide

In a triangular lattice array, removing a row of copper rods from the photonic crystal structure forms the W1 waveguide. Dispersion and transmission characteristics are discussed for a triangular W1 waveguide.

The modal behaviour of the waveguide modes has a strong influence on the transmission characteristics. A high transmission is observed for a photonic crystal waveguide, within the band-gap, provided with a guided mode. Due to the interaction of guided modes with each other or outside the photonic band gap frequencies, transmission dips are observed in the transmission spectra of the waveguide.

In the dispersion diagram of the W1 waveguide presented in Figure 6.20 a), the waveguide is in the Γ - K direction, and for further understanding the triangular lattice band-structure, is shown in the figure with blue solid lines in the given direction. The photonic band-gap is independent of the lattice directions and is indicated with shaded areas. The dispersion curves of the modes are depicted with black dots. Even and odd guided modes in the photonic band-gap of the lattice structure are presented by red dots and red open dots, respectively. The transmission spectrum of the waveguide corresponds to the dispersion diagram shown in Figure 6.20 b) with a red solid line. The high transmission in the triangular W1 waveguide is occasionally interrupted by transmission dips. From the direct comparison between the dispersion and the transmission spectrum, we have a better understanding of both modal behaviour of guided modes and the transmission and transmission dips for W1 waveguide. Within the frequency of the photonic band-gap, the transmis-

sion dips correspond to the mini stop-bands which are observed from the dispersion diagram of the waveguide.

In the given direction that can be seen from the band-gap lines in the figure, there are many modes propagating inside the waveguide. These modes are shown with black dots. In the dispersion diagrams, we indicate only the guided modes as even or odd mode. The guided modes appear in the photonic band-gap, while the other mode lines are the modes outside the photonic band-gap, and therefore are not confined/guided in the line defect properly.

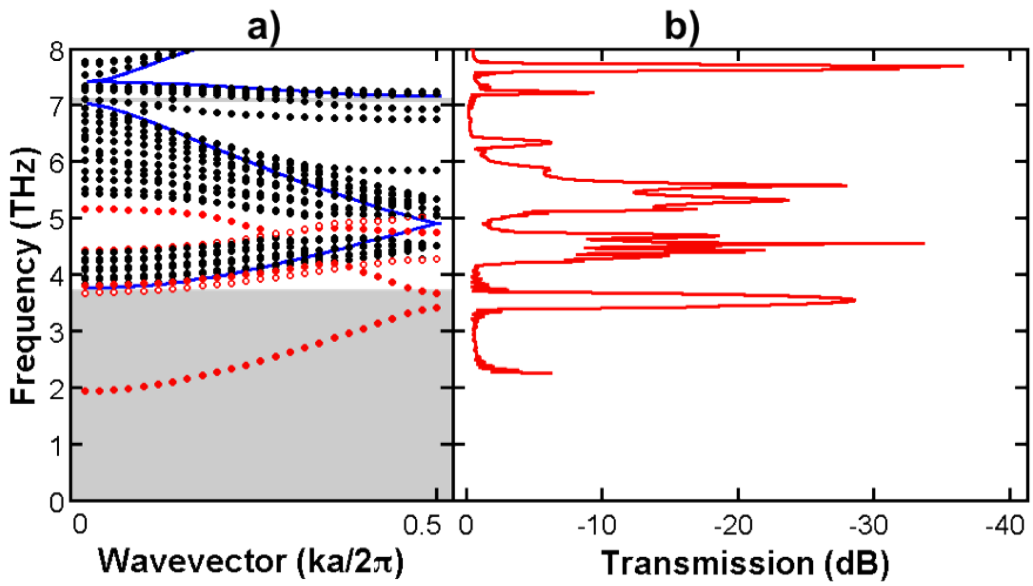

Figure 6.20: a) Dispersion diagram, b) transmission spectrum of W1 waveguide of copper rods in air in triangular lattice pattern for E-polarization. The radius of rods is $0.2a$, with lattice constant of 50μm.

The existence of the waveguide modes in this region is due to the band-gaps. Since an even mode is incident at the input, the fundamental mode is an even mode. An even mode appears between 1.926 - 3.412 THz. In this range the waveguide operates as a single mode waveguide. The fundamental mode folds back at the edge

of Brillouin zone, creating a mini stop-band between 3.412 and 3.666 THz, where the first transmission dip is observed. The folded mode may couple to higher order modes. As seen in the dispersion diagram, this is not provided by a band-gap. The dispersion diagram and corresponding transmission spectra exhibit excellent agreement.

In Figure 6.21 a) transmission, b) reflection and c) absorption spectra are shown for a W1 waveguide which is formed by removing a row of copper rods in an air background with lattice constant of 50 μm with rod radius of $0.2a$, $0.3a$ and $0.4a$, respectively. These waveguides are referred to as triangular W1_0.2, W1_0.3 and W1_0.4. Any transmission below -70 dB is not shown in Figure 6.21 a). Therefore, the transmission dips of -152 dB at 7.74 THz and -90 dB at 9.37 THz for triangular W1 waveguide with rod radius of 0.4a are not visible in the figure. The cut-off frequencies of W1_0.2, W1_0.3 and W1_0.4 are 2.26, 2.65 and 3.22 THz, respectively. The same size rectangular waveguides have cut-off frequencies 2.5222, 2.6501, 3.2187 THz, at very similar values.

Photonic crystals with smaller sizes of rods show a narrower photonic band-gap and this affects the transmission bandwidth of the W1 waveguide. There is also a shift in cut-off frequency values and the spectral positions of the transmission dips. In Figure 6.21 a) the transmission of W1_0.2 waveguide, which is shown in red solid line, has a higher level for the range between the cut-off frequency and the frequency, where the first dip is observed for the W1_0.3 and the W1_0.4 waveguide, shown in blue dash and black dash-dot lines. This range for W1_0.2 waveguide is wider (2.314 - 3.387 THz), than that of W1_0.3 (2.689 - 3.561 THz) and W1_0.4 (3.376 - 3.743 THz) waveguides.

For the W1_0.2 waveguide, the largest 3-dB bandwidth is obtained in the range between 7.745 and 8.96 THz, where the transmission level reaches up to 91.5%.

The highest transmission level, up to 96.1%, is obtained in the range between 6.4 and 7.195 THz. In this range, the waveguide has the lowest reflection values, while the absorption is around 10%. For the W1_0.3 waveguide, the largest 3-dB bandwidth is obtained in the range between 3.972 - 5.86 THz where the transmission level reaches up to 85%. The highest transmission level, up to 95.3%, is obtained between 8.736 and 9.72 THz. The highest reflection and absorption for this waveguide is obtained for 5.86 - 6.72 THz where the transmission is very low, the transmission dip is much wider than the other dips. In the W1_0.4 transmission spectra, the broadest bandwidth is obtained with the W1_0.4 waveguide, in the range between 4.377 and 6.468 THz. Another broad bandwidth region exists in the 7.845 - 9.148 THz range. The transmission level for this waveguide is moderate, mostly around 75%. High transmission levels are obtained for frequencies above 9.6 THz. The absorption is around 20% for a wide frequency range.

6.5.3.2 W3 Waveguide

By removing three adjacent rods in the Γ - K direction of a triangular lattice made of cylindrical copper rods in air, a W3 waveguide is formed. The lattice constant is set to 50 μm. The dispersion relation of the W3 waveguide with rod radius of $0.2a$ is calculated by computing the eigenmodes using FEM for E-polarization. This is shown in Figure 6.22 and compared to a transmission spectrum of a 25-lattice period long W3 waveguide. In Figure 6.22 a) the dispersion curves of the modes are depicted with black dots, while even and odd modes are plotted as red dots or red open dots respectively. The photonic band-gap is independent of the lattice directions and is indicated with shaded areas. The photonic band structure in the Γ - K direction is shown with blue solid lines. The guiding is achieved for frequencies within the band-gap regions, while outside these regions the modes are not confined in the waveguide. These modes represent the leaky modes where most of the energy

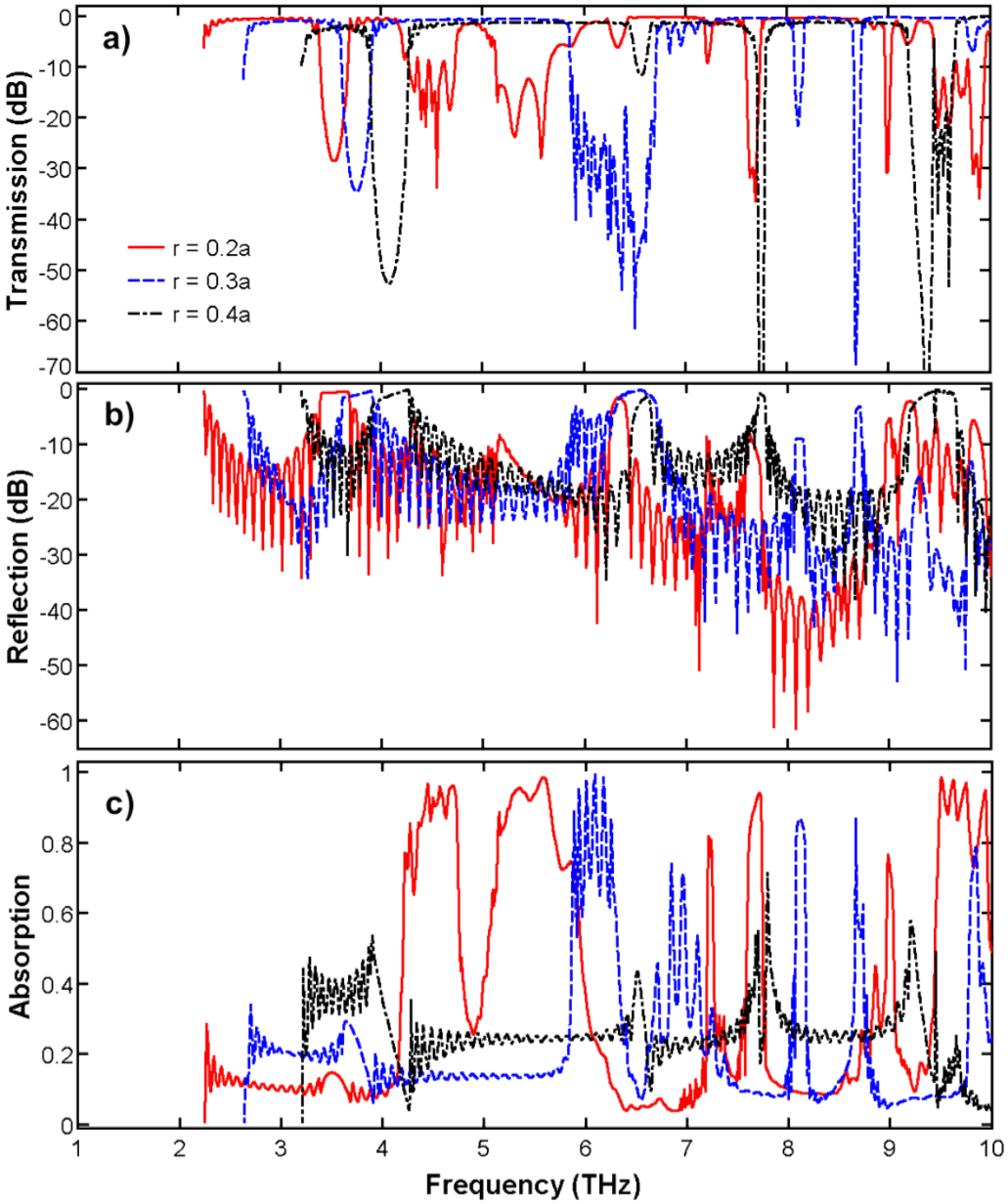

Figure 6.21: a) Transmission, b) reflection and c) absorption spectra for different W1 waveguides in triangular lattice array with rod sizes $0.2a$ (red solid line), $0.3a$ (blue dash line), $0.4a$ (black dash dot line) with lattice constant of 50 μm. Transmission, reflection in dB scale and absorption is calculated in linear scale.

is spread through the photonic crystal structure.

The transmission spectrum of the waveguide is shown in Figure 6.22 b) with a red solid line. The W3 waveguide supports more modes than the W1 waveguide, as the width of the waveguide is wider. In the calculation only E-polarization and the input wave that has an even parity with respect to the waveguide axis are considered. As discussed in the dispersion analysis of the W3 waveguide, within the first band-gap one odd and two even modes exist. In the transmission spectra of the W3 waveguide in Figure 6.22 b), a very narrow transmission dip is obtained between 3.03 and 3.22 THz due to the mini stop-band between 3.115 and 3.145 THz. Since the fundamental mode is well confined in the waveguiding channel within the photonic band-gap of the lattice, the dip is not deep. In the range between 3.54 and 3.73 a sharp transmission dip is obtained in the transmission spectra. However, a mini stop-band corresponding to this dip is not seen in the dispersion relation, since only coupling between even modes are considered.

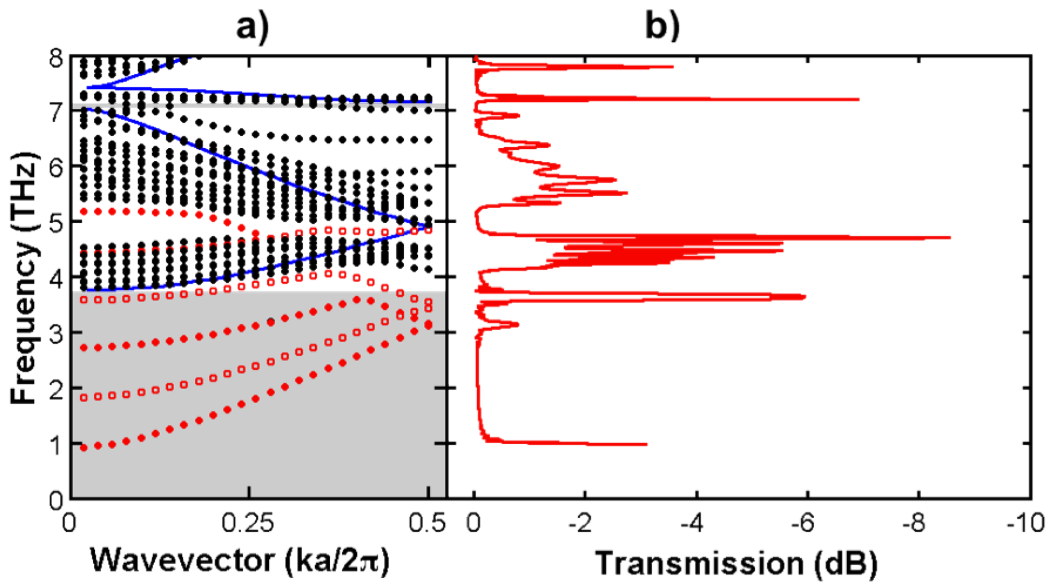

Figure 6.22: a) Dispersion diagram, b) transmission spectrum of W3 waveguide of copper rods in air in triangular lattice pattern for E-polarization. The radius of rods is $0.2a$, with lattice constant of 50 μm.

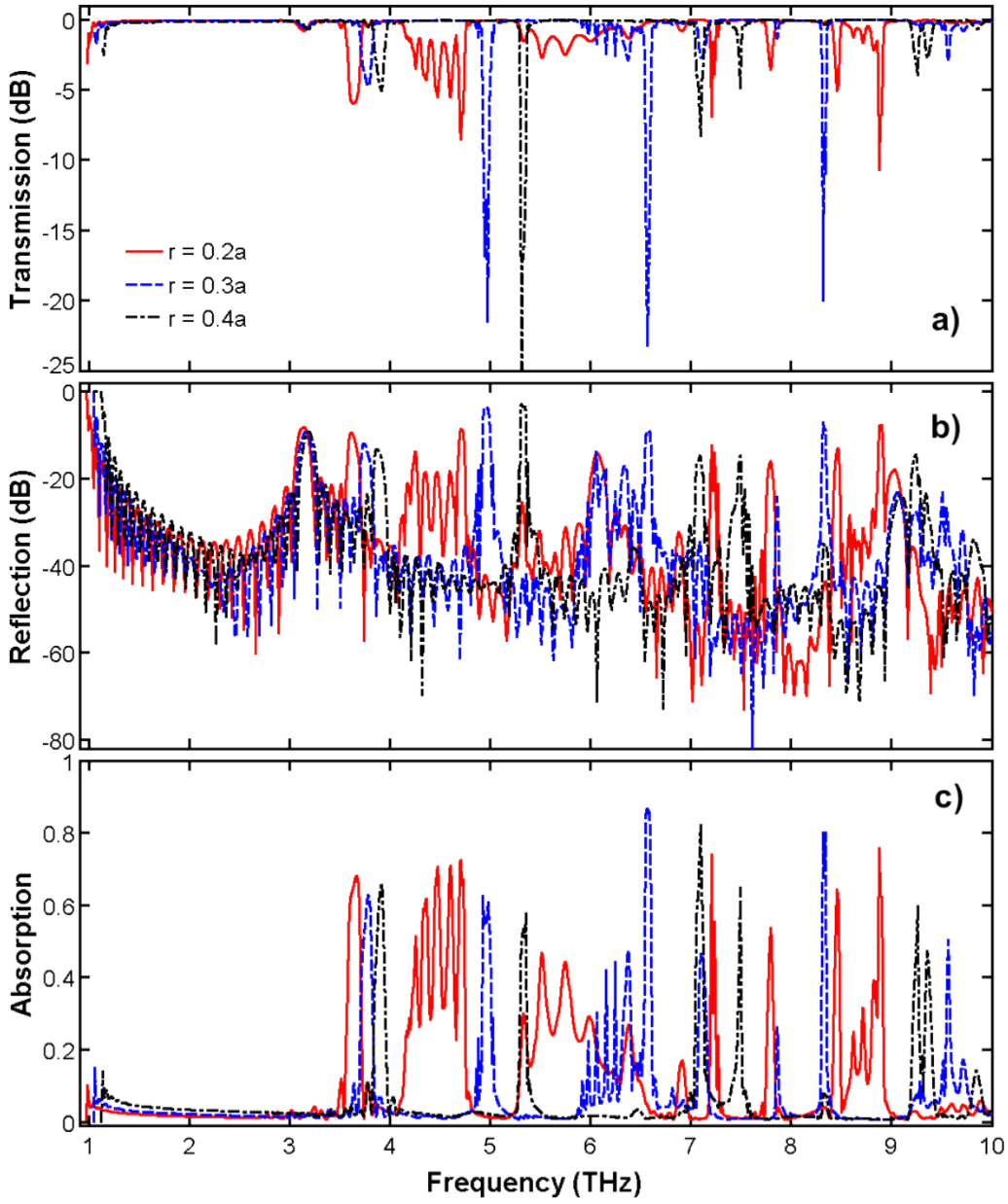

Figure 6.23: a) Transmission, b) reflection and c) absorption spectra for different W3 waveguides in triangular lattice array with rod sizes $0.2a$ (red solid line), $0.3a$ (blue dash line), $0.4a$ (black dash dot line) with lattice constant of 50 μm. Transmission, reflection in dB scale and absorption is calculated in linear scale.

In Figure 6.23. a) transmission, b) reflection and c) absorption spectra of W3 waveguides consisting of triangular lattice array of copper rods in air with lattice period

of 50 μm and rod radius equal to equal to $0.2a$ (10 μm), $0.3a$ (15 μm) and $0.4a$ (20 μm) are compared. The solid red line shows the transmission, reflection and absorption of a W3 waveguide with rod radius $0.2a$ while blue dash and black dash-dot line show that of a W3 waveguide with rod radius $0.3a$ and $0.4a$, respectively. In the figure, transmission and reflection are expressed in dB while absorption is expressed in linear scale. In the transmission figure, the dip of -34 dB at 5.31 THz for W3_0.4 waveguide is not shown, since the figure is scaled to show the transmission up to -25 dB. As can be seen from Figure 6.23. a) the cut-off frequencies obtained for triangular lattice waveguides W3_0.2, W3_0.3 and W3_0.4, are very close to each other at 0.979, 1.0474 and 1.1261 THz, respectively. These values are in good agreement with the cut-off frequencies calculated for the same size rectangular waveguides, which are 0.98, 1.05 and 1.13 THz respectively.

Broad bandwidths are obtained for the W3_0.2 waveguide between 0.98 - 3.575 THz and between 4.742 - 7.201 THz. For these frequency ranges, the transmission is also very high, over 95%. The largest bandwidth is obtained for the W3_0.3 waveguide in the range between 1.046 - 4.915 THz. The broadest 3-dB bandwidth of 2.73 THz is obtained in the range between 1.128 and 3.859 THz with the W3_0.4 waveguide. In the frequency range roughly between 1 - 4 THz, the absorption is very low for all waveguides. For the W3_0.4 waveguide, the absorption is very low, even below 5%, except at the frequencies corresponding to the sharp transmission dips.

Compared to the triangular W1 waveguide where the transmission characteristics are shown in Figure 6.21. a), the transmission characteristics of W3 waveguides show better properties in terms of 3 dB-bandwidth and transmission levels as can be seen in Figure 6.23 a). For all the triangular W3 waveguides compared in these figures, high transmission levels up to 99.5% and broad bandwidths over 1.5 THz are obtained.

6.6 Conclusion

2D metallic photonic crystal waveguides formed by line defects have been studied in this chapter for the use in THz application. Both transmission and dispersion characteristics have been investigated.

Firstly, we introduced the dispersion diagram of waveguides. In order to calculate guided modes in a line defect waveguide, eigenvalue calculations based on FEM were carried out using periodic boundary conditions over a supercell that takes into account the symmetry of the waveguide including the line defects, in a similar way to band- gap calculations over a unit cell of the lattice crystal. Two types of lattice pattern have been considered: W1 and W2 waveguides in square lattice pattern and W1 and W3 waveguides in triangular lattice pattern. All the structures are modelled with 2D approximations. The obtained band-gap diagrams for square and triangular lattices are important in order to select the frequency region where high transmission is expected. However, it is not enough to explain the transmission losses within the band-gap frequencies. In a waveguide both symmetric and anti-symmetric modes are active. The losses within the band-gap frequencies are associated with interaction, i.e. coupling, between the guided modes. By examining modal behaviour of guided modes, these losses can be explained.

In the transmission spectrum of a waveguide, the losses experienced due to a transmission dip are explained by the existence of mini stop- bands. There is a strong correlation between the dispersion diagrams and transmission spectra of the waveguides. The calculated transmission results show excellent agreement with the dispersion diagram in the (1-1) direction of waveguides, namely, in Γ - M for square lattice, and Γ - K for triangular lattice waveguide. The positions and the width of mini stop-bands in dispersion diagrams are well reproduced in the transmission

spectra as transmission losses.

We also employed FEM to calculate the transmission, reflection, absorption and dispersion characteristics of 2D metallic photonic crystal waveguides for E- polarizations. We introduced several photonic crystal waveguides made of copper cylinders in air. In the calculations copper has been used not only for its high reflectivity but also its low attenuation values for W1 waveguides with respect to gold, silver and aluminium. The attenuation is calculated from the transmission spectra of W1 waveguides by varying lengths.

Waveguides with larger widths, even though the single mode frequency window is small comparing to W1 waveguides, are better candidates for low loss THz transmission. For wider waveguides, the cut-off frequencies are obtained at lower frequencies, and this results in an increase in the transmission interval. Comparing the square lattice W2 waveguide with W1 waveguides and triangular W3 waveguides with W1 waveguides, the losses are higher in narrower waveguides. This can be explained by energy confinement in the guiding channel. More energy is confined in the wider waveguides than a narrow waveguide. Not only the transmission bandwidths increase but also transmission levels are more independent from the rod sizes. Up to 96% transmission is obtained in a square lattice W2 waveguide, for which a 2.8 THz- wide bandwidth is obtained. In a triangular W3 waveguide, a 2.73 THz-wide bandwidth is obtained with transmission levels up to 99.5%.

In the next chapter, we will focus our attention on the bend waveguides. Low loss bends in photonic crystal waveguides have attracted a great deal of attention. Sharp bend waveguides suffer from high reflection losses but with a careful design these losses can be reduced. Therefore, the studies are mostly concerned with the improvement of the bend waveguides to obtain broad bandwidths with low losses.

References

[1] J. D. Joannopoulos, *Photonic crystals: molding the flow of light*. Princeton University Press, Feb. 2008.

[2] K. Sakoda, *Optical properties of photonic crystals*. Springer, 2005.

[3] J. Smajic, C. Hafner, K. Rauscher, and D. Erni, "Computation of radiation leakage in photonic crystal waveguides," in *Progress in Electromagnetic Research Symposium*, (Pisa, Italy), p. 2124, 2004.

[4] M. Qiu and S. He, "Guided modes in a two-dimensional metallic photonic crystal waveguide," *Physics Letters A*, vol. 266, pp. 425–429, Feb. 2000.

[5] M. Augustin, R. Iliew, C. Etrich, F. Setzpfandt, H. Fuchs, E. Kley, S. Nolte, T. Pertsch, F. Lederer, and A. Tnnermann, "Dispersion properties of photonic crystal waveguides with a low in-plane index contrast," *New Journal of Physics*, vol. 8, p. 210, 2006.

[6] S. Olivier, M. Rattier, H. Benisty, C. Weisbuch, C. J. M. Smith, R. M. De La Rue, T. F. Krauss, U. Oesterle, and R. Houdr, "Mini-stopbands of a one-dimensional system:the channel waveguide in a two-dimensional photonic crystal," *Physical Review B*, vol. 63, p. 113311, Mar. 2001.

[7] M. Agio and C. M. Soukoulis, "Ministop bands in single-defect photonic crystal waveguides," *Physical Review E*, vol. 64, p. 055603, Oct. 2001.

[8] M. Qiu, K. Azizi, A. Karlsson, M. Swillo, and B. Jaskorzynska, "Numerical studies of mode gaps and coupling efficiency for line-defect waveguides in two-dimensional photonic crystals," *Physical Review B*, vol. 64, no. 15, p. 155113, 2001.

[9] S. Olivier, H. Benisty, C. Weisbuch, C. Smith, T. Krauss, and R. Houdr, "Coupled-mode theory and propagation losses in photonic crystal waveguides," *Opt. Express*, vol. 11, no. 13, p. 14901496, 2003.

[10] H. Jia and K. Yasumoto, "Rigorous analysis of guided modes of Two-Dimensional metallic electromagnetic crystal waveguides," *Journal of Electromagnetic Waves and Applications*, vol. 19, no. 14, pp. 1919–1933, 2005.

[11] COMSOL Multiphysics, ver. 3.5a, *User's Guide and RF Module User's Guide*. COMSOL AB, 2009.

[12] E. I. Smirnova, C. Chen, M. A. Shapiro, J. R. Sirigiri, and R. J. Temkin, "Simulation of photonic band gaps in metal rod lattices for microwave applications," *Journal of Applied Physics*, vol. 91, p. 960, 2002.

[13] Y. Zhao and D. R. Grischkowsky, "2-D terahertz metallic photonic crystals in Parallel-Plate waveguides," *IEEE Transactions on Microwave Theory and Techniques*, vol. 55, pp. 656–663, Apr. 2007.

[14] E. Degirmenci, F. Surre, and P. Landais, "2-D numerical analysis of metallic band-gap crystal waveguide in THz," in *34th International Conference on Infrared, Millimeter, and Terahertz Waves, 2009. IRMMW-THz 2009*, pp. 1–2, IEEE, Sept. 2009.

[15] X. Cui, *Photonic crystals with metallic inclusions*. PhD thesis, Swiss Federal Institute of Technology Zurich, 2006.

Chapter 7

METALLIC PHOTONIC CRYSTAL DEVICES

This chapter focuses on the design of THz waveguide bends and splitters based on metallic photonic band-gap (PBG) crystals. Transmission and reflection characteristics of 2D metallic photonic crystals bend waveguides and splitters are investigated for THz wave guiding. Simulations are carried out for both design and optimization of the structure in order to increase the bandwidth and the transmission level.

As pointed out earlier, the photonic crystal structures can be utilized to confine the wave or to propagate EM waves within the defects introduced in their structure using the band gap effect (1). The defects are introduced into the photonic crystal through removing rods not only to form a linear-line defect as in waveguide case but also other waveguiding devices such as bends, splitters, couplers, etc. By removing the rods, defect can be in any form depending on the design, such as a L-shaped in 90° bends or Y- or T-shaped as in power splitters. In order to design these devices, metals are preferred as a material especially for use in high power THz applications where devices made of dielectric material might not be a good option (2).

7.1 Bend Waveguides

For interconnection to other devices, optical waveguides are required to have flexibility of bending. However, bends introduce losses arising from total internal reflection. Conventional dielectric waveguides support guided modes with high efficiencies but transmission is limited in the case of bends as they need large radii of curvature to keep the bending losses at a reasonable level. To overcome this problem, PhCs have been studied because of their low losses and low dispersion properties. Indeed, almost perfect transmission has been obtained with sharp bends (3; 4). Nevertheless, metallic photonic crystals have demonstrated important advantages over the dielectric photonic crystals, such as wider band-gaps and smaller sizes (5; 6; 7). Metallic photonic crystals have been studied mostly in microwave and millimeter frequency range due to their low propagation losses (8; 9; 10). In this work, designs of metallic photonic crystal waveguide bends are proposed. Assessment of their performance has been studied by numerical simulations taking into account optimum parameters in terms of lattice constant and radius.

In the case of bending structures, transmission depends on the size and/or location of circular rods/holes on the bending corner, with losses due to reflections occurring in the bend and consequently the bending losses. Furthermore the design of bending corners becomes especially crucial for 90° bends. In order to improve the performance and to reduce the bending losses, many approaches have been developed. One of the most common approaches is to modify the geometry around the bending corner of 2D photonic crystals. Redeploying geometry of bending points in 2D photonic crystals (11), changing the rod/hole size (12) or replacing rods/holes on the corner with larger or smaller ones (13; 14; 15; 16), varying the width of line defects (17), or applying some optimization algorithms (18; 19) can be given as examples. Previous studies have even demonstrated that the bending losses can be

drastically reduced in curved bend waveguides (20; 21; 22).

In this section, different bend waveguides are compared and the effect of the corner rods on the losses is identified. Here, two types of bend waveguides studied here are 90° and 60° bends. When square lattice pattern is more convenient for 90° bends, 60° bends achieved easily with triangular lattice pattern.

7.1.1 90° Bend Waveguides

In this paragraph, we investigate different types of 90° bends on 2D metallic photonic crystals composed of square lattice arrays of cylindrical metallic rods in air. Waveguides are implemented by removing one or two rows of rods from their square array creating W1 (single-line defect) or W2 (double-line defect) structures. Basically, the only difference between W1 and W2 designs is the width of the waveguide. In the W2 waveguide, the waveguide width is a lattice constant wider than that of the W1 waveguide. The transmission and reflection performance of a THz linear waveguide based on this structure is presented. From these results, we design various 90° bend waveguides. An improved curve bend design is proposed as an efficient solution for a THz 90° bend waveguide (23). From our simulations with the improved bend waveguide design suppression of bending losses and transmission levels comparable to that of straight linear waveguides has been achieved.

Based on the dispersion diagrams of W1 and W2 waveguides discussed in the previous chapter, five 90° bend structures have been analyzed in this section. A schematic of the W1 bend waveguides is depicted in Figure 7.1 a) and Figure 7.2 a) along with the transmission and reflection spectra for W1 and W2 bend structures. Analyzed bend geometries have been labeled from sharp bend (bend I) to curved bend (bend V). With respect to the sharp bend, bend II is designed by replacing one rod

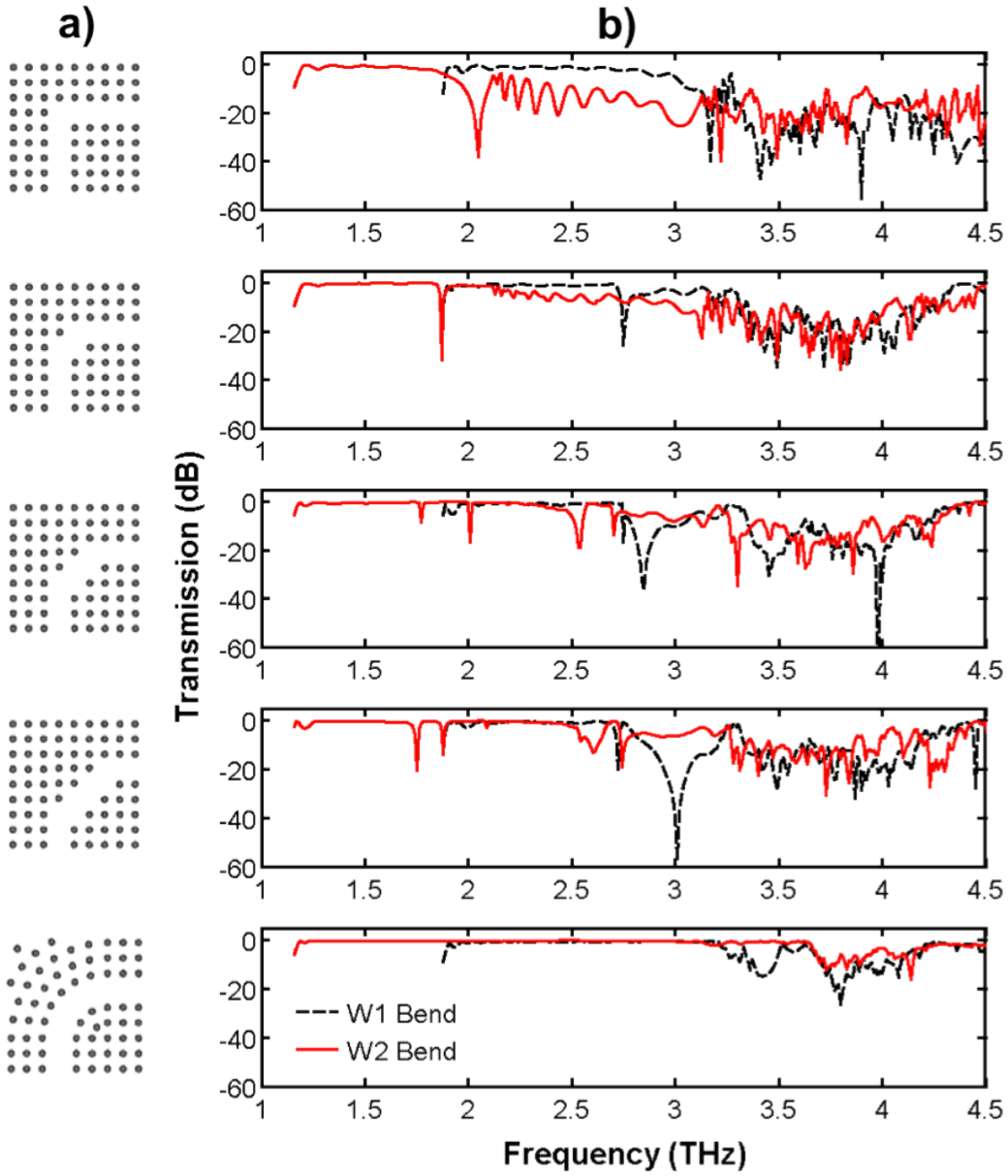

Figure 7.1: a) Schematic of the five bend designs and b) transmission spectra for five different 90° bend designs as a function of frequency, from 1 to 4.5 THz. For each given design a schematic illustration of W1 bend waveguides is depicted on the right hand side of the spectrum, for bends I to V. W2 bend waveguide geometries are similar to W1 except for the width of the waveguides. Black dashed-line corresponds to the W1 while red solid is for W2 bend waveguide.

from inner-edge position to the outer-edge position. Following the same procedure, bend III and bend IV are designed by replacing three and six rods, respectively. Bend V is formed by arranging the rods on the bending corner in order to obtain an arc-shape of a quarter-circle. A simple algorithm determines the position of rods on the arc-shapes to keep a fixed lattice constant distance between rods and also to keep the axial symmetry of the bends as much as possible. An exception has been made on the smallest arc of the bend V design: the lattice constant distance becomes smaller (39.27 μm) than a due to the extra rod added to the bend arc to ensure the symmetry. Otherwise in bend V the distance between two successive rods is kept uniform at a lattice constant length. The results presented here are based on square arrays of 26 and 27 rods per side for W1 and W2 bend waveguides, respectively. Once the bend is optimized, the attenuation inherent to the metallic material exhibits a secondary effect on the waveguide effective length. Therefore, depending on the length of the waveguide transmission level can be slightly higher or lower. However, it is seen that as long as the channel length is not altered, increasing the number of columns of rods ($>$5) on each side of the wave- guiding channel does not change the transmission or reflection level.

The guiding mechanism in photonic crystal structures is based on the photonic band-gap effect; it is different from conventional dielectric waveguides, which relies on total internal reflection. Therefore, it is expected that losses will be seen in photonic crystal structures when the frequency does not fall within the PBG range as the structure becomes transparent when it is reflective for the frequencies in the PBG. When a bend is introduced into a PhC waveguide, in PBG range, as no power is radiated out of the waveguide, the wave is guided through the bend. However, it still experiences some losses.

Our aim is to design such a bend waveguide to reduce the bending losses and to achieve a level of the transmission comparable to that of a linear waveguide.

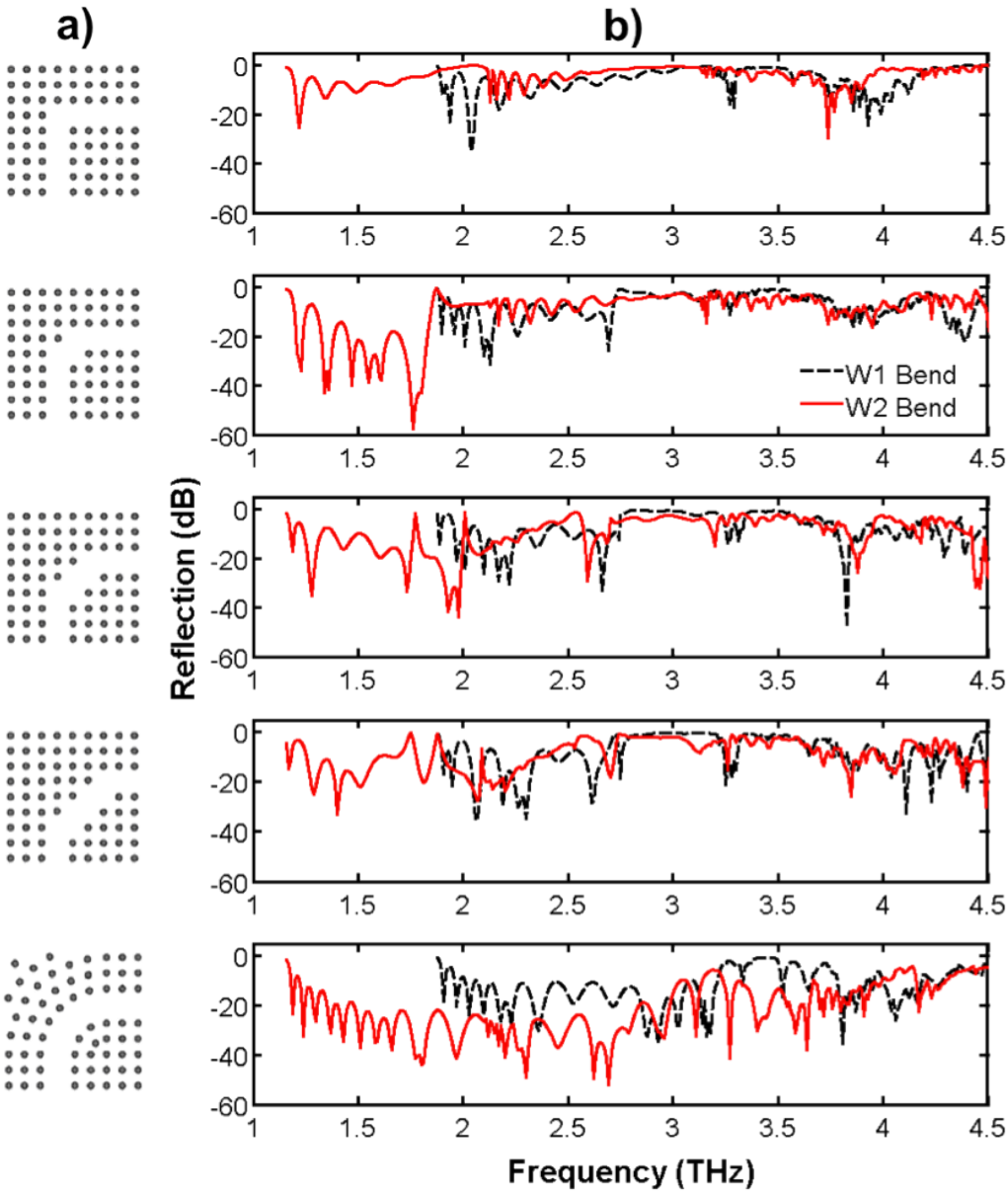

Figure 7.2: a) Schematic of the five bend designs and b) reflection spectra for five different 90° bend designs as a function of frequency, from 1 to 4.5 THz. For each given design a schematic illustration of W1 bend waveguides is depicted on the left hand side of the spectrum, for bends I to V. W2 bend waveguide geometries are similar to W1 except for the width of the waveguides. Black dashed-line corresponds to the W1 while red solid is for W2 bend waveguide.

Analysis can be easily achieved by comparing the transmission spectra with linear waveguides. When designing a bend structure it is essential to suppress losses arising from the bend. The losses in a PBG bend waveguide are mainly due to either the band- gap, the characteristics of the material (the losses which exist in the case of linear waveguides) or the losses occurring because of the bend itself such as back reflection and modal mismatch (24). Moreover, metals are known for their reflective properties especially in the microwave region. As they are still reflective in THz range, some losses originating from metal reflection are expected in addition to the bending losses.

The characterization of five designs is carried out in terms of propagation performance of 90° bend waveguides. A sharp corner is firstly studied and then making the bend corner smoother at each successive step, transmission spectra and reflection spectra are obtained for the frequency range between 1 to 4.5 THz where single mode is the predominant operating mode, as depicted in Figure 7.1 b) and Figure 7.2 b), respectively. Because higher order modes are strongly affected by bends, transmission of single mode is preferred in the bend waveguides based on photonic crystals.

There are issues that affect wave propagation in a bend, such as losses generated around the bending corner itself or reflection from rods placed in the corner. Reflection losses can be minimized by improving the design of the corner (smoothening the corner) and increasing its length. Not only the transmission level but also the bandwidth can be improved. For instance, a given improvement in terms of transmission level and bandwidth can be observed comparing the performance of the bend I design with respect to bend II to IV, as shown in Figure 7.1 b) and Figure 7.2 b).

There are sharp dips observed, mostly visible in the transmission spectra of bend

waveguides presented in Figure 7.1 b). In order to address the reasons of these dips, whether they are due to the losses arise from the bending geometry or originated from the dispersion characteristic of photonic crystal, it is needed to take a closer look at the dispersion diagram of corresponding waveguide. For instance, in the case of W1 bend waveguides, (this can be observed from the dispersion diagram of W1 waveguide studied in the previous chapter) the guided modes clearly indicate that the sharp loss peaks at $\sim$3.2 THz are observed caused by mini stop-band due to gap created when the mode folding at the Brillouin zone occurs during the transition from single mode to multimode. This can be also seen from the transmission spectra of W1 linear waveguide. The guided mode for bends is shifted to the lower frequency, creating a smaller gap on the boundary of Brillouin zone resulting in sharp dips in the transmission spectra. Another dip is seen at $\sim$3.8 THz, which corresponds to the pass band of the metallic photonic crystal structure, which is observed in the photonic band-gap diagram of square lattice structure. The positions of these dips are changing from one bend to another; the dips are shifted in frequency mainly due to their bend region length.

The transmission level still presents losses in the high frequency part of the spectrum over 3 THz, which should be reduced. Another important issue affecting the bending losses is that the modes propagating in the waveguide may not be compatible with the bend geometry, triggering the higher order modes, especially as the frequency increases. This segment and the bending corner might not be the same; a reasonable solution is to bend the waveguide while keeping the width size of the corner by curving the PBG structure. In this context, curved bend structure (bend V) has been simulated and it is seen that with this structure an optimization can also be obtained for metallic photonic crystal waveguides. The curved bend shows better characteristics, as the size of wave guiding channel in the corner and at junctions to the linear waveguide is almost identical for the whole waveguide.

As one more row of rods is removed in W2 design the width changes from 80 μm to 130 μm and as a consequence, the cut-off frequency shifts from 1.875 THz to 1.15 THz. In this regard, for W2 bends, the bandwidth is extended for the interval positioned between these two cut-offs. Comparing the transmission results for W1 and W2 bend waveguides for the first four designs, W2 bend waveguides give a wider transmission bandwidth. However, for the frequency interval between 1.8 THz and 3.1 THz, the transmission level is lower than that of W1 bend waveguides for bend I and bend II and there is a small decrease in bend IV in comparison to bend III. Despite these, both transmission level and bandwidth improve with the bend smoothening. As depicted in Figure 7.1 b), a significant improvement is demonstrated for design V in relation to the other four designs in terms of transmission level and bandwidth for both W1 and W2 bend waveguides. As can also be seen from Figure 7.2 b) in parallel with Figure 7.1 b), with the degradation of reflection losses, transmission is improved. With bend V waveguide a level of reflection up to -50 dB is obtained. Comparing the sharp and the curved bends, transmission level improves from -0.6048 dB to -0.3152 dB for W1 bend waveguides and the largest 3-dB bandwidth improves from 0.8 THz (1.956 THz - 2.769 THz) to 1.3 THz (1.916 THz - 3.24 THz) when we compare the sharp bend with the curved bend. For W2 design improvement is more significant. The transmission increases from -0.4096 dB to -0.0877 and the largest 3-dB bandwidth from 0.7 THz (1.164 THz - 1.85 THz) to 2.5 THz (1.164 THz - 3.671 THz).

Additionally, the overall bandwidth also improve when bend I and bend V are compared. Here, the overall bandwidth is defined as the sum of frequency intervals where the transmission is within 3-dB. For W1 bend waveguide, the overall 3-dB bandwidth improves from 0.921 THz to 1.699 THz, giving the proportion of overall bandwidth to whole frequency interval (from the cut-off at 1.875 THz to 4.5 THz) of 35% and 65% for bend I and bend V, respectively. For W2 bend waveguide, overall bandwidth is 0.686 THz and 2.793 THz, giving the ratio of overall 3-dB

bandwidth to whole frequency interval (from the cut-off at 1.15 THz to 4.5 THz) of 20% and 83% for bend I and bend V, respectively.

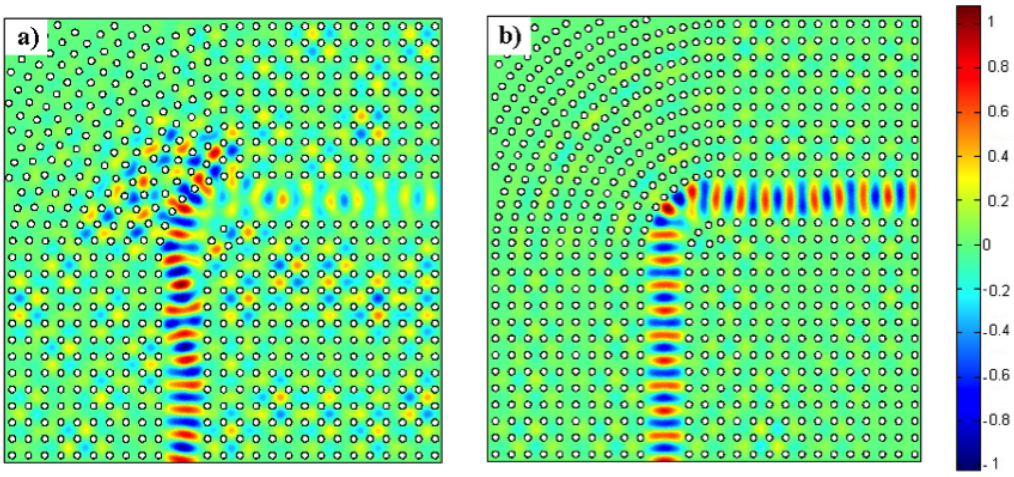

Figure 7.3: Illustration of the wave propagation of a) bend V and b) improved bend V waveguides at 4.1 THz where transmission is improved with the design. Blue and red regions show the positive and negative parts of electric field distribution. The electromagnetic wave is confined and propagates perfectly within the guiding channel in improved bend design formed by removing two rows of rods. Geometry of this design can also be seen, in which circles correspond to the metallic cylinder rods.

According to the obtained results, even in the case of bend V in which most of the losses are suppressed, there are still losses above 3.2 THz where higher order modes are active. With further analysis, wave propagation shows that in the high frequency region, even though most of the energy is confined in the waveguide with an appropriate design, some of the energy that is lost leaks through the rods, especially around the bend, as presented in Figure 7.3. By applying some geometrical re-arrangements on curved bend design, these losses can be reduced and the quality of transmission can also be improved in the high frequency region. The aim is to maintain a high transmission level and to increase the bandwidth even further. With this in mind, the effect of increasing the number of rods on the bending arcs without

changing the size of rods is investigated. On the bending arc the r/a ratio becomes 0.2546 instead of 0.2. In this case, on the bending arc the lattice constant distance changes from 50 μm to 39.27 μm, while for the rest of the waveguide, the lattice constant is still 50 μm. In order to distinguish this design from bend V, it has been named as improved bend V. The waveguide design of bend V and improved bend V, and the propagation of a 4.1 THz electromagnetic wave within these bends are depicted in Figure 7.3. At this frequency while almost all the wave leaks through the outer corner of bend V (see Figure 7.3 a)), the wave leaks are stopped around the bend within the improved bend as seen in Figure 7.3 b).

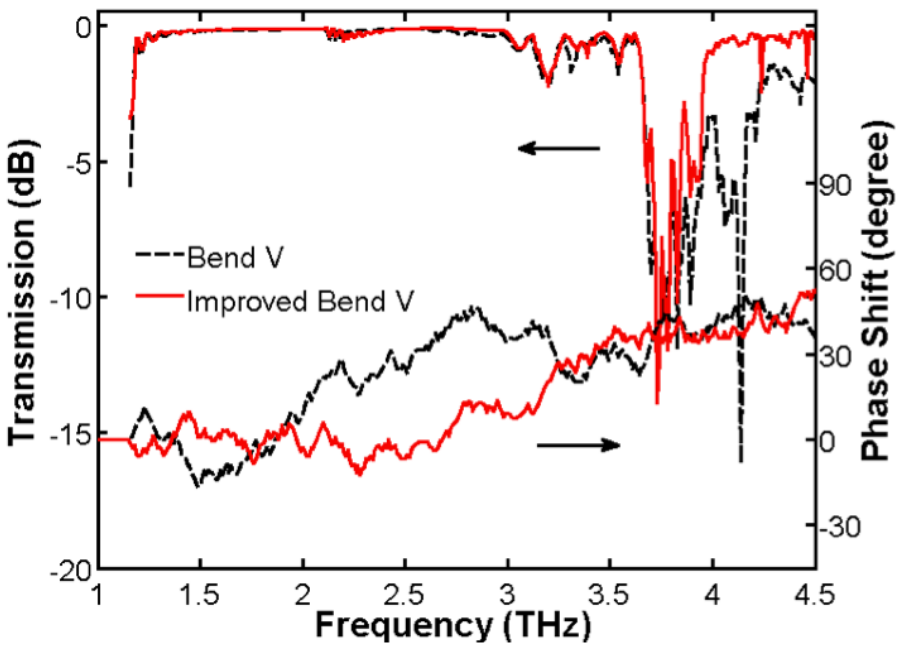

Figure 7.4: Transmission spectra and frequency dependence of the phase shift for bend V (black dashed line) and improved bend V (red solid line) waveguides in the case of two rows of rods are removed from metallic band-gap structure.

Transmission characteristics are compared for bend V and improved bend V for W2 waveguide where two rows of rods are removed in the metallic photonic crystal waveguide. The new proposed structure provides a significant improvement in bandwidth and transmission not only for W1 but also for W2 bend waveguides, as

illustrated in Figure 7.4. By using this design transmission level is improved, especially for the frequencies where the bending losses are higher (between 3.67 and 4.5 THz). It can be clearly seen in Figure 7.4 that dramatic enhancement is obtained especially for frequencies above 3.95 THz. The improved bend V waveguide has a high transmission performance of up to 98%. More than 97.5% transmission is achieved between 2.451-2.592, 2.607-2.748 and 4.53-4.544 THz. The largest 3-dB bandwidth transmission is obtained from 1.165 THz to 3.669 THz (2.5 THz), and overall 3-dB bandwidth is wider than that of bend V (3.1 THz), giving the proportion to the frequency interval of 91% for double-line defect. For W1 design, transmission is improved to -0.2687 dB and overall bandwidth is to 71%. This improvement can also be observed in the frequency dependence of the phase shift based on the reflection coefficient. Phase-shift spectra are obtained in order to determine the dispersion properties of PhC bend structures. The frequency-dependent phase shift spectrum provides the information about electromagnetics wave reflected from the bend structures.

Bend V shows a variation of the phase shift from -15° to +40° over a spectral range of 1.5 THz to 4.5 THz. The improved bend V exhibits almost no phase shift from the cut-off frequency 1.15 THz to 3.1 THz and then presents a quasi-linear frequency dependence to reach a value of +50° at 4.5 THz. The negative (positive) phase shift in the spectral domain leads to a waveform appearing earlier (latter) in the temporal domain. Hence the improved bend V structure produces a positive dispersion for a broad bandwidth signal above 3.1 THz.

A comparison between a linear waveguide with equivalent length is presented in Figure 7.5. Such a simulation allows for the identification of the losses inherent to the bend, providing an insight on the performance of the improved bend waveguide for frequencies around 3.8 THz, where the largest losses are obtained. The valley in the transmission spectrum has already been encountered in linear waveguides. It

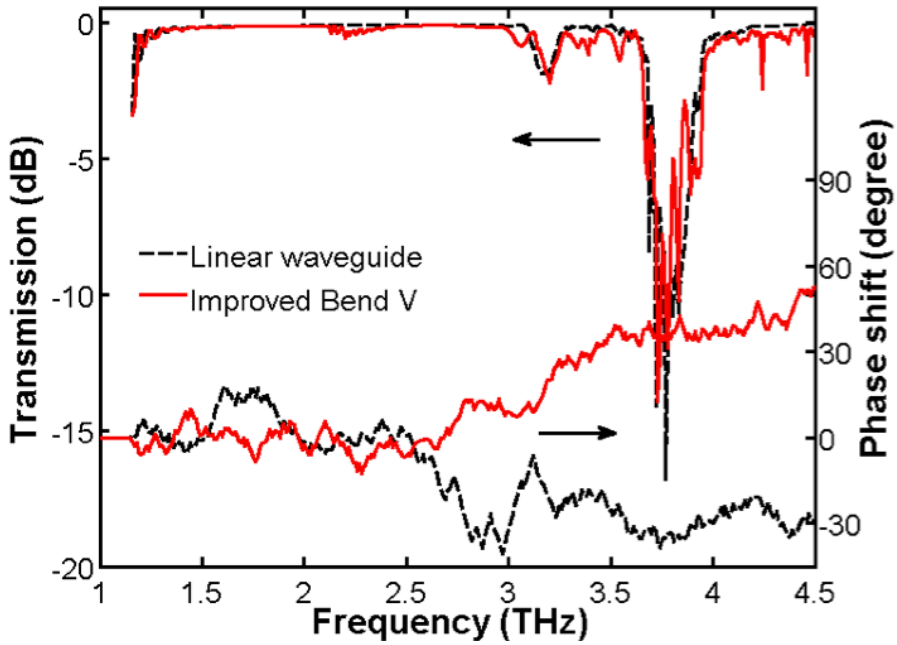

Figure 7.5: Transmission spectra and frequency dependence of the phase shift for improved bend V (black dashed line) and same length linear (red solid line) waveguides in the case of two rows of rods are removed from metallic band-gap structure.

is attributed to the band-gap characteristics of metallic photonic crystal waveguides associated to its band-pass. Therefore, we have succeeded in drastically suppressing the bending losses by improving bend V design, obtaining not only a higher transmission and larger bandwidth but also reaching the transmission level of same length linear waveguide composed of the same material and keeping the same lattice constant and rod radius. The frequency dependence of the phase shift of the linear waveguide is almost 0° between 2 THz and 2.6 THz and then is set at -30° up to 4.5 THz. In the single mode region the phase of waveguide is in line with linear waveguide, however, as the higher order modes have different phase velocities there is a phase shift between band waveguide and the linear waveguide. It is worth noting that the frequency dependence of phase shifts of the linear waveguide and the improved bend V are opposite. A combine use of these waveguides results in quasi no dispersion of a broad THz signal over the spectral range achievable.

As it is presented here, the proposed waveguide improved bend V is quite effective in reducing the losses with a small dispersion and yet easy to implement, as the size of rods are the same for the whole structure, which is an important issue for the fabrication process. Metallic band-gap structures for THz bend and linear waveguides have been simulated using the Finite Element Method. Transmission characteristics of 90° bend waveguides have been investigated for various square array waveguide designs. The simulation results reveal that the transmission of sharp bends can be improved with design modifications on the bending corner. After several steps we finally achieved a high performance for the transmission and dispersion with an improved curved bend design in the case of double-line defect waveguide. We have also demonstrated that the level of reflection can be decreased and reach the transmission level of a linear waveguide with the proposed improved curved bend structure.

7.1.2 60° Bend Waveguides

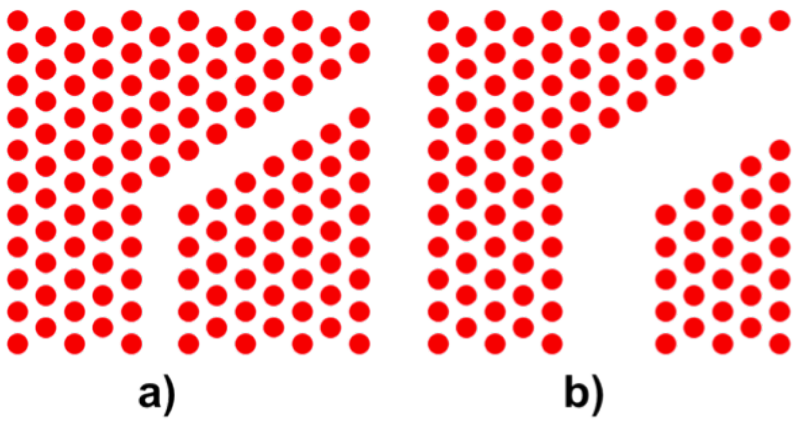

Figure 7.6: Schematic illustration of a) W1 and b) W3 photonic crystal bend waveguides in triangular lattice array.

We have carried out this study, on same type of structure, metallic cylindrical rods in air medium. 60° waveguide bends are best achieved in triangular lattice structure because of its natural shape; by removing the rods in order to form a cavity has a

60° curvature. This type of bend waveguide actually used mostly for inverse configuration (air holes in a structure with solid material), i.e. photonic crystal slabs, since triangular lattice presents larger band-gaps in this configuration for dielectric photonic crystals (17; 25; 26; 27; 28).

For the frequencies in the band gap of the structure, modes propagate along the wave-guiding channel. Light continues propagating and turn the corner when there is a bend. However, light propagation around the corner causes a loss in the propagation. There can be many reasons for these losses, but the back reflections can be considered as one of the main reasons that significant amount of energy cannot be transferred to the output. Another reason of losses associated with bends is the discontinuities between linear waveguide and the bending region, which may lead to excitation of higher order modes mostly evanescent.

In our design for optimization of bend waveguides, considering the fabrication of such devices, we keep the same rod size in the whole structure. Therefore, we avoid replacing rods on the bending corner with smaller or larger rods; instead we re-placed the rods on the bend to achieve a smoother bending corner. We also keep in mind that, symmetry in these structures should be kept considering the use of two or more bend structure together in cascade.

Waveguides in triangular lattice are formed by introducing line defect of rods in the Γ - K direction of the PhC. Simulations carried out for optimizing the lattice parameters and the bending corner. The structure under investigation has lattice parameters: rods having a radius of 15 μm (0.3a) in a triangular lattice with lattice period, a, of 50 μm. These parameters are determined from linear waveguide analysis that gives large transmission bandwidth with fabrication practicality is considered. In order to improve the transmission and enlarge the transmission bandwidth, 60° waveguide bends are tested. Transmission is calculated in dB and 3-dB

bandwidth is used to describe broadness of bandwidth, transmission level also highlighted in percentage. Despite the fact that parameters are optimized for waveguide case, the 60° waveguide bend before any optimization gives a narrow transmission bandwidth. We can describe this bend as sharp bend or bend I as it was in 90° waveguide as seen in Figure 7.6.

For the 90° bend waveguide design, by replacing the sharp bending corner with a curved bend, we have obtained better results as discussed in the previous section. Smoother bend design as well as keeping the width size at the bending corner were the key points of designing an improved 90° bending corner. In order to design smoother bending corner for 60° bend, we have utilized 2nd degree Bézier curves (29).

In order to create an arc between two linear sections with a 60° angle, 3 control points are needed to construct a quadratic Bézier curve. Construction of the Bézier curve for 60° bend corner is shown in Figure 7.7. P_0 and P_2 are the end points and P_1 is the intermediate point. The details on Bézier curve approximation can be found in Appendix B.

Similarly to 90° curved bend waveguide design, in which rods around the bending corner are positioned on the curve of quarter of a circle, an algorithm based on quadratic Bézier curve approximation is used in order to find the rods spatial positions in the bending geometry of 60° bend waveguide. This design is named as bend II. Rods positioned equal distant from each other on a quadratic Bézier curve. On the bending corner of bend I design 3 layers of rods are replaced with Bézier design of upper and lower corner of the bend. On the diagonal axis of bends, additional rods are placed in order to prevent wave localization in the defect form between sharp and the curved geometries.

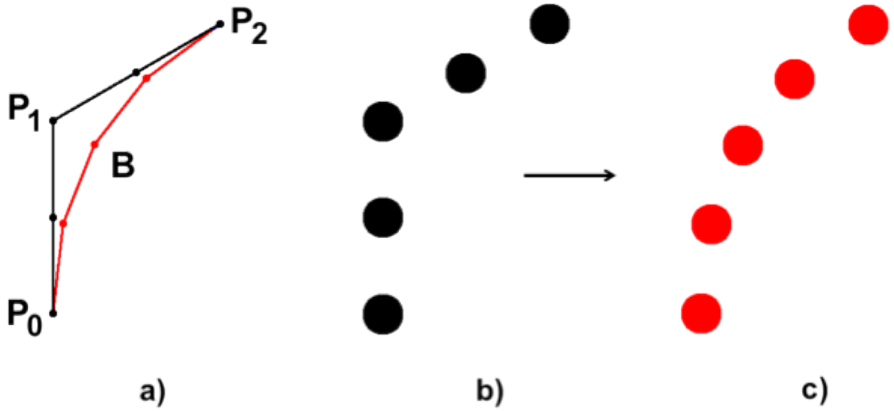

Figure 7.7: a) Construction of a quadratic Bézier curve for 60° bend design. b) the rods on the sharp bending corner c) the rods positioned according to the Bézier curve.

Triangular W1 waveguide with $r = 0.3a$ exhibit high transmission between 2.65 - 5.86 THz, however this range experiences a transmission dip between 3.6 - 3.9 THz. In Figure 7.8, bend waveguides also have this dip around 3.75 THz corresponding to the mini stop-band of W1 waveguide. The cutoff frequency for W1 waveguide is 2.65 THz, and this matches the cutoff frequency of same width rectangular waveguide. However, when we look at the transmission spectra of 60° bend waveguides, we see that, there is a region below the cut-off frequency, between 2.15 and 2. 65 THz. In the calculations this transmission is detected. The transmission here, is very low, the propagation of electromagnetic field is very weak and it can be ignored. On the other hand when we look at the reflection spectra, we have seen the real cut-off frequency as 2.65 THz as in the waveguide case.

In Figure 7.8, bend I and bend II exhibit very similar transmission characteristics in terms of transmission level and bandwidth in the 2.67 - 3.6 THz range. For frequencies over 4 THz, transmission is improved with bend II waveguide. In this range, as can be seen from Figure 7.8 b), the reflection is lower than bend I. Bend II waveguide is in the 3-dB bandwidth for 3.9 - 4.9 THz, in the range between 4.5 and 4.9 THz, the transmission has some fluctuations, while bend I waveguide has a

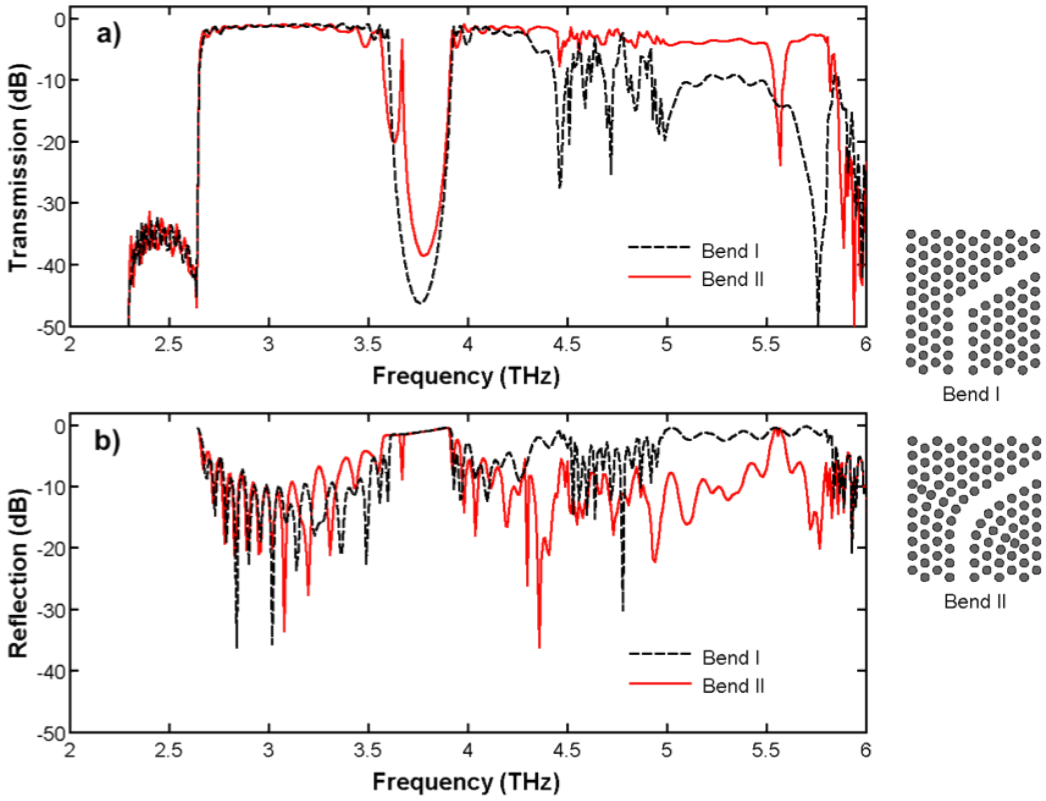

Figure 7.8: a) Transmission and b) reflection spectra of 60° bend designs as a function of frequency, from 2 to 6 THz. The schematic illustrations of W1 bend waveguides are depicted on the right hand side of the transmission figure. Black dashed-line corresponds to the Bend I while red solid line is for Bend II waveguides.

3-dB bandwidth between 3.9 and 4.3 THz with a small dip between 3.98-4 THz. In this 4 - 6 THz range the transmission of bend II waveguide is up to 80%, while for bend I waveguide it is up to 70%.

In Figure 7.9, transmission spectra and phase shift are compared for W1 linear waveguide and bend II waveguide. As seen in the figure, even though the transmission of bend II reaches the level of transmission of linear waveguide in the 3.9 - 4.5 THz range, for frequencies above 4.5 THz transmission is lower than linear waveguide. The frequency dependence of the phase shift results show that the phase of bend II waveguide is in line with linear waveguide. In the single mode region

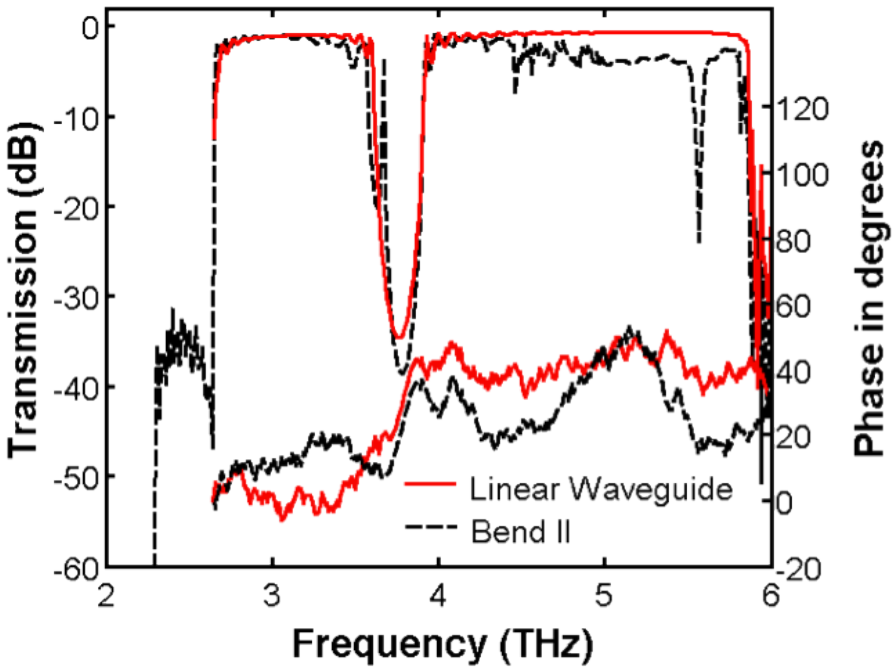

Figure 7.9: Transmission spectra and frequency dependence of the phase shift for bend II (black dashed line) and W1 linear (red solid line) waveguides.

of W1 linear waveguide, both bend I and bend II waveguides have high transmission as in the linear waveguide. Losses are started to be seen in the high frequency range where multimodes start to be active. Therefore, the bend structure experiences some losses. This can be attributed to the modal mismatch between the linear part and the bending corner of the bend waveguide instead of back reflection losses.

Transmission characteristics of W3 bend waveguides are also studied. Transmission and reflection spectra of sharp bend and curved bend in W3 structure are shown in Figure 7.10. As seen from the figure, bend II waveguide improves the transmission generally, however, it suffers to reduce the losses. In 1.046 - 3.716 THz range, as discussed in the previous chapter, W3 linear waveguide has very wide bandwidth and the transmission in this region is over 95%. Within band-gap of the W3 waveguide, between 1.144 - 1.775 THz, transmission of bend II is slightly higher than bend I, where for both waveguides transmission is over 90%.

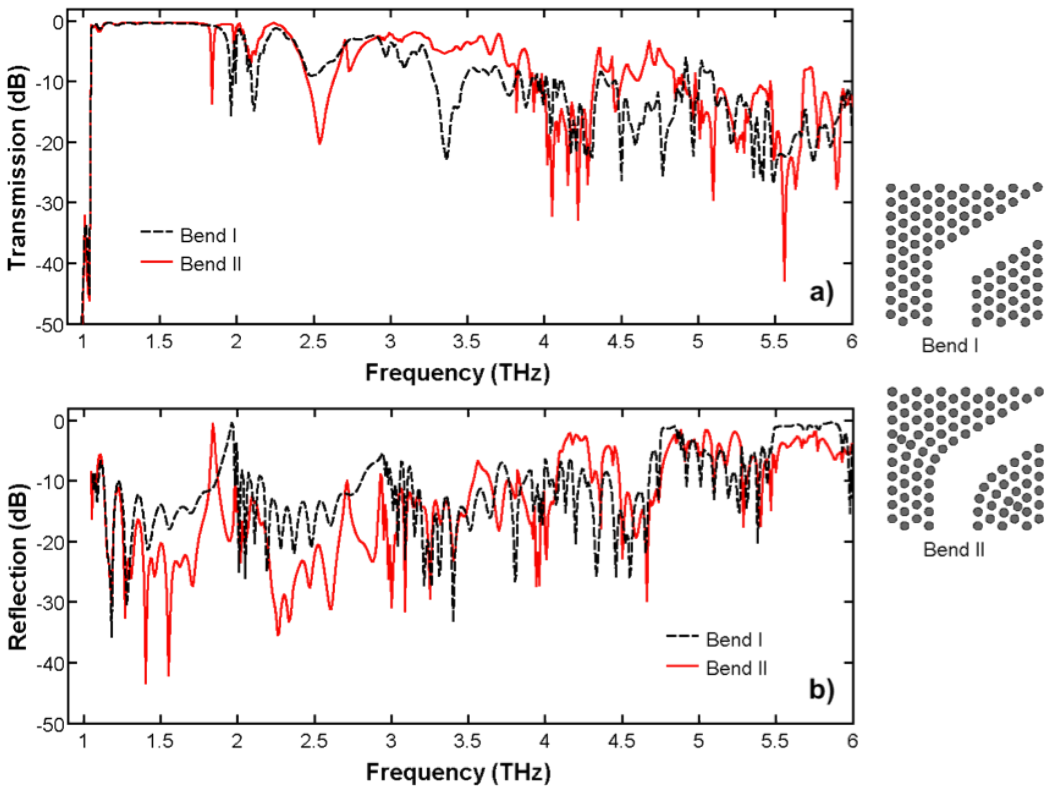

Figure 7.10: a) Transmission and b) reflection spectra of 60° bend designs as a function of frequency, from 2 to 6 THz. The schematic illustrations of W3 bend waveguides are depicted on the right hand side of the transmission figure. Black dashed-line corresponds to the Bend I while red solid line is for Bend II waveguides.

The electromagnetic wave propagation in a W3 bend II waveguide at 1.5 THz is shown in Figure 7.11 a). In the single mode region where bend II waveguide has a high transmission, wave is confined and transmitted perfectly. On the other hand, at 2.5 THz where a transmission dip is observed in the transmission spectra in Figure 7.10 a). The wave propagation at this frequency can be seen in Figure 7.11 b). While in the linear section up to the bending section even mode is propagating, multi mode is starting propagate after bending section. A modal mismatch occurs in the bending section, since the within the band-gap, all the wave is confined in the waveguiding area. The reason of the losses is the modal mismatch. Since the

symmetric mode cannot couple anti-symmetric modes, transmission is degraded.

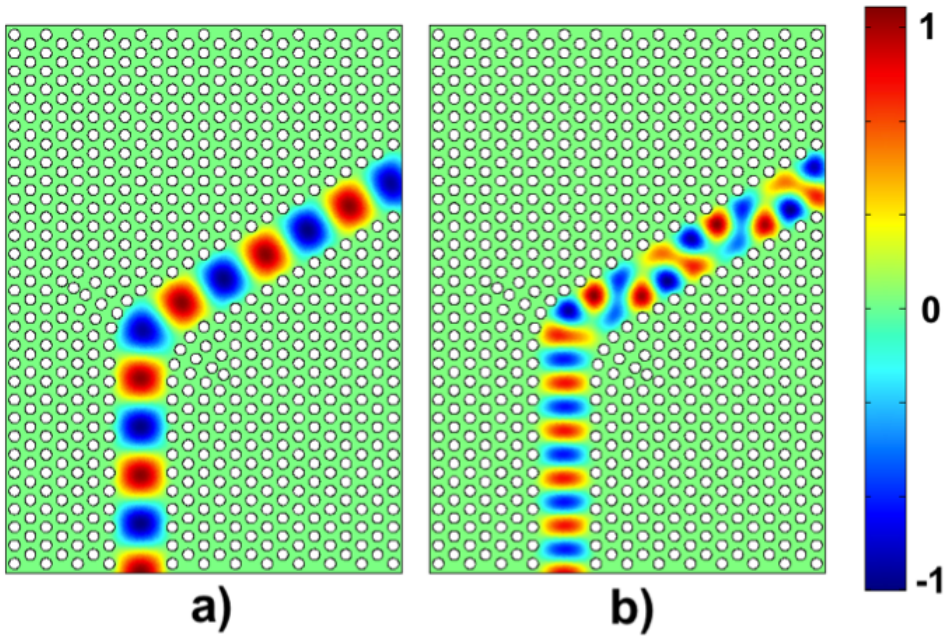

Figure 7.11: Illustration of the wave propagation of W3 bend waveguide at a) 1.5 THz and V and b) 2.5 THz. Blue and red regions show the positive and negative parts of electric field distribution. The electromagnetic wave is confined and propagates perfectly within the guiding channel in bend II design formed by removing three rows of rods. The circles correspond to the metallic cylinder rods.

7.2 Power Splitters

For frequencies within the band-gap, photonic crystals are convenient to design different devices by introducing defects. The wave propagation in a photonic crystal can be controlled and manipulated by using these defects. Power splitters based on a T-junction (30; 31; 32) and Y-junctions (33; 34; 35) of photonic crystals have been investigated in this paragraph.

Power splitters based on square and triangular lattice are investigated. Square lattice

is more suitable to form T-splitter, while triangular lattice is mostly used to form Y-splitter. Power splitters have one input and two output ports. If the symmetry is considered on the output ports, the input wave power is evenly divided by the structure. Since splitters can be considered combination of two or more bend waveguides, to improve the transmission power splitters, similar methods can be used as in bend waveguides.

T-splitter with curved splitting section show better performance over the T-splitter structures compared. The transmission reaches up to 88% with 1.044 THz bandwidth is achieved. Y-Splitter consists of three W1 defect connected to achieve 120°-angle between each other exhibits transmission of 80% with 0.853 THz bandwidth.

7.2.1 T-Splitters

We have studied several T-splitters based on square lattice. In the structure there exists one input and two output ports. The structure is symmetric with respect to the propagation direction of the incoming wave and wave is divided equally between two output branches. In T-splitter with no optimization, there are two sharp 90° bend corners. The T-splitter structures are based on square lattice of copper rods in air with lattice constant, a, and rod radius are set to 50 μm and 10 μm (0.2a), respectively.

First, we study simple T-splitter structures. Before any improvements take place, T-splitter with one rod on each corners removed are analysed. Transmission and reflection spectra of these two structures are shown in Figure 7.12 a) and b) with their schematic illustrations on the left hand side of each figure. It should be noted that, the transmission corresponds to one of the equally output branches, in other word, half of the total transmission. Therefore, 6-dB bandwidth is considered in

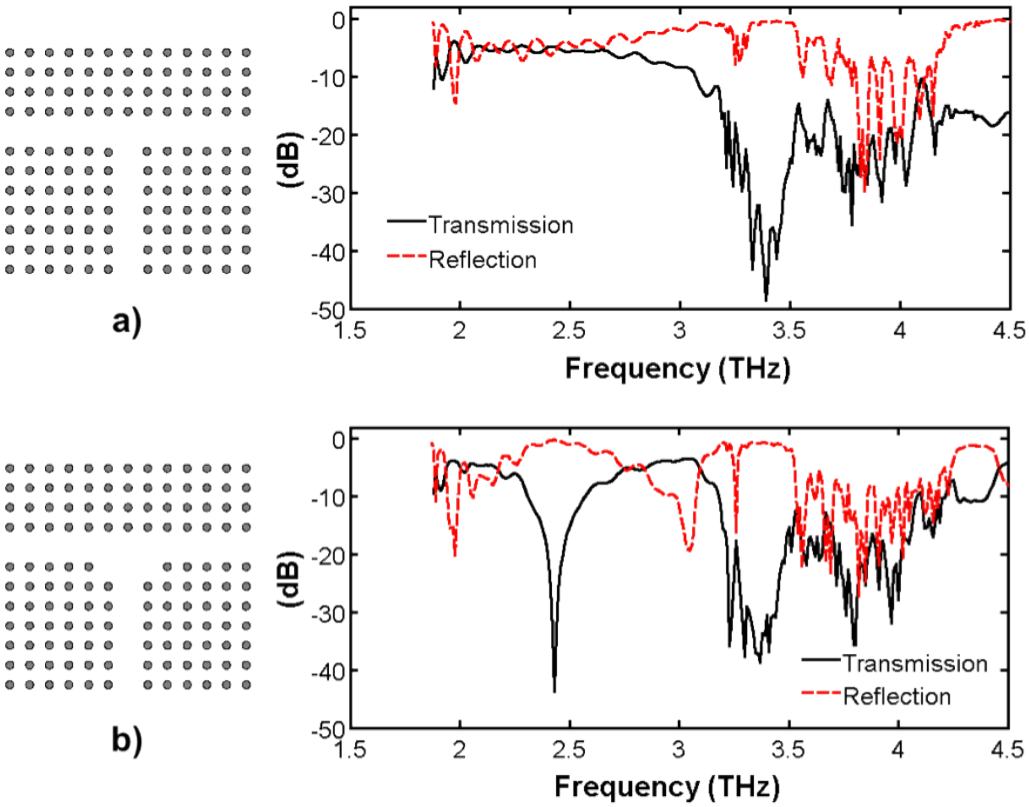

Figure 7.12: Transmission and reflection spectra of T-splitter a) without any modification b) with one rod are removed from each corner. Schematic illustrations of T-splitters compared are given on the left hand side of each transmission/reflection spectra.

this investigation.

For frequencies above 3.2 THz, the transmission for both structures is severely degraded. T-splitter is shown in Figure 7.12 a), has a 6-dB bandwidth between 1.949-2.81 THz with some fluctuations. The maximal value of transmission is 40%, which means 80% of total transmission reaches the outputs of this structure. In the range between the cut-off frequency at 1.88 and 3.2 THz, for the transmission spectrum of T-splitter shown in Figure 7.12 b) there is a dip at 2.43 THz which creates a wide gap between 2.187-2.722 THz. The transmission is improved in 6-dB regions between 1.933-2.187 THz by 2%, and 2-722-3.107 THz by over 5% and total trans-

mission reaches up to 91.7%.

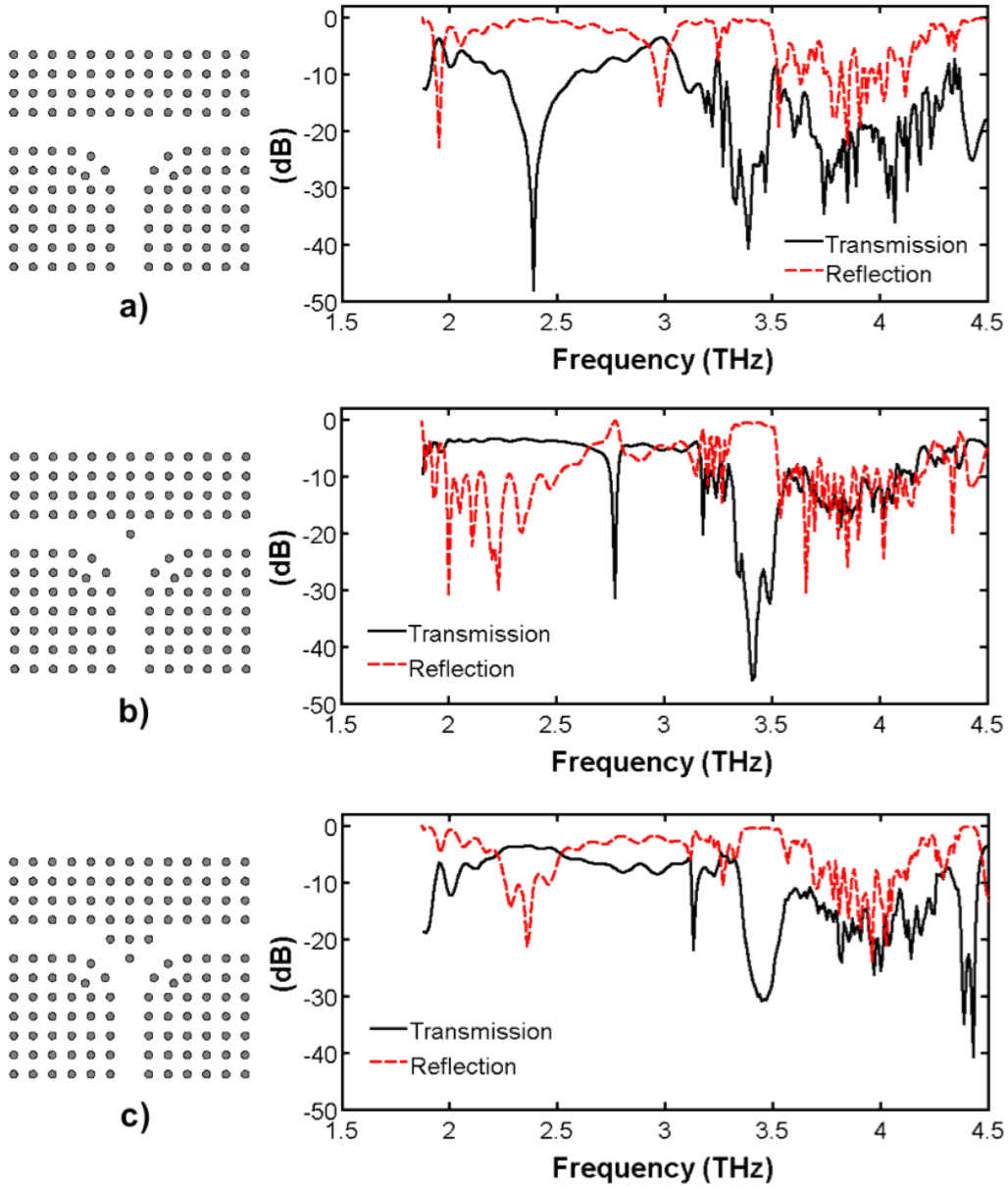

Figure 7.13: Transmission and reflection spectra of T-splitter where the corners are replaced with curved design a) without any additional rods, b) with one additional rods and c) four added rods Schematic illustrations of T-splitters compared are given on the left hand side of each transmission/reflection spectra.

T-splitters can be considered as the combination of two 90° bends. Therefore, the

losses caused by the bending corners before splitting can be prevented by using the improved bending corners. In Figure 7.13, transmission and reflection spectra of three T-splitters in which the corners are replaced with curved design a) without any additional rods, b) with one additional rods and c) four added rods are investigated. The schematic of these structures are shown on the left hand side of the Figure 7.13. In the transmission characteristics of the structure shown in Figure 7.13 a) is very similar to the transmission of the structure shown in Figure 7.12 b). The dip in the 1.88-3.2 THz region is shifted to 2.39 THz. This forms two 6-dB regions between 1.926-1.977 THz and 2.875-3.035 THz, where maximum transmission of 41% and 44% are obtained, respectively. For these regions the total transmission of T-splitters improves up to 2% and 8%, respectively.

As shown in Figure 7.13 b), by adding a rod to the T-splitter structure, a flatter transmission spectrum is obtained. The dip is shifted to 2.77 THz. A very wide 6-dB bandwidth is obtained between 1.886-2.711 THz with a maximal transmission of 45.11% which results in a total transmission increased up to 90%. In 2.798-3.116 THz range, 6-dB bandwidth is achieved with 40% transmission. In Figure 7.13 c) where four rods are added to the original T-splitter presented in Figure 7.13 a), a narrow bandwidth is obtained between 2.167-2.612 THz with maximum transmission of 44.6%.

T-splitter with curved corners and one added rod exhibit wide transmission bandwidth and transmission level. In Figure 7.14, this design is modified by creating a curve in the upper region of the bifurcation area. The position of the rod in the middle is at the same location as that in Figure 7.13 b) but with additional rods. With this design, the dip is shifted from 2.77 THz to 3 THz, creating a wide range between the cut-off and 3THz. A 6-dB bandwidth is obtained between 1.894 and 2.938 THz with transmission of 44%. In the second bandwidth range, 3.076 - 3.15, the transmission is rather low at 33%.

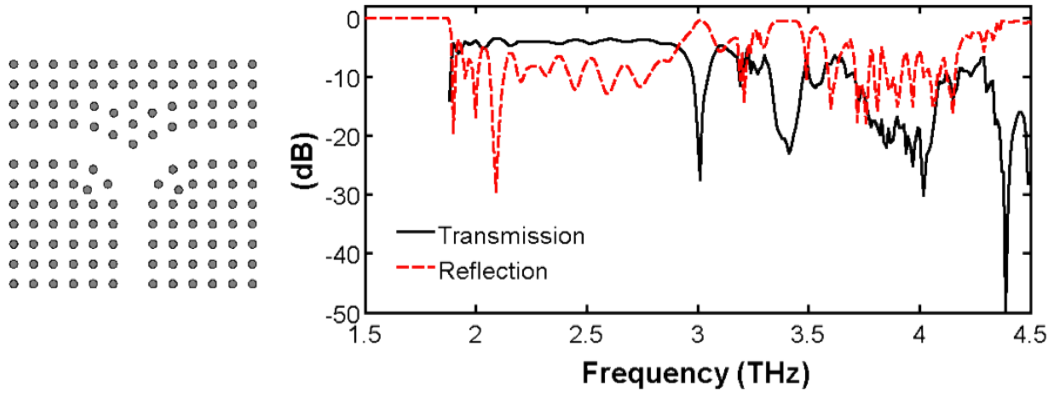

Figure 7.14: Transmission and reflection spectra of T-splitter where the corners are replaced with curved design a) without any additional rods, b) with one additional rods and c) four added rods Schematic illustrations of T-splitters compared are given on the left hand side of each transmission/reflection spectra.

Both T-splitter structures shown in Figure 7.13 b) and Figure 7.14, exhibits good transmission performances. With the first design 90% transmission is obtained with 0.825 THz bandwidth. The second design exhibits the widest bandwidth of 1.044 THz with 88% transmission level.

The transmission spectra of the improved T-splitter, based on curved bend design is enhanced and the reflection losses in 90° bends waveguides are reduced. This design gives the widest transmission bandwidth and a higher transmission level than that of the initial design shown in Figure 7.12 a). Figure 7.15 gives a comparison between the transmission of these structures. An improvement of 8% in transmission level is noticeable.

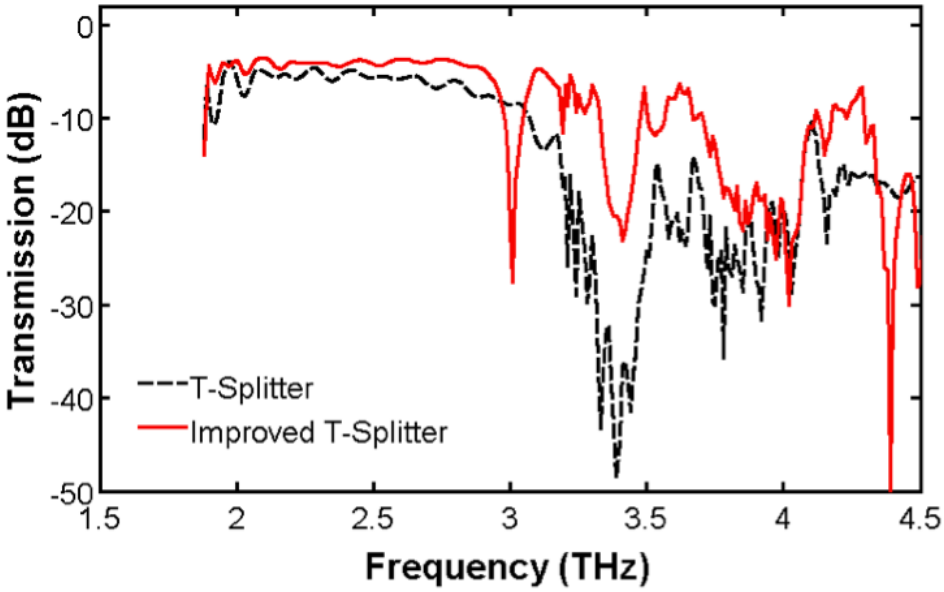

Figure 7.15: Transmission spectra of original T-splitter and the improved T-Splitter.

7.2.2 Y-Splitters

Y-splitters based on metallic cylindrical rods in air medium are also studied. In the structures there exists one input and two output ports. The structure is symmetric with respect to the propagation direction of the incoming wave and wave is shared equally between two output branches.

Two types of Y-splitters are considered, the first Y-splitter consists of three W1 defect connected to achieve 120°-angle between each other, the second one consists of Y-junction whose branches are extended by linear waveguides parallel to the input branch. These Y-splitter structures are based on triangular lattice of copper rods in air with lattice constant, a, and rod radius are set to 50 μm and 15 μm ($0.3a$), respectively.

The transmission spectra of the Y- splitter structures shown in Figure 7.16 a) and b), exhibit very similar characteristics, the 6-dB bandwidths are between 2.697 - 3.55

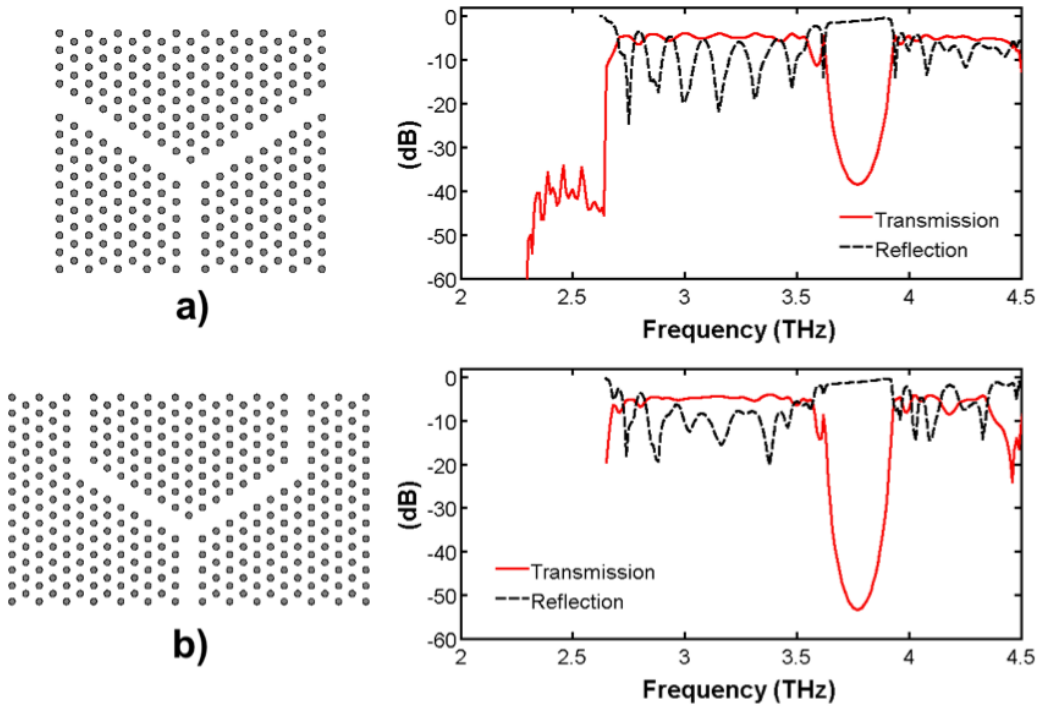

Figure 7.16: Transmission and reflection spectra of Y-splitters. Schematic illustrations of Y-splitters are given on the left hand side of each transmission/reflection spectra. Worth noting that the transmission corresponds to half of the total power transmitted.

THz and 2.729 - 3.571 THz, respectively. The transmission level for both structures is 40%. The reflection spectra exhibit also similarity with each other in terms of transmission levels. In the range 3.9 - 4.5 THz, the first Y-splitter shows slightly better performance than the second one. The 6-dB bandwidth of the first Y-Splitter is between 3.93 and 4.35 THz. In this range the reflection level of second structure is higher than the first one. This can be attributed to number of bending corner, since in the second structure includes two more corners. Due to the fact that 60° counterparts of Y-splitters are subject to losses caused by modal mismatch. Modal mismatch occurs, when an incoming wave expands, within a region larger than the line-defect, it causes the excitation of higher order modes with odd parity. Since the incoming wave cannot propagate in the output waveguides, losses occur. The range

between 2.67 - 3.6 THz corresponds to the 3-dB bandwidth of 60° bend waveguide. The transmission level of 60° bend waveguide is 80%. The transmission spectra of Y-splitters show good agreements with their 60° bends counterparts.

A recent study has been conducted on photonic crystal Y-splitter based on square lattice silicon rods for THz frequencies. 0.224 THz 3-dB bandwidth is obtained (36). Comparing the bandwidth achieved with our metallic photonic crystal structures, the bandwidth of dielectric photonic crystal structures is smaller. This explains by a smaller band-gaps.

7.3 Conclusion

In this chapter, 90° and 60° bend waveguides based on a two dimensional (2D) photonic crystal with metallic cylinders arranged in a square and triangular lattice are studied. Considering W1 and W2 waveguides, five different designs are investigated and assessed in terms of their transmission performance for 90° bend waveguide. A better structure is proposed by increasing the number of rods in the bending arc, thus achieving a superior performance of the transmission characteristics in comparison to that of the former five designs. A comparison of the improved bend waveguide with a linear waveguide shows a significant reduction of the bending losses. Transmission levels of up to 98% within a 2.5 THz bandwidth (from 1.2 to 3.7 THz) have been accomplished. A similar design is proposed for 60° bending corners considering W1 and W3 waveguides. In the single mode region while high transmission up to 95% is achieved, in the multi mode region, bend waveguides experienced losses arising from the multi mode behavior of bending corner. Transmission is affected by the modal mismatch between linear section and bending corner.

Several splitter structures based on square and triangular lattices have been considered. Performances of each structure were compared in terms of bandwidth and their transmission level. Our aim was to achieve a wide frequency bandwidth and high transmission level. T-splitters are optimized with their 90° counterparts the transmission reaches up to 88% with 1.044 THz bandwidth were achieved. Y-splitter based on 60° bend corners produced a 0.853 THz bandwidth with 80% of transmission is obtained.

References

[1] J. D. Joannopoulos, *Photonic crystals: molding the flow of light*. Princeton University Press, Feb. 2008.

[2] M. Wachter, M. Nagel, and H. Kurz, "Metallic slit waveguide for dispersion-free low-loss terahertz signal transmission," *Applied Physics Letters*, vol. 90, p. 061111, 2007.

[3] S. Lin, E. Chow, V. Hietala, P. R. Villeneuve, and J. D. Joannopoulos, "Experimental demonstration of guiding and bending of electromagnetic waves in a photonic crystal," *Science*, vol. 282, pp. 274 –276, Oct. 1998.

[4] A. Mekis, J. C. Chen, I. Kurland, S. Fan, P. R. Villeneuve, and J. D. Joannopoulos, "High transmission through sharp bends in photonic crystal waveguides," *Physical Review Letters*, vol. 77, pp. 3787–3790, Oct. 1996.

[5] V. Kuzmiak, A. A. Maradudin, and F. Pincemin, "Photonic band structures of two-dimensional systems containing metallic components," *Physical Review B*, vol. 50, pp. 16835–16844, Dec. 1994.

[6] D. R. Smith, S. Schultz, N. Kroll, M. Sigalas, K. M. Ho, and C. M. Soukoulis, "Experimental and theoretical results for a two-dimensional metal photonic band-gap cavity," *Applied Physics Letters*, vol. 65, pp. 645–647, Aug. 1994.

[7] M. M. Sigalas, C. T. Chan, K. M. Ho, and C. M. Soukoulis, "Metallic photonic band-gap materials," *Physical Review B*, vol. 52, pp. 11744–11751, Oct. 1995.

[8] F. Gadot, A. de Lustrac, J. M. Lourtioz, T. Brillat, A. Ammouche, and E. Akmansoy, "High-transmission defect modes in two-dimensional metallic photonic crystals," *Journal of Applied Physics*, vol. 85, pp. 8499–8501, June 1999.

[9] M. Bayindir, E. Cubukcu, I. Bulu, T. Tut, E. Ozbay, and C. M. Soukoulis, "Photonic band gaps, defect characteristics, and waveguiding in two-dimensional disordered dielectric and metallic photonic crystals," *Physical Review B*, vol. 64, p. 195113, Oct. 2001.

[10] E. R. Brown and O. B. McMahon, "Large electromagnetic stop bands in metallodielectric photonic crystals," *Applied Physics Letters*, vol. 67, p. 2138, 1995.

[11] K. Rauscher, D. Erni, J. Smajic, and C. Hafner, "Improved transmission for 60° photonic crystal waveguide bends," in *Progress in Electromagnetic Research Symposium*, p. 2528, 2004.

[12] J. Smajic, C. Hafner, and D. Erni, "Design and optimization of an achromatic photonic crystal bend," *Optics Express*, vol. 11, pp. 1378–1384, June 2003.

[13] Y. Zhang and B. Li, "Ultracompact waveguide bends with simple topology in two-dimensional photonic crystal slabs for optical communication wavelengths," *Optics Letters*, vol. 32, pp. 787–789, Apr. 2007.

[14] M. Moghaddam, M. Mirsalehi, and A. Attari, "A 60° photonic crystal waveguide bend with improved transmission characteristics," *Optica Applicata*, vol. 39, no. 2, p. 307317, 2009.

[15] P. Xing, P. Borel, L. Frandsen, A. Harpth, and M. Kristensen, "Optimization of bandwidth in 60° photonic crystal waveguide bends," *Optics Communications*, vol. 248, pp. 179–184, Apr. 2005.

[16] N. Moll and G. L. Bona, "Bend design for the low-group-velocity mode in photonic crystal-slab waveguides," *Applied Physics Letters*, vol. 85, pp. 4322–4324, Nov. 2004.

[17] A. Talneau, L. Le Gouezigou, N. Bouadma, M. Kafesaki, C. M. Soukoulis, and M. Agio, "Photonic-crystal ultrashort bends with improved transmission and low reflection at 1.55 μm," *Applied Physics Letters*, vol. 80, p. 547, 2002.

[18] A. Cicek and B. Ulug, "Polarization-independent waveguiding with annular photonic crystals," *Optics Express*, vol. 17, no. 20, pp. 18381–18386, 2009.

[19] J. S. Jensen and O. Sigmund, "Systematic design of photonic crystal structures using topology optimization: Low-loss waveguide bends," *Applied Physics Letters*, vol. 84, pp. 2022–2024, Mar. 2004.

[20] Y. Zhang and B. Li, "Photonic crystal-based bending waveguides for optical interconnections," *Optics Express*, vol. 14, pp. 5723–5732, June 2006.

[21] J.-i. Sugisaka, N. Yamamoto, M. Okano, K. Komori, T. Yatagai, and M. Itoh, "Development of curved two-dimensional photonic crystal waveguides," *Optics Communications*, vol. 281, pp. 5788–5792, Dec. 2008.

[22] S. Xiao and M. Qiu, "Study of transmission properties for waveguide bends by use of a circular photonic crystal," *Physics Letters A*, vol. 340, pp. 474–479, June 2005.

[23] E. Degirmenci, F. Surre, S. Philippe, R. Maldonado-Basilio, and P. Landais, "Improved bend waveguide design for terahertz transmission," *Terahertz Science and Technology, IEEE Transactions on*, vol. 2, pp. 137 –143, jan. 2012.

[24] L. Dekkiche and R. Naoum, "Optimal design of 90° bend in two dimensional photonic crystal waveguides," *Journal of Applied Sciences*, vol. 8, no. 13, p. 24492455, 2008.

[25] A. Chutinan, M. Okano, and S. Noda, "Wider bandwidth with high transmission through waveguide bends in two-dimensional photonic crystal slabs," *Applied Physics Letters*, vol. 80, p. 1698, 2002.

[26] E. Chow, S. Y. Lin, J. R. Wendt, S. G. Johnson, and J. D. Joannopoulos, "Quantitative analysis of bending efficiency in photonic-crystal waveguide bends at λ = 1.55 μm wavelengths," *Optics Letters*, vol. 26, pp. 286–288, Mar. 2001.

[27] M. Loncar, D. Nedeljkovic, T. Doll, J. Vuckovic, A. Scherer, and T. P. Pearsall, "Waveguiding in planar photonic crystals," *Applied Physics Letters*, vol. 77, p. 1937, 2000.

[28] S. Olivier, H. Benisty, C. Weisbuch, C. J. M. Smith, T. F. Krauss, R. Houdr, and U. Oesterle, "Improved 60° bend transmission of Submicron-Width waveguides defined in Two-Dimensional photonic crystals," *Journal of Lightwave Technology*, vol. 20, p. 1198, July 2002.

[29] G. Dahlquist and . Bjrck, *Numerical methods in scientific computing*. SIAM, 2008.

[30] M. Bayindir, B. Temelkuran, and E. Ozbay, "Photonic-crystal-based beam splitters," *Applied Physics Letters*, vol. 77, p. 3902, 2000.

[31] S. Fan, S. G. Johnson, J. D. Joannopoulos, C. Manolatou, and H. A. Haus, "Waveguide branches in photonic crystals," *Journal of the Optical Society of America B*, vol. 18, pp. 162–165, Feb. 2001.

[32] T. Sndergaard and K. H. Dridi, "Energy flow in photonic crystal waveguides," *Physical Review B*, vol. 61, pp. 15688–15696, June 2000.

[33] S. Boscolo, M. Midrio, and T. F. Krauss, "Y junctions in photonic crystal channel waveguides: high transmission and impedance matching," *Optics Letters*, vol. 27, pp. 1001–1003, June 2002.

[34] S. Y. Lin, E. Chow, J. Bur, S. G. Johnson, and J. D. Joannopoulos, "Low-loss, wide-angle y splitter at approximately ˜1.6 μm wavelengths built with a two-

dimensional photonic crystal," *Optics Letters*, vol. 27, no. 16, pp. 1400–1402, 2002.

[35] R. Wilson, T. J. Karle, I. Moerman, and T. F. Krauss, "Efficient photonic crystal y-junctions," *Journal of Optics A: Pure and Applied Optics*, vol. 5, pp. S76–S80, July 2003.

[36] S. Li, H. Zhang, Q. Wen, F. Bai, W. Ling, Y.-s. Xie, and Y. Li, "Improved y-splitter photonic crystal waveguides in terahertz regime," *Applied Physics B*, vol. 99, pp. 709–716, Mar. 2010.

Chapter 8

CONCLUSIONS AND FUTURE WORK

With the development of compact THz sources and efficient detection scheme, low cost, low loss and compact THz devices such as filters, waveguides, polarizers and resonant cavities are required. In this thesis, metallic photonic crystals have been extensively studied in order to design a variety of waveguiding components, such as waveguides, bends and splitters for the THz regime. Metallic photonic crystals have been selected over dielectric photonic crystals as they exhibit some key advantages such as wider band-gaps and smaller sizes. Moreover, metals are a more reasonable choice for applications requiring high power in THz.

Firstly, fundamental concepts of photonic crystals have been introduced and photonic band-gap calculations have been presented. Numerical methods used for photonic crystal calculations have been explained. Through out this study, Finite Element Method has been used to analyse metallic photonic crystals.

The transmission and dispersion characteristics of 2D metallic photonic crystals ar-

ranged in square and triangular lattice patterns for E- and H-polarization have been analysed according to design parameters such as size and location of the metallic rods, lattice constant of the structures, frequency and angle of incident of the wave. In the computation investigations, the position and width of the photonic band gap are well established in transmission spectra. Both square and triangular lattice structures show large photonic band gaps for E- polarization in the THz band.

Based on these investigations, 2D metallic photonic crystal waveguides formed by line defects have been studied. Transmission and dispersion characteristics of metallic photonic crystal waveguides have been calculated. Band-gap diagrams are important for selecting the frequency band for which the photonic crystal structure is highly reflective. However, band-gap diagrams become inadequate to explain the transmission losses within the band-gap frequencies. By examining modal behaviour of guided modes, these losses can be explained. In a waveguide both symmetric and anti-symmetric modes are active. The losses within the band-gap frequencies are associated with interaction, i.e. coupling, between the guided modes of different parity. There is a strong correlation between the dispersion diagrams and transmission spectra of the waveguides. In the transmission spectrum of a waveguide, the losses experienced due to a transmission dip are explained by the existence of mini stop-bands. The calculated transmission results show excellent agreement with dispersion diagrams. The positions and the width of mini stop-bands in dispersion diagrams are well reproduced in the transmission spectra as transmission losses.

Compared to W1 waveguides, waveguides with larger widths showed better characteristics for low loss THz transmission. Not only the transmission bandwidths increase but also the transmission levels are also higher, independent of the rod sizes. Up to 96% transmission was obtained in square lattice W2 waveguide, for which a 2.8 THz-wide bandwidth was obtained. In triangular W3, a 2.73 THz-wide

bandwidth was achieved with transmission levels up to 99.5%.

Finally, we focused our attention to the bend waveguides and splitters. Sharp bend waveguides suffer from high reflection losses which can be reduced by an appropriate design. Our aim was to maintain the high transmission and increase bandwidth further. 90° and 60° bend waveguides based on a two dimensional photonic crystal with metallic cylinders arranged in a square and triangular lattice have been optimised. A significant reduction of the bending losses was achieved with curved bend design. Transmission levels of up to 98% within a 2.5 THz bandwidth (from 1.2 to 3.7 THz) have been accomplished. A similar design is proposed for 60° waveguides. While high transmission up to 95% is achieved in the single mode region, in the multi mode region bend waveguides experience losses arising from the multimodal behaviour of bending corner. The transmission is affected by the modal mismatch between linear section and bending corner. When T-splitters are optimized with their 90° counterparts, the transmission reaches up to 88% with 1.044 THz bandwidth achieved. A Y-splitter based on 60° bend corners produced a 0.853 THz bandwidth with 80% transmission.

There are two prominent areas in which future studies could be pursued: surface plasmons or metamaterials. Surface plasmons are associated with evanescent electromagnetic fields that extend into the dielectric medium at the metal-dielectric interface. Surface plasmon excitation in metallic nanoparticles provides a strongly enhanced electromagnetic field. Coupling into the plasmonic modes enhancement of the transmission at the interface and guided THz waves in sub-diffraction length scale should be achieved. A study of surface plasmon propagation through metallic nanoparticles should be conducted.

Metamaterials have recently received a lot of attention due to their ability to exhibit enhanced electromagnetic responses compared to natural materials. These are

composed of sub-wavelength structures organised together to exhibit the required values of permittivity and permeability in the desired frequency range. Negative refraction and artificial magnetism are some examples of properties that can be obtained and controlled with these materials. These metamaterials should be useful in the design of THz devices, such as lenses. More computation studies should be done on this topic. The positive point is that these studies can be carried out based on the work presented in this report.

Appendix A

LIST OF PUBLICATIONS

Book chapter:

"THz Waveguide and Bends Based on Metallic Photonic Crystals", E. Degirmenci, F. Surre, and P. Landais in Terahertz and Mid Infrared Radiation: Generation, Detection and Applications, 1st ed., Mauro F. Pereira, Ed., Oleksiy Shulika, Ed.,Springer, Mar. 2011, pp.23-27

Peer reviewed journal:

"Improved Bend Waveguide Design for Terahertz Transmission", E. Degirmenci, F. Surre, S. Philippe, R. Maldonado-Basilio, and P. Landais, Terahertz Science and Technology, IEEE Transactions on, vol.2, no.1, pp.137-143, Jan. 2012

Peer reviewed conferences:

"Improved 60° Photonic Crystal Bend Waveguides for THZ Range", E. Degirmenci, F. Surre, and P. Landais, Photonics Ireland 2011 Conference, September 7-9, 2011, Dublin, Ireland.

"Improved Photonic Crystal Based 90° Bends for THz Transmission", E. Degir-

menci, F. Surre and P. Landais, IRMMW-THz 2010, The 35th International Conference on Infrared, Millimeter Wave and Terahertz Waves, September 5-10, 2010, Rome, Italy

"Metallic Band-Gap Crystals for THz Transmission", E. Degirmenci, F. Surre and P. Landais, RIA The Royal Irish Academy Committee on Communications and Radio Science, Wireless as an enabling technology - "Innovation for a Critical Infrastructure", April 21-22, 2010, Dublin, Ireland

"2-D Metallic Photonic Crystal Waveguide Bends for Terahertz Range", E. Degirmenci, F. Surre and P. Landais, OWTNM 10, The XIXth International Workshop on Optical Waveguide Theory and Numerical Modelling, April 4-9, 2010, Cambridge, UK.

"Guiding and Bending Through 2-D THz Metallic Photonic Crystals", E. Degirmenci, F. Surre and P. Landais, TERA-MIR 2009, NATO Advanced Research Workshop on Terahertz and Mid Infrared Radiation: Basic Research and Applications, November 3-6, 2009, Turunç-Marmaris, Turkey

"2-D Numerical Analysis of Metallic Band-Gap Crystal Waveguide in THz", E. Degirmenci, F. Surre, P. Landais, IRMMW-THz 2009, The 34th International Conference on Infrared, Millimeter, and Terahertz Waves, September 21-25, 2009, Busan, South Korea.

"Design of 2D TeraHertz Band-gap Photonic Waveguides Using an Accelerated Integral Equation Technique", D. Bogusevschi, E. Degirmenci, C. Brennan, P. Landais, International Conference on Electromagnetics in Advanced Applications, September 14-18, 2009, Torino, Italy.

“Transmission Analysis of 2D Metallic Photonic Band-Gap Waveguide in THz Range”, E. Degirmenci and P. Landais, Photonics Ireland 2009, September 14-16, 2009, Kinsale, County Cork, Ireland

“CuCl: A Potential Material for THz Photonic Crystals”, D. Danieluk, A.L. Bradley, E. Degirmenci, P. Landais, Photonics Ireland 2009, September 14-16, 2009, Kinsale, County Cork, Ireland

“Numerical Analysis of Metallic Band-Gap Crystals in THz Range”, E. Degirmenci, F. Surre, P. Landais, SIOE 2009, Semiconductor and Integrated Optoelectronics, April 6-8, 2009, Cardiff/Wales, UK

“CuCl Photonic Crystal THz Waveguide”, D. Danieluk, A. L. Bradley,E. Degirmenci, P. Landais, SIOE 2009, Semiconductor and Integrated Optoelectronics, April 6-8, 2009, Cardiff/Wales, UK

“A Theoretical Study of Metallic Rectangular Waveguides in the THz Range”, E. Degirmenci, F. Surre, and P. Landais, China-Ireland International Conference on Information and Communications Technologies, September 26-28, 2008, Beijing, China

“A Theoretical Study of Metallic Rectangular Waveguides in the THz Range”, E.Degirmenci, F.Surre, P.Landais, In: IOP ed.THz sensing: Techniques and Applications, June 30, 2008, London, UK

Appendix B

BÉZIER CURVE APPROXIMATION

A Bézier curve is a parametric curve used in computer graphics and related fields, mostly to model smooth curves for a given fewest number of discrete points. The general form for the nth degree Bézier curve is expressed as a linear interpolation between two $(n-1)^{th}$ degree Bézier curves. A Bézier curve is denoted by $B(t)$ and defined by a set of control points $P_0, P_1, \ldots, P_n$. The curve is always contained in the convex hull of its control points since each point of the curve is a linear combination of its control points. The general form of the Bézier curves is [1]:

$$B(t) = \sum_{i=0}^{n} \binom{n}{i} (1-t)^{(n-i)} t^i P_i \tag{B.1}$$

$$B(t) = (1-t)^n P_0 + \binom{n}{1} (1-t)^{(n-1)} t P_i + \cdots + \binom{n}{n-1} (1-t) t^{n-1} P_{n-1} + t^n P_n, \quad t \in [0,1] \tag{B.2}$$

where t is the weight is given by $0 \leq t \leq 1$ and $\binom{n}{i}$ is the binomial coefficient:

$$\binom{n}{i} = \frac{n!}{i!(n-1)!} \tag{B.3}$$

A quadratic Bézier curve is a 2nd order Bézier curve which traces the path with the function $B(t)$ for given points P_0, P_1 and P_2. It can be interpreted as the linear interpolant corresponding to the linear Bézier curves from P_0 to P_1 and from P_1 to P_2 respectively.

$$B(t) = (1-t)^2 P_0 + 2(1-t) + P_1 + t^2 P_2, \quad t \in [0,1] \tag{B.4}$$

In order to create an arc between two linear sections with a 60°-angle, 3 control points are needed to construct a quadratic Bézier curve. P_0 and P_2 are the end points and P_1 is the intermediate point. Between two linear sections $P_0 - P_1$ and $P_1 - P_2$, without lying on the intermediate point, a Bézier curve can be plotted following the below equation between end points. The Bézier curve is tangent to $P_0 - P_1$ and $P_1 - P_2$ for weight $t = 0$ and $t = 1$. This can be seen from the derivative of the Bézier curve:

$$B'^{(}t) = 2(1-t) + (P_1 - P_0) + 2t(P_2 - P_1) + P_1 + t^2 P_2 \tag{B.5}$$

When computing points of a Bézier curve, in order to accelerate the calculations the Horner's scheme is used to express the Bézier polynomial for the evaluation of a single point. Horner's rule provides a fast and efficient method of evaluating polynomials in monomial form. Horner's rule requires n multiplications and n additions for the evaluation of a point [2].

At a specific value of x, In order to evaluate the given polynomial

$$p(x) = \sum_{i=0}^{n} a_i x_i = a_0 + a_1 x + a_2 x^2 + a_3 x^3 + \cdots + a_n x^n \tag{B.6}$$

Using Horner's rule the polynomial can be written in the form

$$p(x) = a_0 + x\left(a_1 + x(a_2 + \cdots + x(a_{n-1} + a_n x) \cdots)\right) \tag{B.7}$$

where $a_0, \cdots, a_n$ are the real numbers.

1. G. Dahlquist and Å. Björck, Numerical methods in scientific computing. SIAM, 2008.

2. N. J. Higham, Accuracy and stability of numerical algorithms. SIAM, 1996.